Université Fédérale
Toulouse Midi-Pyrénées

THÈSE

En vue de l'obtention du
DOCTORAT DE L'UNIVERSITÉ DE TOULOUSE

Délivré par l'Université Toulouse 3 - Paul Sabatier

Présentée et soutenue par

Luis Enrique OLIVERA GUERRA

Le 11 décembre 2019

Suivi des ressources en eau des cultures irriguées par télédétection multi-spectrales optique/thermique

---

Ecole doctorale : **SDU2E - Sciences de l'Univers, de l'Environnement et de l'Espace**

Spécialité : **Surfaces et interfaces continentales, Hydrologie**

Unité de recherche :
CESBIO - Centre d'Etudes Spatiales de la Biosphère

Thèse dirigée par
Olivier MERLIN et Salah ER-RAKI

Jury

M. Thierry PELLARIN, Rapporteur
Mme Catherine OTTLé, Rapporteure
M. Jean-Louis ROUJEAN, Examinateur
M. SAID KHABBA, Examinateur
M. Olivier MERLIN, Directeur de thèse
M. Salah ER-RAKI, Co-directeur de thèse

A mis Padres
…en memoria de mi Taita

To my parents
…in memory of my Father

Acknowledgement

First and foremost, I would like to thank my supervisors Olivier Merlin and Salah Er-Raki for the trust and freedom they have given me to carry out my PhD in the best possible manner. Thanks to them for their support and guidance, especially in the moments when I saw that there was no way out of trouble. I am deeply grateful to Olivier for giving me so many wonderful opportunities, including this PhD and working with him in Chile and Morocco before this PhD. Many thanks Olivier, the best supervisor I could have had.

I am grateful to the director of the CESBIO laboratory, Laurent Polidori, and also Yann Kerr not only for having welcomed me into the lab but also for their friendly support.

I would like to thank the jury members of this thesis and the members of my thesis committee, who have kindly accepted this role.

I also gratefully acknowledge the funding sources (CONICYT-CHILE PhD fellowship and H2020 RISE REC project) that made my PhD thesis possible.

I am also grateful to Fransesc Ferrer, Maria-José Escorihuela and Saïd Khabba, for giving me the opportunity to join their team as intern, and who gave access to the laboratory and research facilities. Special mention goes to Fransesc for giving me the opportunity to carry out an experimental campaign in Lleida during my stay in LabFerrer. Thanks to the LabFerrer members (Mireia, Gemma, Manel, Carla and Astrid) who have been immensely welcoming, helpful and friendly and because the work with them passes with good humor. I also thank Maria-José for the warm welcome she has provided me at isardSAT, as well as the trust placed in me to apply to proposals for future work together. Thanks to CESBIO, isardSAT and LMI-TREMA teams for great moments spent in your centers. Special mention goes to Emilie from CESBIO to support and manage my different stays.

My thanks also to the friends met during these last 3 years. Special thanks to my '*hermano Negrito Hakim de Foumouzguido*' for the great and fun moments experienced here and there. Special mention to *Magic*, the best *coloc* ever, including hospitality services with the best dishes (breakfast and dinner!), support and personal coaching to get up early during the last month in order to finish my thesis.

Last and not least, I would like to thank my parents, brother, sister, aunts and uncles for their love and spiritual support. And most of all, I am deeply grateful to my lovely and *mignonne copine* Nicole, for her love, encouragement and faithful support. Thanks to Nicole for being supportive and her help on organizing ideas, for her motivation and our clarifying discussions.

Thanks to the Universe and its wonderful Energies that have given me so much.

Abstract

Irrigated agriculture is an important pressure on water resources, consuming more than 70% of the mobilized freshwater resources at global scale. However, the information on irrigation, which is crucial for the sustainability of water resources in agricultural regions, is often unavailable. Therefore, monitoring and quantifying the crop water budget over extended areas is critical.

This PhD thesis aims to integrate optical/thermal remote sensing data into a simplified crop water balance model for monitoring the water budget of irrigated agricultural areas. For this purpose, an innovative and stepwise approach is developed to estimate simultaneously the irrigation, the evapotranspiration (ET) and the root-zone soil moisture (RZSM) at crop field scale (100 m resolution) on a daily basis.

In a first step, a feasibility study is carried out using in situ optical/thermal measurements collected over a winter wheat field of the Haouz plain, Morocco. A crop water stress coefficient (Ks) derived from the land surface temperature (LST) and vegetation index (NDVI) is first translated into RZSM diagnostic estimates, which is then used to estimate irrigation amounts and dates along the season. Next, the retrieved irrigations allow forcing the dual crop coefficient FAO-56 model (FAO- 2Kc) to re-analyze the daily ET and RZSM. The re-analyzed RZSM is significantly improved with respect to RZSM diagnostic estimates, reaching the same accuracy as that obtained by using actual irrigations (RMSE = 0.03 m^3m^{-3} and $R^2 = 0.7$). However, the approach needs to be tested using satellite data in order to demonstrate its real applicability.

The next step consists in adapting the previous approach to spatially integrated but temporally sparse Landsat NDVI/LST data. For this purpose, a contextual method is first used to derive Landsat-derived estimates (crop coefficients and RZSM), which are used to re-initialize a FAO-based model and propagate this information daily throughout the season. Then, the retrieved pixel-scale irrigations are aggregated to the crop field-scale. The approach is applied to three agricultural areas (12 km by 12 km) in the semi-arid region of Haouz Plain, and validated over five winter wheat fields with different irrigation techniques (drip-, flood- and no-irrigation). The results show that the seasonal irrigation amounts over all the sites and seasons is accurately estimated (RMSE = 44 mm and R = 0.95), regardless of the irrigation techniques. Acceptable errors (RMSE = 27 mm and R = 0.52) are obtained for irrigations cumulated over 15 days, but poor agreements at daily to weekly scales are found in terms of irrigation. However, the daily RZSM and ET are accurately estimated using the retrieved irrigation and are very close to those estimated using actual irrigations (overall RMSE equal to 0.04 m^3m^{-3} and 0.83 $mm.d^{-1}$ for RZSM and ET, respectively).

In a final step, an operational LST disaggregation method based on NDVI/LST and Landsat/MODIS relationships is implemented for enhancing the spatio-temporal resolution of LST as input to the irrigation retrieval approach. The disaggregation method is tested over an arid region of Chile and our study area in the Haouz Plain. Combining both disaggregated LST and Landsat LST data sets, thanks to the increase in the temporal frequency of LST data, results in a better detection of irrigation events and amounts. The overall RMSE of cumulated irrigation at different time scales is decreased from 46 to 34 mm, while the R is increased from 0.50 to 0.64. Consistently, the RZSM estimated using the disaggregated LST in addition to Landsat LST as input is improved by 26% and 14% in terms of RMSE and R, respectively.

Keywords: remote sensing optical/thermal, irrigation, root-zone soil moisture, evapotranspiration, water balance model.

Résumé

L'agriculture est une pression importante sur les ressources en eau, consommant plus de 70% de l'eau douce mobilisée à l'échelle mondiale. Cependant, les informations sur l'irrigation, pourtant cruciales pour assurer une durabilité de la ressource, sont souvent indisponibles. Par conséquent, il est essentiel d'estimer les différents termes du bilan d'eau des cultures à grande échelle.

Cette thèse vise à intégrer les données de télédétection optique/thermique dans un modèle simplifié de bilan d'eau des cultures pour le suivi du bilan d'eau des zones agricoles irriguées. Une approche innovante est développée pour estimer simultanément l'irrigation, l'évapotranspiration (ET) et l'humidité en zone racinaire (RZSM) journalières à l'échelle de parcelle (ou à 100 m de résolution).

Dans une première partie, une étude de faisabilité est réalisée à l'aide de mesures optiques/thermiques in situ collectées sur une parcelle de blé d'hiver dans la plaine du Haouz, au Maroc. En pratique, un coefficient de stress hydrique (Ks) dérivé de la température de surface (LST) et d'un indice de végétation (NDVI) est d'abord traduit en une première approximation de RZSM, qui est utilisée pour estimer les quantités et les dates d'irrigation au cours de la saison. Les irrigations obtenues permettent ensuite de forcer le modèle FAO-56 à coefficient cultural double (FAO-2Kc) et de fournir des ré-analyses ET et RZSM journalières. La RZSM ré-analysée est significativement améliorée par rapport aux premières estimations de RZSM, atteignant la même précision que celle obtenue en utilisant les irrigations réelles (RMSE=0,03 m^3m^{-3} et R^2=0,7). Toutefois, l'approche doit encore être testée avec des données satellitaires afin de démontrer son applicabilité dans le cas réel.

La deuxième partie consiste à adapter l'approche précédente aux données optiques/thermiques Landsat à faible fréquence temporelle. Une méthode contextuelle est utilisée pour obtenir des estimations dérivées de Landsat (coefficients de culture et RZSM), qui sont utilisées pour réinitialiser un modèle basé sur le FAO-2Kc et propager ces informations à l'échelle journalière tout au long de la saison. Ensuite, les irrigations obtenues à l'échelle des pixels sont agrégées à la parcelle pour ré-analyser l'ET et la RZSM journalières. L'approche est appliquée sur trois zones agricoles (12 km x 12 km) de la région semi-aride de la plaine du Haouz et validée sur cinq parcelles de blé d'hiver avec différentes techniques d'irrigation (goutte à goutte, gravitaire et sans irrigation). Les résultats montrent que l'irrigation saisonnière sur l'ensemble des sites et des saisons est estimée avec une bonne précision (RMSE=44 mm et R=0,95), et ce quelque soit la technique d'irrigation. Des erreurs acceptables (RMSE=27 mm et R=0,52) sont obtenues pour des irrigations cumulées sur 15 jours, mais les erreurs sont beaucoup plus importants à l'échelle journalière et hebdomadaire. Cependant, les RZSM et ET

journalières sont estimées avec précision à l'aide de des irrigations inversées et sont même très proches de celles estimées à l'aide des irrigations réelles (RMSE=0,04 m^3m^{-3} pour RZSM et RSME=0,83 $mm.d^{-1}$ pour ET).

Dans la troisième partie, une méthode opérationnelle de désagrégation des données de LST basée sur les relations NDVI/LST et Landsat/MODIS est mise en œuvre pour améliorer la résolution spatio-temporelle de la LST utilisée en entrée de l'approche d'estimation de l'irrigation. La méthode de désagrégation est testée sur une région aride du Chili et sur notre zone d'étude dans la plaine du Haouz. La combinaison des données deLST Landsat et des données de LST désagrégées permet, grâce au gain en résolution temporelle, une meilleure détection des événements et des quantités d'irrigation. Le RMSE global de l'irrigation cumulée à différentes échelles de temps est réduite de 46 à 34 mm, tandis que le R passe de 0,50 à 0,64. La RZSM estimée à partir du jeu de LST désagrégée en plus des observations Landsat est améliorée de 26% et 14% en termes de RMSE et de R, respectivement.

Mots-clés : télédétection optique/thermique, irrigation, humidité en zone racinaire, évapotranspiration, modèle de bilan hydrique.

Contents

ACKNOWLEDGEMENT III
ABSTRACT V
RÉSUMÉ VII
LIST OF FIGURES XIII
LIST OF TABLES XVII
CHAPTER 1. INTRODUCTION 1
1.1. General context *2*
1.2. Remote sensing data relevant to crop water budget monitoring *3*
1.2.1. Visible – Near Infrared data *5*
1.2.2. Thermal infrared data *6*
1.2.3. Microwave data *8*
1.3. Modelling the crop water budget components from remote sensing data *10*
1.3.1. Evapotranspiration modelling *11*
1.3.2. Root-Zone Soil Moisture modelling *14*
1.3.3. Irrigation modelling *15*
1.4. Objectives *17*
CHAPTER 1. INTRODUCTION (FRANÇAIS) 21
1.1. Contexte général *22*
1.2. Données de télédétection pertinentes pour le suivi du bilan hydrique des cultures *23*
1.2.1. Données Visible - Proche infrarouge *25*
1.2.2. Données thermiques infrarouges *27*
1.2.3. Données micro-ondes *29*
1.3. Modélisation des composantes du bilan hydrique des cultures à l'aide de la télédétection *31*
1.3.1. Modélisation de l'évapotranspiration *32*
1.3.2. Modélisation de l'humidité en zone racinaire *36*
1.3.3. Modélisation de l'irrigation *37*
1.4. Objectifs *39*
CHAPTER 2. DATA 43
2.1. Introduction *44*

2.2. Morocco: Haouz Plain ... *44*
2.2.1. Meteorological data ... *46*
2.2.2. Flux data (Eddy-covariance system) ... *46*
2.2.3. Soil Moisture ... *46*
2.2.4. Irrigation ... *47*
2.2.5. Fractional green vegetation cover ... *48*
2.2.6. Temperature data ... *50*
2.3. Chile: Copiapó Valley ... *51*
2.3.1. Meteorological data ... *52*
2.3.2. Ground-based land surface temperature ... *53*
2.4. Remote sensing data ... *53*
2.4.1. Landsat data ... *53*
2.4.2. ASTER Global Emissivity Datasets (ASTER GED) ... *56*
2.4.3. MODIS data ... *56*
2.5. Conclusion ... *57*
CHAPTER 3. RETRIEVING IRRIGATION AND WATER BUDGET COMPONENTS: A FEASIBILITY STUDY ... 59
3.1. Introduction ... *60*
3.2. FAO-56 dual crop coefficient method ... *61*
3.2.1. Basal crop coefficient (Kcb) ... *61*
3.2.2. Evaporation reduction coefficient (Ke) ... *62*
3.2.3. Water stress coefficient (Ks) ... *63*
3.3. Remote sensing data integrated into FAO-2Kc ... *64*
3.4. Estimating water budget components from ground-based optical/thermal data ... *65*
3.4.1. Implementation of a contextual method at in situ level ... *66*
3.4.2. Root-zone and soil surface water status from optical/thermal data: Ks and Kr estimation ... *70*
3.4.3. First-guess water budget components ... *70*
3.4.4. Re-analysis of water budget components ... *73*
3.5. Summary and conclusions ... *75*
3.6. ARTICLE: Estimating the water budget components of irrigated crops: Combining the FAO-56 dual crop coefficient with surface temperature and vegetation index data ... *76*
CHAPTER 4. REAL-LIFE APPLICATION OF THE IRRIGATION RETRIEVAL APPROAC 89
4.1. Introduction ... *90*
4.2. Issues for implementing the crop water balance modelling over large areas ... *91*
4.3. Contextual methods for detecting soil and crop water status ... *91*

4.4. Landsat-derived estimates integrated into a crop water balance model for irrigation retrieval *93*

4.5. From pixel-scale to field-scale irrigation *95*

4.6. Crop coefficients Kcb and Ke derived from contextual methods *97*

4.7. Main results of the spatial application to Haouz Plain *100*

4.8. Summary and conclusions *105*

4.9. ARTICLE: Irrigation retrieval from Landsat optical/thermal data integrated into a crop water balance model: A case study over winter wheat fields in a semi-arid region *106*

CHAPTER 5. DISAGGREGATION OF THERMAL DATA FOR IMPROVING THE WATER BUDGET COMPONENTS ESTIMATION 125

5.1. Introduction *126*

5.2. Disaggregation of LST data *127*

5.2.1. Operational method for disaggregating LST data *128*

5.3. Application in Copiapo River Basin – Chile: main results *131*

5.3.1. Disaggregated LST product *132*

5.3.2. Operational estimation of ET every 8 days *134*

5.4. Application over a winter-wheat field (R3) in Haouz Plain – Morocco *136*

5.4.1. Disaggregated LST *137*

5.4.2. Irrigation retrieval by using disaggregated LST *138*

5.4.3. Daily RZSM and ET *141*

5.5. Summary and conclusions *143*

5.6. ARTICLE: An operational method for the disaggregation of land surface temperature to estimate actual evapotranspiration in the arid region of Chile *144*

CHAPTER 6. CONCLUSIONS AND PERSPECTIVES 157

6.1. Summary of results *158*

6.2. Identifying the main limitations of the methods *160*

6.2.1. Irrigation retrieval approach *161*

6.2.2. LST disaggregation method *162*

6.3. Perspectives *163*

6.3.1. Towards the improvement in spatial and temporal resolution *163*

6.3.2. Towards the use of radar data for a better representation of hydrological processes *164*

6.3.3. Partitioning soil/vegetation components *165*

CHAPTER 6. CONCLUSIONS ET PERSPECTIVES (FRANÇAIS) 169

6.1. Résumé des résultats *170*

6.2. Principales limites des méthodes *173*
6.2.1. Approche d'estimation d'irrigation *173*
6.2.2. Méthode de désagrégation LST *175*
6.3. Perspectives *176*
6.3.1. Vers l'amélioration de la résolution spatiale et temporelle *176*
6.3.2. Vers l'utilisation des données radar pour une meilleure représentation des processus hydrologiques *177*
6.3.3. Partition entre les composants de sol et de végétation *178*
BIBLIOGRAPHY 181
APPENDICES 200
Appendix 1. Reference evapotranspiration (ET_0) *200*
Appendix 2. Energy balance model for bare soil *203*
Appendix 3. List of publications *206*
Appendix 4. List of presentations and posters in peer reviewed conferences *207*

List of Figures

Fig. 1.1. Global distribution of Mediterranean regions. 2
Fig. 1.2. The ability of multi-spectral remote sensing data to characterize the soil and vegetation states that are useful for monitoring the crop water budget. Source: Amazirh (2019). 4
Fig. 1.3. Different spatial and temporal resolution of current and near future thermal satellite observations related to different target observation scales. 7
Fig. 1.4. Schematic representation of surface energy (A), water (B) and carbon cycle. ET is represented as latent heat flux in A, as soil evaporation and plant transpiration in B and is strongly linked to photosynthesis and soil respiration in C. Source: Bonan (2008). 12
Fig. 1.5. Schematic representation of soil moisture in root zone and the relation with evaporative fraction and vegetation water stress. Source: based on Allen et al. (1998). 14
Fig. 1.1. Distribution globale des régions méditerranéennes. 22
Fig. 1.2. Différentes résolutions spatiales et temporelles des observations actuelles et futures des satellites thermiques liées aux différentes échelles d'observation ciblées. 28
Fig. 1.3. Schéma représentant les cycles de l'énergie de surface (A), de l'eau (B) et du carbone. L'ET est représentée comme un flux de chaleur latente en A, comme l'évaporation du sol et la transpiration des plantes en B et l'ET est fortement liée à la photosynthèse et à la respiration du sol en C. Source: Bonan (2008). 33
Fig. 1.4. Schéma représentant l'humidité du sol dans la zone racinaire et sa relation avec la fraction évaporative et le stress hydrique de la végétation. Source: based on Allen et al. (1998). 35
Fig. 2.1. Study areas and field crops where the developed approach is evaluated. 45
Fig. 2.2. Irrigation events along the agricultural growing for the winter wheat field in R3 and Chichaoua area for the different seasons. 48
Fig. 2.2. Daily NDVI, fraction of green vegetation cover (fvg) and fraction of total vegetation cover (fc) along the agricultural growing for the winter wheat field in R3 area. 50
Fig. 2.3. Copiapó Valley divided in 6 sectors (red line) over which the study area (blue line) and the meteorological station over olive and vineyard crops (square and circle, respectively) are located in the sectors 5 and 6. In the figure the land cover of the main crops are showed: olives, vineyards and pomegranates. 52
Fig. 2.4. Relative spectral responses (RSR) and effective wavelengths (λ) for Landsat-7 band 6 (B6_ L7), Landsat-8 band 10 (B10_L8) and ASTER bands 13 and 14 (AST_13 and AST_14) sensors. 55

Fig. 2.5. Comparison between Landsat soil emissivity against the simulated Landsat soil emissivity from the linear regression by using ASTER bands 13 and 14 (Eq. 2.7) for the 52 soil types available in the ASTER spectral library (Baldridge et al., 2009). The dotted line represents the line 1:1. 56
Fig. 3.1. Basal crop coefficient curve during for the four stages throughout the growing season (Allen and Pereira, 2009). 62
Fig. 3.2. Flowchart of the estimation of the main crop water budget components (irrigation, RZSM and ET) from the main intermediate variables. 66
Fig. 3.3. Polygon defined in the LST-fc space where four distinct zones A, B, C, and D are constrained. Tv and Ts are estimated from the hourglass approach (left plots) as in Merlin et al., (2012) except in zones A and D, where Tv and Ts are estimated respectively from TVDI method to avoid constant values (right plots). In the hourglass approach, the interception of the grey dotted lines in the bare soil (fc=0) and in the full-cover vegetation (fc=1) edges represent the maximum and minimum soil and vegetation temperatures, which are averaged to estimate the most probable Ts and Tv, respectively. 70
Fig. 3.4. Comparison of evapotranspiration (ET), transpiration (T) and evaporation (E) temporal series over the R3-4ha site (winter wheat field) for the 2002-2003 season estimated from the a) standard, b) NDVI-calibration, c) Local-calibration and d) thermal-based FAO-2Kc. The ground-based ET (ET_{obs}) and ET_0 are depicted for reference. The validation of ET from every method against ET_{obs} is shown by means of bias, RMSE, R^2 and slope of the linear regression. 72
Fig. 3.5. First-guess (thermal-derived) RZSM ($RZSM_{LST}$) over the winter wheat field R3-4ha for the season 2002-2003. $RZSM_{LST}$ during unstressed periods when Ks=1 is corrected through a water budget ($RZSM_{LST,cor}$). The periods of significant increase in $RZSM_{LST,cor}$ are marked in the x axis (cyan) where the water budget is computed in order to invert the irrigation. In this case, three irrigation events are detected of the four periods where a water balance was applied (blue bars). The grey bars show the precipitations. 74
Fig. 3.6. LST-derived RZSM ($RZSM_{LST}$) and FAO-simulated RZSM by forcing the FAO-2Kc model using retrieved irrigation ($RZSM_{FAO+LST}$) versus ground-based RZSM. 75
Fig. 4.1. In the right plot, an example of LST-fv feature space constrained by the polygon Ts_{min}-Tv_{min}-Tv_{max}-Ts_{max} from the linear regression of the minimum (blue circles) and maximum (red circles) LST by fv classes. A conceptual diagram (left plot) of the LST-fv polygon to partition LST for two pixels (fv,LST) (yellow points) showing its corresponding Ts (red points, right plot) and Tv (green points, right plot) values following the TSEB assumptions. 92
Fig. 4.2. Schematic representation of pixel-scale irrigation retrieval between two successive Landsat overpass dates in four different cases: stressed-stressed (a), stressed-unstressed (b), unstressed-stressed (c) and unstressed-unstressed (d). 95

Fig. 4.3. Schematic diagram presenting the plot-scale irrigation retrieval from pixel-scale irrigation for an example of a 30-pixel field crop. 96
Fig. 4.4. Comparison of evapotranspiration (ET), transpiration (T) and evaporation (E) temporal series over the R3-4ha site (winter wheat field) for the 2002-2003 season estimated from the a) standard, b) NDVI-calibration, c) Local-calibration and d) generic Kcb and Ke FAO-2Kc. The ground-based ET (ET_{obs}) and ET_0 are depicted for reference. The validation of ET from every method against ET_{obs} is shown by means of bias, RMSE, R^2 and slope of the linear regression. 100
Fig. 4.5. Spatial distribution of daily ET showing the temporal dynamics on five selected dates along the 2016 growing season over R3 area. 101
Fig. 4.6. Temporal series of ET and its partition into transpiration (T) and evaporation (E) forced by the actual irrigations (FAO-$2Kc_{Iobs}$ in top plots) and retrieved irrigations (FAO-$2Kc_{Landsat}$ in bottom plots) over the R3-4ha (left plots) and R3-2ha winter wheat field (right plots) along the 2016 growing season. Observed ET (ET_{obs}) and ET_0 are shown as reference. 102
Fig. 4.7. Comparison of ET forced by the actual irrigations (FAO-$2Kc_{Iobs}$) and retrieved irrigations (FAO-$2Kc_{Landsat}$) against the observed ET without applying the Bowen correction (ET_{obs}) over the R3-4ha site along the 2016 growing season..... 103
Fig. 4.8. Spatial distribution of monthly ET from January to May 2016 along the growing season over R3 area. 103
Fig. 4.9. Spatial distribution of daily RZSM showing the temporal dynamics on five selected dates along the 2016 growing season over R3 area. 104
Fig. 4.10. Spatial distribution of cumulated irrigation over 15 days along the 2016 growing season over R3 area. The dates indicate the first day of the 15-days period. 104
Fig. 4.11. Spatial distribution of monthly irrigation from January to May 2016 along the growing season over R3 area. 105
Fig. 4.12. Spatial distribution of the total irrigation depth for the 2016 growing season over R3 area. 105
Fig. 5.1. In the top plots, linear relationship between *LST* and *NDVI* from Landsat-8 image for a selected date on winter (Plot A) and summer (Plot B). In the bottom plots, sinusoidal functions (dashed line) are adjusted to intercepts and slopes of the linear relationship *LST-NDVI* from the Landsat images for the years 2013 and 2014 according to the day of year. The intercept and slope for Plot A and B are highlighted in red and green, respectively. The statistical parameters of the sinusoidal fit for intercept and slope are shown in the box of every plot. 129
Fig. 5.2. Landsat-8 LST (blue circle), 8-day composite MODIS LST (red circle) over a vineyard pixel and the ratio between Landsat-8 and MODIS LST (ω_{100m}, triangle) for all Landsat image dates during 2013 and 2014. The sinusoidal functions of ω_{100m} according to the day of the year (ω_{8day_100m}, dashed line). 131

Fig. 5.3. Scatterplot between disaggregated LST at 100 m (DLST) from Eq. 5.3 and the averaged in situ LST over 8 days at MODIS overpass time over the olive and vineyard stations. 133
Fig. 5.4. Scatterplot between Landsat-8 LST at 100 m and in situ LST over the olive and vineyard stations. 133
Fig. 5.5. Comparison between the composite 8-day MODIS *LST* (*LST_1km*), the disaggregated *LST* at 250 m from MODIS NDVI (*LST_250m*) using Eq. 5.1, the disaggregated *LST* at 100 m from MODIS *LST* (*LST_100m*) using Eq. 5.2 and the final disaggregated *LST* at 100 m (*DLST_100m*) from Eq. 5.3. 134
Fig. 5.6. Comparison between the cumulated *ET* over 8 days from the MODIS LST at 1km (left figures) and from the disaggregated LST at 100 m (right figures) for two selected dates in summer (2014001) and winter (2015209). 136
Fig. 5.7. Comparison between disaggregated LST (DLST) against Landsat LST for five selected dates along the growing season over R3 area. 137
Fig. 5.8. Comparison between irrigation applied by the farmer (green) and retrieved irrigation (red) by using only Landsat LST (top plots) and the combined Landsat and disaggregated LST data (bottom plots) along the season 2016 for both monitored sites in R3 area. The horizontal and vertical error bars represent the standard deviation of the retrieved irrigation in dates and amounts, respectively. The dashed lines represent the availability of LST data. 139
Fig. 5.9. Comparison of statistical parameters R (solid line), RMSE (dashed line) and bias (dotted line) between observed and retrieved irrigation by using Landsat LST only (blue lines) and both Landsat and disaggregated LST data (red lines) cumulated from 1 to 90 days through a moving window over both R3-4ha and R3-2ha sites during 2016 season. 140
Fig. 5.10. Ground-based RZSM is plotted versus the RZSM simulated by the FAO-2Kc forced by: observed irrigation (black), irrigation retrieved from our approach by using Landsat LST only (blue) and irrigation retrieved from our approach by using Landsat LST together with disaggregated LST (red). The correlation coefficient (R) and root mean square error (RMSE) are shown for RZSM from FAO-based models forced by the three different irrigation data sets. 142
Fig. 5.11. Ground-based ET is plotted versus the ET simulated by the FAO-2Kc forced by: observed irrigation (black), irrigation retrieved from our approach by using Landsat LST only (blue) and irrigation retrieved from our approach by using Landsat LST together with disaggregated LST (red). The correlation coefficient (R) and root mean square error (RMSE) are shown for ET from FAO-based models forced by the three different irrigation data sets. 142

List of Tables

Table 1.1. Main characteristics of remote sensing data relevant to crop water budget monitoring..... 4
Table 2.1. Experimental sites of winter wheat field by agricultural area. 45
Table 2.2. Depths to which the TDR probes were installed at every experimental site...47
Table 5.1. Statistical parameters between disaggregated LST against Landsat LST for all the dates available during the growing season 2016 over R3. 138

Chapter 1. Introduction

Contents

1.1. General context 2
1.2. Remote sensing data relevant to crop water budget monitoring 3
1.2.1. Visible – Near Infrared data 5
1.2.2. Thermal infrared data 6
1.2.3. Microwave data 8
1.3. Modelling the crop water budget components from remote sensing data 10
1.3.1. Evapotranspiration modelling 11
1.3.2. Root-Zone Soil Moisture modelling 14
1.3.3. Irrigation modelling 15
1.4. Objectives 17

1.1. General context

In recent decades, pressure on natural resources has been strongly intensified mainly due to an exponential growth of population, a growing economy and an increasingly consumerist society. In particular, agriculture is an important pressure on water resources where water consumption by crops is by far the largest use of freshwater on Earth (Anderson et al., 2012a) requiring more and more resources to satisfy the growing demand. In fact, irrigated agriculture consumes more than 70% of the mobilized freshwater resources at global scale (Foley et al., 2011) and even more than 80-90% in semi-arid and arid regions (Chehbouni et al., 2008; Garrido et al., 2010; Scanlon et al., 2012). Therefore, freshwater resources are becoming increasingly limited in many parts of the world (Anderson et al., 2012a). The water resources availability is particularly sensitive in Mediterranean regions (illustrated in Fig. 1.1), which are considered one of the most sensitive areas to climate change due to a large decrease in annual precipitation with increasing temporal variability and an observed trend to warmer conditions (Giorgi, 2006; IPCC, 2013).

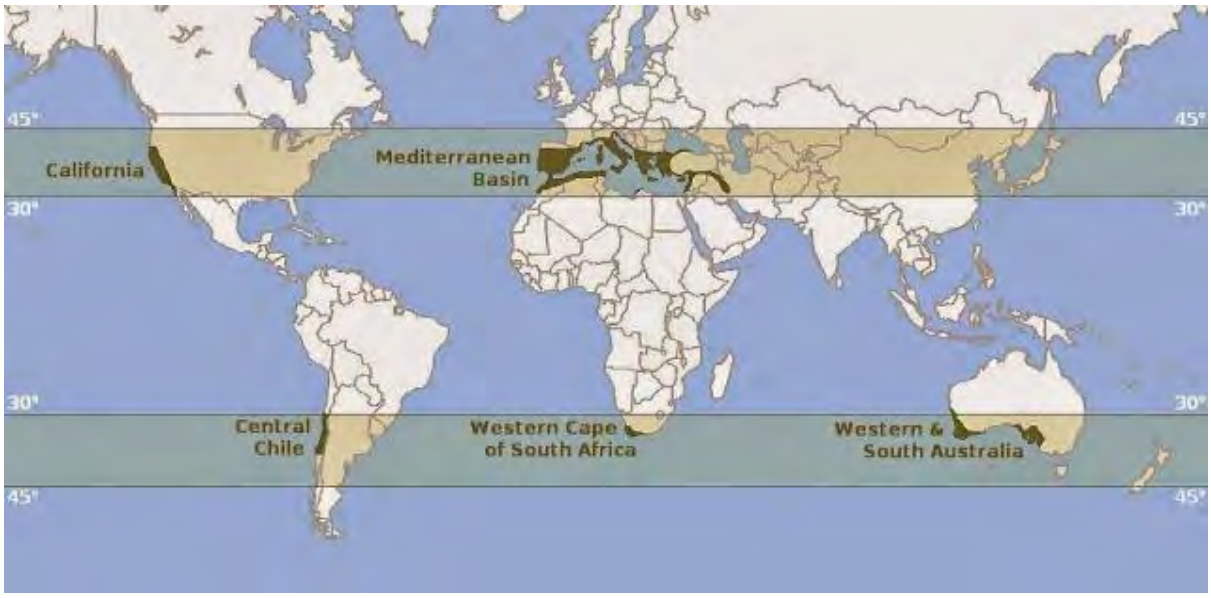


Fig. 1.1. Global distribution of Mediterranean regions.

In this context, increasing the water use efficiency in agriculture has been identified as one of the key topic related to water scarcity and droughts (Werner et al., 2012), being essential for the sustainability of water resources. Therefore, optimizing on-farm irrigation management is becoming a matter of increasing urgency, which can be reached by adjusting irrigation to the crop water requirements throughout the crop growing season. In practice, this means that crops be neither over- nor under-irrigated in order to avoid an unnecessary increase of water consumption or a decrease of crop yields, respectively. Nevertheless, despite the important pressure of agriculture on water resources, information on the amount of irrigated water is often unavailable. Therefore,

monitoring and quantifying water resources over extended areas are critical for an efficient management of water resources. This can be achieved by means of the synergy between the modelling, in situ measurements and remote sensing data.

Modelling the water resources over agricultural areas has been extensively used in order to simulate the different components of the crop water budget. A large variety of approaches to simulate the crop water requirements has been developed in the last decades, which are generally focused on simulating the water needs by means of evapotranspiration (ET). Regarding in situ measurements, a cutting-edge solution is based on measurements of the root-zone soil moisture (RZSM) to detect the onset of crop water stress and then to trigger irrigation. However, field measurements are costly, are not available over extended areas and may not be representative at the field scale. By contrast, remote sensing is presently the most cost-effective and suited technique for mapping and monitoring the surface states at both field and regional scales.

In the next sections, we present: i) an overview of existing remote sensing data relevant for monitoring the crop water budget, ii) the modelling of the main components of water budget (ET, RZSM and irrigation) from remote sensing data, and iii) the objectives of this thesis.

1.2. Remote sensing data relevant to crop water budget monitoring

Remote sensing offers the only possibility for monitoring land surface variables at different spatial resolutions and temporal frequencies, thus facilitating a systematic and comprehensive observation over extended areas. Furthermore, remote sensing observations are especially practical in areas where man-made measurements are difficult to perform or simply unavailable (Li et al., 2009; Rango, 1995). Remote sensing has played an important role in the development and application of several models over extended areas for monitoring water resources, being able to map ET and its associated variables, such as vegetation cover, land surface temperature and soil moisture (Fig. 1.2). Remote sensing has the particular interest of being cost effective and operational in its implementation over extended areas, allowing estimating energy-water balance components and its associated variables at multiple spatial and temporal scales. This advantage allows coupling remote sensing data, water and surface energy model in order to better understand the hydrological processes at different scales. The remote sensing data especially relevant for the monitoring of water resources are presented in Table 1.1 and detailed below.

Table 1.1. Main characteristics of remote sensing data relevant to crop water budget monitoring.

Spectral region	Wavelength	Spatial resolution	Temporal resolution	Current satellite missions	Applications	References
Visible-Near Infrared (VNIR)	0.4 – 1.3 µm	1 m – 5 km	15 min – 16 days	Sentinel-2, Formosat, Landsat, ASTER, MODIS, SEVIRI, VIIRS, Sentinel-3	Vegetation indices Vegetation parameters Albedo Crop coefficient	Bannari et al. (1995) Pinter et al. (2003) Qu et al. (2015) Singh and Irmak (2009)
					Soil moisture indices	Wang and Qu (2009)
Thermal Infrared	8 – 14 µm	60 m – 5 km	15 min – 16 days	Landsat, ASTER, MODIS, Sentinel-3, VIIRS, SEVIRI, GOES	Land surface temperature Emissivity Crop water stress	Z.-. Li et al., (2013); Sobrino et al. (2016) Z. L. Li et al., (2013) Kullberg et al. (2016)
Microwave (passive / active)	1 mm – 1 m	10 m – 60 km	1 – 6 days	Sentinel-1, SMAP, SMOS, ASCAT, AMSR-2	Surface soil moisture Surface roughness	Brocca et al., (2017) Zribi and Dechambre (2003)

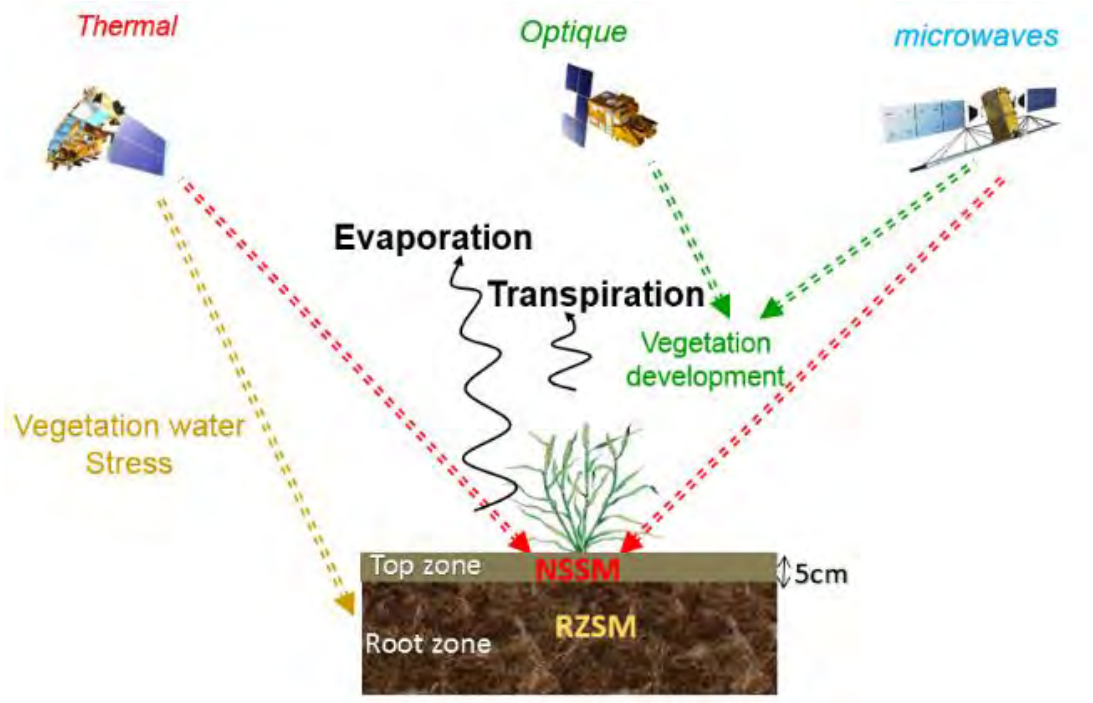


Fig. 1.2. The ability of multi-spectral remote sensing data to characterize the soil and vegetation states that are useful for monitoring the crop water budget. Source: Amazirh (2019).

1.2.1. Visible – Near Infrared data

Visible and near infrared (VNIR) reflectances have the advantages of monitoring vegetation/crops in terms of phenology, health and vigor among others. This is because green plant leaves show very low reflectance in visible regions (0.4 – 0.7 μm) due to a strong absorptance by photosynthetic and plant pigments and very high reflectance in the near infrared regions (0.7 – 1.3 μm) due to a low absorptance by subcellular particles or pigments and as well as a considerable scattering at mesophyll cell wall interfaces (Gausman, 1977). These characteristics have served as the basis for many applications of remote sensing to crop management by using mainly vegetation indices (VI) (i.e. differences, ratios, or linear combinations of reflectances in visible and near infrared wavebands). VI have shown good correlations with plant growth parameters such as green biomass (Pinter et al., 2003), leaf area index (Duchemin et al., 2006), and fraction of absorbed photosynthetically active radiation (Pinter et al., 1994), among others.

In crop water management, VI have been widely used to derive crop coefficients (e.g. defined as the ratio of ET and a reference ET value in optimal ET conditions) (Bausch and Neale, 1987; Choudhury et al., 1994; Singh and Irmak, 2009). This is because crop coefficients primarily depend on the dynamics of canopies (cover fraction, leaf area index, greenness and phenology). Hence, VI-based crop coefficients have been of great value in ET and irrigation scheduling algorithms in order to estimate the crop water requirements (Allen et al., 2011; Pereira et al., 2015; Singh and Irmak, 2009). Several studies have proven that local adjustment by phenology and crop coefficient are expected to be more suitable for estimating ET and crop water needs than the use of tabulated crop coefficient values (Allen et al., 2011; Bausch, 1995; Pereira et al., 2015). Such local adjustments usually rely on site-specific measurements or observations of crop growth and, consequently, VI based approaches are recommended for crop coefficients and irrigation management.

In addition, VNIR have received an especial interest for energy balance applications, providing robust estimates of the fraction of net radiation going into soil heat flux by means of VI (Daughtry et al., 1990) or for estimating surface albedo (Liang, 2001; Qu et al., 2015). VI are also essential auxiliary data in the estimation of surface emissivity to estimate the land surface temperature (LST) from thermal infrared data (Jiménez-Muñoz et al., 2006; José A Sobrino et al., 2008). Furthermore, VNIR are needed to detect the full range of surface conditions in vegetation cover needed in several methods based on the contextual information in remotely sensed LST and VI data (Merlin, 2013; Merlin et al., 2014; Moran et al., 1994).

One of the main advantages of VNIR sensors over other spectral sensors is the high spatial resolution suitable for crop monitoring. Resolution less than 100 m (e.g. Landsat, ASTER, Sentinel-2) allows only one to six observations per month in orbital cycle. However, SPOT series or other commercial satellites (e.g. QuickBird, Worldview, GeoEye) with very high

(< 10 m) spatial resolution are generally cost prohibitive and hence they are not useful for operational implementations. The launch of Sentinel-2A/B represents a breakthrough for freely available VNIR missions, providing VNIR data at ~10 m resolution to systematically monitor crops at a weekly repeat cycle (from 5 to 12 days).

Despite plant water stress and senescence period can be detected by VI time series (Adams et al., 1999), water stress-induced impact in these wavelengths is not sufficiently large over biologically significant changes in plant water content for practical uses in the monitoring of water stress in the field (Bowman, 1989; Carter, 1991). Unlike VNIR, thermal infrared data have proven to be very useful in assessing the crop water stress (Jackson, 1982) as it is presented in the next section.

1.2.2. Thermal infrared data

Land surface temperature (LST) is an essential variable that modulates radiative, latent and sensible heat fluxes at the soil-plant-atmosphere interface. LST can be obtained globally and operationally from thermal infrared remote sensing observations. Hence, LST is a useful variable for monitoring the carbon, water and energy fluxes from field to regional scales (Anderson et al., 2008).

LST data have been a key land surface variable as input for many environmental and hydro-meteorological applications, including climatological studies (Anderson et al., 2007; Hansen et al., 2010), extreme weather monitoring such drought monitoring (Anderson et al., 2011; Jiménez-Muñoz et al., 2016; McVicar and Jupp, 1998), soil moisture estimates (Amazirh et al., 2018; Merlin et al., 2012b) and irrigation and water resource management (Anderson et al., 2012b; Bastiaanssen et al., 2007; Droogers et al., 2010). LST is particularly useful for the monitoring of crop water management since it is very sensitive to plant water stress and a strong indicator of changes in root-zone soil moisture (Anderson et al., 2012a, 1997; Moran et al., 2009). Thus, LST can be related to the root-zone soil moisture (RZSM) by means of the canopy temperature and its associated plant transpiration (Boulet et al., 2007; Hain et al., 2009; Moran et al., 1994) given the coupling between the surface energy and water balance (e.g. Wetzel et al., 1984).

LST can be derived from satellite thermal sensors at different spatial and temporal scales. However, the main limitation in the existing thermal missions is the unavailability of high spatial and temporal resolutions at the same time. For instance, missions offering high revisit time (e.g. MODIS, AVHRR, MSG/SEVIRI, VIIRS and Sentinel-3) usually provide a low spatial resolution, and conversely, those offering high spatial resolution (e.g, Landsat and ASTER) provide a low temporal resolution (Fig. 1.3). Therefore, the ability for monitoring water resource at crop field scale (~100 m) is limited by the low revisit time

and even hampered by cloudy conditions, hence preventing the monitoring of rapid changes of the vegetation water status.

Recent studies have highlighted the importance of thermal observations at high resolution with a near daily revisit for vegetation water status monitoring (Cao et al., 2019; Guzinski and Nieto, 2019; Sobrino et al., 2016). Thus, ideally a constellation of polar orbiting satellites (e.g. Landsat, ASTER) would appear to be the best solution to meet these requirements, which is potentially achieved by the ECOSTRESS mission (Hulley et al., 2017), recently launched in June 2018, or the foreseen TRISHNA mission (Lagouarde and Bhattacharya, 2018). ECOSTRESS, onboard of International Space Station, will address critical questions on plant-water dynamics and future ecosystem changes with climate by means of LST, ET, Water Use Efficiency, and Evaporative Stress Index data products at ~60 m spatial resolution every few days (<5) at varying times of day. Consequently, the detection is further enhanced in heterogeneous environments (such as agricultural areas) by the high spatiotemporal resolution (Hulley et al., 2017). However the ECOSTRESS overpass time changes and does not offer global coverage, therefore it is not optimal for monitoring crop management under operational implementations. The TRISHNA mission will combine a high spatial resolution (50 m) and high revisit time (about 3 days) in the thermal domain with a global coverage. The two main scientific objectives driving the mission are the monitoring of energy and water budgets of the continental biosphere and the monitoring of coastal and continental waters (Lagouarde and Bhattacharya, 2018).

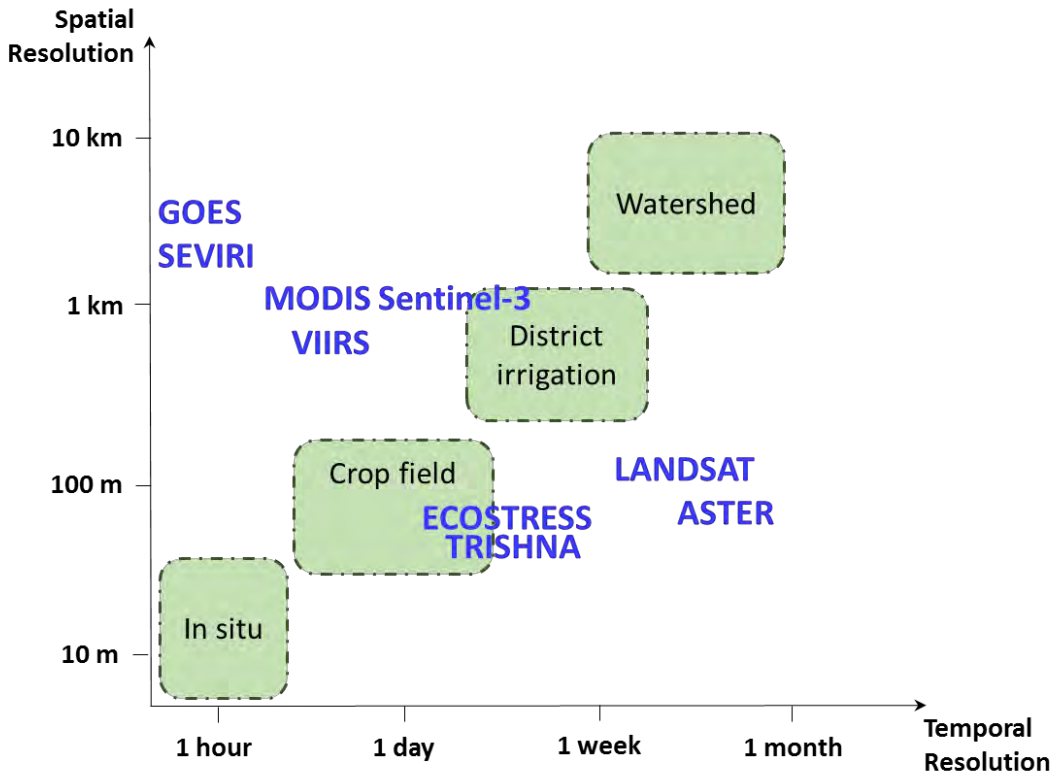


Fig. 1.3. Different spatial and temporal resolution of current and near future thermal satellite observations related to different target observation scales.

Before the launch of TRISHNA mission, the disaggregation of existing low resolution LST data to high spatial resolution with a relatively satisfying accuracy can be performed. Disaggregation methods focus on decomposing pixel-based temperatures providing a better dataset of LST with finer temporal and spatial resolutions based on the information obtained from different sensors. Therefore, disaggregation methods aim to achieve appropriate LST data for monitoring crop water budget at crop field scale (illustrated in Fig. 1.3). The basic idea behind these methods is to establish either a statistical relationship or a physically based model between coarse scale LST and fine scale auxiliary variables. In these methods, satellite data in the VNIR wavelengths available at a resolution finer than that of most thermal sensors have been essential to bridge the gap between the low spatial resolution and the high temporal resolution of available LST observations (Zhan et al., 2013). Consequently, most common disaggregation LST methods have been based on a scale invariant relationship between LST and VI, largely related to the fractional vegetation cover. The VI-based methods are still the most used operational approaches due to the availability of data at high spatial and temporal resolutions, such as DisTrad, TsHarp, among other algorithms (Agam et al., 2007a; Bindhu et al., 2013; Kustas et al., 2003; Mukherjee et al., 2014; Zhan et al., 2013).

In addition to the use of VNIR data, other more complex disaggregation methods have proposed the use of the LST-VI feature space to derive soil water status indices that could better represent the variability in LST and hence improving the disaggregation accuracy over agricultural areas with high moisture content (Chen et al., 2010; Sandholt et al., 2002; Yang et al., 2010). This procedure has been further extended by using additional factors that modulate the LST, reflecting the soil moisture content and vegetation type (Amazirh et al., 2019; Merlin et al., 2012a, 2010; Yang et al., 2011). For instance, Merlin et al. (2010) distinguished between photosynthetically and non-photosynthetically active vegetation from time series of optical shortwave data to be included in the disaggregation procedure. Then soil moisture proxies derived from microwave data can take into account the soil moisture effects on the disaggregation of LST (Merlin et al., 2012a; Amazirh et al., 2019). Although these latter methods can provide better accuracies than using only LST-VI relationships, they require additional parameters, which make them difficult to be implemented operationally. Therefore, implementing disaggregation methods on an operational basis with reasonable accuracies implies new challenges in the methods.

1.2.3. Microwave data

Microwave wavelengths are one of the most sensitive to the variations in soil moisture given the large contrast of the emission from the earth's surface between the water and land. Thus, surface soil moisture (SSM) can be estimated from remote sensing (Entekhabi

et al., 1994; Kerr et al., 2010). However, remote sensing instruments are only able to collect soil moisture information to an estimated depth of approximately the first 5-10 cm of the surface. Indeed, the microwave emission in this frequency is severely attenuated in the soil porous medium (Entekhabi et al., 1994; Kerr et al., 2010).

According to Schmugge et al. (2002), microwave data are characterized by four unique advantages over other spectral regions: i) the atmosphere is effectively transparent providing all weather coverage; ii) vegetation is semi-transparent allowing the observation of underlying surfaces; iii) the microwave measurement is strongly dependent on the dielectric properties of the target, which for soil is a function of the amount of water present; and iv) the microwave measurement is independent of solar illumination, which allows day or night observation.

There are two microwave remote sensing techniques: the passive and active microwave sensors. The passive microwave sensors (radiometers) detect the naturally emitted microwave energy within its field of view using very sensitive detectors. However the amounts of energy are generally very small due to the wavelengths, which are much longer compared to optical wavelengths. Thus, the fields of view must be large to detect enough energy to record a signal. Most passive microwave sensors are therefore characterized by a low (~30 – 60 km) spatial resolution. Among satellite passive missions, the SMOS satellite, launched in 2009, has been widely used for SSM retrieval, with an accuracy requirement of 4%. It is based on an L-band (1.4 GHz) antenna and is the first space mission dedicated to observe SSM globally (Kerr et al., 2010). The AMSR-E mission, launched in 2002, provides brightness temperature measurements at six frequencies from 6.9 to 89 GHz in horizontal and vertical polarizations, of which C-band (6.9 GHz) and X-band (10.7GHz) channels are suitable for retrieving SSM (Njoku et al., 2003) at spatial resolutions ranging between 25 and 50 km. The SMAP mission, launched in 2015, combines a radiometer (passive) and a Synthetic Aperture Radar (SAR, active) instrument within the L-band range (1.20–1.41 GHz) to provide measurements of SSM moisture with a global coverage in 2–3 days. The ASCAT sensor is a C-band scatterometer (5.255 GHz, VV polarization) at a spatial resolution of about 50 km, operating on-board the Meteorological Operational (MetOp) satellite since 2006.

Regarding the active sensors, the most popular is the Sentinel-1 mission, launched in 2014, providing C-band SAR data at 20 m spatial resolution with an unprecedented repeat cycle of 6 days by combining both ascending and descending overpasses (3 days by combining the two satellites available since 2015). Although backscatter signals data have potential to monitor SSM (e.g. Amazirh et al., 2018; Gao et al., 2017; Zribi et al., 2011), there is currently no global operational SSM product at such fine resolution. This is notably due to the difficulty to model in time and over extended areas the impact of vegetation cover/structure and surface roughness on the backscatter signal (Zribi et al., 2011, 2008).

1.3. Modelling the crop water budget components from remote sensing data

Remote sensing data has shown a great value to detect key land surface variables for monitoring the crop water budget from instantaneous observations at the time of satellite overpass. However, retrieving the different crop water budget components requires an appropriate coupling strategy between remote sensing data and the surface modelling. This involves taking advantage of multispectral and multi-resolution remote sensing data as well as filling the gap between the remotely sensed observations and water fluxes and between instantaneous observations and the temporal resolution suitable for crop water management.

Knowledge of crop water requirements is key for optimizing the crop water use efficiency. Crop water balance models simulate the relations between soil, plant and atmosphere by simulating the crop water requirements. In this context, crop water balance models are efficient tools in the management of water resources. These models are based mainly on the representation of the variability of soil moisture in the water storage capacity (ΔS) by solving a water budget between the water supplies and water losses. The water balance can be expressed and simplified as:

$$\Delta S = P + I - ET - DP - RO \qquad \text{Eq. 1.1}$$

In this water balance, the water supplies are represented by precipitations (P) and irrigations (I), and water losses are represented mainly by ET and deep percolation (DP). The runoff (RO), both surface and subsurface, can be also an important source of water loss in sloped area and under significant water supplies, such as heavy rainfall or flooded irrigations. However, in agricultural areas with flat surfaces RO can be assumed negligible. In Eq. 1.1, the diffusion processes in the vertical soil profile, such as capillarity rise is neglected. In several agricultural areas in semi-arid to arid regions, the capillarity rise can be neglected due to significant deep water tables, i.e. several meters deeper than the water storage capacity available for plants.

Several models have been proposed in the literature (e.g. FAO-56, SAFY, STICS, AquaCrop) for modelling crop water needs by means of ET. These models can provide quantitative estimates of crop yields under different environmental conditions, as well as simulation of water balance. For instance, the FAO-56 (Allen et al., 1998) is a simplified water balance model driven by: 1) meteorological forcing variables to estimate the atmospheric evaporative demand represented by a reference evapotranspiration (ET_0) and 2) water supplies by precipitation and irrigation. Relying on the Eq. 1.1, the FAO-56 model simulates the soil water availability for ET, which can be extended to a double source model to simulate the soil water availability in the top surface layer and the root-zone layer for soil evaporation and plant transpiration, respectively. The SAFY model is a

daily time step vegetation model to estimate crop yields (Duchemin et al., 2008). It simulates the time courses of green leaf area index and the dry aboveground biomass along the growing season. The outputs of SAFY model have been used to control the ET (or its soil and vegetation components) of a soil–water balance. Thus, this model has been coupled to FAO-56 model for simulating the crop water needs and crop yields (Battude et al., 2017, 2016; Hadria et al., 2010). The STICS crop model (Brisson et al., 1998; 2002; 2003) simulates the processes associated with plant growth and senescence. The validation of STICS for different climates (Bhattarai et al., 2018; Brisson et al., 2002; Hadria et al., 2007, 2006) has shown that the model simulates accurately the water balance when the leaf area index is correctly estimated.

The monitoring of the soil water content available for plants is the essential variable for modelling the water resources, and specifically for estimating the crop water requirements by means of ET. The monitoring of the soil water content can be represented by temporal dynamics of the root-zone soil moisture (RZSM), which is defined as the water content of the soil column that may be extracted by evaporation at the surface, through root extraction or by capillary rises (Calvet and Noilhan, 2000). For the monitoring of water resources, the irrigation is one of the main forcing in the agricultural areas, notably in semi-arid to arid regions. However, irrigation is usually unavailable over extended areas. In this context, this thesis focuses on the estimation of these main crop water budget components: ET, RZSM and irrigation. Below is described the main characteristics of ET, RZSM and irrigation components, the associated estimation methods and their modelling over extended areas from remote sensing observations.

1.3.1. Evapotranspiration modelling

Evapotranspiration (ET) is the term used to describe the loss of water from the Earth's surface to the atmosphere by the combined processes of evaporation from the soil (as well as open water bodies and plant surfaces) and transpiration from vegetation. ET is a key component in the processes that control the energy and mass exchange (water and carbon) between terrestrial ecosystems and the atmosphere. Hence, ET is responsible of the coupling between the water balance and the surface energy balance (Fig. 1.4).

During the last decades, several works have documented the essential role of ET in the water balance for its critical importance on resource availability (Oki and Kanae, 2006), hydrologic and meteorological forecasts (Findell et al., 2011), climate change scenarios related to drought indexes (Gao et al., 2011) and agricultural irrigation scheduling (Allen et al., 2005; Senay et al., 2013a). Therefore, knowledge of ET is essential for monitoring water resources in areas of water scarcity since the actual rate of the water use by vegetation can differ significantly from potential ET rates (Anderson et al., 2012a).

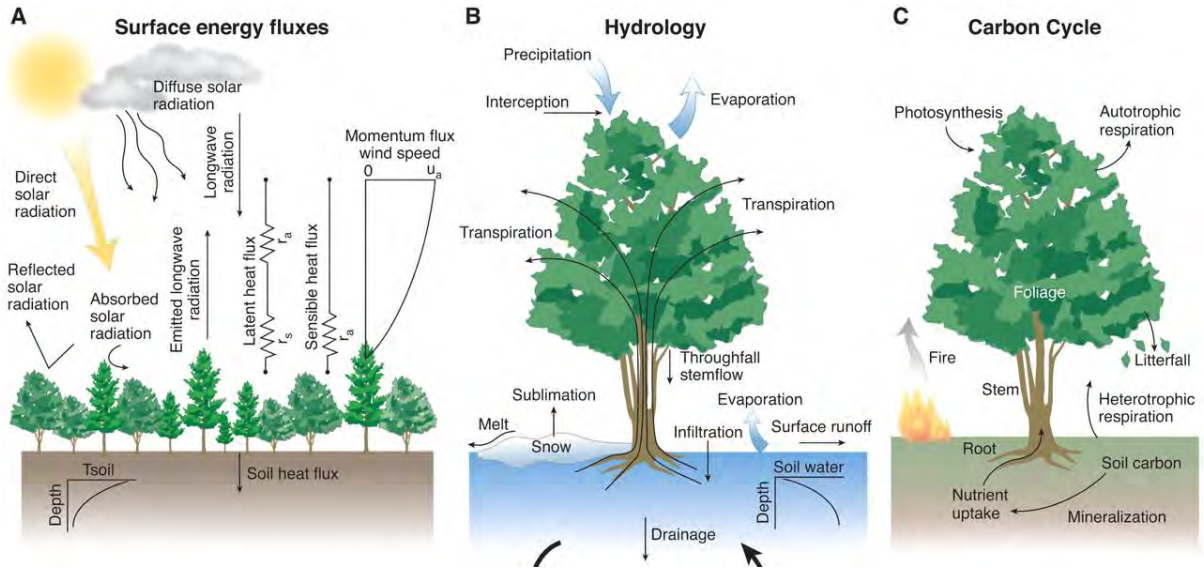


Fig. 1.4. Schematic representation of surface energy (A), water (B) and carbon cycle. ET is represented as latent heat flux in A, as soil evaporation and plant transpiration in B and is strongly linked to photosynthesis and soil respiration in C. Source: Bonan (2008).

There are different methods that allow quantifying ET by means of direct measurements. The direct measurements are technically ground-based estimates obtained from different techniques such as: i) hydrological approaches (e.g. weighing lysimeters), ii) plant physiological approaches (e.g. sap flow and chamber methods) and iii) micrometeorological approaches (e.g. Bowen ratio, eddy covariance and scintillometry). These techniques differ also in the scale of measurements. For instance at local scale, sap flow sensors allow providing individual plant transpiration while lysimeters allow providing the ET from a small surface or evaporation when the surface is under bare soil conditions. On the other side, eddy covariance techniques allow providing ET at field scale (~100 m), which is more suitable for monitoring crop water needs. Scintillometers can provide the ET over a larger scale from several hundreds of meters to 10 km. Despite these techniques can provide long time series at a very high frequency (~10 Hz), these systems do not provide spatial distributions at regional scale over heterogeneous surfaces, especially in regions with advective climatic conditions. Remote sensing based ET models are better suited for estimating the crop water use at regional scale, offering a cost-effective solution for monitoring extended areas.

Numerous remote sensing-based approaches with varied complexity have been developed for monitoring the crop water requirements by means of ET estimates. For instance FAO-56 model has been extensively used at the field scale to estimate the crop water requirements by means of the simulated ET. As it was mentioned in Section 1.2.1, crop coefficients have been estimated from satellite based VI to better constrain the phenological stages, which has been also included in the FAO-56 model (Er-Raki et al., 2010, 2007; González-Dugo and Mateos, 2008; Hunsaker et al., 2005). Thus, the FAO-56 models coupled with VI have shown a significant improvement against the classic FAO-

2Kc. Given thermal data are more suited to detect water stress than VI, LST has been assimilated into the FAO-56 method (Er-Raki et al., 2008), and more recently, used for water stress coefficient to better constraint the FAO-56 method (Dejonge et al., 2015; Ihuoma and Madramootoo, 2017; Kullberg et al., 2016).

The asset of thermal data comes from the advantage of detecting information on the vegetation water status and the ability to study the variability in water consumption in individual fields or even within the field (Anderson et al., 2012a). This advantage is given mainly by the spatial resolution of thermal data of about 100 m. Thus, different methods have been developed in the last decades to estimate ET by using LST data as main input, demonstrating its immense value in ET monitoring (Gowda et al., 2008; Kalma et al., 2008; Li et al., 2009). Most of these methods are based on solving the surface energy balance, from which three broad approaches can be distinguished according to Su (2002): i) residual approaches, ii) Land Surface Models, and iii) evaporative fraction methods. The residual methods estimate the sensible heat flux (H) and then obtain the latent heat flux (i.e. ET expressed as energy) as the residual of the surface energy balance equation. The second approaches estimate all the energy budget components at the land surface with continuous Land Surface Models by including Soil–Vegetation–Atmosphere Transfer (SVAT) models. The third approaches estimate ET as a fraction of either potential ET (Moran et al., 1994), or available energy (Long and Singh, 2012; Roerink et al., 2000). The evaporative fraction (EF) is defined as the ratio of ET to available energy (net radiation minus soil heat flux). EF can be estimated from the contextual information of remotely sensed optical/thermal images, where dry and wet conditions are identified from the LST – VI (e.g. Long and Singh, 2012; Moran et al., 1994) space, the LST – albedo (e.g. Roerink et al., 2000) space or by combining both spaces (Merlin, 2013; Merlin et al., 2014). It is for this reason that those approaches have been called contextual approaches, which have received an especial interest in the scientific community for its simplicity and operational implementation over large areas.

The EF values can define two main ET regimes: a soil moisture-limited and an energy-limited regime (Seneviratne et al., 2010). The soil moisture-limited ET regime is characterized by EF values below 1 with soil moisture values below a given critical soil moisture (SM_{crit}), thus leading to vegetation stress conditions (Fig. 1.5). Above SM_{crit}, EF is independent of soil moisture content (energy-limited ET regime), meaning that vegetation is unstressed with EF values equal to 1. SM_{crit} is thus defined between the soil moisture at field capacity (SM_{fc}, above which water cannot be held against gravitational drainage) and the soil moisture at permanent wilting point (SM_{wp}, below which water is not accessible to plants). From these definitions, wet ($SM>SM_{crit}$, EF equal to 1), dry ($SM<SM_{wp}$, with EF values equal to 0) and transitional ($SM_{wp}<SM<SM_{crit}$) regimes can be defined from thermal-based models by means of contextually-derived EF. These insights are essential in this thesis because they allow us to relate the contextual information detected from optical/thermal data to the root-zone soil moisture. More details about soil moisture are presented below.

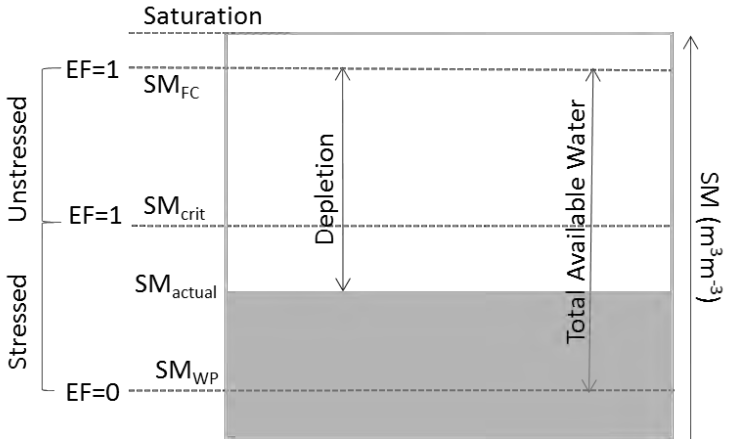


Fig. 1.5. Schematic representation of soil moisture in root zone and the relation with evaporative fraction and vegetation water stress. Source: based on Allen et al. (1998).

1.3.2. Root-Zone Soil Moisture modelling

Soil moisture (SM) is an important hydrological state variable, being essential in land-atmosphere interactions through ET and the other energy fluxes. SM also controls the partition of rainwater between infiltration and runoff as well as latent and sensible heat fluxes. A better knowledge of SM is therefore of prime interest for monitoring water resources and consequently for optimizing the irrigation water use.

There are several methods that allow providing SM estimates for its monitoring. First, direct measurements of SM are only obtained from destructive methods like gravimetric measurements. This method consists in quantifying in laboratory the water evaporated from a volume of soil that was previously extracted in order to calculate the mass of water divided by the mass of dry soil. The gravimetric method is hence impractical for measurements over extended areas or for monitoring through long SM time series. Second, indirect measurements provide SM estimates based on measurements of a physical variable strongly linked to SM (e.g. apparent dielectric of the soil). The sensors that measure SM thus allow providing long SM time series. However, the measurements are representative of a specific point, not providing spatial trends or distributions at regional scale (horizontal) or in the soil profile (vertical).

SM can be also estimated from remote sensing instruments, which can be from the ground (on towers), airborne or satellite platforms. However, remote sensing instruments are only able to collect SM information of the shallow near-surface layer so that it is usually referred to as near-surface soil moisture (SSM). Even though SSM can be estimated by microwave remote sensing, the variable of interest for applications in short- and medium-range meteorological modelling, hydrological studies over vegetated areas and in agriculture is the root-zone soil moisture (RZSM), which controls plant transpiration

(Albergel et al., 2008). RZSM represents the water content of the soil column that may be extracted by evaporation at the surface, through root extraction or by capillary rises (Calvet and Noilhan, 2000). The depth of this reservoir may vary from about 0.1 to few meters depending on soil type, bioclimatic conditions and the vegetation type (crop types in agricultural applications).

The SSM is related to the RZSM through dynamical processes of soil water transfer (Noilhan and Planton, 1989). It is therefore possible to implement retrieval algorithms to obtain the soil moisture profile and hence the RZSM from observed SSM time series (e.g. Albergel et al., 2008; Calvet and Noilhan, 2000; Kornelsen and Coulibaly, 2014; Wagner et al., 1999). In the last two decades, several studies retrieved RZSM or profile soil moisture either by using in situ (Albergel et al., 2008; Calvet and Noilhan, 2000) or satellite (Calvet et al., 1998; Ford et al., 2014; Sabater et al., 2007) SSM observations. Among the numerous studies about RZSM retrieval from observed SSM, a large part of these are based on assimilation algorithms (e.g. Albergel et al., 2008; Calvet and Noilhan, 2000; Dumedah et al., 2015; Entekhabi et al., 1994; Walker et al., 2001). However, such approaches for retrieving RZSM suffer from a low spatial resolution given that the operational SSM products are available at very low (>25 km) spatial resolution only (Entekhabi et al., 2010; Kerr et al., 2010; Peng et al., 2017). Even though disaggregated satellite SSM data sets have been assimilated into land surface models for improving both the RZSM estimation and its spatial resolution (Dumedah et al., 2015; Merlin et al., 2006), such a coupled approach is still not suitable for routinely monitoring the crop water demand at the crop field (~100 m) scale.

Alternatively to SSM, LST can be used in the calculation of thermal-based proxy variables for RZSM through indices by using the canopy temperature, and the associated transpiration rate (Boulet et al., 2007; Hain et al., 2009; Moran et al., 1994). Hence, one key step to estimate thermal-derived RZSM is the partitioning of LST into soil and canopy temperatures (Merlin et al., 2014, 2012b; Moran et al., 1994). In summary, SSM and LST are both valuable state variables that can help constrain a land surface model to retrieve the RZSM at the field scale for crop water managements. Therefore a coupling between remote sensing data and land surface modelling could be developed for that purpose.

1.3.3. Irrigation modelling

Irrigation is one of the most important component in the consumption of water resources, representing about 70% of the mobilized freshwater at global scale (Foley et al., 2011) and can be raised to more than 80-90% in semi-arid and arid regions (Chehbouni et al., 2008; Garrido et al., 2010; Scanlon et al., 2012). Thus, increasing the water use efficiency in agriculture has been identified as one of the key topic related to water scarcity and droughts (Werner et al., 2012), being essential for the sustainability of water resources. Despite the important pressure of agriculture on water resources, irrigation information

is often spatially unavailable, hampering a proper water management. Therefore, quantifying the amount and timing of irrigation over extended areas is essential for an efficient water resources management.

Irrigation is referred to the man-made water supplied to the field in order to meet the crop water requirements. Although irrigation is closely related to the crop water requirements, the latter may differ considerably from actual irrigation amounts. Despite the large variety of existing approaches to estimate crop water by means of ET estimates, irrigation is generally simulated from the modeled water needs (e.g. Allen et al., 1998; Bastiaanssen et al., 2007; Battude et al., 2017; Corbari et al., 2019; Duchemin et al., 2008). In the simulation of irrigation based on the modeling of soil moisture dynamics from the water balance or the energy-water coupled balance, significant uncertainties can be obtained, especially when no information is available on the actual crop water status over time.

In an attempt to estimate the irrigation volumes from remote sensing data, some recent studies have explored the utility of SSM estimates from micro-wave sensors (Brocca et al., 2018, 2017; Escorihuela and Quintana-Seguí, 2016; Jalilvand et al., 2019; Kumar et al., 2015; Lawston et al., 2017b; Malbéteau et al., 2018; Zhang et al., 2018). In particular, Brocca et al. (2018) developed an approach to quantify the irrigation amounts by combining the currently available coarse resolution satellite SSM products (e.g. SMAP, SMOS, ASCAT, AMSR-2) and a soil water balance. This work was applied over various semi-arid and semi-humid regions worldwide but could not be quantitatively assessed due to the unavailability of reliable in situ observations of irrigation over corresponding irrigated perimeters. However, this approach was quantitatively assessed at ~50 km resolution over a semi-arid region (Jalilvand et al., 2019). Some deficiencies were obtained over periods with sustained rainfalls and the method was not implemented in winter (Brocca et al., 2018). This makes the approach unsuitable for winter crops, which are especially important in the Mediterranean. Nevertheless, the ability to quantify monthly irrigations was demonstrated under specific conditions: during prolonged periods of low rainfall and using satellite SSM data with a low uncertainty and a frequency higher than 3 days.

Alternatively, land surface models (LSMs) have had an increasing interest in the scientific community in better simulating irrigation processes (Felfelani et al., 2018; Lawston et al., 2017a; Pokhrel et al., 2016). LSMs have included irrigation modules to be able to represent irrigations by improving the amount, method, and timing of irrigation (Pokhrel et al., 2012). As in the modelling of crop water requirements above mentioned, these irrigation modules usually determine the timing and amounts of irrigation based on the RZSM deficit. Thus, irrigation is triggered when RZSM drops below a specified threshold and then is calculated as the amount required to bring the RZSM to the target level. Hence, simulations may differ considerably from actual irrigation. Given the demonstrated

utility of microwave-derived SSM to detect seasonal timing and spatial signature of irrigation (Brocca et al., 2018; Lawston et al., 2017b; Malbéteau et al., 2018). Felfelani et al. (2018) has recently assimilated SMAP SSM data into a large-scale LSM to better constrain and improve irrigation simulations and also to enhance SSM simulations. However, as in the methods based on microwave-derived SSM data, the spatial resolution is too coarse for monitoring water resources at field scale.

At a spatial scale more suitable for the management of crop water, some recent studies (e.g. Corbari et al., 2019; Chen et al., 2018) have used optical data for the irrigation timing and scheduling. Corbari et al. (2019) have coupled remote sensing optical data, soil water-energy hydrological modeling and meteorological forecasts in order to predict the water needs for irrigation scheduling for up to 3 days. Here, land surface variables from optical/thermal data were used to initialize and calibrate the energy-water balance. Another different approach for detecting the timing of irrigation from optical data (vegetation index by using reflectance data) was proposed by Chen et al. (2018). The method was demonstrated to be promising in detecting irrigation events. However, it was applicable during the first half of the growing season only and it was not able to retrieve the irrigation amount.

Despite the advances and attempts in the last years to estimate the irrigation, no method or approach is yet available for estimating the irrigation at crop field scale (~100 m) over extended areas.

1.4. Objectives

Regarding the state-of-the-art, one of the main limitations in modelling the crop water budget is the lack of irrigation data over extended areas, of which all water fluxes essentially depend on the water inputs. However, remote sensing has proven a great potential in monitoring key land surface variables to solve the coupled water-energy balance. In particular, instantaneous thermal images are able to detect surface states that can be integrated in the coupled water-energy balance in order to solve its components.

The general objective of this thesis thus consists to estimate the main water budget components of agricultural systems, such as the ET, RZSM and irrigation, at crop field scale (100 m) on a daily basis over extended areas (the irrigated perimeter of some kilometers of extension). For this purpose, the coupling between remote sensing optical/thermal data and a FAO-based model is proposed by taking into account the following key advantages: i) the availability of optical/thermal data at a spatial resolution suitable for monitoring the crops, ii) the simplicity of contextual methods from optical/thermal data in the estimation of ET and the monitoring of vegetation water stress, and iii) the utility of optical/thermal data as proxy of SSM and RZSM.

This PhD thesis played an important role in the REC project entitled "Root zone soil moisture Estimates at the daily and agricultural parcel scales for Crop irrigation management and water use impact - a multi–sensor remote sensing approach, http://rec.isardsat.com". This project (March 2015 - March 2019) was supported by the European Commission Horizon 2020 Program for Research and Innovation (H2020) in the context of the Marie Sklodowska-Curie Research and Innovation Staff Exchange (RISE) action. The project has been carried out from 2015 to 2019 by an international and multi-sectorial collaboration between: CESBIO (Centre d'Etudes Spatiales de la Biosphère) – Toulouse, Université Cadi Ayyad – Marrakech, isardSAT and LabFerrer – Catalonia. My Thesis thus directly fed the REC objectives that were: i) to estimate the RZSM on a daily basis at crop field scale and ii) to quantitatively evaluate the different components of the water budget at the crop field scale from readily available remote sensing data.

LMI-TREMA (Laboratoire Mixte International – Télédétection et Ressources en Eau en Méditerranée semi-Aride) at Marrakech aims to improve the management of irrigation water by developing tools that can help use water in a rational way. For this purpose, LMI-TREMA has had several experimental sites since 2002 in the Haouz Plain, Morocco (Jarlan et al., 2015), which have been used to test the approaches proposed in this thesis. LMI-TREMA works in close collaboration with the regional public agency ORMVAH (Regional Office for the Agricultural Development of Haouz), which has been responsible since 1966 for the design and construction of large irrigation schemes and their management, as well as agricultural developments in a 7000 km^2 area in the Haouz plain.

Despite the irrigation at field scale being a critical forcing for monitoring the crop water management in irrigated agricultural areas, it is one of the water balance components least investigated in terms of estimation at integrated spatial scales. Consequently, one key step on the development of the approach is the estimation of irrigation since no method is yet available to retrieve the timing and amounts of irrigation at crop field and daily scale, and all water fluxes essentially depend on the water inputs. The modelling approach relies on the synergy between remote sensing optical data, contextual methods and a water balance model to invert first the irrigation and then the other water budget components. Two areas are used to validate the modelling approach developed in this thesis: one semi-arid region in Morocco and one arid region in Chile.

This thesis follows a stepwise approach and is structured in three main and complementary steps.

In the first step (Chapter 3), a feasibility study is carried out at in situ scale over a winter wheat field by integrating ground-based optical/thermal data into a FAO-based water balance model. This approach seeks to retrieve the irrigation at daily scale along the agricultural season in order to force the crop water balance model and estimate the daily RZSM and ET throughout the season. Given this approach is implemented with ground-

based observations on a daily basis, the approach is assessed for different observation frequencies ranging from 1 to 16 days to mimic the availability of remote sensing observation.

The application of the previous approach to Landsat data corresponds to the second step (Chapter 4) of this thesis. In this step, the specific objectives are the same as in the first step with the difference that the irrigation amounts and timing, ET and RZSM are estimated over extended areas. For this purpose, some significant changes are adopted to implement the approach with readily available remote sensing data over three areas in the semi-arid region in central Morocco. Five experimental sites covered by winter wheat fields with two different irrigation techniques (drip- and flood-irrigation) and one no-irrigation field are used to validate the approach. This approach seeks to estimate, for the first time, the irrigation at crop field scale on a daily basis over extended areas from readily available remote sensing data for a further operational implementation.

In the third step (Chapter 5), an operational disaggregation method of thermal data is presented in order to estimate the ET every 8 days. The method is developed and evaluated in an arid region of Chile over a vineyard and olives orchard field. The disaggregation is a key input in our proposed approach as well as for many thermal-based ET methods. Thus, the availability of the thermal data at a suitable spatial and temporal resolution is of prime interest for the monitoring of the water management at field scale. In this vein, the last step of this thesis involves the implementation of the irrigation retrieval approach using disaggregated thermal data as input in order to ensure the availability of the main input data every 8 days and even every 4 days when combining Landsat-7, -8 and disaggregated LST data sets.

Chapter 1. Introduction (français)

Contents

1.1. Contexte général *22*

1.2. Données de télédétection pertinentes pour le suivi du bilan hydrique des cultures *23*

1.2.1. Données Visible - Proche infrarouge *25*

1.2.2. Données thermiques infrarouges *27*

1.2.3. Données micro-ondes *29*

1.3. Modélisation des composantes du bilan hydrique des cultures à l'aide de la télédétection *31*

1.3.1. Modélisation de l'évapotranspiration *32*

1.3.2. Modélisation de l'humidité en zone racinaire *36*

1.3.3. Modélisation de l'irrigation *37*

1.4. Objectifs *39*

1.1. Contexte général

Au cours des dernières décennies, la pression sur les ressources naturelles s'est fortement intensifiée, principalement en raison d'une croissance exponentielle de la population, d'une économie croissante et d'une société de plus en plus consumériste. En particulier, l'agriculture est une pression importante sur les ressources en eau où la consommation d'eau par les cultures est de loin la plus grande utilisation d'eau douce sur Terre (Anderson et al., 2012a), ce qui nécessite de plus en plus de ressources pour satisfaire la demande croissante. Ainsi, l'agriculture irriguée consomme plus de 70% de l'eau douce mobilisée à l'échelle mondiale (Foley et al., 2011) et même plus de 80-90% dans les régions semi-arides et arides (Chehbouni et al., 2008; Garrido et al., 2010; Scanlon et al., 2012). Par conséquent, les ressources en eau douce sont de plus en plus limitées dans de nombreuses régions du monde (Anderson et al., 2012a). La disponibilité des ressources en eau est particulièrement sensible dans les régions méditerranéennes (Fig. 1.1), qui sont considérées comme l'une des zones les plus sensibles au changement climatique en raison de la forte diminution des précipitations annuelles avec une variabilité temporelle croissante et une tendance observée aux conditions plus chaudes (Giorgi, 2006; IPCC, 2013).

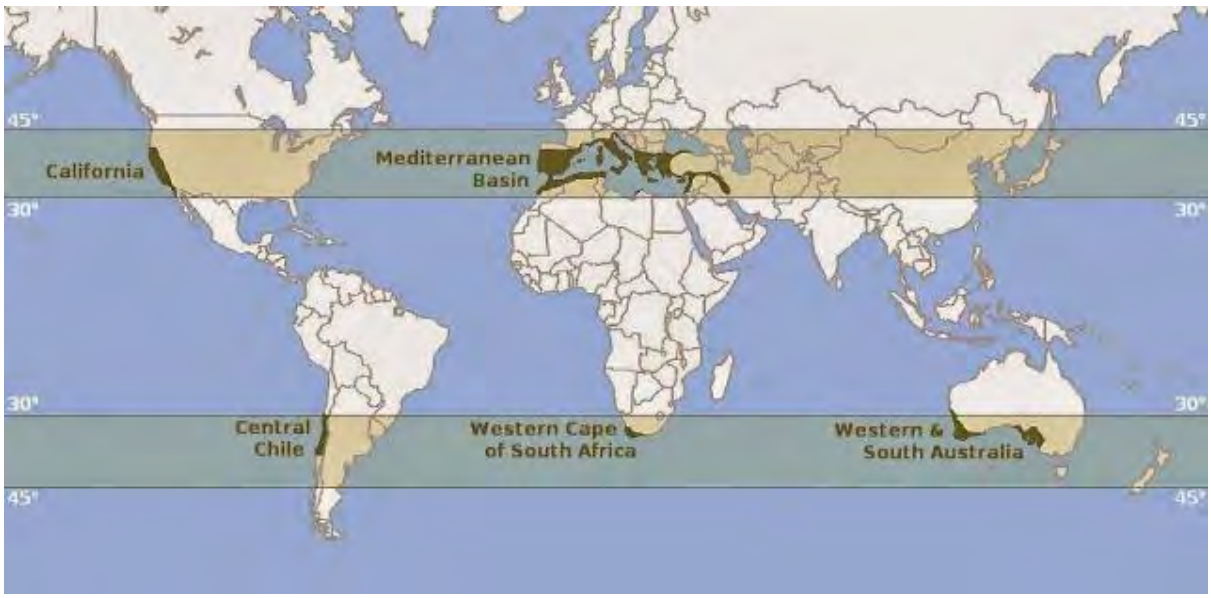


Fig. 1.1. Distribution globale des régions méditerranéennes.

Dans ce contexte, l'amélioration de l'efficacité de l'utilisation de l'eau dans l'agriculture a été identifiée comme l'un des thèmes clés liés à la rareté de l'eau et à la sécheresse (Werner et al., 2012), étant essentiel pour la durabilité des ressources en eau. Par conséquent, l'optimisation de la gestion de l'irrigation à l'échelle de la parcelle devient de plus en plus urgente, ce qui peut être atteint en ajustant l'irrigation aux besoins en eau des cultures tout au long de la saison de croissance des cultures. En pratique, cela signifie que les cultures ne doivent pas être sur- ou sous-irriguées afin d'éviter une augmentation

inutile de la consommation d'eau ou une diminution du rendement des cultures, respectivement. Malgré la pression importante de l'agriculture sur les ressources en eau, les informations sur la quantité d'eau irriguée sont souvent indisponibles. Par conséquent, la surveillance et la quantification des ressources en eau sur des zones étendues sont essentielles pour une gestion efficace des ressources en eau. Cet objectif peut être atteint grâce à la synergie entre la modélisation, les mesures in situ et les données de télédétection.

La modélisation des ressources en eau dans les zones agricoles a été largement utilisée afin de simuler les différentes composantes du bilan hydrique des cultures. Une grande variété d'approches pour simuler les besoins en eau des cultures a été développée au cours des dernières décennies, qui sont généralement axées sur la simulation des besoins en eau au moyen de l'évapotranspiration (ET). En ce qui concerne les mesures in situ, une solution de pointe est basée sur la mesure de l'humidité du sol dans la zone racinaire (RZSM) pour détecter l'apparition du stress hydrique des cultures et déclencher ensuite l'irrigation. Cependant, les mesures sur le terrain sont coûteuses, ne sont pas disponibles sur de larges zones et peuvent ne pas être représentatives à l'échelle du terrain. En revanche, la télédétection est actuellement la technique la plus rentable et la plus appropriée pour cartographier et surveiller l'état de surface à l'échelle régionale et sur la parcelle agricole.

Dans les sections suivantes, il est présenté : i) un aperçu des données de télédétection existantes pertinentes pour le suivi du bilan hydrique des cultures, ii) la modélisation des principales composantes du bilan hydrique (ET, RZSM et irrigation), et iii) les objectifs de cette thèse.

1.2. Données de télédétection pertinentes pour le suivi du bilan hydrique des cultures

La télédétection offre la seule possibilité de surveiller les variables de surface à différentes résolutions spatiales et fréquences temporelles, facilitant ainsi une observation systématique et complète sur de zones étendues. De plus, les observations de télédétection sont particulièrement pratiques dans les régions où les mesures in situ sont difficiles à effectuer ou simplement non disponibles (Li et al., 2009; Rango, 1995). La télédétection a joué un rôle important dans l'élaboration et l'application de plusieurs modèles pour le suivi des ressources en eau sur de zones étendues, permettant de cartographier l'ET et ses variables associées, comme la couverture végétale, la température de surface et l'humidité du sol (Fig. 1.2). L'application de la télédétection a l'intérêt particulier d'être rentable et opérationnelle dans sa mise en œuvre sur des zones étendues, ce qui permet d'estimer les composantes du bilan énergie-hydrique et ses variables associées à des échelles spatiales et temporelles multiples. Cet avantage permet

de coupler les données de télédétection, l'eau et le modèle énergétique de surface afin de mieux comprendre les processus hydrologiques à différentes échelles. Les données de télédétection spécifiquement pertinentes pour la surveillance des ressources en eau sont présentées dans le tableau 1.1 et détaillées ci-dessous.

Tableau 1.1. Principales caractéristiques des données de télédétection pertinentes pour la surveillance du bilan hydrique des cultures.

Région Spectral	Longueur d'onde	Résolution spatial	Résolution temporelle	Missions satellites en cours	Applications	Références
Visible-Proche Infrarouge (VNIR)	0.4 – 1.3 µm	1 m – 5 km	15 min – 16 jours	Sentinel-2, SPOT, Formosat, Lansat, ASTER, MODIS, AVHRR, MSG/SEVIRI, VIIRS, Sentinel-3	Indices de Végétation	Bannari et al. (1995)
					Paramètres de Végétation	Pinter et al. (2003)
					Albédo	Qu et al. (2015)
					Coefficient de culture	Singh and Irmak (2009)
					Indices d'humidité du sol	Wang and Qu (2009)
Infrarouge thermique	8 – 14 µm	60 m – 5 km	15 min – 16 jours	Lansat, ASTER, MODIS, Sentinel-3, AVHRR, VIIRS, MSG/SEVIRI, GOES	Température de surface	Z.-. Li et al., (2013); Sobrino et al. (2016)
					Emissivité	Z. L. Li et al., (2013)
Micro-onde (passive / active)	1 mm – 1 m	10 m – 60 km	1 – 6 jours	Sentinel-1, SMAP, SMOS, ASCAT, AMSR-2	Stress hydrique	Kullberg et al. (2016)
					Humidité du sol	Brocca et al., (2017)
Microwave (passive / active)	1 mm – 1 m	10 m – 60 km	1 – 6 days	Sentinel-1, SMAP, SMOS, ASCAT, AMSR-2	Humidité du sol	Brocca et al., (2017)
					Rugosité de surface	Zribi and Dechambre (2003)

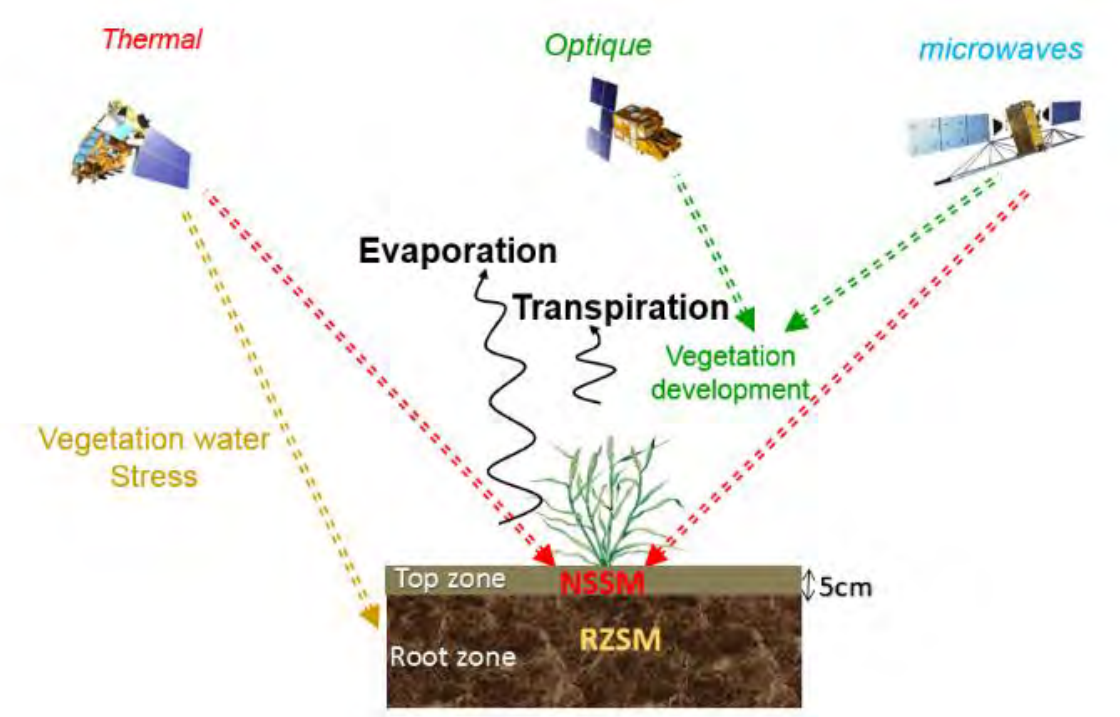


Fig. 1.2. Capacité des données de télédétection multispectrales à caractériser l'état du sol et de la végétation pour le suivi du bilan hydrique des cultures. Source : Amazirh (2019).

1.2.1. Données Visible - Proche infrarouge

Les réflectances visible et proche infrarouge (VNIR) ont l'avantage de surveiller la végétation/cultures en termes de phénologie, de santé, de vigueur, etc. En effet, les feuilles de plantes vertes présentent une très faible réflectance dans les régions visibles (0,4 - 0,7 µm) en raison de leur forte absorption par les pigments photosynthétiques et végétaux et d'une très forte réflectance dans le proche infrarouge (0,7 - 1,3 µm) en raison de leur faible absorption par les particules ou pigments subcellulaires ainsi que d'une diffusion considérable aux interfaces des parois cellulaires mésophiles (Gausman, 1977). Ces caractéristiques ont servi de base à de nombreuses applications de la télédétection à la gestion des cultures en utilisant principalement des indices de végétation (VI) (i.e. différences, rapports ou combinaisons linéaires de réflectances dans les bandes d'ondes visible et proche infrarouge). VI ont montré de bonnes corrélations avec des paramètres de croissance des plantes tels que la biomasse verte (Pinter et al., 2003), l'indice de surface foliaire (Duchemin et al., 2006), la fraction du rayonnement photosynthétiquement actif absorbé (Pinter et al., 1994), entre autres.

Dans la gestion de l'eau des cultures, les VI ont été largement utilisés pour calculer le coefficient de culture (défini comme le rapport entre l'ET et une ET de référence) (Bausch et Neale, 1987; Choudhury et al, 1994; Singh et Irmak, 2009). En effet, les coefficients de culture dépendent principalement de la dynamique des canopées (fraction de couverture,

indice de surface foliaire et phénologie). Par conséquent, les coefficients de culture basés sur les VI ont été d'une grande valeur dans les algorithmes de estimation de l'ET et de planification de l'irrigation afin d'estimer les besoins en eau des cultures (Allen et al., 2011; Pereira et al., 2015; Singh et Irmak, 2009). Plusieurs études ont démontré que l'ajustement local en fonction de la phénologie et du coefficient de culture devrait être plus approprié que l'utilisation des valeurs tabulées pour estimer l'ET et les besoins en eau des cultures (Allen et al., 2011; Bausch, 1995; Pereira et al., 2015). Ces ajustements locaux reposent généralement sur des mesures ou des observations de la croissance des cultures spécifiques au site et, par conséquent, des approches basées sur les VI sont recommandées pour les coefficients de culture et la gestion de l'irrigation.

De plus, le VNIR a reçu un intérêt particulier pour les applications de bilan d'énergie de surface, fournissant des estimations robustes de la fraction du rayonnement net entrant dans le flux thermique du sol au moyen de VI (Daughtry et al., 1990) ou pour estimer l'albédo en surface (Liang, 2001; Qu et al., 2015). VI sont également des données auxiliaires essentielles dans l'estimation de l'émissivité de surface pour estimer la température à la surface du sol (Jiménez-Muñoz et al., 2006; José A. Sobrino et al., 2008), comme celles utilisées dans cette étude. De plus, les VNIR sont nécessaires pour détecter toute la gamme des conditions de surface du couvert végétal nécessaires dans plusieurs méthodes basées sur des informations contextuelles sur des données LST et VI obtenues par télédétection (Merlin, 2013; Merlin et al., 2014; Moran et al., 1994).

L'un des principaux avantages des capteurs VNIR par rapport aux autres capteurs spectraux est la haute résolution spatiale appropriée au suivi des cultures. La résolution inférieure à 100 m (p. ex. Landsat, ASTER, SPOT, Sentinel-2) ne permet qu'une à six observations par mois en cycle orbital. Cependant, les séries chronologiques d'images de SPOT ou d'autres satellites commerciaux (p. ex. QuickBird, Worldview, GeoEye) à très haute résolution (< 10 m) et à résolution temporelle (temps de revisite inférieur à 5 jours) sont prohibitives et ne sont donc pas utiles pour des applications opérationnelles. Le lancement de Sentinel-2A/B représente une percée pour les missions VNIR librement disponibles, fournissant des données VNIR à une résolution de 10 m avec une opportunité unique de surveiller systématiquement les cultures à un cycle de répétition hebdomadaire (de 5 à 12 jours).

Malgré le fait que le stress hydrique et la période de sénescence des plantes peuvent être détectés par VI (Adams et al., 1999), l'influence du stress hydrique dans ces longueurs d'onde n'est pas suffisamment importante par rapport aux changements biologiquement significatifs de la teneur en eau des plantes pour des utilisations pratiques dans le suivi du stress hydrique sur le terrain (Bowman, 1989; Carter, 1991). Contrairement au VNIR, les données infrarouges thermiques se sont montrées très utiles pour évaluer le stress hydrique des cultures (Jackson, 1982), tel qu'il est présenté dans la section suivante.

1.2.2. Données thermiques infrarouges

La température de surface (LST) est une variable essentielle qui module les fluxes de chaleur radiative, latente et sensible à l'interface sol-plante-atmosphère. La LST peut être obtenu globalement et opérationnellement à partir d'observations de télédétection infrarouge thermique. Par conséquent, la LST est une variable utile pour le suivi des flux de carbone, d'eau et d'énergie des champs aux échelles régionales (Anderson et al., 2008).

La LST a été une variable de surface clé pour de nombreuses applications environnementales et hydrométéorologiques, y compris les études climatologiques (Anderson et al., 2007; Hansen et al., 2010), la surveillance des conditions météorologiques extrêmes comme le suivi de la sécheresse (Anderson et al.., 2011; Jiménez-Muñoz et al. 2016; McVicar et Jupp, 1998), des estimations de l'humidité du sol (Amazirh et al. 2018; Merlin et al. 2012b) et de l'irrigation et la gestion des ressources en eau (Anderson et al. 2012b; Bastiaanssen et al. 2007; Droogers et al. 2010). La LST est particulièrement utile pour le suivi de la gestion de l'eau des cultures, car il est très sensible au stress hydrique des plantes et constitue un bon indicateur des changements de l'humidité du sol dans la zone racinaire (Anderson et al., 2012a, 1997; Moran et al., 2009). Ainsi, le LST peut être relié à l'humidité du sol de la zone racinaire (RZSM) au moyen de la température de la canopée et de la transpiration de la plante associée (Boulet et al., 2007; Hain et al., 2009; Moran et al., 1994) étant donné le couplage entre le bilan d'énergie de surface et le bilan hydrique.

La LST peut être dérivé de capteurs thermiques satellitaires à différentes échelles spatiales et temporelles, mais la principale limite des missions thermiques existantes est l'indisponibilité de hautes résolutions spatiales et temporelles en même temps. Par exemple, les missions offrant un temps de revisite haut (e.g. MODIS, MSG/SEVIRI, VIIRS et Sentinel-3) offrent habituellement une faible résolution spatiale et, inversement, celles offrant une résolution spatiale élevée (e.g. Landsat et ASTER) offrent une faible résolution temporelle (Fig. 1.3). Par conséquent, la capacité de surveiller les ressources en eau à l'échelle de la parcelle agricole (~100 m) est limitée par le peu de temps de revisite et même entravée par des conditions nuageuses, ne permettant pas de surveiller les changements rapides de l'état de la végétation.

Des études récentes ont mis en évidence l'importance des observations thermiques à haute résolution avec une revisite quasi journalière de l'état hydrique de la végétation (Cao et al., 2019; Guzinski et Nieto, 2019; Sobrino et al., 2016). Ainsi, idéalement, une constellation de satellites en orbite polaire (e.g. Landsat, ASTER) apparaîtrait comme la meilleure solution pour répondre à ces exigences, qui est potentiellement capable d'accomplir la mission ECOSTRESS (Hulley et al., 2017), lancée récemment en juin 2018, ou la future mission TRISHNA (Lagouarde et Bhattacharya, 2018). ECOSTRESS, à bord de la Station Spatiale Internationale, abordera des questions cruciales sur la dynamique eau-plante et les changements futurs des écosystèmes en fonction du climat au moyen des

produits de données de LST, ET, Efficacité de l'utilisation de l'eau, et Indice de Stress d'Evaporation à une résolution spatiale de ~60 m tous les 2 – 5 jours à différents temps de passage. Par conséquent, la détection est encore améliorée dans les environnements hétérogènes (comme les zones agricoles) par la haute résolution spatio-temporelle (Hulley et al., 2017). Cependant, le temps de passage de ECOSTRESS change et n'offre pas une couverture globale, il n'est donc pas optimal pour le suivi de la gestion des cultures dans le cadre de mises en œuvre opérationnelles. La mission TRISHNA combinera une haute résolution spatiale (50m) et un haut temps de revisite (environ 3 jours) dans le infrarouge thermique avec une couverture globale. Les deux principaux objectifs scientifiques de la mission sont le suivi des bilans énergétiques et hydriques de la biosphère continentale et le suivi des eaux côtières et continentales (Lagouarde et Bhattacharya, 2018).

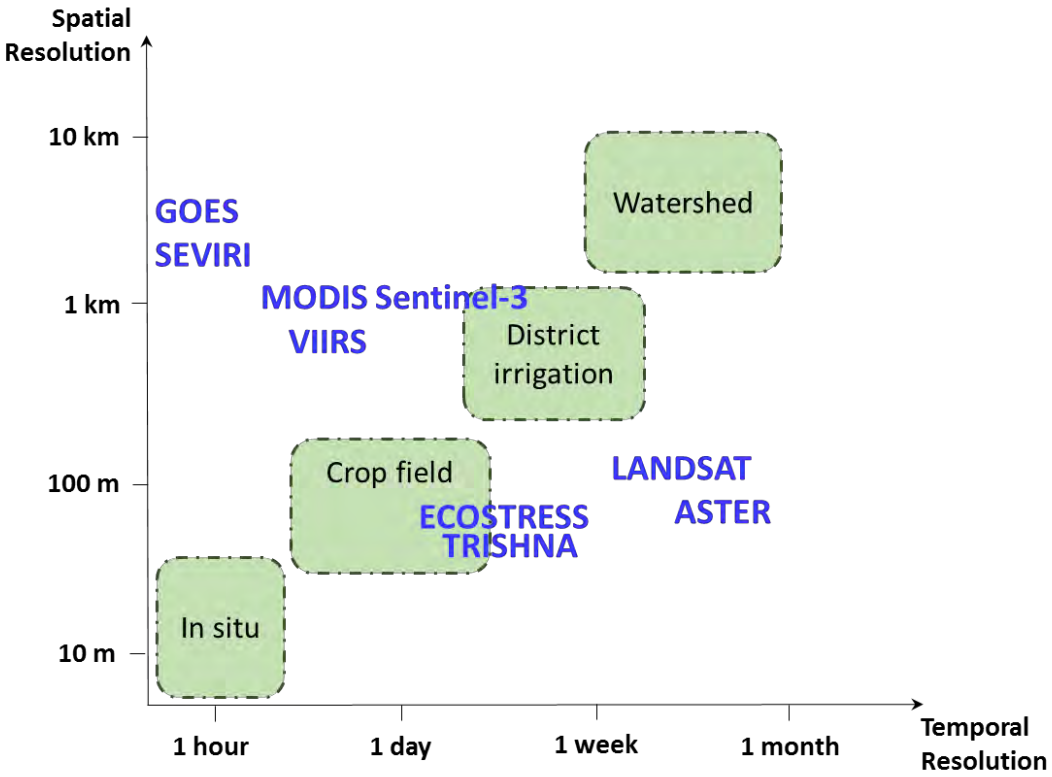


Fig. 1.2. Différentes résolutions spatiales et temporelles des observations actuelles et futures des satellites thermiques liées aux différentes échelles d'observation ciblées.

Avant le lancement de la mission TRISHNA, il est possible de désagréger les données LST à basse résolution existantes à haute résolution spatiale avec une précision relativement satisfaisante. Les méthodes de désagrégation se centrent sur la décomposition des températures au sein du pixel, ce qui permet d'obtenir un meilleur ensemble de données LST avec des résolutions temporelles et spatiales plus fines à partir des informations obtenues par différents capteurs. Par conséquent, les méthodes de désagrégation visent à obtenir des données LST appropriées pour le suivi du bilan hydrique des cultures à

l'échelle de la parcelle agricole (illustré dans la Fig. 1.3). L'idée de base derrière ces méthodes est d'établir une corrélation statistique ou un modèle physique entre LST à faible échelle et les variables auxiliaires à échelle fine. Dans ces méthodes, les données satellitaires dans les longueurs d'onde VNIR disponibles à une résolution plus fine que celle de la plupart des capteurs thermiques ont été des données auxiliaires essentielles pour combler l'écart entre une faible résolution spatiale et une haute résolution temporelle de LST (Zhan et al., 2013). Par conséquent, la plupart des méthodes de désagrégation ont été basées sur une relation d'invariance d'échelle entre LST et VI, en grande partie liée à la couverture végétale. Les méthodes basées sur de VI restent les approches opérationnelles les plus utilisées en raison de la disponibilité de données à haute résolution spatiale et temporelle, telles que DisTrad, TsHarp, entre autres algorithmes (Agam et al., 2007a; Bindhu et al, 2013; Kustas et al, 2003; Mukherjee et al, 2014; Zhan et al., 2013). En plus de l'utilisation des données VNIR, d'autres méthodes de désagrégation plus complexes ont été proposées: l'utilisation de l'espace à deux dimensions LST-VI pour dériver des indices d'état hydriques du sol/végétation qui pourraient mieux représenter la variabilité du LST et ainsi améliorer la précision de la désagrégation sur des zones agricoles à forte teneur en eau (Chen et al., 2010; Sandholt et al., 2002; Yang et al., 2010). Cette procédure a été étendue à l'utilisation des facteurs supplémentaires qui modulent le LST, reflétant la teneur en humidité du sol et le type de végétation (Amazirh et al., 2019; Merlin et al., 2012a, 2010; Yang et al., 2011). Par exemple, Merlin et al. (2010) ont établi une distinction entre la végétation photosynthétiquement active et la végétation non photosynthétiquement active à partir de séries temporelles de données optiques à ondes courtes à inclure dans la procédure de désagrégation. Ensuite, les variables substitutives MSS dérivées des données micro-ondes peuvent prendre en compte les effets de l'humidité du sol sur la désagrégation du LST (Merlin et al., 2012a; Amazirh et al., 2019). Bien que ces dernières méthodes puissent fournir de meilleures précisions que l'utilisation des seules relations LST-VI, elles nécessitent des paramètres supplémentaires qui deviennent difficiles à mettre en œuvre sur le plan opérationnel. Par conséquent, la mise en œuvre de méthodes de désagrégation sur une base opérationnelle avec une précision raisonnable implique de nouveaux défis dans les méthodes.

1.2.3. Données micro-ondes

Les longueurs d'ondes micro-ondes sont l'une des plus sensibles aux variations de l'humidité du sol, étant donné le contraste important des émissions de la surface de la terre entre l'eau et la terre. Ainsi, l'humidité du sol en surface (SSM) peut être estimée à l'aide de la télédétection (Entekhabi et al., 1994; Kerr et al., 2010). Toutefois, les instruments de télédétection ne sont capables de capter des informations sur l'humidité du sol que jusqu'à une profondeur d'environ 5-10 cm de la surface. En effet, l'émission de

micro-ondes à cette fréquence est fortement atténuée dans le milieu poreux du sol (Entekhabi et al., 1994; Kerr et al., 2010).

Selon Schmugge et al (2002), les données micro-ondes présentent quatre avantages uniques par rapport à d'autres régions spectrales: i) l'atmosphère est effectivement transparente, ce qui permet de couvrir toutes les conditions météorologiques; ii) la végétation est semi-transparente et permet l'observation des surfaces sous-jacentes; iii) la mesure micro-ondes dépend fortement des propriétés diélectriques de la cible, qui pour le sol dépend de la quantité d'eau présente; iv) la mesure micro-ondes est indépendante de la lumière solaire, permettant une observation jour et nuit.

Il existe deux techniques de télédétection micro-onde: les capteurs micro-onde passifs et actifs. Les capteurs hyperfréquences passifs (radiomètres) détectent l'énergie micro-onde émise naturellement dans leur champ de vision à l'aide de détecteurs très sensibles. Cependant, les quantités d'énergie sont généralement très faibles en raison des longueurs d'onde, qui sont beaucoup plus longues que les longueurs d'onde optiques. Ainsi, les champs de vision doivent être grands pour détecter suffisamment d'énergie pour enregistrer un signal. La plupart des capteurs micro-onde passifs se caractérisent donc par une faible résolution spatiale (~30 - 60 km). Parmi les missions passives, le satellite SMOS, lancé en 2009, a été largement utilisé pour l'estimation de SSM, avec une précision requise de 4 %. Basée sur une antenne en bande L (1,4 GHz), il s'agit de la première mission spatiale dédiée à l'observation du SSM au niveau mondial (Kerr et al., 2010). La mission AMSR-E, lancée en 2002, fournit des mesures de température de brillance à six fréquences de 6,9 à 89 GHz en polarisation horizontale et verticale, dont les canaux en bande C (6,9 GHz) et en bande X (10,7 GHz) conviennent pour la récupération de SSM (Njoku et al., 2003) à des résolutions spatiales comprises entre 25 et 50 km. La mission SMAP, lancée en 2015, combine un radiomètre (passif) et un radar à synthèse d'ouverture (SAR, actif) dans la bande L (1,20-1,41 GHz) pour fournir des mesures de SSM avec une couverture globale en 2-3 jours. Le capteur ASCAT est un diffusiomètre en bande C (5,255 GHz, polarisation VV) à une résolution spatiale d'environ 50 km, qui fonctionne à bord du satellite MetOp (Meteorological Operational) depuis 2006.

En ce qui concerne les capteurs actifs, le plus populaire est la mission Sentinel-1, lancée en 2014, qui fournit des données SAR en bande C à une résolution spatiale de 20 m avec un cycle de répétition sans précédent de 6 jours en combinant les passages ascendants et descendants (3 jours en combinant les deux satellites disponibles depuis 2015). Bien que les données de signaux de rétrodiffusion aient le potentiel de surveiller le SSM (e.g. Amazirh et al., 2018; Gao et al., 2017; Zribi et al., 2011), il n'existe actuellement aucun produit SSM opérationnel mondial à une résolution aussi fine. Ceci est notamment dû à la difficulté de modéliser dans le temps et sur des zones étendues l'impact du couvert végétal/structure et de la rugosité de surface sur le signal de rétrodiffusion (Zribi et al., 2011, 2008).

1.3. Modélisation des composantes du bilan hydrique des cultures à l'aide de la télédétection

Les données de télédétection se sont révélées très utiles pour détecter les principales variables de la surface terrestre afin de surveiller le bilan hydrique des cultures à partir d'observations instantanées au moment du passage du satellite. Cependant, l'estimation des différentes composantes du bilan hydrique des cultures nécessite une stratégie de couplage appropriée entre les données de télédétection et la modélisation de la surface. Cela implique de tirer parti des données de télédétection multispectrales et multi-résolution et de combler l'écart entre les observations par télédétection et les flux d'eau et entre les observations instantanées et la résolution temporelle adaptée à la gestion de l'eau des cultures.

La connaissance des besoins en eau des cultures est essentielle pour optimiser l'efficacité de l'utilisation de l'eau des cultures. Les modèles de bilan hydrique des cultures simulent les relations entre le sol, les plantes et l'atmosphère en simulant les besoins en eau des cultures. Dans ce contexte, les modèles de bilan hydrique des cultures sont des outils efficaces dans la gestion des ressources en eau. Ces modèles sont basés principalement sur la représentation de la variabilité de l'humidité du sol dans la capacité de stockage de l'eau (ΔS) en résolvant un bilan hydrique entre les apports et les pertes en eau. Le bilan hydrique peut être exprimé et simplifié comme suit:

$$\Delta S = P + I - ET - DP - RO \qquad \text{Eq. 1.1}$$

Dans ce bilan hydrique, les approvisionnements en eau sont représentés par les précipitations (P) et les irrigations (I), et les pertes d'eau sont principalement représentées par l'ET et la percolation profonde (DP). Le ruissellement (RO), tant en surface que sous la surface, peut également être une source importante de perte d'eau dans les zones en pente et sous des apports d'eau importantes, telles que les fortes pluies ou les irrigations inondées. Toutefois, dans les zones agricoles avec des surfaces planes, on peut supposer que le RO est négligeable. Dans l'Eq. 1.1, les processus de diffusion dans le profil vertical du sol, comme l'élévation de capillarité, sont négligés. Dans plusieurs zones agricoles des régions semi-arides à arides, l'augmentation de la capillarité peut être négligée en raison de la profondeur importante des nappes phréatiques, plusieurs mètres plus profonde que la capacité de stockage d'eau disponible pour les plantes.

Plusieurs modèles ont été proposés dans la littérature (FAO-56, SAFY, STICS, AquaCrop) pour modéliser les besoins en eau des cultures au moyen de l'ET. Ces modèles peuvent fournir des estimations quantitatives du rendement des cultures dans différentes

conditions environnementales, ainsi qu'une simulation du bilan hydrique. Par exemple, le modèle FAO-56 (Allen et al., 1998) est un modèle simplifié de bilan hydrique piloté par: 1) des variables de forçage météorologique pour estimer la demande évaporative atmosphérique représentée par une évapotranspiration de référence (ET0) et 2) les apports en eau par précipitation et irrigation. En s'appuyant sur l'Eq. 1.1, le modèle FAO-56 simule la disponibilité de l'eau du sol pour l'ET, qui peut être étendue à un modèle à double source pour simuler la disponibilité de l'eau du sol dans la couche superficielle supérieure et dans la couche de la zone racinaire pour l'évaporation du sol et la transpiration des plantes, respectivement. Le modèle SAFY est un modèle de végétation journalière pour estimer le rendement des cultures (Duchemin et al., 2008). Il simule l'évolution temporelle de l'indice de surface foliaire verte et de la biomasse aérienne sèche tout au long de la saison de croissance. Les résultats du modèle SAFY ont été utilisés pour contrôler l'ET (ou ses composantes sol et végétation) d'un bilan d'eau dans le sol. Ainsi, ce modèle a été couplé au modèle FAO-56 pour simuler les besoins en eau et les rendements des cultures (Battude et al., 2017, 2016; Hadria et al., 2010). Le modèle de culture STICS (Brisson et al., 1998; 2002; 2003) simule les processus associés à la croissance et à la sénescence des plantes. La validation du STICS pour différents climats (Bhattarai et al., 2018; Brisson et al., 2002; Hadria et al., 2007, 2006) a montré que le modèle simule précisément le bilan hydrique lorsque l'indice foliaire est correctement estimé.

Le suivi de la teneur en eau du sol disponible pour les plantes est la variable essentielle pour la modélisation des ressources en eau, et en particulier pour l'estimation des besoins en eau des cultures au moyen de l'ET. Le suivi de la teneur en eau du sol peut être représenté par la dynamique temporelle de l'humidité du sol dans la zone racinaire (RZSM), définie comme la teneur en eau de la colonne du sol qui peut être extraite par évaporation en surface, par extraction racinaire ou par remontées capillaires (Calvet et Noilhan, 2000). Pour le suivi des ressources en eau, l'irrigation est l'un des principaux forçages dans les zones agricoles, notamment dans les régions semi-arides à arides. Cependant, l'irrigation n'est généralement pas disponible sur de grandes superficies. Dans ce contexte, cette thèse se concentre sur l'estimation de ces principales composantes du bilan hydrique des cultures: ET, RZSM et irrigation. Les principales caractéristiques des composantes de l'ET, du RZSM et de l'irrigation, les méthodes d'estimation associées et leur modélisation sur des zones étendues à partir des observations de télédétection sont décrites ci-dessous.

1.3.1. Modélisation de l'évapotranspiration

L'évapotranspiration (ET) est le terme utilisé pour décrire la perte d'eau de la surface de la Terre vers l'atmosphère par les processus combinés d'évaporation du sol (ainsi que

des plans d'eau libres et des surfaces végétales) et de transpiration de la végétation. L'ET est un élément clé dans les processus qui contrôlent l'échange d'énergie et de masse (eau et carbone) entre les écosystèmes terrestres et l'atmosphère. L'ET est donc responsable du couplage entre le bilan hydrique et le bilan énergétique superficiel (Fig. 1.4).

Au cours des dernières décennies, plusieurs travaux ont documenté le rôle essentiel de l'ET dans le bilan hydrique pour son importance critique sur la disponibilité des ressources (Oki et Kanae, 2006), les prévisions hydrologiques et météorologiques (Findell et al., 2011), les scénarios de changement climatique liés aux indices de sécheresse (Gao et al., 2011) et le calendrier d'irrigation agricole (Allen et al., 2005; Senay et al., 2013a). Par conséquent, la connaissance de l'ET est essentielle pour le suivi des ressources en eau dans les régions où il y a pénurie d'eau puisque le taux réel d'utilisation de l'eau par la végétation peut différer considérablement des taux potentiels d'ET (Anderson et al., 2012a).

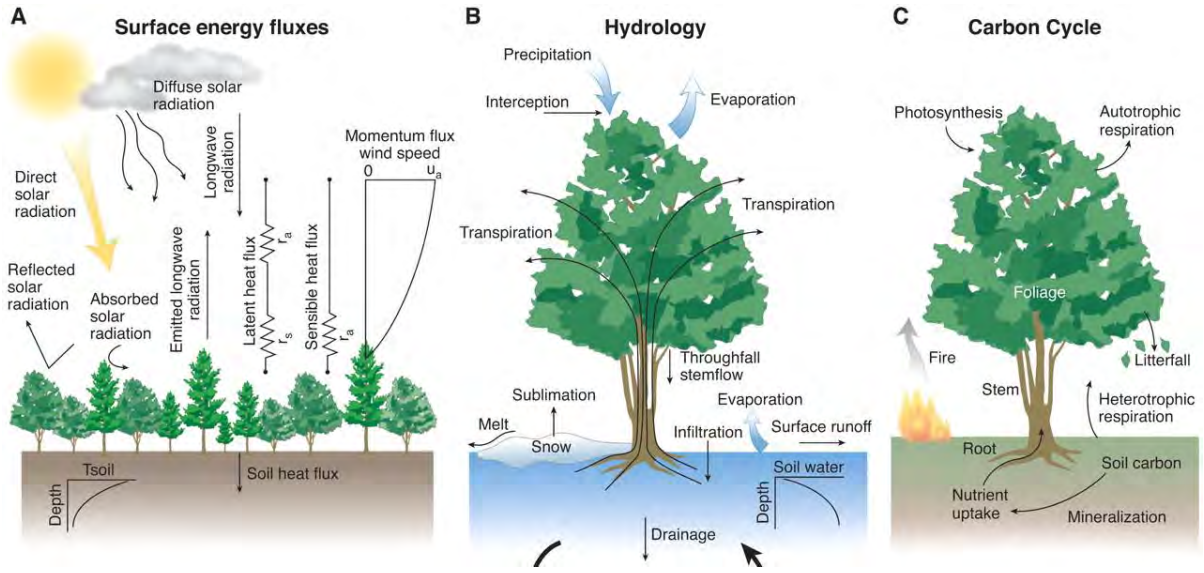


Fig. 1.3. Schéma représentant les cycles de l'énergie de surface (A), de l'eau (B) et du carbone. L'ET est représentée comme un flux de chaleur latente en A, comme l'évaporation du sol et la transpiration des plantes en B et l'ET est fortement liée à la photosynthèse et à la respiration du sol en C. Source: Bonan (2008).

Il existe différentes méthodes qui permettent de quantifier l'ET au moyen de mesures directes. Les mesures directes sont des estimations techniques au sol obtenues à partir de différentes techniques telles que: i) les approches hydrologiques (p. ex. lysimètres), ii) les approches physiologiques des plantes (p. ex. débit de sève et méthodes en chambre) et iii) les approches micro-météorologiques (p. ex. rapport Bowen, eddy covariance et scintillomètre). Ces techniques diffèrent également par l'échelle des mesures. Par exemple, à l'échelle locale, les capteurs de flux de sève permettent d'assurer la transpiration de chaque plante tandis que les lysimètres permettent d'assurer l'ET à partir d'une petite surface ou l'évaporation lorsque la surface se trouve dans des conditions de sol nu. D'autre part, les techniques d'Eddy covariance permettent d'obtenir

une ET à l'échelle de la parcelle (~100 m), ce qui est plus approprié pour le suivi des besoins en eau des cultures. Les scintillomètres peuvent fournir l'ET sur une plus grande échelle de plusieurs centaines de mètres à une dizaine de kilomètres. Bien que ces techniques puissent fournir de longues séries temporelles à très haute fréquence (~10 Hz), ces systèmes ne fournissent pas de distributions spatiales à l'échelle régionale sur des surfaces hétérogènes, en particulier dans les régions aux conditions climatiques advectives. Les modèles d'ET à l'aide de la télédétection sont mieux adaptés à l'estimation de l'utilisation de l'eau des cultures à l'échelle régionale, offrant une solution rentable pour le suivi des zones larges.

De nombreuses approches basées sur la télédétection, de complexité variable, ont été mises au point pour le suivi des besoins en eau des cultures à l'aide d'estimations d'ET. Par exemple, le modèle FAO-56 a été largement utilisé à l'échelle de la parcelle pour estimer les besoins en eau des cultures au moyen de l'ET simulée. Comme il a été mentionné à la section 1.2.1, les coefficients des cultures ont été estimés à partir des VI issue de la télédétection pour mieux contraindre les stades phénologiques, ce qui a également été inclus dans le modèle FAO-56 (Er-Raki et al., 2010, 2007; González-Dugo et Mateos, 2008; Hunsaker et al., 2005). Ainsi, les modèles FAO-56 couplés à VI ont montré une amélioration significative par rapport au modèle classique FAO-2Kc. Etant donné que les données thermiques sont plus aptes à détecter le stress hydrique que VI, le LST a été assimilé à la méthode FAO-56 (Er-Raki et al., 2008), et plus récemment, utilisé pour le coefficient de stress hydrique pour mieux contraindre la méthode FAO-56 (Dejonge et al., 2015; Ihuoma et Madramootoo, 2017; Kullberg et al., 2016).

L'atout des données thermiques vient de l'avantage de détecter l'information sur l'état hydrique de la végétation et de la capacité d'étudier la variabilité de la consommation d'eau dans des parcelles individuelles ou même pour la variabilité intra-parcellaire (Anderson et al., 2012a). Cet avantage est donné principalement par la résolution spatiale des données thermiques d'environ 100 m. Ainsi, différentes méthodes ont été développées au cours des dernières décennies pour estimer l'ET en utilisant les données LST comme entrée principale, démontrant son immense valeur dans le suivi de l'ET (Gowda et al, 2008; Kalma et al, 2008; Li et al., 2009). La plupart de ces méthodes sont basées sur la résolution du bilan énergétique de surface, dont trois grandes approches peuvent être distinguées selon Su (2002): i) les approches résiduelles, ii) les modèles de surface terrestre et iii) les méthodes de fraction évaporative. Les méthodes résiduelles estiment le flux de chaleur sensible (H) et obtiennent ensuite le flux de chaleur latente (i.e. ET exprimé en énergie) comme résiduel de l'équation du bilan énergétique de surface. La deuxième approche consiste à estimer toutes les composantes du bilan énergétique à la surface du sol à l'aide de modèles continus de surface du sol en incluant des modèles SVAT (Sol-Végétation-Atmosphère Transfer). La troisième approche estime l'ET comme une fraction de l'ET potentielle (Moran et al., 1994) ou de l'énergie disponible (Long et Singh, 2012; Roerink et al., 2000). La fraction évaporative (EF) est définie comme

le rapport entre la ET et l'énergie disponible (rayonnement net moins flux de chaleur du sol). L'EF peut être estimée à partir de l'information contextuelle des images optiques/thermiques issue de la télédétection, où les conditions sèches et humides sont identifiées à partir de l'espace LST - VI (e.g. Long et Singh, 2012; Moran et al., 1994), l'espace LST - albedo (e.g. Roerink et al., 2000) ou par combinaison des deux espaces (Merlin, 2013; Merlin et al., 2014). C'est pour cette raison que ces approches ont été appelées approches contextuelles, qui ont suscité un intérêt particulier dans la communauté scientifique pour leur simplicité et leur mise en œuvre opérationnelle sur de larges surfaces.

Les valeurs d'EF peuvent définir deux régimes d'ET principaux: un régime limité par l'humidité du sol et un régime limité par l'énergie (Seneviratne et al., 2010). Le régime d'ET limité en humidité du sol est caractérisé par des valeurs d'EF inférieures à 1 et des valeurs d'humidité du sol inférieures à une humidité critique du sol (SM_{crit}) donnée, ce qui entraîne des conditions de stress de la végétation (Fig. 1.5). Au-dessus de SM_{crit}, l'EF est indépendant de la teneur en humidité du sol (régime d'ET à énergie limitée), ce qui signifie que la végétation n'est pas dans des conditions de stress avec des valeurs d'EF égales à 1. SM_{crit} est donc défini entre l'humidité du sol à capacité au champ (SM_{fc}, au-dessus de laquelle l'eau ne peut être retenue contre le drainage gravitaire) et celle du sol au point permanent de flétrissement (SM_{wp}, au-dessous duquel l'eau n'est pas accessible aux plantes). A partir de ces définitions, des régimes humides ($SM > SM_{crit}$, EF = 1), secs ($SM < SM_{wp}$, EF = 0) et transitoires ($SM_{wp} < SM < SM_{crit}$, $0 < EF < 1$) peuvent être définis à partir de modèles à l'aide de la télédétection thermique au moyen d'EF dérivés de la information contextuelle. Ces aperçus sont essentiels dans cette thèse parce qu'elles nous permettent d'établir un lien entre l'information contextuelle détectée à partir des données optiques et thermiques et l'humidité du sol dans la zone racinaire. Plus de détails sur l'humidité du sol sont présentés ci-dessous.

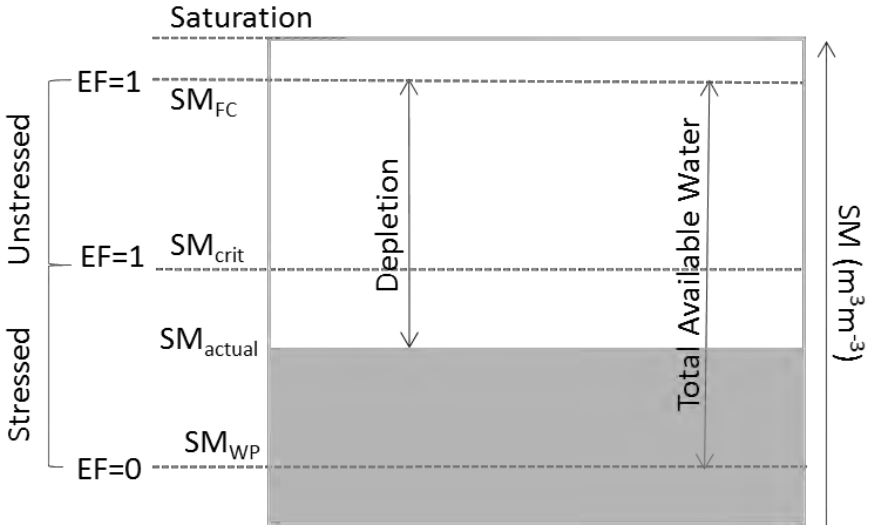


Fig. 1.4. Schéma représentant l'humidité du sol dans la zone racinaire et sa relation avec la fraction évaporative et le stress hydrique de la végétation. Source: based on Allen et al. (1998).

1.3.2. Modélisation de l'humidité en zone racinaire

L'humidité du sol (SM) est une variable hydrologique importante, car elle est essentielle dans les interactions surface-atmosphère par l'ET et les autres flux énergétiques. SM contrôle également la répartition de l'eau de pluie entre l'infiltration et le ruissellement, ainsi que les flux de chaleur latente et sensible. Une meilleure connaissance de la SM est donc d'un intérêt primordial pour le suivi des ressources en eau et par conséquent pour optimiser l'utilisation de l'eau destinée à l'irrigation.

Il existe plusieurs méthodes qui permettent de fournir des estimations de la SM pour son suivi. Premièrement, les mesures directes de la SM ne sont obtenues que par des méthodes destructives comme les mesures gravimétriques. Cette méthode consiste à quantifier en laboratoire l'eau évaporée d'un volume de sol préalablement extrait afin de calculer la masse d'eau divisée par la masse de sol sec. La méthode gravimétrique n'est donc pas pratique pour les mesures sur des zones larges ou pour le suivi par de longues séries temporelles de SM. Deuxièmement, les mesures indirectes fournissent des estimations de la SM basées sur les mesures d'une variable physique fortement liée à la SM (e.g. le diélectrique apparent du sol). Les capteurs qui mesurent la SM permettent ainsi de fournir de longues séries temporelles. Cependant, les mesures sont représentatives d'un point spécifique, ne fournissant pas de tendances ou de distributions spatiales à l'échelle régionale (horizontale) ou dans le profil du sol (verticale).

La SM peut également être estimée à partir d'instruments de télédétection, qui peuvent être au sol (sur des tours), en vol ou sur des plates-formes satellites. Cependant, les instruments de télédétection ne peuvent observer que de SM de la couche peu profonde près de la surface, de sorte qu'on l'appelle habituellement humidité du sol près de la surface (SSM). Même si la SSM peut être estimée par télédétection micro-onde, la variable d'intérêt pour les applications en modélisation météorologique à court et moyen terme, en études hydrologiques sur les zones végétalisées et en agriculture est l'humidité du sol en zone racinaires (RZSM), qui contrôle la transpiration des plantes (Albergel et al., 2008). RZSM représente la teneur en eau de la colonne de sol qui peut être extraite par l'évaporation en surface, par extraction racinaire ou par remontées capillaires (Calvet et Noilhan, 2000). La profondeur de ce réservoir peut varier d'environ 0,1 à quelques mètres selon le type de sol, les conditions bioclimatiques et le type de végétation (types de cultures en application agricole).

La SSM est relié au RZSM par des processus dynamiques de transfert d'eau du sol (Noilhan et Planton, 1989). Il est donc possible de mettre en œuvre des algorithmes pour obtenir le profil d'humidité du sol et donc le RZSM à partir de séries temporelles de SSM observées (e.g. Albergel et al., 2008; Calvet et Noilhan, 2000; Kornelsen et Coulibaly, 2014; Wagner et al., 1999). Au cours des deux dernières décennies, plusieurs études ont

permis d'extraire de la RZSM ou du profile de l'humidité du sol soit en utilisant des observations in situ de SSM (Albergel et al., 2008; Calvet et Noilhan, 2000) ou par satellite (Calvet et al., 1998; Ford et al., 2014; Sabater et al., 2007). Parmi les nombreuses études sur la récupération des RZSM à partir de SSM observées, une grande partie d'entre elles sont fondées sur des algorithmes d'assimilation (e.g. Albergel et al., 2008; Calvet et Noilhan, 2000; Dumedah et al., 2015; Entekhabi et al., 1994; Walker et al., 2001). Cependant, de telles approches de récupération des RZSM souffrent d'une faible résolution spatiale étant donné que les produits opérationnels de SSM ne sont disponibles qu'à très faible résolution spatiale (>25 km) (Entekhabi et al., 2010; Kerr et al., 2010; Peng et al., 2017). Même si des jeux de données satellitaires désagrégées de SSM ont été assimilés dans des modèles de surface pour améliorer à la fois l'estimation de RZSM et sa résolution spatiale (Dumedah et al., 2015; Merlin et al., 2006), une telle approche couplée ne convient toujours pas pour le suivi régulier de la demande en eau des cultures à l'échelle de la parcelle (~100 m).

Alternativement à la SSM, la LST peut être utilisé dans le calcul des variables indirectes à l'aide du thermique pour la RZSM à travers d'indices en utilisant la température de la canopée et le taux de transpiration associé (Boulet et al., 2007; Hain et al., 2009; Moran et al., 1994). Par conséquent, une étape clé pour estimer la RZSM à partir du thermique est la partition du LST en températures du sol et de la végétation (Merlin et al., 2014, 2012b; Moran et al., 1994). En résumé, la SSM et la LST sont deux variables d'état précieuses qui peuvent aider à contraindre un modèle de surface pour estimer la RZSM à l'échelle de la parcelle pour la gestion de l'eau des cultures. Un couplage entre les données de télédétection et la modélisation de la surface pourrait donc être mis au point à cette fin.

1.3.3. Modélisation de l'irrigation

L'irrigation est l'une des composantes les plus importantes de la consommation des ressources en eau, représentant environ 70% de l'eau douce mobilisée à l'échelle mondiale (Foley et al., 2011) et peut être portée à plus de 80-90% dans les régions semi-arides et arides (Chehbouni et al., 2008; Garrido et al., 2010; Scanlon et al., 2012). Ainsi, l'augmentation de l'efficacité de l'utilisation de l'eau dans l'agriculture a été identifiée comme l'un des sujets clés liés à la pénurie en eau et à la sécheresse (Werner et al., 2012), étant essentiel pour la durabilité de la ressource. Malgré la pression importante de l'agriculture sur les ressources en eau, les informations sur l'irrigation sont souvent indisponibles dans l'espace, ce qui entrave une bonne gestion de l'eau. Il est donc essentiel de quantifier la quantité et le moment de l'irrigation sur des zones larges pour une gestion efficace des ressources en eau.

L'irrigation se réfère à l'eau fournie par l'agriculteur à la parcelle afin de répondre aux besoins en eau des cultures. Bien que l'irrigation soit étroitement liée aux besoins en eau

des cultures, ces derniers peuvent différer considérablement des quantités réelles d'irrigation. Malgré la grande variété d'approches existantes pour estimer l'eau des cultures au moyen d'estimations ET, l'irrigation est généralement simulée à partir des besoins en eau modélisés (e.g. Allen et al., 1998; Bastiaanssen et al., 2007; Battude et al., 2017; Corbari et al., 2019; Duchemin et al., 2008). Dans la simulation de l'irrigation basée sur la modélisation de la dynamique de l'humidité du sol à partir du bilan hydrique ou du bilan couplé d'énergie-eau, des incertitudes significatives peuvent être obtenues, surtout lorsqu'aucune information n'est disponible sur l'état hydrique réel des cultures dans le temps.

Pour tenter d'estimer les volumes d'irrigation à partir des données de télédétection, des études récentes ont exploré l'utilité des estimations de SSM à partir de capteurs micro-ondes (Brocca et al., 2018, 2017; Escorihuela et Quintana-Seguí, 2016; Jalilvand et al, 2019; Kumar et al, 2015; Lawston et al, 2017b; Malbéteau et al, 2018; Zhang et al, 2018). En particulier, Brocca et al. (2018) ont mis au point une méthode pour quantifier les quantités d'irrigation en combinant les produits de SSM à partir de satellite actuellement disponibles aven une résolution grossière (SMAP, SMOS, ASCAT, AMSR-2) et un bilan hydrique du sol. Ce travail a été appliqué sur diverses régions semi-arides et semi-humides dans le monde mais n'a pas pu être quantitativement évalué en raison de l'absence d'observations in situ fiables de l'irrigation sur les périmètres irrigués correspondants. Cependant, cette approche a été quantitativement évaluée à une résolution d'environ 50 km sur une région semi-aride (Jalilvand et al., 2019). Certaines déficiences ont été obtenues sur des périodes de pluies soutenues et la méthode n'a pas été mise en œuvre en hiver (Brocca et al., 2018). Cette approche ne convient donc pas aux cultures d'hiver, qui sont particulièrement importantes en Méditerranée. Néanmoins, la capacité de quantifier les irrigations mensuelles a été démontrée sous certaines conditions: pendant des périodes prolongées de faibles précipitations et en utilisant des données de SSM satellitaires avec une faible incertitude et une fréquence supérieure à 3 jours.

Par ailleurs, la communauté scientifique s'intéresse de plus en plus aux modèles de surface (LSMs) pour mieux simuler les processus d'irrigation (Felfelani et al., 2018; Lawston et al., 2017a; Pokhrel et al., 2016). Les LSMs ont incorporé des modules d'irrigation pour pouvoir représenter les irrigations en améliorant la quantité, la méthode et le moment de l'irrigation (Pokhrel et al., 2012). Comme dans la modélisation des besoins en eau des cultures mentionnée ci-dessus, ces modules d'irrigation déterminent généralement le moment et les quantités d'irrigation en fonction du déficit en RZSM. Ainsi, l'irrigation est déclenchée lorsque le RZSM tombe en dessous d'un seuil spécifié et est ensuite calculée comme la quantité nécessaire pour amener le RZSM jusqu'au niveau ciblé. Par conséquent, les simulations peuvent différer considérablement des irrigations réelles. Étant donné l'utilité démontrée de la SSM dérivée des micro-ondes pour détecter le timing tout au long de la saison et la signature spatiale de l'irrigation (Brocca et al., 2018; Lawston et al., 2017b; Malbéteau et al., 2018). Felfelani et al (2018)

a récemment assimilé les données de SSM issue de SMAP dans une LSM à grande échelle pour mieux contraindre et améliorer les simulations d'irrigation et également pour améliorer les simulations de SSM. Cependant, comme dans les méthodes basées sur des données de SSM issue des capteurs micro-ondes, la résolution spatiale est trop grossière pour le suivi des ressources en eau à l'échelle de la parcelle.

A une échelle spatiale plus appropriés à la gestion de l'eau agricole, certaines études récentes (e.g. Corbari et al., 2019; Chen et al., 2018) ont utilisé des données optiques pour déterminer le timing et la planification de l'irrigation. Corbari et al. (2019) ont couplé les données optiques de télédétection, la modélisation hydrologique de l'eau et de l'énergie en surface et les prévisions météorologiques afin de prédire les besoins en eau pour l'irrigation jusqu'à 3 jours. Ici, les variables de surface issue de données optiques/thermiques ont été utilisées pour initialiser et calibrer le bilan d'énergie-eau. Chen et al (2018) ont proposé une autre approche différente pour détecter le moment de l'irrigation à partir de données optiques (VI issue des données de réflectance). La méthode s'est montrée prometteuse pour la détection des événements d'irrigation. Cependant, il n'était applicable que pendant la première moitié de la saison de croissance et il n'a pas été en mesure d'estimer les quantités d'irrigation.

Malgré les progrès et les tentatives des dernières années pour estimer l'irrigation, aucune méthode ou approche n'est encore disponible pour estimer l'irrigation à l'échelle de la parcelle agricole (~100 m) sur de larges surfaces.

1.4. Objectifs

En ce qui concerne l'état de l'art, l'une des principales limites de la modélisation du bilan hydrique des cultures est le manque de données d'irrigation sur des zones larges, dont tous les flux d'eau dépendent essentiellement des apports en eau. Cependant, la télédétection s'est avérée très utile pour le suivi des variables de surface clés afin de résoudre le bilan couplé d'eau-énergie. En particulier, les images thermiques instantanées sont capables de détecter les états de surface qui peuvent être intégrés dans le bilan couplé d'eau-énergie afin de résoudre ses composants.

L'objectif général de cette thèse consiste donc à estimer les principales composantes du bilan hydrique des systèmes agricoles, tels que l'ET, le RZSM et l'irrigation, à l'échelle de la parcelle (100 m) sur une base journalière et sur de larges zones (le périmètre irrigué de quelques kilomètres d'extension). A cette fin, le couplage entre les données optiques/thermiques issue de la télédétection et un modèle basé sur la FAO est proposé en tenant compte des principaux avantages suivants: i) la disponibilité de données optiques/thermiques à une résolution spatiale appropriée pour le suivi des cultures, ii) la simplicité des méthodes contextuelles à l'aide des données optiques/thermiques dans

l'estimation de l'ET et le suivi du stress hydrique végétal, et iii) l'utilité des données optiques/thermiques comme approximation de la RZSM et de la SSM.

Cette thèse de doctorat a joué un rôle important dans le projet REC intitulé "Root zone soil moisture Estimates at the daily and agricultural parcel scales for Crop irrigation management and water use impact - a multi-sensor remote sensing approach, http://rec.isardsat.com". Ce projet (mars 2015 - mars 2019) a été soutenu par le programme de recherche et d'innovation Horizon 2020 de la Commission européenne (H2020) dans le cadre de l'action Marie Sklodowska-Curie Research and Innovation Staff Exchange (RISE). Le projet a été réalisé par une collaboration internationale et multisectorielle entre: CESBIO (Centre d'Etudes Spatiales de la Biosphère) - Toulouse, Université Cadi Ayyad - Marrakech, isardSAT et LabFerrer - Catalogne. Ma thèse a donc directement nourri les objectifs du projet REC qui étaient: i) d'estimer la RZSM sur une base journalière à l'échelle de la parcelle agricole et ii) d'évaluer quantitativement les différentes composantes du bilan hydrique à l'échelle de la parcelle agricole à l'aide des données de télédétection facilement disponibles.

LMI-TREMA (Laboratoire Mixte International – Télédétection et Ressources en Eau en Méditerranée semi-Aride) à Marrakech vise à améliorer la gestion de l'eau destinée à l'irrigation en développant des outils permettant une utilisation rationnelle de l'eau. Pour ce faire, LMI-TREMA dispose depuis 2002 de plusieurs sites expérimentaux dans la plaine du Haouz, au Maroc (Jarlan et al., 2015), qui ont été utilisés pour tester les approches proposées dans cette thèse. LMI-TREMA travaille en étroite collaboration avec l'agence publique régionale ORMVAH (Office Régional de Développement Agricole du Haouz), responsable depuis 1966 de la conception et de la construction de grands périmètres irrigués et de leur gestion, ainsi que du développement agricole sur une superficie de 7000 km^2 dans le Haouz.

Bien que l'irrigation à l'échelle de la parcelle agricole soit un forçage critique pour le suivi de la gestion de l'eau dans les zones agricoles irriguées, elle est l'une des composantes du bilan hydrique les moins étudiées en termes d'estimation aux échelles spatiales intégrées. Par conséquent, une étape clé dans le développement de l'approche est l'estimation de l'irrigation puisqu'aucune méthode n'est encore disponible pour estimer le timing et les quantités d'irrigation à l'échelle de la parcelle et à l'échelle journalière, et que tous les flux d'eau dépendent essentiellement des apports en eau. L'approche de modélisation repose sur la synergie entre les données optiques de télédétection, les méthodes contextuelles et un modèle de bilan hydrique pour inverser d'abord l'irrigation, puis les autres composantes du bilan hydrique. Deux zones sont utilisées pour valider l'approche de modélisation développée dans cette thèse: une région semi-aride au Maroc et une région aride au Chili.

Cette thèse suit une approche par étapes et est structurée en trois étapes principales et complémentaires.

Dans un premier temps (Chapitre 3), une étude de faisabilité est réalisée à l'échelle in situ sur une parcelle de blé d'hiver en intégrant des données optiques/thermiques dans un modèle de bilan hydrique basé sur la FAO-56. Cette approche vise à estimer l'irrigation à l'échelle journalière au cours de la saison agricole afin de forcer le modèle de bilan hydrique des cultures et d'estimer la RZSM et l'ET journalières tout au long de la saison. Étant donné que cette approche est mise en œuvre au moyen d'observations in situ sur une base journalière, elle est évaluée pour différentes fréquences d'observation allant de 1 à 16 jours pour ressembler la disponibilité de l'observation par télédétection.

L'application de l'approche précédente aux données Landsat correspond à la deuxième étape (Chapitre 4) de cette thèse. Dans cette étape, les objectifs spécifiques sont les mêmes que dans la première étape, à la différence que les quantités et le timing d'irrigation, l'ET et la RZSM sont estimés sur de grandes superficies. A cette fin, des changements importants sont adoptés pour mettre en œuvre l'approche avec des données de télédétection facilement disponibles sur trois zones de la région semi-aride du centre du Maroc. Cinq sites expérimentaux couverts par des champs de blé d'hiver avec différentes techniques d'irrigation (goutte à goutte, inondation et sans irrigation) sont utilisés pour valider l'approche. Cette approche vise à estimer, pour la première fois, l'irrigation à l'échelle de la parcelle agricole sur une base journalière sur de larges superficies à partir de données de télédétection facilement disponibles pour une mise en œuvre opérationnelle ultérieure.

Dans la troisième étape (chapitre 5), une méthode opérationnelle de désagrégation des données thermiques est présentée afin d'estimer l'ET tous les 8 jours. La méthode est développée et évaluée dans une région aride du Chili sur de vignes et un verger d'oliviers. La désagrégation est un élément clé de l'approche que nous proposons ainsi que de nombreuses méthodes d'ET à l'aide de télédétection thermique. Ainsi, la disponibilité des données thermiques à une résolution spatiale et temporelle appropriée est d'un intérêt primordial pour le suivi de la gestion de l'eau à l'échelle du terrain. Dans le même ordre d'idées, la dernière étape de cette thèse implique la mise en œuvre de l'approche d'estimation des données d'irrigation en utilisant des données thermiques désagrégées comme données d'entrée afin d'assurer la disponibilité des principales données d'entrée tous les 8 jours et même tous les 4 jours en combinant les données Landsat-7, -8 et LST désagrégées.

Chapter 2. Data

Contents

2.1. Introduction *44*

2.2. Morocco: Haouz Plain *44*

2.2.1. Meteorological data *46*

2.2.2. Flux data (Eddy-covariance system) *46*

2.2.3. Soil Moisture *46*

2.2.4. Irrigation *47*

2.2.5. Fractional green vegetation cover *48*

2.2.6. Temperature data *50*

2.3. Chile: Copiapó Valley *51*

2.3.1. Meteorological data *52*

2.3.2. Ground-based land surface temperature *53*

2.4. Remote sensing data *53*

2.4.1. Landsat data *53*

2.4.2. ASTER Global Emissivity Datasets (ASTER GED) *56*

2.4.3. MODIS data *56*

2.5. Conclusion *57*

2.1. Introduction

The approaches developed in this thesis have been tested over two regions characterized by an irrigated agriculture with water scarcity issues and over-exploited water resources: Haouz Plain in central Morocco and Copiapo Valley in north Chile. Haouz Plain region is characterized by a semi-arid Mediterranean climate, with an average yearly precipitation of about 250 mm, while Copiapo Valley is characterized by an arid climate with low annual precipitation of about 28 mm. Haouz Plain is an extended flat agricultural area covered mainly by winter wheat and tree crops (e.g. olives, oranges), while the Copiapo Valley has a narrow flat area surrounding of mountainous desert cultivated mainly by characteristic tree crops of Mediterranean regions (e.g. olives, vineyards). Therefore, both regions have experienced an intensive and significant pressure on water resources by the agriculture. In addition, an important mining activity has been developed in Copiapo Valley, which has exerted a systematic stress on the water resources, especially on the aquifer. This critical situation has led to the fact that almost the entire Copiapo Valley irrigation techniques has been converted to technified irrigation (mainly drip systems). While Haouz Plain has recently initiated an ongoing conversion to drip irrigation systems given the Green Morocco Plan (PMV, 2013) to optimize the crop water use efficiency.

Therefore, the approaches have been implemented over these regions primarily because of the water scarcity issue in the Mediterranean, which might be more critical according to predictions of climate change with warming trends and a greater variability in precipitations (Giorgi, 2006; IPCC, 2013). The critical water scarcity in Copiapo Valley might be an example of future conditions of Mediterranean regions or under droughts, such as the southern Mediterranean regions in central Chile that has being afflicted by an unprecedented 'mega-drought' since 2010 (Garreaud et al., 2019, 2017).

This chapter aims to present the data used during this thesis (in situ and satellite data) over the chosen study areas. The chapter is divided into two main sub-sections to present both study areas, describing the in situ and satellite data are described in each of them.

2.2. Morocco: Haouz Plain

The Haouz plain is situated in central Morocco surrounding Marrakech city and covers about 6000 km^2 of almost flat surface. The climate is semi-arid Mediterranean, with an average annual precipitation of about 250 mm, of which 75% are concentrated during winter and spring (November-April). The annual evaporative demand exceeds significantly the annual precipitation with about 1600 mm, according to the reference ET (Duchemin et al., 2006). In the Haouz plain, the agriculture consumes about 85% of

available water (Abdelghani Chehbouni et al., 2008) and the flood irrigation technique is the most widely used method. The main crops in the region consist of winter wheat, olives and oranges. The aquifers have been heavily over-exploited resulting in a decrease in water table of over 20 m between 1980 and 2010 and local decrease of over 60 m (Malbéteau, 2016).

This thesis specifically focuses on three 12 x 12 km agricultural areas mainly covered by winter wheat crops (Fig. 2.1). Six experimental sites comprising three flood irrigation, two drip irrigation and one rainfed wheat fields were monitored during five agricultural seasons. Details about irrigation systems, crop field area and monitoring period per area, named Chichaoua, R3 and Sidi Rahal are shown in Table 2.1. The differences in irrigations techniques (mainly water amounts, timing and wetted surface) are useful to assess under different conditions the approaches proposed in this thesis focused on estimating irrigations.

The site of Sidi Rahal (Bour) was maintained under bare soil conditions during the 2015-2016 season due to the dry winter of 2015.

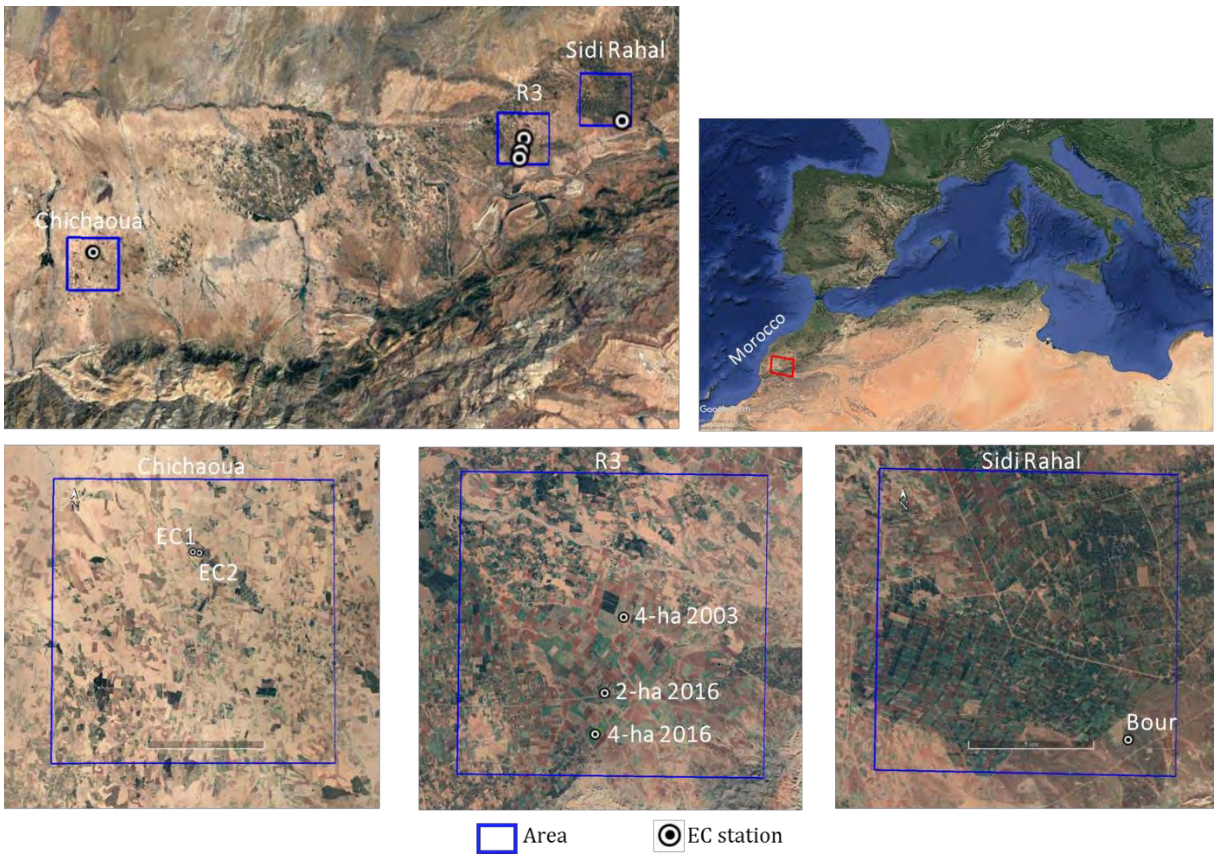


Fig. 2.1. Study areas and field crops where the developed approach is evaluated.

Table 2.1. Experimental sites of winter wheat field by agricultural area.

Area name	Sites name	Crop field area	Irrigation type	Monitoring period (mm/yyyy)

Chichaoua	EC1 – EC2	~1.5 ha – 1.5 ha	Drip-irrigated	11/2016 – 05/2018
R3	4ha-2003	4 ha	Flood-irrigated	12/2002 – 05/2003
	2ha[1] – 4ha-2016	2 ha – 4 ha	Flood-irrigated	12/2015 – 05/2016
Sidi Rahal	Bour	~1 ha	Rainfed	10/2014 – 05/2018

1. R3-2ha field is actually irrigated by drip system with amounts and quantities according to a flood irrigation system. Thus, R3-2ha is considered as flood-irrigated site.

2.2.1. Meteorological data

Automatic meteorological stations were installed in the three experimental areas. In Chichaoua and R3 areas the meteorological station was installed over an alfalfa field while in Sidi Rahal area it was installed over the monitored rainfed wheat field. Meteorological data including air temperature, solar radiation, relative humidity, wind speed and rainfall were collected continuously every 30 minutes at 2 m height during all the agricultural seasons.

2.2.2. Flux data (Eddy-covariance system)

Six micro-meteorological stations equipped with open-path eddy-covariance systems were installed in each experimental site. Here, four components of net radiation were measured by NR01 (Hukseflux) or CNR (Kipp & Zonen) radiometers, depending on the station. Soil heat fluxes were estimated from two HFP-01 heat flux plates (Hukseflux) per site buried at 5 cm. Finally, latent and sensible heat fluxes were acquired with an infrared gas analyzer (Li7500, Licor) or krypton KH2O hygrometers (Campbell) depending on the station and CSAT3 3D Sonic Anemometers at a frequency of 10 Hz and averaged over 30 min.

The closure of the energy balance is verified over the six sites and a correlation coefficient R^2 between 0.68 and 0.93 was found (Ait Hssaine et al., 2019; Amazirh et al., 2017; Rafi et al., 2019). Both sensible and latent heat fluxes were therefore corrected to force the closure of the energy balance by the Bowen ratio method (Twine et al., 2000). In this correction, the daily Bowen ratio (computed using 30-minute estimates between 9 am and 5 pm) and the 30-minute flux estimates are combined to derive the corrected 30-minute latent and sensible heat fluxes.

2.2.3. Soil Moisture

Soil water content at different depths were measured from time domain reflectometry (TDR) probes (CS615 and CS655, Campbell Scientific), which were installed near the fluxes measurement tower at every experimental site. The TDR probes were buried at different depths (Table 2.1) in order to monitor the soil water available in the entire soil profile. However in the rainfed wheat field, the TDR probes were installed only at the soil surface layer (at 5 and 10 cm). The measurements at different depths were used to estimate the soil moisture integrated over the root zone ($RZSM_{obs}$). $RZSM_{obs}$ was estimated by interpolating the soil moisture observations of the different depths belonging to the root-zone of wheat as follows:

$$RZSM_{obs} = \frac{d_i SM_{d_i} + (d_{i+1} - d_i) SM_{d_{i+1}} + \cdots + (d_n - d_{n-1}) SM_{d_n}}{d_i + (d_{i+1} - d_i) + \cdots + (d_n - d_{n-1})} \qquad \text{Eq. 2.1}$$

where SM_{di} (m^3m^{-3}) is the soil moisture measured at depth d_i and d_n is the deeper depth where there is a measurement that belongs to the root-zone. In this study, it is assumed that rooting depth varies linearly according to the vegetation cover between a minimum value set to 0.1 m (for bare soil) and a maximum value set to 1 m (for fully covering green vegetation).

Table 2.2. Depths to which the TDR probes were installed at every experimental site.

Area	Site names	Depths (m)
R3	4ha-2003	0.05 - 0.10 - 0.20 - 0.30 - 0.50 - 1.00
	2ha	0.05 - 0.15 - 0.30 - 0.50 - 0.80
	4ha-2016	0.05 - 0.15 - 0.25 - 0.35 - 0.50 - 0.80
Chichaoua	EC1	0.05 - 0.15 - 0.25 - 0.35 - 0.50 - 0.80
	EC2	0.05 - 0.15 - 0.30 - 0.50 - 0.80
Sidi Rahal	Bour	0.05 - 0.10

2.2.4. Irrigation

The distribution and management of water resources is different in the experimental sites depending on the location of agricultural areas.

In R3 area, the ORMVAH (*Office Régional de Mise en Valeur Agricole du Haouz*) has managed the distribution of water in the irrigated area since 1999. ORMVAH is in charge of the dam water distribution during the agricultural season starting from December through May. Flood irrigation system is the most widely used method in this area where the fields are irrigated by using concrete canals that carry water from the main canal to the irrigated units. In particular, the 4ha-2003 and 4ha-2016 fields were irrigated by flooding with 4 and 7 irrigation events regardless of the precipitation and thus of soil moisture conditions. The 2-ha field was instead irrigated by drip technique but was

nevertheless considered as flood-irrigated field since the irrigation amounts and timing were according to a flood irrigation system.

In Chichaoua area, both EC-1 and EC-2 fields were irrigated by drip system. During 2016-2017 season, both fields had the same irrigation scheduling programs according to the crop water needs estimated by the FAO method except that one field was voluntary stressed during controlled stress periods when irrigation was stopped. The total irrigation was 374 and 504 mm for the controlled (EC-1) and reference (EC-2) crop field, respectively. During 2017-2018 season, the irrigation was stopped earlier in the season (beginning of February for EC-1 and mid-March for EC-2) while in the previous season the irrigation was stopped mid-April. However, the total irrigation during the agricultural season was very close to that of the previous season, 327 and 528 mm for the EC-1 and EC-2 crop field, respectively. The difference lies in the application of water, because the farmer applied more than double water during the initial stage (December) in the 2017-2018 season. The mean irrigation amount during both seasons was 15 mm for both crop fields. The daily irrigation amounts over every site for the different seasons are depicted in the Fig. 2.2.

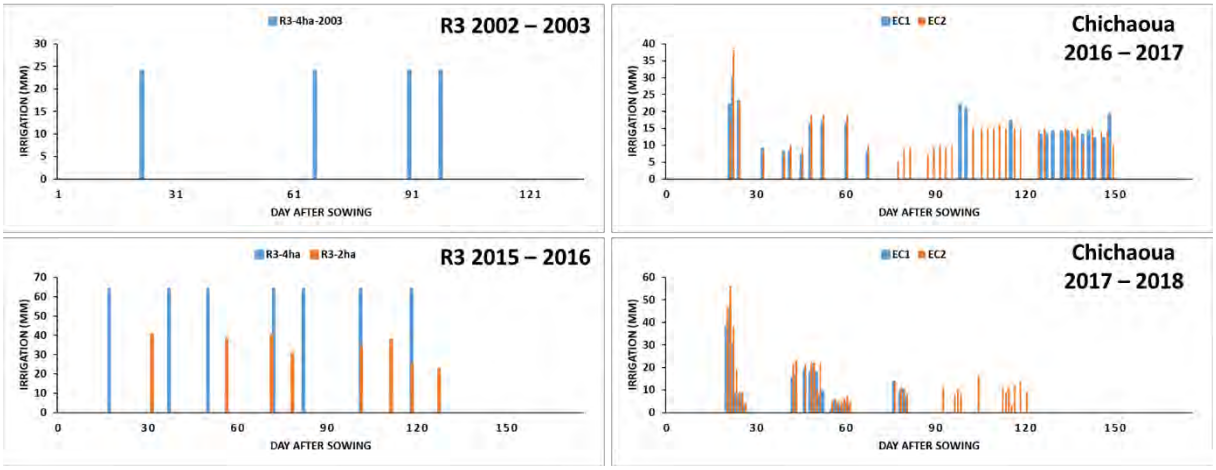


Fig. 2.2. Irrigation events along the agricultural growing for the winter wheat field in R3 and Chichaoua area for the different seasons.

In Sidi Rahal area, the crops are mainly irrigated tree and annual crops but there is also an important rainfed area devoted mainly to winter wheat crops. The experimental site Bour consists in a rainfed winter wheat field that although no irrigation are applied, it is used as benchmark to assess the retrieval irrigation method and the water budget components during the four agricultural seasons that was monitored (2014 – 2018).

2.2.5. Fractional green vegetation cover

Given that this thesis involves the development of a novel approach that integrates optical data into a crop water balance model, this work was first carried out at in situ level by using ground-based measurements in order to reduce uncertainties in the data with regard to satellite-derived data. For this purpose, over the 4ha-2003 site in R3 area, the vegetation was monitored from canopy reflectance in order to obtain a vegetation index and the fractional vegetation cover. Ground-based surface reflectance data over the field were collected using a MSR87 multispectral radiometer (Cropscan Inc., USA) every week. The radiometer was inter-calibrated with an ASD (Analytical Spectral Device) before the start of the agricultural season of 2002–2003. Fifteen sets of canopy reflectance measurements were made between January 8 and May 27 2003. Each measurement was taken with the MSR87 sensor 3 m high in a vertical position (an area of about 2 m^2 per sample) along three transects every 10 m. Reflectance values centered on red (0.63–0.69 µm) and near infrared (0.76–0.90 µm) bands are used to obtain NDVI (Normalized Difference Vegetation Index). The average of NDVI values was computed from all measurements of the whole field. More details about the NDVI measurement procedure can be found in Er-Raki et al. (2007).

The fractional green vegetation cover (fvg) is then estimated from a linear relationship from the NDVI according to Gutman and Ignatov (1998) as follows:

$$f_{vg} = \frac{NDVI - NDVI_s}{NDVI_v - NDVI_s} \qquad \text{Eq. 2.2}$$

where NDVI is the near-infrared to red reflectance difference divided by their sum. $NDVI_s$ and $NDVI_v$ correspond to NDVI for bare soil (fvg = 0) and fully covering green vegetation (fvg = 1), respectively. The $NDVI_s$ was equal to the minimum value measured in the field (0.14) and $NDVI_v$ was defined at 0.93 after looking at maximum values taken on individual plots over the study area (Duchemin et al., 2006).

In addition, the fractional total vegetation cover (fc) was also measured using a hemispherical digital camera equipped with a fisheye lens with a field-of-view of 183° (Nikon Coolpix 950®). fc could be also derived from fvg by assuming that once fvg has reached its maximum value, it keeps equal to this maximum value until the end of the agricultural season as is shown in the Fig. 2.3. A comparison of fvg- against photo-derived fc estimates before the maximum value of fvg revealed a good agreement with a root mean square error (RMSE) and coefficient of determination (R^2) equals to 3.5% and 1.0, respectively.

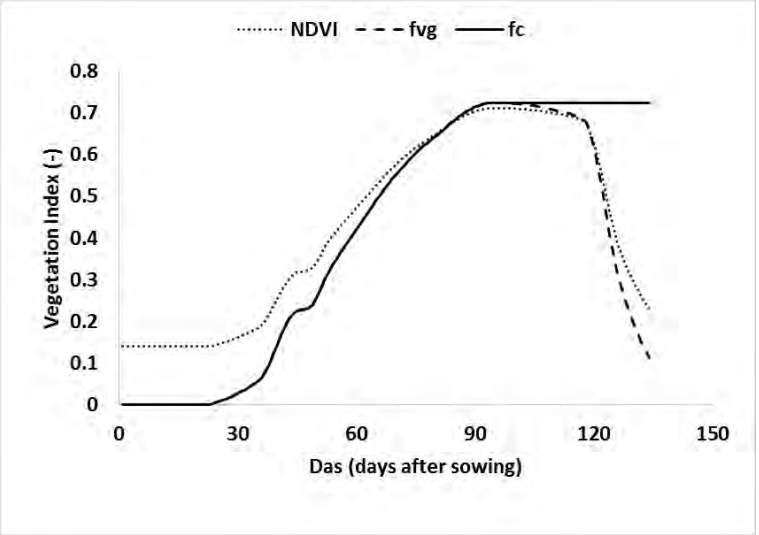


Fig. 2.3. Daily NDVI, fraction of green vegetation cover (fvg) and fraction of total vegetation cover (fc) along the agricultural growing for the winter wheat field in R3 area.

2.2.6. Temperature data

2.2.6.1. Land Surface Temperature

In every experimental site, ground-based LST is derived from thermal infrared radiances emitted from the surface ($L_{rad,\lambda}$) and long-wave down-welling radiance from the sky ($L_{down,\lambda}$). The thermal radiances from the surface were measured by a thermal radiometer (Apogee SI-series) installed vertically at 2 m height, while the down-welling radiance from the sky was measured by net radiometer (NR01 or CNR, depending on the site). The Apogee thermal radiometers are only sensitive from 8 to 14 µm matching the atmospheric window to minimize the influence of water vapor and CO2 on the measurement. Instead, the down-welling radiance from the sky is measured from about 5 to 50 µm so that it is converted to the same spectral range of the thermal radiometer (8 – 14 µm). For this purpose, the temperature corresponding to the down-welling radiance is estimated by using the Stefan–Boltzman constant and the atmospheric emissivity. This estimated temperature is then used to estimate the down-welling radiance at the effective wavelength of the thermal radiometer from the Planck's law. The measurements were sampled at 1 Hz and averaged over 30 min. The averaged radiance is converted to LST by inverting the Planck's law:

$$B(LST) = \frac{L_{rad,\lambda} - (1-\varepsilon_\lambda)L_{down,\lambda}}{\varepsilon_\lambda} \qquad \text{Eq. 2.3}$$

where $L_{rad,\lambda}$ is the land leaving radiance (W m^{-2}), $L_{down,\lambda}$ is the long-wave downwelling irradiance (W m^{-2}) corresponding to the effective wavelength λ, ε_λ is the spectral land

surface emissivity at the effective wavelength λ, to which is centered the specific domain of the Apogee sensor (8 – 14 μm), and *B(LST)* is Planck's law for the *LST* (W $m^{-2}sr^{-1}\mu m^{-1}$). The ε_λ was retrieved from the simplified NDVI threshold method (José A Sobrino et al., 2008) that weights the soil and vegetation emissivity through the fractional green vegetation cover (fvg). The soil emissivity was measured by Olioso et al., (2007) over the study area and the vegetation emissivity was considered equal to 0.99 (Sobrino et al., 2008).

2.2.6.2. Vegetation temperature

In the 4ha-2003 field in R3 area, in addition to radiometric temperatures the vegetation temperature was measured with Type-J thermocouples (seven replications, one sensor per plant), which were set up in the apex vegetation near the location of the thermal radiometer. The sensors were changed every week to be set up at the vegetation apex and to measure the youngest leaves of the plant along the growing season. Thermocouple measurements will be used to evaluate the vegetation temperature estimates that will be achieved from the partition method of LST.

2.3. Chile: Copiapó Valley

Copiapó Valley is situated south of the Atacama Desert, Chile. The whole valley has an area of about 18,538 km^2 divided in longitudinal sectors from The Andes Highlands (sector 1) to the coast (sector 6) (*Fig. 2.4*). The study of this thesis is focused on the lower part of the valley in the aquifer Sectors 5 and 6. The study area has a surface of about 1,670 km^2, and is located in the flat lands around the Copiapo River of Sectors 5 and 6. It is an agricultural area mainly covered by olives, vineyards, pomegranates and natural vegetation (Fig. 1). The climate is arid with low mean annual precipitation of 38 mm and hot and dry summers (December-February) and cold and dry winters (June-August). In terms of water resources, the Copiapó Valley is characterized by acute water scarcity mainly attributed to the low annual precipitation and the systematic stress put onto the aquifer by water consumers, mainly agriculture and mining (Oyarzún and Oyarún, 2011; Suárez et al., 2014). This situation has brought about the Copiapó Valley's current critical situation, resulting from the extraction of groundwater in recent decades, which has risen to rates greater than the natural replenishing of the aquifer (demand equal to 8.2 m^3/s over a replenishing equal to 6.3 m^3/s) with a notorious decrease in the water table (Oyarzún and Oyarún, 2011). The pressure on water resources is thus increasing and generating a new regional scenario for water use efficiency.

An olive orchard and a vineyard field are monitored from LAB-network (here in-after LAB-net) (Mattar et al., 2016). The LAB-net station over olives orchards is located in a plot of land measuring about 17 hectares with a fraction vegetation cover of 25%

distributed uniformly. Whereas the LAB-net station over vineyards is located in an area of 28 hectares with a homogeneous fraction vegetation cover.

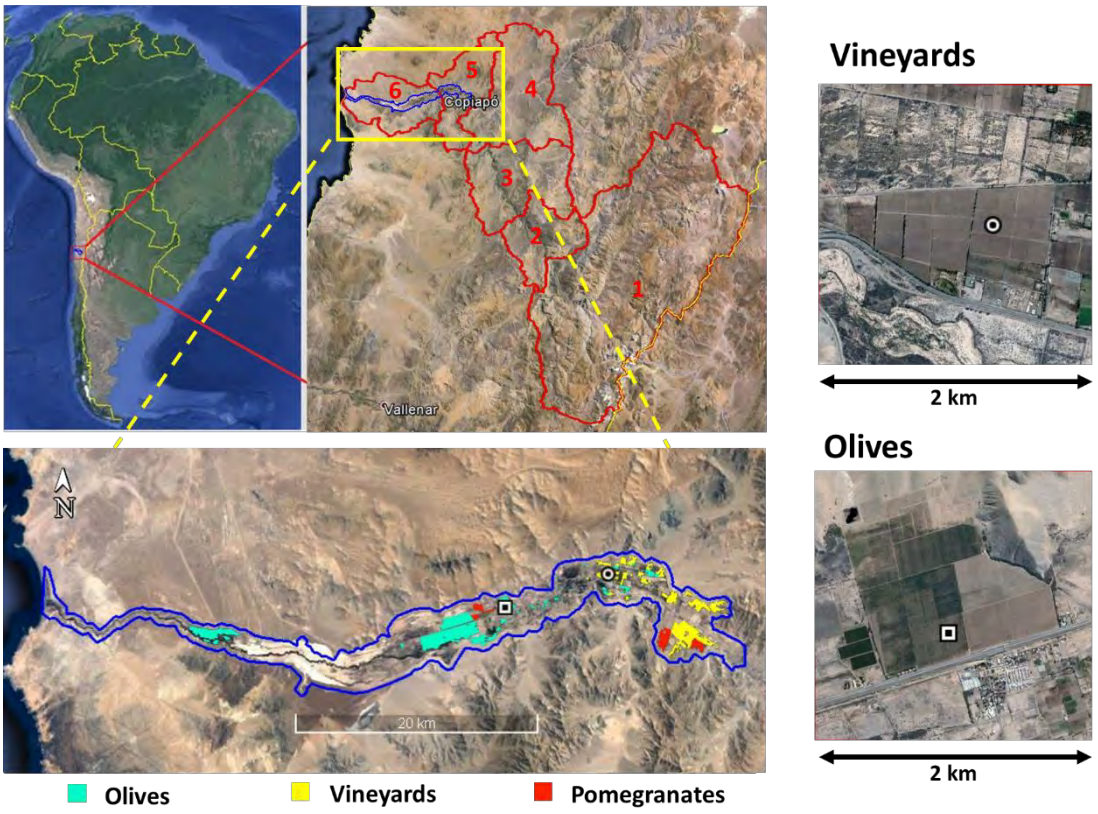


Fig. 2.4. Copiapó Valley divided in 6 sectors (red line) over which the study area (blue line) and the meteorological station over olive and vineyard crops (square and circle, respectively) are located in the sectors 5 and 6. In the figure the land cover of the main crops are showed: olives, vineyards and pomegranates.

2.3.1. Meteorological data

Automatic meteorological stations from the GEA ("*Grupo de Estudios del Agua*", www.agro- clima.cl) network, in addition to two meteorological and radiative flux stations from LAB-net data sets (Mattar et al., 2016), were used. In the Copiapó Valley, the GEA network includes twelve meteorological stations, four of which are located in the study area used in this thesis. These stations were located in vineyards and olives orchards, and they provide basic meteorological data. Meteorological data GEA network including air temperature, solar radiation, relative humidity, wind speed and rainfall were collected between January 2013 and December 2014. In addition to these meteorological data, LAB-net included infrared thermal, global and net radiation over an olive orchard and vineyards fields, which were processed between July 2014 and December 2016.

2.3.2. Ground-based land surface temperature

Over the vineyard and olive fields in Copiapó valley, the ground-based LST is derived according to the Eq. 2.3 from thermal radiances from the surface measured by a thermal radiometer (Apogee SI-111) installed 2 m height above the canopy. Here, the four components of net radiation were unavailable so that the down-welling radiance from the sky was estimated using the methodology proposed by Jiménez-Muñoz et al. (2010), by processing an atmospheric MOD07 product (i.e. temperature and moisture profiles, and atmospheric water vapor) from MODIS satellite into the MODTRAN radiative transfer code and convoluting the down-welling radiance spectra by using the Apogee SI-111 relative spectral response. The surface emissivity was acquired from the ASTER Global Emissivity Data Base (Hulley et al., 2015) and the emissivity was converted from narrow band to broad band by using the method proposed by Ogawa and Schmugge (2004).

2.4. Remote sensing data

This thesis focused mainly on the use of optical (shortwave and thermal) remote sensing data for monitoring the water resources over agricultural areas. Remote sensing data are collected over both sites from the following thermal missions: Landsat, ASTER and MODIS, which are described below.

2.4.1. Landsat data

Over the agricultural areas in Morocco, Landsat-7 and -8 data were collected between October 2014 and June 2018, while over Copiapó Valley only Landsat-8 data were used for the full time series available from April 2013 to December 2016.

2.4.1.1. Surface Reflectance data

Surface reflectance data were collected from the Landsat Collection Level-2 (https://earthexplorer.usgs.gov/). Landsat Level-2 data product provides surface spectral reflectance atmospherically corrected (i.d. as it would be measured at ground level in the absence of atmospheric scattering or absorption). Landsat-7 surface reflectance are atmospherically corrected by using the radiative transfer model 6S (*Second Simulation of a Satellite Signal in the Solar Spectrum,* Vermote et al. (1997)) while Landsat-8 uses the internal algorithm LaSRC (*Landsat Surface Reflectance Code*, Vermote et al. (2016)). Surface reflectances are generated at 30-meter spatial resolution. The red

and near-infrared bands were used only to estimate the NDVI and fractional green vegetation (fvg) cover over every study area: Haouz Plain and Copiapó Valley. NDVI and fvg are obtained in the same way from ground-based measurements in the Section 2.2.5.

2.4.1.2. Thermal data

Thermal data from Landsat-7 (band 6) and -8 (band 10) were collected from the Landsat Collection Level-1 to estimate LST. Landsat-8 provides 2 thermal bands but only one band was used since the USGS recommends the Single Channel method (based on one thermal band) avoiding the stray light effect observed in the split-window method (based on two thermal bands) (Montanaro et al., 2014). Thus, we only use the band 10 without option to select the split-window method from the two thermal bands. Therefore, the LST is estimated by using the Single-Channel (SC) algorithm described in Jiménez-muñoz et al. (2014, 2009) and based on the work proposed by Sobrino et al. (1996) and is represented as follows:

$$LST = \gamma \left[\frac{1}{\varepsilon} (\varphi_1 \cdot L_{sen} + \varphi_2) + \varphi_3 \right] + \delta \qquad \text{Eq. 2.4}$$

where ε is the spectral land surface emissivity at effective wavelength λ of Landsat-7/8 thermal band; γ and δ are two parameters which depend on the Plank's function and the at-sensor brightness temperature (for more details see Jiménez-Munoz et al. (2009)); φ_1, φ_2 and φ_3 are atmospheric functions described as:

$$\varphi_1 = \frac{1}{\tau} \qquad \varphi_2 = -L_{down} - \frac{L_{up}}{\tau} \qquad \varphi_3 = L_{down} \qquad \text{Eq. 2.5}$$

where τ is the atmospheric transmissivity, L_{down} and L_{up} are the down-welling and up-welling (path radiance) atmospheric radiance, respectively. All the parameters involved in Eq. 2.4 and Eq. 2.5 are wavelength (or band) dependent, but spectral notation will be omitted for simplicity. The atmospheric functions φ_1, φ_2 and φ_3 are estimated as approximation by using a second-order polynomial fit from the atmospheric water vapor content (W). The W was derived from the daily MODIS Precipitable Water product (MOD05). The coefficients of the polynomial fit were obtained by Jiménez-muñoz et al. (2014, 2009) from radiative transfer simulation using the TOVS Initial Guess Retrieval (TIGR, Scott and Chedin, 1981) and Global Atmospheric Profiles from Reanalysis Information (GAPRI, Mattar et al., 2015) databases for Landsat-7 and -8, respectively.

Similarly to ground-based LST estimates in Section 2.2.6.1, the ε is estimated using the simplified NDVI thresholds method (Sobrino et al., 2008), with the difference that the spectral vegetation emissivity ($\varepsilon_{v,\lambda}$) is set to 0.99 and the spectral soil emissivity ($\varepsilon_{s,\lambda}$) is spatially obtained from the ASTER Global Emissivity Datasets (ASTER GED, Hulley et al., 2015). ASTER GED provides an average spectral emissivity from ASTER scenes from 2000

to 2008 at 100 m spatial resolution in the wavelength range between 8 and 12 µm (bands 10 – 14). ASTER GED also provides the mean NDVI for the same period (2000-2008), which allows deriving the $\varepsilon_{s,\lambda}$ for every ASTER band according to the soil and vegetation fraction (Sobrino et al., 1990):

$$\varepsilon_{s,AST_i} = \frac{\varepsilon_{AST_i} - \varepsilon_{v,AST_i} fvg_{AST}}{1 - fvg_{AST}} \quad \text{Eq. 2.6}$$

where fvg_{AST} is estimated as in Eq. 2.2 from the mean NDVI calculated from visible ASTER data bands. ε_{s,AST_i} is the ASTER soil emissivity. ε_{v,AST_i} is the ASTER vegetation emissivity that is set equal to $\varepsilon_{v,\lambda}$ for every ASTER band. Given that the $\varepsilon_{s,\lambda}$ is needed for Landsat thermal bands, ε_{s,AST_i} are adjusted to the Landsat thermal bands using the broadband regression approach proposed by Ogawa and Schmugge (2004) as was used in Duan et al. (2018) and Malakar et al. (2018). As is shown in the *Fig. 2.5*, the band 13 and 14 of ASTER are used only since they are superposed with the Landsat thermal bands. The adjustment from ASTER to Landsat bands is made by a linear regression where the coefficients between the soil emissivity for Landsat and ASTER bands were derived by convoluting the soil emissivity spectra of all soil types available in the ASTER spectral library (Baldridge et al., 2009) for all thermal bands, which are 52 in total.

$$\varepsilon_{s,Landsat} = a\varepsilon_{s,AST_13} - b\varepsilon_{s,AST_{14}} + c \quad \text{Eq. 2.7}$$

where $\varepsilon_{s,Landsat}$, ε_{s,AST_13} and ε_{s,AST_14} are the soil emissivity by convolving the spectral response function of Landsat thermal band (band 6 for Landsat-7 or band 10 for Landsat-8), the ASTER band 13 and 14, respectively, with the emissivity spectra. The coefficients a, b and c are estimated for Landsat-7 and -8 separately. As is shown in Fig. 2.6, high accuracies are obtained with a R^2 of 0.98 and 0.99 for Landsat-7 and -8 thermal band, respectively, and a RMSE lower than 0.001 for both sensors (by using the ASTER spectral library dataset).

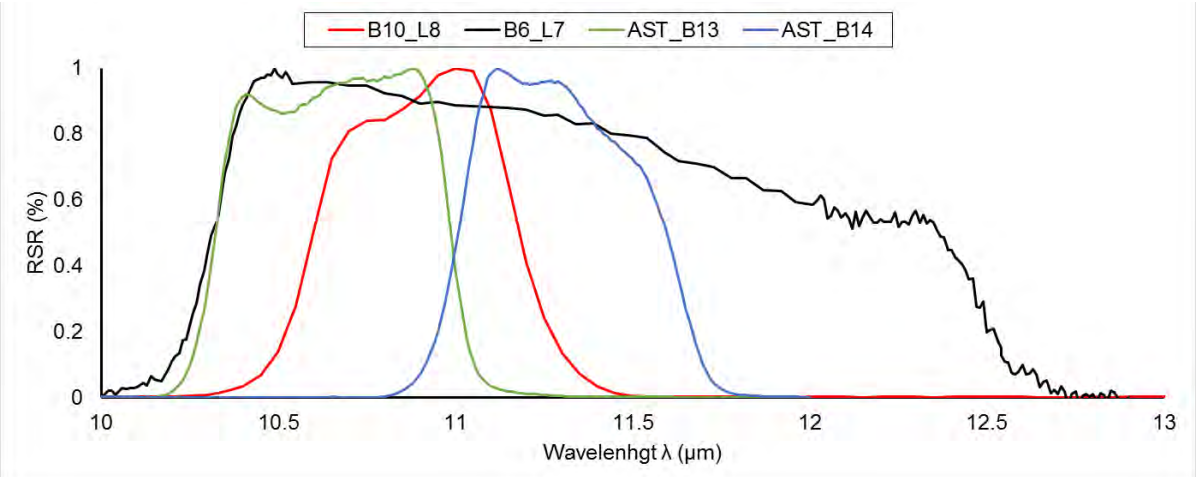


Fig. 2.5. Relative spectral responses (RSR) and effective wavelengths (λ) for Landsat-7 band 6 (B6_ L7), Landsat-8 band 10 (B10_L8) and ASTER bands 13 and 14 (AST_13 and AST_14) sensors.

Finally, the reliability of LST estimates was assessed in Amazirh et al. (2019, 2017) over the sites of the study area in Morocco, finding a relatively good agreement between satellite and ground-based LST with a RMSE lower than 2.4 K. In the study area in Copiapo Valley, the RMSE was higher (equal to 3.2 K) over olives and vineyards crops mainly due to a higher heterogeneity and the complexity of the surface.

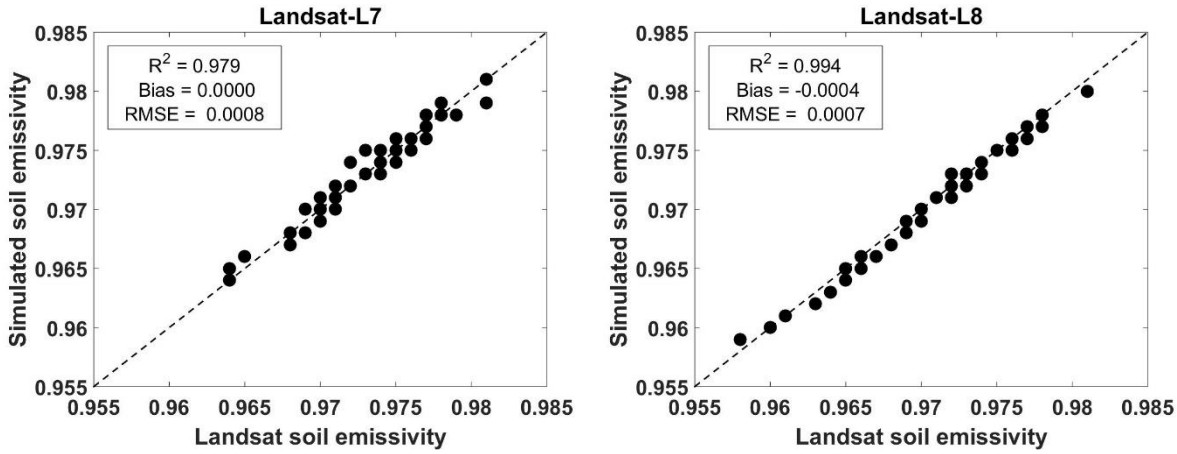


Fig. 2.6. Comparison between Landsat soil emissivity against the simulated Landsat soil emissivity from the linear regression by using ASTER bands 13 and 14 (Eq. 2.7) for the 52 soil types available in the ASTER spectral library (Baldridge et al., 2009). The dotted line represents the line 1:1.

2.4.2. ASTER Global Emissivity Datasets (ASTER GED)

Advanced Spaceborne Thermal Emission Reflection Radiometer (ASTER) is a multi-spectral imager on NASA's Terra platform with a 16–day revisit cycle. ASTER GED product provides the average spectral emissivity for its 5 thermal bands (10 to 14) as well as the mean NDVI calculated from the cloud-free ASTER scenes for the period between 2000 and 2008. The spectral emissivity and NDVI are provided at 100 m spatial resolution.

2.4.3. MODIS data

The Moderate Resolution Imaging Spectroradiometer (MODIS) is a sensor on board of NASA's Terra platform. MODIS data over the agricultural areas in Morocco and Copiapó Valley are collected for the same periods to which Landsat data are collected. Three different products are used in this thesis, which are described below.

2.4.3.1. Land Surface Temperature product (MOD11)

MODIS/Terra Land Surface Temperature and Emissivity (MOD11) is used to obtain the daily (at 10:30 am overpass time) LST at 1 km spatial resolution (MOD11A1) and the composite 8-day (MOD11A2). MOD11A2 is a simple average of all the corresponding MOD11A1 LST pixels collected within that 8-day period. The MOD11A1 LST data are retrieved by the generalized split-window algorithm from bands 31 and 32.

2.4.3.2. Vegetation Index product (MOD13)

MODIS/Terra Vegetation Index (MOD13) provides NDVI and Enhanced Vegetation Index (EVI) at 16-day intervals period and at multiple spatial resolutions. Here, it is used the NDVI at 250 m from the MOD13Q1 product. NDVI is derived from daily atmospherically-corrected surface reflectance in the red and near-infrared wavebands, which have been masked for water, clouds, heavy aerosols, and cloud shadows. The compositing product is chosen from the two highest NDVI values in the 16-days period and the pixels that are closest-to-nadir.

2.4.3.3. Atmospheric water vapor product (MOD05)

The MODIS Precipitable Water product (MOD05) consists of column water-vapor amounts retrieved from Level 2 at 1 km spatial resolution. MOD05 is obtained from a near-infrared algorithm that is applied over clear land areas of the globe and above clouds over both land and ocean. The retrieval algorithm relies on observations of water-vapor attenuation of reflected solar radiation in the near-infrared MODIS channels so that the product is produced only over areas where there is a reflective surface in the near-infrared.

2.5. Conclusion

This chapter presents the dataset by study area that have been used to implement the approaches proposed in this thesis. The agricultural areas in both a semi-arid Mediterranean region in central Morocco and an arid region in north of Chile have been used to evaluate the approaches for monitoring the water resources in these areas under water scarcity issues.

An experimental site fully equipped over a winter wheat field in Haouz Plain (Morocco) has been used as feasibility study to develop and assess an approach to estimate the water fluxes (irrigation, RZSM and ET) at in situ level (Chapter Chapter 3). Three areas of 12 by 12 km in Haouz Plain have been used to implement spatially the approach by using satellite data (Chapter Chapter 4). Here, five experimental sites over winter wheat fields

under different irrigation techniques has been used to validate the approach in terms of irrigation, RZSM and ET. The narrow Copiapo Valley (Chile) has been used to implement an operational disaggregation LST method, which has been validated over two experimental fields under vineyards and olive orchards (Chapter Chapter 5).

Chapter 3. Retrieving irrigation and water budget components: a feasibility study

Contents

3.1. Introduction *60*

3.2. FAO-56 dual crop coefficient method *61*

3.2.1. Basal crop coefficient (Kcb) *61*

3.2.2. Evaporation reduction coefficient (Ke) *62*

3.2.3. Water stress coefficient (Ks) *63*

3.3. Remote sensing data integrated into FAO-2Kc *64*

3.4. Estimating water budget components from ground-based optical/thermal data *65*

3.4.1. Implementation of a contextual method at in situ level *66*

3.4.2. Root-zone and soil surface water status from optical/thermal data: Ks and Kr estimation *70*

3.4.3. First-guess water budget components *70*

3.4.4. Re-analysis of water budget components *73*

3.5. Summary and conclusions *75*

3.6. ARTICLE: Estimating the water budget components of irrigated crops: Combining the FAO-56 dual crop coefficient with surface temperature and vegetation index data *76*

3.1. Introduction

The main objective of this thesis is to integrate multi-spectral remote sensing data into a land surface model in order to estimate the water budget components (ET, RZSM and irrigation) on a daily basis over extended areas at crop field scale (~100 m). In the last decades, different methods have been developed for monitoring the crop water requirements usually by means of ET estimates. Those models are based either on the water balance, on the surface energy balance or on the coupling between both of them (energy-water balance). Among the water balance models, FAO-56 model (Allen et al., 1998) has been extensively used to estimate the crop water needs at crop field scale. This model require few input data, among phenological, meteorological and irrigation data, providing quite acceptable ET estimates when is compared to more physically based -but often over-parameterized- models. FAO-56 model is thus chosen by its simplicity and operational basis, being attractive for farmers and agricultural applications. However, its operational application to extended areas still faces the need of in situ data for calibration on one side, and the unavailability of irrigation data at field scale on the other side. Among the energy balance models, remotely sensed optical/thermal data have been essential to develop several methods based on surface variables (vegetation index, surface albedo, LST) that allow estimating the surface energy fluxes over extended areas at different spatio-temporal scales. In particular, the so-called contextual approaches (based on the contextual information on remotely sensed optical/thermal data) have received considerable interest from the scientific community for its simplicity, operationality and robustness over large areas by using minimal or no in situ data.

In this chapter, a new retrieval approach of the main water budget components in arid/semi-arid irrigated agricultural areas (ET, RZSM and irrigation) is developed by integrating optical/thermal data into the FAO-56 model. The feasibility of this method is evaluated using ground-based measurements (optical/thermal) over a winter wheat field. For this purpose, the approach adapts the thermal-based contextual models implemented with remote sensing data to ground-based measurements in order i) to take advantage of the simplicity and robustness of these contextual methods and ii) to be applicable to large areas by using satellite data. This approach allow retrieving the irrigation volumes and dates from optical/thermal-derived ET and RZSM, and to re-analyze all water-budget components (including ET and RZSM) from the retrieved irrigation data. The approach would allow retrieving the irrigation that is the key variable to force the FAO-56 model over extended areas in order to estimate the water budget components at daily and parcel scale.

3.2. FAO-56 dual crop coefficient method

The FAO-2Kc is a water balance model driven by meteorological forcing variables including 1) air temperature, air humidity, wind speed and solar radiation to calculate reference evapotranspiration ET_0 and 2) precipitation and irrigation that jointly determine the water supply to simulate the soil water availability for soil evaporation and plant transpiration. In practice, FAO-2Kc estimates ET by multiplying ET_0 by a two separate crop coefficients for transpiration and evaporation as:

$$ET = (Ks \cdot Kcb + Ke)ET_0 \qquad \text{Eq. 3.1}$$

where Kcb is the basal crop transpiration, Ks the stress coefficient (0 – 1) that represents the vegetation water status and a reduction factor of transpiration (T = Kcb ET_0) and Ke the evaporation coefficient that allows estimating the evaporation (E = Ke ET_0). ET_0 is calculated according to the FAO Penman–Monteith equation (Allen et al., 1998) at daily scale, which is described in detail in the Appendix 1. The estimation of every coefficient is briefly described below.

3.2.1. Basal crop coefficient (Kcb)

The basal crop coefficient (Kcb, unitless) mainly depends on crop types and crop growth stages, and it is adjusted by the climatic conditions. According to Allen et al. (1998), four growth stage periods are identified in the full growing season: initial, crop development, mid-season and late season. The initial and mid-season stages are characterized by a constant Kcb value while the development and late season stages have increasing and dropping values proper to the rapid growing and senescent periods of the crops, respectively. Then, three Kcb values (Kcb_{ini}, Kcb_{mid} and Kcb_{end}) and the lengths of the four growth stages (l_{ini}, l_{dev}, l_{mid} and l_{end}) are needed to account with the Kcb curve, as it is shown in Fig. 3.1.

Allen et al. (1998) proposed Kcb values (denoted with the suffix *tab* in the Eq. 3.2) and lengths of the growing stages for different crop types, which correspond to the values for standard climatic conditions having an average daytime minimum relative humidity (RH_{min}) of about 45% and calm to moderate wind speeds of about 2 m s^{-1} at 2 m height (u_2). For different climatic conditions, Allen et al. (1998) proposes to adjust the Kcb_{mid} and Kcb_{end} as follows:

$$Kcb_{mid,end} = Kcb_{mid,end(tab)} + \left(0.04(u_2 - 2) - 0.004(RH_{min} - 45)\right)\left(\frac{h}{3}\right)^{0.3} \qquad \text{Eq. 3.2}$$

where $Kcb_{mid,end(tab)}$ is the value for Kcb_{mid} or proposed by Allen et al. (1998) and h is the mean maximum plant height (m) during the midseason period or full cover period, u_2 and

RH_{min} are the average values during the mid-season or late season growth stage. Despite the adjustment for climatic conditions, these values can differ significantly due to other factors such as: soil type, the particular crop and its varieties, irrigation method, soil water, nutrient content and plant phenology (Allen et al., 1998). Consequently, Kcb values and lengths of the growing stages need specific adjustments, including calibration against ground-based transpiration or ET estimates (e.g. Er-Raki et al., 2007; Poblete-Echeverría and Ortega-Farias, 2013; Rafi et al., 2019; Zhao et al., 2015).

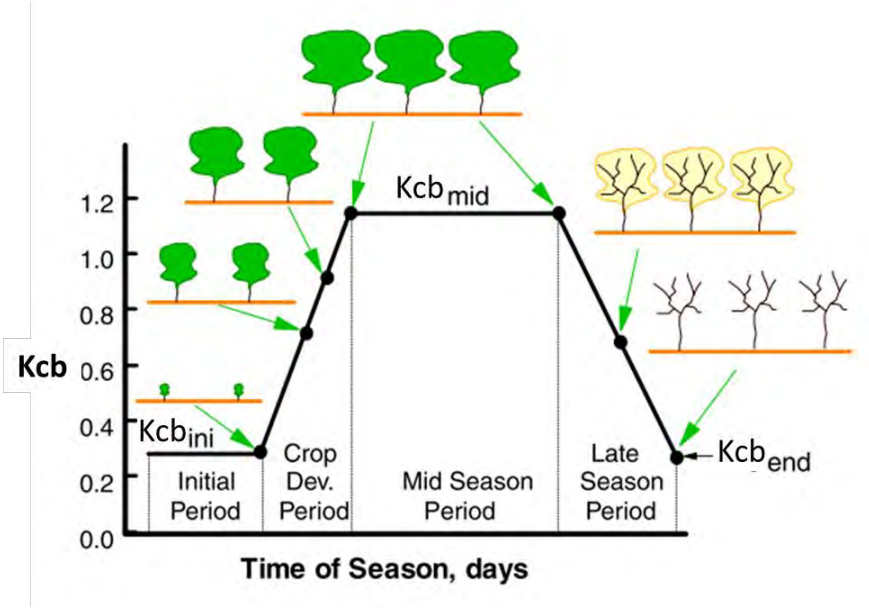


Fig. 3.1. Basal crop coefficient curve during for the four stages throughout the growing season (Allen and Pereira, 2009).

3.2.2. Evaporation reduction coefficient (Ke)

The evaporation coefficient (Ke, unitless) is calculated based on daily computation of the water balance for the surface soil evaporation layer with depth equal to Ze (in m). Ke depends on the evaporation reduction coefficient (Kr, unitless) as well as the exposed and wetted soil fraction (f_{ew}), which can be expressed as follows:

$$Ke = Kr(Kc_{max} - Kcb) \leq f_{ew} Kc_{max} \qquad \text{Eq. 3.3}$$

where Kc_{max} is the maximum value of Kc following rain or irrigation representing an upper limit on the E and T from any cropped surface, which is calculated as follows:

$$Kc_{max} = max\left\{1.2 + \left(0.04(u_2 - 2) - 0.004(RH_{min} - 45)\right)\left(\frac{h}{3}\right)^{0.3}, \; Kcb + 0.05\right\} \quad \text{Eq. 3.4}$$

where h (m) is the mean plant height during the growing stage of calculation (initial, development, mid-season, or late-season), and the max{ } indicates the selection of the maximum Kc_{max} value, ensuring that Kc_{max} is always greater or equal to Kcb+0.05. Kc_{max} can range from about 1.0 to 1.3.

Kr represents the water status of the top surface evaporable layer (Ze) that is estimated as follows.

$$K_r = \frac{TEW - D_{e,i-1}}{TEW - REW} \quad \text{Eq. 3.5}$$

where TEW (mm) is the total evaporable water, REW (mm) is the readily evaporable water and $D_{e,i-1}$ (mm) is the cumulative water depletion from Ze of the previous day. Kr (0 –1) is maintained constant when $D_{e,i-1}$ is smaller than REW, otherwise it is lower than 1. TEW depends on the soil parameters such as the soil moisture at field capacity (SM_{FC}) and at the wilting point (SM_{WP}) and the depth of Ze, which is set constant equal about 0.10 – 0.15 m.

$$TEW = 1000\left(SM_{FC} - 0.5SM_{wp}\right)Z_e \quad \text{Eq. 3.6}$$

Another parameter referred to as the fraction of exposed and wetted soil fraction (few) is needed for the calculation of Ke. Since the soil is fully wetted following flood irrigation or rainfall, the parameter few depends only on fraction of vegetation cover (fc), which is estimated from Kcb according to Allen et al. (1998). SM_{WP} and SM_{FC} the soil moisture at permanent wilting point (below which water is not accessible to plants) and the soil moisture at field capacity (above which water cannot be held against gravitational drainage), respectively. Allen et al. (1998) propose values of the soil parameters (SM_{WP}, SM_{FC} and REW) for different soil texture classes.

3.2.3. Water stress coefficient *(Ks)*

Similarly to the Kr estimation, the water stress coefficient (Ks, unitless) is calculated based on daily computation of the water balance for the root-zone layer Zr (m) as follows:

$$K_s = \frac{TAW - D_r}{TAW - RAW} = \frac{TAW - D_r}{TAW(1 - p)} \quad \text{Eq. 3.7}$$

where Dr (mm) is root zone depletion, TAW (mm) is total available soil water in the root zone, and p is the fraction of TAW that a crop can extract from the root zone without suffering from water stress. TAW is estimated as the difference between the water content at field capacity and wilting point:

$$TAW = 1000(SM_{FC} - SM_{wp})Z_r \quad \text{Eq. 3.8}$$

The rooting depth Zr is assumed to vary between a minimum value (maintained during the initial crop growth stage and equal to Ze) and a maximum value (reached at the beginning of the mid-season stage).

Water stress occurs when Dr becomes greater than RAW (Ks < 1). In contrast, when Dr is lower than RAW, Ks is equal to 1. Dr is calculated from the daily water balance as follows:

$$Dr_i = Dr_{i-1} + ET_i - P_i - I_i + DP_i - CR_i + RO_i \quad \text{Eq. 3.9}$$

where P is the precipitation, DP the deep percolation, CR the capillarity rise, RO the surface runoff and I the irrigation. Every term is expressed in mm for the day *i* (and *i–1* for Dr). In agricultural areas with flat surfaces and water table significant deep (several meters of depth) CR and RO can be assumed negligible.

In Eq. 3.7, p values for several crop types are recommended by Allen et al. (1998) for ET rates without stress (Ks=1) of 5 mm day^{-1}. These values should be adjusted when ET differs from this rate and should be limited between 0.1 and 0.8 according to the crop and climatic demand. For winter wheat, a p value of 0.55 is recommended. In this work, p was considered constant for simplicity given that the difference between using a p fraction constant and adjusted by ET rates was negligible. The comparison between ground-based ET (from eddy covariance) against ET estimates from standard FAO-2Kc by using a p fraction constant and by using a p fraction adjusted by potential ET obtained almost the same RMSE and R^2 (not shown here), with a variation lower than 1%.

3.3. Remote sensing data integrated into FAO-2Kc

One of the main issues of the FAO-2Kc is the need of parameters and coefficients that are taken from the proposed values by Allen et al. (1998) and should be usually calibrated against in situ ground-based transpiration or ET estimates. To overcome this issue, several studies have estimated these coefficients from remote sensing data. One of the first studies that related the crop development, transpiration and canopy reflectances was developed in the beginning of 1980s (Jackson et al., 1981). Then, several studies have used remote sensing data along with FAO-56 in order to estimate crop coefficients from remotely sensed spectral reflectance or derived vegetation indices (e.g. Bausch, 1995;

Calera et al., 2017; Choudhury et al., 1994; Duchemin et al., 2006; Er-Raki et al., 2007). The coupling between FAO-2Kc and vegetation indices (VI) have shown a significant improvement against the standard FAO-2Kc. Despite the demonstrated improvements of the Kcb-based vegetation index in the performance of FAO-2Kc, some of these works have been used to estimate crop ET under standard conditions such as without undergoing water stress. In order to address this issue, the LST derived from thermal infrared data has been used for taking into account the water stress given the strong link between the land surface/canopy temperature and water status (Jackson et al., 1981; Moran et al., 1994). Thus, Er-Raki et al. (2008) assimilated remote sensed LST-derived ET estimates into the FAO-56 single crop coefficient approach to improve the ET estimates from the FAO-56 model. They used temporally-sparse available thermal data together with a surface energy balance to estimate the ET, which was assimilated into the FAO model to estimate daily ET estimates over an olive orchard in a semi-arid region. The LST-derived ET allowed detecting water stress periods that the FAO model alone was not able to identify. In recent works, water stress indices as Ks used in FAO-2Kc was retrieved from LST data (Dejonge et al., 2015; Ihuoma and Madramootoo, 2017; Kullberg et al., 2016).

In such a way, it has been widely demonstrated the potential and utility of the use of optical/thermal data in the estimation of coefficients of FAO-2Kc, especially for estimating the Kcb and Ks. However, its operational application to large scales (e.g. irrigation perimeter) still faces two critical issues: the unavailability (over most irrigated areas) of real- or near-real time irrigation data at the field scale, and 2) the difficulty in modeling RZSM from meteorological data alone. These issues are essential to apply the FAO-2Kc over irrigated areas where the irrigation is the main input of water. Therefore, the water supply allows forcing the model and determining the root-zone depletion or RZSM that controls ET. Consequently, knowledge and quantification of irrigation data spatially distributed over extended areas is still outstanding in order to estimate the water budget components that allow monitoring the water managements over agricultural areas.

3.4. Estimating water budget components from ground-based optical/thermal data

The FAO-2Kc is a water balance model forced by the water supply (i.d. precipitation and irrigation) that allows simulating the soil water availability for soil evaporation and plant transpiration. The water balance is expressed by means of the water depletion from the soil surface layer (De) and the root zone (Dr) and both allow adjusting the evaporation and transpiration rate, respectively, through the Kr and Ks coefficients. Despite the irrigation at field scale being a critical input for monitoring the crop water management

in irrigated agricultural areas, it is one of the water balance components least investigated in terms of estimation spatially distributed.

In order to address this critical issue, we propose an approach to retrieve/invert the irrigation from optical/thermal-derived estimates and then re-analyze the water budget components (ET and RZSM) from the FAO-2Kc forced by the retrieved irrigation. For this purpose, the approach seeks to take advantage of: i) the simplicity and robustness of the thermal-based contextual ET models, ii) the utility of LST/VI data for water budget components (evaporation/transpiration, RZSM) and iii) the availability of LST/VI data at a spatial resolution suitable for monitoring crops (~100 m).

The method is developed and assessed by using ground-based optical/thermal data, specifically LST and NDVI. Thus, we avoid uncertainties coming from atmospheric corrections and other error sources related to instrument and satellite observations.

The basic idea behind the approach is to retrieve irrigation from a water balance model and a fist-guess RZSM estimated from optical/thermal-derived indices as proxy of the water status. LST can be related to the RZSM by means of the canopy temperature and its associated transpiration (Boulet et al., 2007; Hain et al., 2009; Moran et al., 1994) given the coupling between the surface energy and water balance (e.g. Wetzel et al., 1984). Hence, one key step to estimate thermal-derived RZSM is the partitioning of LST into soil and canopy temperatures (Merlin et al., 2014, 2012b; Moran et al., 1994). Here, we adopt a thermal-based contextual model to partition the LST given its simplicity and robustness for a further application over extended areas. In the next section the partitioning method is described as well as how it is implemented.

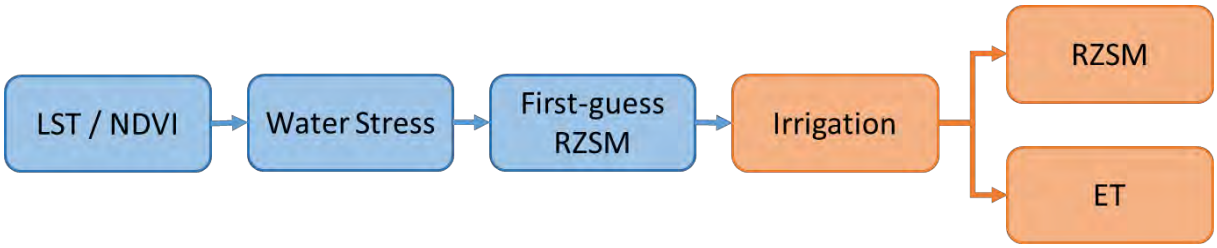


Fig. 3.2. Flowchart of the estimation of the main crop water budget components (irrigation, RZSM and ET) from the main intermediate variables.

3.4.1. Implementation of a contextual method at in situ level

The use of contextual information contained in remotely sensed images is a key advantage of the image-based approach, allowing avoiding some parameterization, in situ data and high accurate satellite observations required as input for other models. The

methods are usually based on a polygon defined in the LST-VI feature space, which is able to detect the full range of surface conditions (in terms of water status and vegetation cover) within the study domain. The dry to well-wetted and bare soil to full-cover vegetation conditions are detected by means of four temperature endmembers: the maximum temperature of a fully dry bare soil (Ts_{max}), the minimum temperature of a fully wet bare soil (Ts_{min}), the maximum vegetation temperature of a fully stressed vegetation (Tv_{max}) and the minimum vegetation temperature of a well-watered unstressed vegetation (Tv_{min}). Given that this feasibility study is implemented by using in situ measurements the full range of surface conditions cannot be observed at a given time, the temperature endmembers in the LST-VI space are simulated from a surface energy balance as in some studies (e.g. Malbéteau et al., 2017; Moran et al., 1994; Stefan et al., 2015). In this study, Ts_{min} and Ts_{max} are simulated by a soil energy balance model as described in detail in Appendix 2. Tv_{min} and Tv_{max} are estimated from the air temperature and the soil temperature endmembers (Ts_{max} and Ts_{min}) since the estimation of canopy resistance can be complex due to the need of some parameters (as vegetation height) difficult to obtain from remote sensing. Thus, Tv_{min} is set to the air temperature and Tv_{max} is defined by assuming that the difference between Ts_{max} and Ts_{min} is the same that between Tv_{max} and Tv_{min}, as in Stefan et al. (2015). In this last work, these assumptions resulted in a RMSE equal to 65 Wm^{-2} between in situ ET and ET estimates from the surface energy balance SEB-1S (Merlin, 2013). Once the polygon is defined in the LST-VI space, the LST is linearly decomposed into its soil and vegetation components to be consistent with the contextual approach and as a good approximation of the relationship with fourth power for temperatures (Anderson et al., 1997; Merlin and Chehbouni, 2004) as follows:

$$LST = fcTv + Ts(1 - fc) \qquad \text{Eq. 3.10}$$

Where fc is the fraction of total vegetation cover, Tv and Ts are the vegetation and soil temperature, respectively. Tv and Ts are obtained from the polygon constrained by the temperatures endmembers defined in the LST – fc space, by using a combination between the 'hourglass' approach (Moran et al., 1994) and the procedure to obtain the Temperature Vegetation Dryness Index (TVDI, Sandholt et al., 2002). Although in previous works the NDVI, the soil-adjusted vegetation index (SAVI) and fraction of green vegetation (fvg) have been commonly used in the LST-VI space, in this study we propose to use the fc. The fc is estimated from fvg as is described in Section 2.2.5. fc is preferred instead of fvg because during the late stage when vegetation is senescent, in the polygon the surface represented by the pair (VI,LST) is confused with bare soil, affecting the partition of LST.

The partitioning procedure is mainly focused on the 'hourglass' approach, in which Tv and Ts are estimated as the most probable vegetation and soil temperatures. Most probable (vegetation and soil) temperatures are defined as the average between the minimum and maximum possible (vegetation and soil) temperatures associated to the temperature endmembers and the linear decomposition of the Eq. 3.10 (Merlin et al., 2012b; Moran et al., 1994). Here, in the polygon we can identify four areas distinguished

in the LST – fc space, which are constrained by the diagonals of the polygon (Fig. 3.3). In zone A, LST is mainly controlled by soil evaporation being more sensitive to SSM. In zone D, LST is mainly controlled by vegetation transpiration being more sensitive to RZSM. In zones B and C, LST is controlled by both soil evaporation and vegetation transpiration with intermediate sensitivity to SSM and RZSM. Based on this understanding, Tv and Ts are estimated according to each zone, which are illustrated in the Fig. 3.3 for clarity. In zone A, this procedure makes Ts constant and equal to the average between Ts_{max} and Ts_{min}, whereas in zone D, Tv is constant and equal to the average between Tv_{max} and Tv_{min}. Therefore, this approach would not allow detecting the temporal dynamics of the water status during the periods when the (*fc, LST*) pair belongs to the zone A or D. To overcome this issue, Tv and Ts are estimated according to the TVDI method in the zone A and D, respectively, as shown in Fig. 3.3. The TVDI method allows obtaining linearly the evaporative fraction (EF) as has been estimated in several contextual method from isopleths that can be drawn in the polygon (Jiang and Islam, 2003; Long and Singh, 2012; Merlin et al., 2014; Sandholt et al., 2002). Then, the TVDI allows obtaining Ts and Tv directly from the isopleths of trapezoid approach as illustrated in the right plots of Fig. 3.3. The isopleths are estimated as the ratio of the distance separating the point (*fc, LST*) from the dry edge to the distance separating the dry and wet edges.

The partitioning method is applied every day along the agricultural season by using the ground-based LST averaged between 10 am and 2 pm, which are consistent with the overpass times of current thermal satellite missions. Therefore, the temperatures endmembers are also simulated every day from the soil surface energy balance and the meteorological data for the same period.

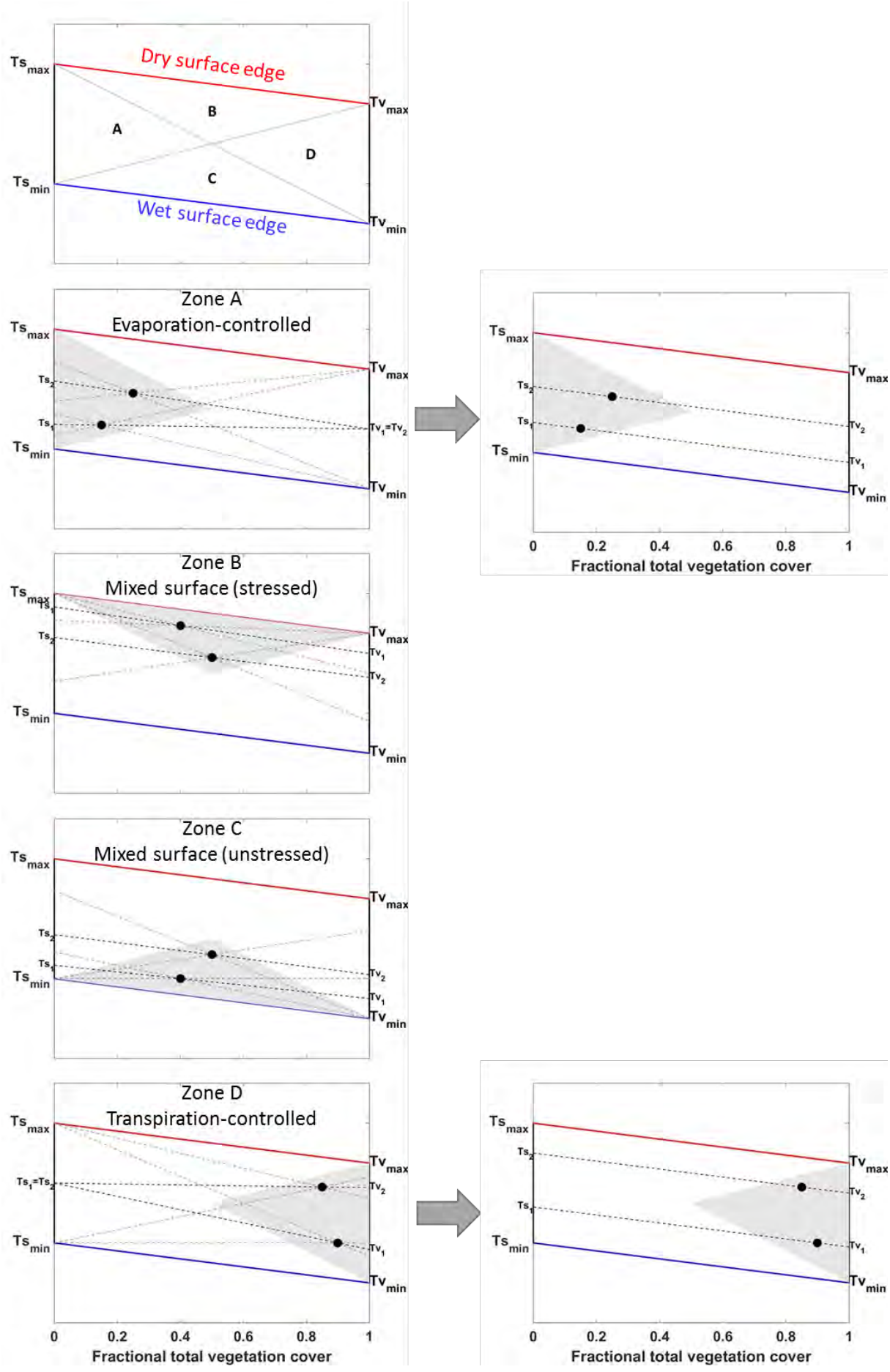

Dry surface edge
Wet surface edge
A
B
C
D
Zone A
Evaporation-controlled
Zone B
Mixed surface (stressed)
Zone C
Mixed surface (unstressed)
Zone D
Transpiration-controlled
Fractional total vegetation cover
Fractional total vegetation cover

Fig. 3.3. Polygon defined in the LST-fc space where four distinct zones A, B, C, and D are constrained. Tv and Ts are estimated from the hourglass approach (left plots) as in Merlin et al., (2012) except in zones A and D, where Tv and Ts are estimated respectively from TVDI method to avoid constant values (right plots). In the hourglass approach, the interception of the grey dotted lines in the bare soil (fc=0) and in the full-cover vegetation (fc=1) edges represent the maximum and minimum soil and vegetation temperatures, which are averaged to estimate the most probable Ts and Tv, respectively.

3.4.2. Root-zone and soil surface water status from optical/thermal data: Ks and Kr estimation

The partitioning method described above is a key procedure to differentiate the relation between the LST and the soil and crop water status by means of the SSM and RZSM and the associated Ts-evaporation and the Tv-transpiration relationships. Like EF has been estimated from contextual method as a ratio of ET to available energy or to potential ET, a ratio can be estimated for the evaporation and transpiration separately from Ts and Tv, respectively. The ratio for the evaporation and transpiration reflects the surface and root-zone layer, respectively, namely the Kr and Ks used in the FAO-2Kc model. As the EF is estimated as the ratio of the maximum to actual LST difference to the maximum to minimum LST difference, Ks and Kr are estimated from the vegetation and soil temperatures, respectively, as follows:

$$Kr_{LST} = \frac{Ts_{max} - Ts}{Ts_{max} - Ts_{min}} \quad \text{Eq. 3.11}$$

$$Ks_{LST} = \frac{Tv_{max} - Tv}{Tv_{max} - Tv_{min}} \quad \text{Eq. 3.12}$$

where Ts and Tv correspond to the temperature of the soil and vegetation component derived from the partitioning method presented above, and the rest of terms are the temperature endmembers simulated from the soil energy balance and meteorological data.

3.4.3. First-guess water budget components

3.4.3.1. Evapotranspiration and its partition

In FAO-2Kc model, the water balance is represented by the estimation of the daily depletion De and Dr for the top soil surface and root-zone layer, respectively. Given that daily values of Kr and Ks are estimated from optical/thermal data, the computation of the soil water balance from FAO-2Kc model is avoided. Thus, the evaporation and transpiration coefficients can be adjusted by thermal-derived coefficients without the need for the water supply from precipitation and irrigation data and the use of parameters such as SM_{FC}, SM_{WP}, Ze and Zr. Then, a thermal-derived ET (ET_{LST}) is calculated from the FAO-2Kc formulation (Eq. 3.1) by using the standard values of Kcb proposed by Allen et al. (1998) and the Kr_{LST} and Ks_{LST} estimated from Eq. 3.11 and Eq. 3.12, respectively. It should be noted that the Kcb was previously evaluated and calibrated with in situ data over this experimental site in Er-Raki et al. (2007). However, this study is only focused on the feasibility and potential of thermal-derived coefficients for computing the water budget components, regardless of water supply to force the water balance modeling. Therefore, the thermal-based FAO-2Kc was evaluated by using the default Kcb values proposed by Allen et al. (1998). Er-Raki et al. (2007) calculated the Kcb from three methods: i) following the Kcb values proposed by the standard FAO-2Kc procedure (No-Calibration FAO-2Kc), ii) calibrating the Kcb from field measurements (Local-Calibration FAO-2Kc), and iii) calibrating the Kcb from ground-based NDVI (NDVI-Calibration FAO-2Kc). They demonstrated on one side the need of local calibration to accurately estimate the ET by means of standard FAO-2Kc, and on the other side, the utility and potential of ground-based vegetation indices to calibrate the Kcb and improve the ET estimates. For instance, they found an important difference (of 18%) between the locally calibrated and non-calibrated Kcb and hence in ET estimates, indicating that the wheat field was not growing in optimal conditions. Therefore, the proposed approach in this study (thermal-based FAO-2Kc) is compared against the standard FAO-2Kc and also with the method calibrated by Er-Raki et al. (2007) in order to assess the performance of the proposed method.

In the Fig. 3.4, the comparison between the temporal series of ET and its partition into evaporation and transpiration from the different FAO-2Kc methods is depicted along the agricultural season. Both locally calibrated methods (NDVI- and Local-Calibration methods) and the thermal-based FAO-2Kc show ET estimates more accurate than that of the standard FAO-2Kc. Although the locally calibrated methods obtain the best agreements and most accurate estimations (in terms of R^2 and RMSE), the proposed thermal-based FAO-2Kc obtains a performance very similar (R^2 equal to 0.75 and RMSE equal to 0.65 mm d^{-1}), with a bias and slope even lower and closer to 1, respectively. Nonetheless, the use of EC measurements for calibration (as was used in the Local-calibration method) is a strong limitation for application of the FAO-2Kc method to large areas. It should be noted that in the late season, the ET from standard, NDVI-calibration and Local-calibration methods obtain an underestimation with respect to the in situ ET and that from the thermal-based method. It might be explained by the fact that the three

first methods does not take into account the capillarity rise in the water balance model while the thermal-based method estimate the stress coefficient by the canopy temperature without regarding the water balance. The effect is more significant in late season when plants undergo water stress because capillarity rises are more important under stress conditions. Therefore, specific conditions (e.g. water stress, crop phenology) can be detected by the proposed approach avoiding both the use of parameters (e.g. SM_{FC}, SM_{WP}, Ze, Zr) and the local calibration of Kcb that requires field-specific measurements.

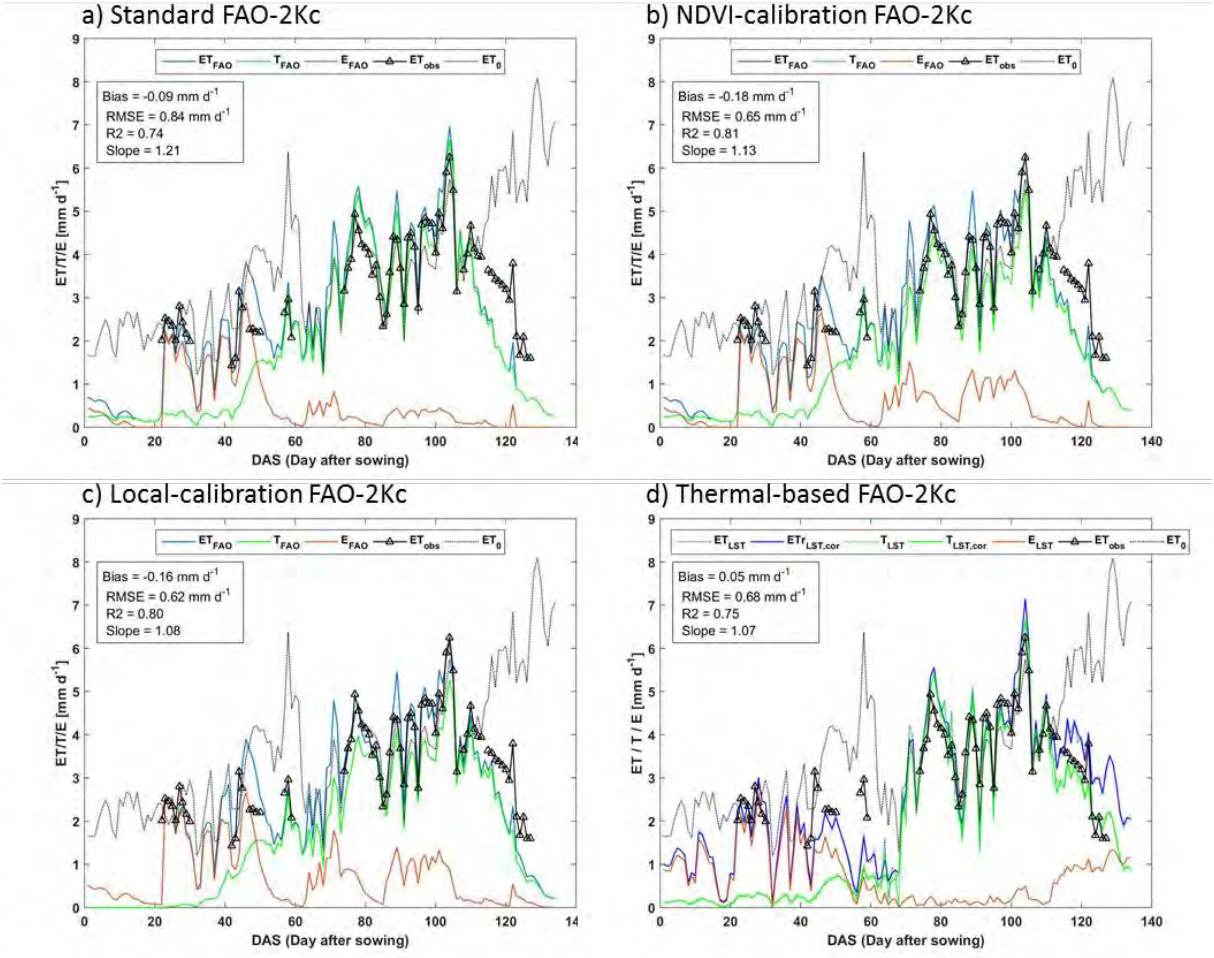


Fig. 3.4. Comparison of evapotranspiration (ET), transpiration (T) and evaporation (E) temporal series over the R3-4ha site (winter wheat field) for the 2002-2003 season estimated from the a) standard, b) NDVI-calibration, c) Local-calibration and d) thermal-based FAO-2Kc. The ground-based ET (ET_{obs}) and ET_0 are depicted for reference. The validation of ET from every method against ET_{obs} is shown by means of bias, RMSE, R^2 and slope of the linear regression.

3.4.3.2. Root-zone soil moisture

The root-zone depletion (D_r) together with some soil parameters used to estimate the total available water (TAW) can be translated to RZSM as follows:

$$RZSM = SM_{WP} + \left(1 - \frac{D_r}{TAW}\right)(SM_{FC} - SM_{WP}) \quad \text{Eq. 3.13}$$

Since the Ks reflects the root-zone water status and is estimated from Dr and TAW (according to Eq. 3.7), the Eq. 3.7 can be inserted into the Eq. 3.13 in order to express the RZSM as a function of Ks during stressed periods (Ks<1, Dr<RAW), as follows:

$$RZSM = SM_{WP} + Ks_{LST}(1 - p)(SM_{FC} - SM_{WP}) \quad \text{Eq. 3.14}$$

Note that the equation above is only valid for stressed periods given that if a Ks equal to 1 for unstressed periods is used, RZSM would be equal to the critical RZSM from which the stressed conditions end ($SM_{Threshold}$). According to the values of SM_{WP}, SM_{FC} and p used in this study (0.17, 0.37 and 0.55, respectively), the $SM_{Threshold}$ is equal to 0.26. Therefore, the thermal-derived Ks is not able to estimate the RZSM for the range from $SM_{Threshold}$ to SM_{FC}. During unstressed periods, RZSM from Eq. 3.14 is thus corrected dynamically for both cumulated precipitation and cumulated ET_{LST} during this period through a daily water balance. If the RZSM reaches a maximum value set to SM_{FC} then the RZSM is reset to the $SM_{Threshold}$ to carry on the correction in the remaining unstressed period.

The first-guess RZSM for the winter wheat field during the growing season 2002-2003 is shown in the Fig. 3.5. Four periods with steady increase in RZSM are detected, showing significant water supplies.

3.4.4. Re-analysis of water budget components

3.4.4.1. Irrigation retrieval

Once the daily first-guess (thermal-derived) RZSM is estimated throughout the complete growing season (as is shown in the Fig. 3.5), the water inputs can be detected from the RZSM dynamics. When significant increases in first-guess RZSM cannot be attributed to precipitation, they are attributed to water supply by means of irrigations. In such a way, irrigation is detected based on significant increase, which is considered with a RZSM change larger than a threshold value set to 0.02 m^3m^{-3}, representing a water supply greater than 10 mm for a 0.5 m root-zone depth. The amount of retrieved/inverted irrigation (I_{inv}) is constrained through the computation of a water budget for the periods with steady increase in RZSM. The water budget is computed from the amounts of precipitation as inflow and the LST-derived ET as outflow, as well as the drainage if it is

produced by precipitation. Note that the irrigation excess that triggers deep percolation is not possible to be detected by this approach. Therefore, the retrieved irrigation is an effective irrigation: irrigation minus drainage. If an irrigation of a minimum threshold of 10 mm is detected for the period with steady increase in RZSM, the estimated date of irrigation is set as the last date of this period, in order to make the maximum thermal-based RZSM consistent with the maximum RZSM simulated from FAO-2Kc.

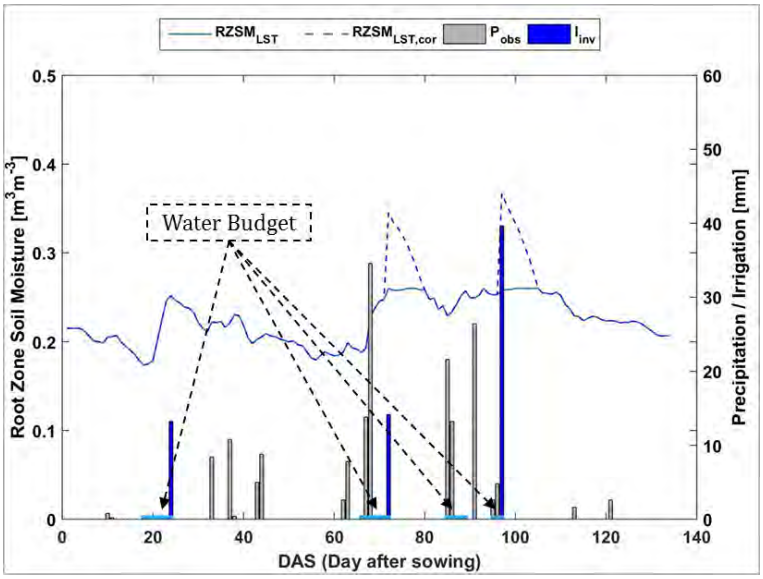


Fig. 3.5. First-guess (thermal-derived) RZSM ($RZSM_{LST}$) over the winter wheat field R3-4ha for the season 2002-2003. $RZSM_{LST}$ during unstressed periods when Ks=1 is corrected through a water budget ($RZSM_{LST,cor}$). The periods of significant increase in $RZSM_{LST,cor}$ are marked in the x axis (cyan) where the water budget is computed in order to invert the irrigation. In this case, three irrigation events are detected of the four periods where a water balance was applied (blue bars). The grey bars show the precipitations.

In the Fig. 3.5, although four periods are detected with significant increase in RZSM, only three irrigation events were detected from the inversion of the water budget though. The period when no irrigation is detected is due to precipitations that significantly increased RZSM according to the computation of the water budget.

3.4.4.2. FAO-2Kc forced by retrieved irrigation

The irrigation retrieved from first-guess RZSM and thermal-derived ET is finally used as forcing to the FAO-2Kc, from which ET (partitioned into evaporation and transpiration) and RZSM can be estimated at daily and crop field scales. The standard FAO-2Kc is implemented by using the default (non-calibrated) parameters given by Allen et al. (1998), but with the difference that the retrieved irrigation (amounts and dates) is introduced as forcing. Thus, ET is estimated according to the Section 3.2 and specifically

from the Eq. 3.1, while RZSM is estimated directly from Eq. 3.13. Here, Dr is controlled by the retrieved irrigation through the water balance implemented in the Section 3.2 for its full range from Dr equal to 0 (RZSM = SM_{FC}) to Dr equal to TAW (RZSM = SM_{WP}).

The Fig. 3.6 shows the validation of RZSM from FAO-2Kc forced by the retrieved irrigation ($RZSM_{FAO+LST}$). The validation of the first-guess RZSM is also shown in order to notice the significant improvement obtained in $RZSM_{FAO+LST}$. Although the first-guess RZSM shows a poor accuracy with a RMSE of 0.061 m^3m^{-3} and a R^2 of 0.42, it is shown an acceptable representativeness of the temporal variability of RZSM that can be seen in the ability to detect the irrigation dates and amounts. Regarding to the first-guess RZSM, $RZSM_{FAO+LST}$ is significantly improved with a RMSE of 0.034 m^3m^{-3}, R^2 of 0.67 and the bias is completely removed. In addition, the results are very close to those when the actual irrigation is used as forcing in the FAO-2Kc (RMSE equal to 0.032 m^3m^{-3} and R^2 equal to 0.73).

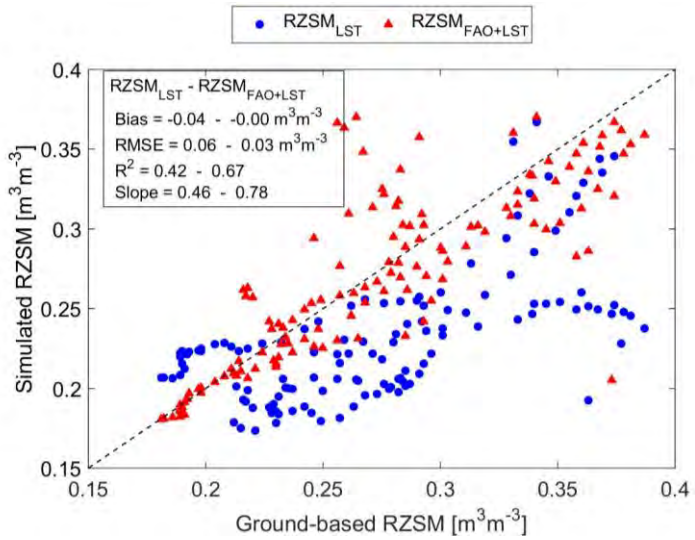


Fig. 3.6. LST-derived RZSM ($RZSM_{LST}$) and FAO-simulated RZSM by forcing the FAO-2Kc model using retrieved irrigation ($RZSM_{FAO+LST}$) versus ground-based RZSM.

3.5. Summary and conclusions

A new approach in the calculation of water budget components, including for the first time the estimation of irrigation amounts and timing, is developed by integrating LST data into the FAO-2Kc model. The approach involves: 1) the estimation of first-guess RZSM from thermal-derived Ks during stressed periods (Ks < 1) and its correction through a water budget during unstressed periods (Ks = 1); 2) the estimation of irrigation amounts and dates along the season from (first-guess) LST-derived RZSM and ET estimates; and 3) the use of retrieved irrigations to force FAO-2Kc to simulate RZSM and ET on a daily basis. The methodology is tested by using ground-based LST and NDVI over an irrigated winter wheat field in the semi-arid region Haouz plain in central Morocco during the 2002-2003 growing season. RZSM and ET are daily estimated along the growing season and they are compared against in situ measurements.

Statistical results indicate that thermal-derived ET (ET_{LST}) is more accurate than the ET from the standard version of FAO-2Kc. The RMSE and slope of the linear regression between estimated and observed ET is decreased from 0.84 to 0.68 mm day^{-1} and from 1.21 to 1.07, respectively. Regarding RZSM, results indicate that first-guess RZSM is significantly improved when FAO-2Kc is implemented by using retrieved irrigation. The R^2 and slope of the linear regression between simulated and observed RZSM is increased from 0.42 to 0.67 and from 0.46 to 0.78, respectively, while the RMSE is decreased from 0.06 to 0.03 m^3m^{-3} and the bias of -0.04 m^3m^{-3} is removed. Results thus show that the proposed approach combining FAO-2Kc and LST/VI data is able 1) to accurately estimate the crop ET using the default (non-calibrated) parameters given by Allen et al. (1998), 2) to estimate the irrigation amounts and dates and 3) to accurately simulate RZSM.

This new methodology demonstrates the feasibility of retrieving the irrigation and then the related water budget components from optical/thermal data. However, this study is implemented by using remote sensing ground-based LST and NDVI at in situ level. Therefore, the approach need to be implemented by using satellite data in order to demonstrate its real applicability. The use of satellite data raises new challenges that need to take into account the nature of these data, in terms of spatial resolution, estimation methods, and notably a weaker and more variable temporal frequency.

3.6. ARTICLE: *Estimating the water budget components of irrigated crops: Combining the FAO-56 dual crop coefficient with surface temperature and vegetation index data*

Agricultural Water Management 208 (2018) 120–131

Contents lists available at ScienceDirect

Agricultural Water Management

journal homepage: www.elsevier.com/locate/agwat

Estimating the water budget components of irrigated crops: Combining the FAO-56 dual crop coefficient with surface temperature and vegetation index data

Luis Olivera-Guerra[a,*], Olivier Merlin[a,c], Salah Er-Raki[b], Saïd Khabba[c], Maria Jose Escorihuela[d]

[a] Centre d'Etudes Spatiales de la Biosphère (CESBIO), Université de Toulouse, CNES, CNRS, IRD, UPS, Toulouse, France
[b] LP2M2E, Département de Physique Appliquée, Faculté des Sciences et Techniques, Université Cadi Ayyad, Marrakech, Morocco
[c] LMME, Faculté des Sciences Semlalia, Université Cadi Ayyad, Marrakech, Morocco
[d] isardSAT, Marie Curie 8-14, Parc Tecnològic Barcelona Activa, Barcelona, Catalunya, Spain

ARTICLE INFO

Keywords:
Evapotranspiration
Root-zone soil moisture
Irrigation
FAO-56
Surface temperature

ABSTRACT

The FAO-56 dual crop coefficient (FAO-2Kc) model has been extensively used at the field scale to estimate the crop water requirements by means of the simulated evapotranspiration (ET) and its two components evaporation (E) and transpiration (T). Given that the main limitation of FAO-2Kc for operational irrigation management over large areas is the unavailability (over most irrigated areas) of irrigation data, this study investigates the feasibility 1) to constrain the FAO-2Kc ET from LST and VI data, 2) to retrieve irrigation amounts and dates from LST and VI data and 3) to estimate the root-zone soil moisture (RZSM) at the daily scale. In practice, the vegetation and soil temperatures retrieved from LST/VI data are used to estimate the FAO-2Kc vegetation stress coefficient (Ks) and soil evaporation reduction coefficient (Kr), respectively. The modeling and remote sensing combined approach is tested over a wheat crop field in central Morocco, and results are evaluated in terms of ET, irrigation and RZSM estimates. ET is estimated with a RMSE of 0.68 mm day-1 compared to 0.84 mm day-1 for the standard (without using LST data) FAO-2Kc based on tabulated values for the parameters. The total irrigation depth (67 mm) is correctly estimated and is very close to the actual effective irrigation (69.8 mm) applied by the farmer. Daily RZSM is estimated with an R2 value of 0.68 (0.42) and a RMSE value of 0.034 (0.061) m3 m-3 by forcing FAO-2Kc using the retrieved irrigation (from LST-derived estimates and precipitation only). Since spaceborne LST data are currently not available at both high-spatial and high-temporal resolution, a sensitivity analysis is finally undertaken to assess the potential and applicability of the proposed methodology to temporally-sparse thermal data.

1. Introduction

Agriculture is an important pressure on water resources, especially in arid and semi-arid regions where irrigation can consume more than 80% of the available water (Chehbouni et al., 2008; Jarlan et al., 2015). Accurate estimation of evapotranspiration (ET), which critically depends upon the root-zone soil moisture (RZSM), is hence paramount to determine the crop water requirements and consequently to optimize the on-farm irrigation management.

The FAO-56 dual crop coefficient (FAO-2Kc, Allen et al., 1998) model has been extensively used at the field scale to estimate the crop water requirements by means of the simulated ET. In FAO-2Kc, the total ET is partitioned between the soil evaporation (E) and the plant transpiration (T) by using a daily water balance for the topsoil layer and the root-zone, respectively. This model is often chosen for its simplicity and operational basis as it requires few input data comprised of phenological, standard meteorological and irrigation data. In addition, FAO-2Kc provides quite acceptable ET estimates when compared to more physically based -but often over-parameterized models (Allen, 2000; Er-Raki et al., 2008; Kite and Droogers, 2000). To better constrain the phenological stages in the FAO model, the basal crop coefficient (Kcb) has been related to satellite based vegetation index (VI) (Er-Raki et al., 2010, 2007; González-Dugo and Mateos, 2008; Hunsaker et al., 2005), showing a significant improvement. However, its operational application to large scales (e.g. irrigation perimeter) still faces two critical issues: 1) the unavailability (over most irrigated areas) of real- or near-real time irrigation data at the field scale, and 2) the difficulty in modeling RZSM from meteorological data alone.

* Corresponding author.
E-mail address: olivera.guerrale@cesbio.cnes.fr (L. Olivera-Guerra).

https://doi.org/10.1016/j.agwat.2018.06.014
Received 22 December 2017; Received in revised form 7 June 2018; Accepted 11 June 2018
0378-3774/ © 2018 Elsevier B.V. All rights reserved.

In other hand, land surface temperature (LST) derived in the thermal infrared has been widely used for estimating ET and water stress indices (e.g. Kalma et al., 2008; Li et al., 2009). LST has been also assimilated into the FAO method (Er-Raki et al., 2008), and more recently, used in FAO-2Kc to retrieve the water stress coefficient (Ks) (Dejonge et al., 2015; Ihuoma and Madramootoo, 2017; Kullberg et al., 2016). Among the variety of available approaches, the so-called contextual approach is quite attractive for operational applications, as it requires few input data. Contextual ET models estimate the ratio of actual ET to either potential ET (Moran et al., 1994) or available energy by using the remotely sensed LST – VI (Long and Singh, 2012) and/or LST – albedo space (Merlin, 2013; Roerink et al., 2000). In addition to the demonstrated utility of LST for estimating ET, its use has been extended to the retrieval of other components of the water budget, including RZSM (Calvet et al., 1998; Crow et al., 2008).

The relationship between RZSM and LST is explained by the link of the canopy temperature to the T rate under water-stress conditions, that is when RZSM is not sufficient to maintain a potential T rate (Boulet et al., 2007 Hain et al., 2009; Moran et al., 1994). Several studies have hence derived RZSM through the assimilation of LST or thermal-based proxy variables into land surface models (Calvet et al., 1998; Crow et al., 2008; Hain et al., 2012; Li et al., 2010). Moreover, with Landsat and ASTER thermal data, the spatial resolution that is potentially achievable for RZSM retrievals is 100 m. Note however that one key step in the estimation of thermal-based RZSM estimates over partially vegetated surfaces is the partitioning of the observed LST into soil and canopy temperatures (Merlin et al., 2014, 2012; Moran et al., 1994). Moran et al. (1994) proposed the water deficit index (WDI) to estimate a most probable range of crop water stress over partially vegetated pixels, which is obtained from the aforementioned LST – VI space (contextual method). This crop water stress index is equivalent to the RZSM normalized by the soil moisture at field capacity and by the soil moisture at wilting point (Bastiaanssen et al., 2000). In the FAO formalism, the same thresholds are set for Ks equal to 1 (soil moisture at field capacity) and for a Ks equal to 0 (soil moisture at wilting point).

In order to take advantage of: i) the simplicity and robustness of the thermal-based contextual ET models, ii) the utility of LST/VI data for water budget components (E/T, RZSM) and iii) the availability of LST/VI data at a spatial resolution suitable for monitoring crops; this study proposes an original approach to better constrain the water budget components of FAO-2Kc from LST and VI data. In practice, the approach seeks to retrieve the irrigation volumes and dates from first-guess (LST-derived) ET and RZSM, and to re-analyze all water-budget components (including ET and RZSM) from the retrieved irrigation data. In this study, the new methodology is tested by using ground-based observations of LST/VI, evaluated against ET, RZSM and irrigation observations. A sensitivity analysis is carried out in order to assess the applicability of the approach to remote sensing data.

2. Data sets

The experimental site (31°40′9.46″N, 7°35′45.64″O, 575 m above mean sea level) is located over an irrigated area in the semi-arid Haouz plain in the centre of Morocco (Fig. 1). The study focuses on a winter wheat crop, which is an irrigated unit that includes six fields of 4 ha each, from January to May 2003. More details about the experimental site can be found in Duchemin et al. (2008, 2006); Er-Raki et al. (2007) and Toumi et al. (2016). Variables of the surface energy and water balance as well as soil and vegetation characteristics were monitored during the entire growing cycle. The data set is described below.

2.1. Meteorological and flux data

Meteorological data including air temperature, solar radiation, relative humidity and wind speed were monitored throughout the agricultural season at a semi-hourly time step from January 14 until May 27, 2003. The four components of net radiation were measured by using a CNR1 radiometer (Kipp and Zonen). An eddy covariance (EC) system was installed over a winter wheat field to measure the latent and sensible heat fluxes. The data were recorded from high frequency (10 Hz) measurements of turbulent structures: a 3D sonic anemometer (CSAT3, Campbell Scientific), which measured the fluctuations in the wind velocity components and temperature; and an open-path infrared gas analyzer (Li7500, Licor), which measured concentration of water vapor and carbon dioxide.

2.2. Soil moisture data

Six time domain reflectometry (TDR) probes (CS615, Campbell Scientific) were installed in a soil pit near the fluxes measurement tower to measure soil water content at different depths (5, 10, 20, 30, 50 and 100 cm) every 30 min. The average ground-based RZSM ($RZSM_{obs}$) was estimated by interpolating the soil moisture observations of the different depths belonging to the root-zone of wheat as follows:

$$RZSM_{obs} = \frac{d_i SM_{d_i} + (d_{i+1}-d_i)SM_{d_{i+1}}+\ldots+(d_n-d_{n-1})SM_{d_n}}{d_i + (d_{i+1}-d_i)+\ldots+(d_n-d_{n-1})} \quad (1)$$

where SM_{di} (m^3m^{-3}) is the soil moisture measured at depth d_i (5–100 cm) and d_n is the deeper depth where there is a measurement that belongs to the root-zone. In this study, it is assumed that rooting depth varies according to the crop growth stages, so that different measurements are considered in the Eq. (1). The variation and values of rooting depth is detailed in the Section 3.1.2.

2.3. Irrigation data

Four irrigation events were applied in the field along the growing season by flooding with about 24 mm of water regardless of the precipitation and thus of soil moisture conditions. The sowing and the irrigation dates are listed in Table 1.

2.4. Fractional green and total vegetation cover

Given that green vegetation cover is commonly estimated from remote sensing data using empirical relations with vegetation indices, in this study the fractional green vegetation cover (fvg) is estimated from a linear relationship with NDVI (Normalized Difference Vegetation Index) as in Gutman and Ignatov, 1998:

$$f_{vg} = \frac{NDVI-NDVI_s}{NDVI_v-NDVI_s} \quad (2)$$

where NDVI is the near-infrared to red reflectance difference divided by their sum and $NDVI_s$ and $NDVI_v$ correspond to NDVI for bare soil (fvg = 0) and fully covering green vegetation (fvg = 1), respectively. The $NDVI_s$ was equal to the minimum value measured in the field (0.14) and $NDVI_v$ was defined at 0.93 after looking at maximum values taken on individual plots over the study area (Duchemin et al., 2006). Ground-based surface reflectance data over the field were collected using a MSR87 multispectral radiometer (Cropscan Inc., USA) every week. Fifteen sets of canopy reflectance measurements were made between January 8 and May 27, 2003. More details about the NDVI measurement procedure can be found in Er-Raki et al. (2007). The fractional total vegetation cover (fc) is derived from fvg by assuming that once fvg has reached its maximum value, it keeps equal to this maximum value until the end of the study period. fc was also measured using a hemispherical digital camera equipped with a fisheye lens with a field-of-view of 183°. Comparing the fvg- and photo-derived fc estimates before the maximum value of fvg revealed a good agreement (data not shown here). The values of root mean square error (RMSE) and coefficient of determination (R^2) were equal to 3.5% and 1.0, respectively.

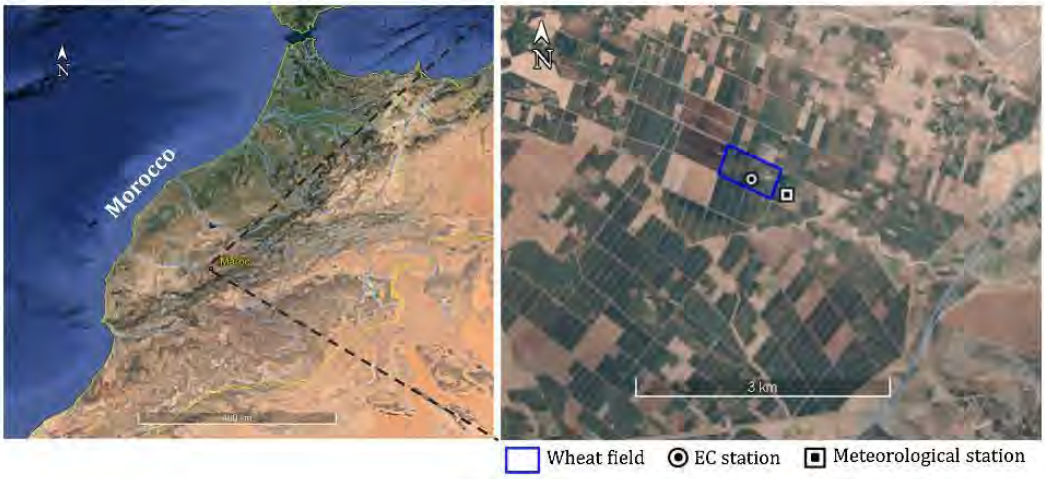


Fig. 1. Study area.

Table 1
Sowing and irrigation dates.

Sowing and irrigation event	Date	Days after sowing (DAS)
Sowing date	14 January	0
First irrigation	4 February	22
Second irrigation	20 March	66
Third irrigation	13 April	90
Fourth irrigation	21 April	98

2.5. Land surface temperature

In situ LST was derived from tower-based measurements of thermal radiances emitted from the surface, which were sampled at 1 Hz and averaged over 30 min. The averaged radiance was converted to LST by inverting Planck's law:

$$B(LST) = \frac{Lrad - (1-\varepsilon)Ldown}{\varepsilon} \quad (3)$$

where *Lrad* is the land leaving radiance (W m^{-2}) measured by a thermal radiometer (SI-111, Apogee), ε is the land surface emissivity, *Ldown* is the long-wave downwelling irradiance (W m^{-2}) and *B(LST)* is Planck's law for the *LST* (W $m^{-2}sr^{-1}\mu m^{-1}$). *Ldown* was retrieved from the incoming longwave radiation measurement from the net radiometer (CNR1, Kipp & Zonen). The ε was retrieved from the simplified NDVI threshold method (Sobrino et al., 2008) that weights the soil and vegetation emissivity through the fractional green vegetation cover (fvg). The soil emissivity was measured by Olioso et al. (2007) over the study area and the vegetation emissivity was considered equal to 0.99 (Amazirh et al., 2017; Sobrino et al., 2008). Only the 30-min LST data collected between 10 a.m. and 2 pm are used in this study, consistent with the overpass times of current thermal satellite missions (e.g. ASTER, Landsat, MODIS). In addition to the radiometric LST, the vegetation temperature was measured with Type-J thermocouples (seven replications, one sensor per plant), which were clumped on the vegetation apex near the location of the thermal radiometer. The sensors were changed every week to be set up at the vegetation apex and to measure the youngest leaves of the plant along the growing season. Thermocouple measurements will be used to evaluate the vegetation temperature estimates from the partition method of LST.

3. Methodology

3.1. Overview of FAO-56 dual crop coefficient method

The FAO-2Kc is a water balance model driven by 1) meteorological forcing variables to calculate reference evapotranspiration ET_0 and 2) precipitation and irrigation that jointly determine the water supply to simulate the soil water availability for soil evaporation and plant transpiration. In practice, FAO-2Kc estimates ET by multiplying ET_0 by a two separate crop coefficients:

$$ET = (KsKcb + Ke)ET_0 \quad (4)$$

where Kcb is the basal crop transpiration, Ks the stress coefficient (0–1) that represents the vegetation water status and a reduction factor of T (Kcb ET_0) and Ke the evaporation coefficient. ET_0 is calculated according to the FAO Penman–Monteith equation (Allen et al., 1998) at daily scale. The values used for Kcb (Kcb_{ini}, Kcb_{mid} and Kcb_{end}) at the three crop growth stages (initial, mid-season and maturity respectively) were taken from Allen et al. (1998). Ks (unitless) is calculated based on daily computation of the water balance for the root-zone layer Zr (m) as follows:

$$K_s = \frac{TAW - D_r}{TAW - RAW} = \frac{TAW - D_r}{TAW\,(1-p)} \quad (5)$$

where Dr (mm) is root zone depletion, TAW (mm) is total available soil water in the root zone, and p is the fraction of TAW that a crop can extract from the root zone without suffering from water stress. Water stress occurs when Dr becomes greater than RAW (Ks < 1). In contrast, when Dr ≤ RAW, Ks = 1 (see Fig. 3). Dr is calculated from the daily water balance. TAW is estimated as the difference between the water content at field capacity (SM_{FC}) and wilting point (SM_{WP}) by the daily crop rooting depth (TAW = 1000 (SM_{FC} – SM_{WP}) Zr). The rooting depth Zr is assumed to vary between a minimum value (maintained during the initial crop growth stage at 0.1 m) and a maximum value (reached at the beginning of the mid-season stage). The maximum value was measured in the field and was equal to 0.52 m according to Er-Raki et al. (2007). The soil parameters SM_{FC} and SM_{WP} were considered equal to an average value of 0.37 and 0.17 m^3m^{-3} respectively, in accordance with the values recommended by Allen et al. (1998) and with the minimum and maximum SM observed in the root-zone for the agricultural season.

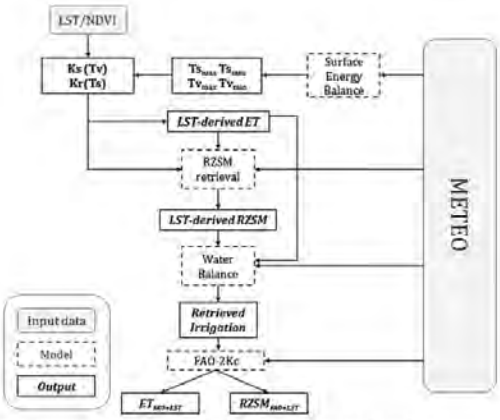


Fig. 2. Schematic diagram presenting an overview of the main inputs, models and outputs of the LST-integrated FAO-2Kc approach.

3.2. LST-integrated FAO-2Kc: new approach in the calculation of water budget components

Given that the main limitation of FAO-2Kc for operational irrigation management over large areas is the unavailability (over most irrigated areas) of irrigation data at the field scale, a new approach (named LST-integrated FAO-2Kc) is proposed to derive the water budget components from LST and VI data. An overview of the methodology is represented in Fig. 2 and is explained below.

Basically, LST is integrated in the standard FAO-2Kc at two levels: the ET and SM modeling components. LST is first partitioned into its soil and vegetation components to force E and T separately via thermal-derived estimates of Ks and Kr, respectively (ET modeling component). Note that the thermal-derived Ks is also used to derive a first-guess (LST-derived) RZSM estimate, based on the FAO-2Kc relationship between TAW and Ks (SM modeling component). The dynamic of first-guess RZSM is then analyzed to retrieve the irrigation amounts and dates. The FAO-2Kc is next forced by the previously retrieved irrigation and re-analyzed estimates of RZSM ($RZSM_{FAO+LST}$) and ET ($ET_{FAO+LST}$) are finally provided. The different components of LST-integrated FAO-2Kc (namely LST partitioning, thermal-derived Ks and Kr, first-guess ET and RZSM, irrigation retrieval, and re-analyzed ET and RZSM) are described in the following sections.

3.2.1. Partitioning LST

The method used for partitioning LST into vegetation and soil components relies on the combination between the hourglass approach (Moran et al., 1994) and the procedure to obtain the Temperature Vegetation Dryness Index (Sandholt et al., 2002). These two methods are based on the polygon defined in the LST – VI space. Ts_{max} is the temperature of a fully dry bare soil. Ts_{min} is the temperature of a fully wet bare soil. Tv_{max} is the maximum vegetation temperature corresponding to fully stressed (non-transpiring) vegetation. Tv_{min} is the minimum vegetation temperature corresponding to well-watered unstressed vegetation (transpiring at potential rate). Since this study tests the feasibility of the proposed methodology from in situ measurements, the image-based polygon cannot be plotted to constrain the temperature endmembers (Ts_{max}, Ts_{min}, Tv_{max}, Tv_{min}). Therefore, these temperatures are simulated by using the energy balance model proposed by Stefan et al. (2015). Ts_{min} and Ts_{max} are simulated by a soil energy balance model, while Tv_{min} is set to the air temperature and Tv_{max} is defined according to the assumptions that the difference between Ts_{max} and Ts_{min} is the same that between Tv_{max} and Tv_{min} (Stefan et al., 2015). Once the temperature endmembers have been defined, Tv is obtained by using the hourglass approach or TVDI method according to the position of the (fc, LST) point in the polygon. In practice, the diagonals are plotted in the polygon LST – fc space by distinguishing four areas (evaporation- and transpiration-controlled, unstressed and stressed mixed surface), as they were defined in Merlin et al. (2012). If the (fc, LST) point belongs to the unstressed mixed or stressed mixed zone, Tv is calculated according to Merlin et al. (2012). If the (fc, LST) point belongs to the evaporation-controlled or transpiration-controlled zone, Tv is calculated by using the TVDI method, by interpolating the temperature between the Tv_{max} and Tv_{min}.

Derivation of Ts is based on a linear decomposition of the LST into its soil and vegetation components as a good approximation of the relationship with fourth power for temperatures (and consistent with the contextual approach) as follows:

$$Ts = \frac{LST - fcTv}{1 - fc} \tag{6}$$

3.2.2. Retrieving stress coefficient (Ks) and evaporation reduction coefficient (Kr) from thermal data

LST data are used to reflect the soil and crop water status by calculating stress indices for the surface and root-zone layer, respectively, namely the E reduction coefficient (Kr), and the stress coefficient (Ks). The Ks (Kr) was estimated by relating the vegetation (soil) temperature to cold and hot extreme temperatures of vegetation (soil) that represent wet and dry vegetation (soil) as follows:

$$K\eta_{LST} = \frac{Ts_{max} - Ts}{Ts_{max} - Ts_{min}} \tag{7}$$

$$Ks_{LST} = \frac{Tv_{max} - Tv}{Tv_{max} - Tv_{min}} \tag{8}$$

where Ts and Tv correspond to the temperature of the soil and vegetation component derived from the partitioning method presented above.

Given that we have daily LST observation, Ks_{LST} may show significant day-to-day variability associated with uncertainties in the LST partitioning method, the LST-derived Ks was smoothed to reduce random uncertainties. A weighting function is applied to the Ks_{LST} values estimated during a 3-day sliding period:

$$Ks_{LST,cor,i} = \sum_{i-1}^{i+1} \frac{w_i Ks_{LST,i}}{\sum w_i};\ w_i = 1 - \frac{error}{Tv_{max,i} - Tv_{min,i}} \tag{9}$$

where $Ks_{LST,cor,i}$ is the smoothed Ks_{LST}, w_i (0–1) is the weight corresponding to the Ks_{LST} of day i and the subscript '*i*–1' and '*i* + 1' is referred to the day before and after, respectively. The *error* is the uncertainty considered for the LST partitioning method (i.e. uncertainty in Tv estimates). We define the weight w_i such as: i) the higher the (Tv_{max} – Tv_{min}) difference, the higher the weight w_i, and ii) w_i is set to 0 for (Tv_{max} – Tv_{min}) < *error*. The smoothing procedure become necessary since RZSM is derived from thermal-derived Ks and to obtain a temporal dynamic more consistent with RZSM observations.

3.2.3. First-guess ET

A thermal-based ET (ET_{LST}) is calculated by using the FAO-2Kc formulation (Eq. (4)) and the coefficients Kr_{LST} and Ks_{LST} (Eqs. (7) and (9)).

3.2.4. First guess RZSM

The procedure to estimate first-guess (LST-derived) RZSM is described below. RZSM can be derived from the root-zone depletion (D_r) and the soil parameter used in the FAO-56 formalism (SM_{WP}, SM_{FC}, TAW) as follows:

$$RZSM = SM_{WP} + \left(1 - \frac{D_r}{TAW}\right)(SM_{FC} - SM_{WP}) \tag{10}$$

By inserting the Eq. (5) into the Eq. (10), RZSM is expressed as a

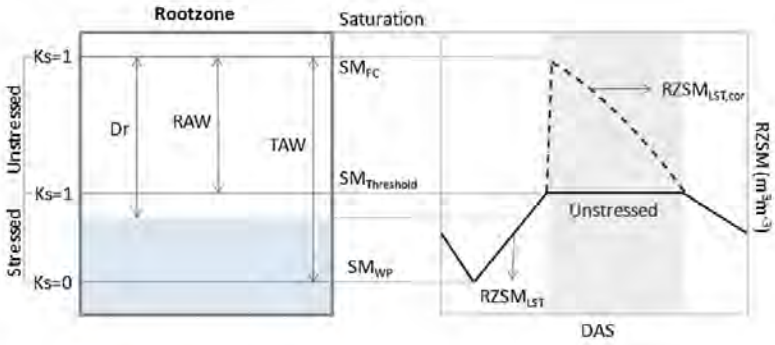


Fig. 3. Schematic representation of RZSM retrieval for stressed (Ks < 1) and unstressed (Ks = 1) periods. The left box represents the variation of RZSM according to the depletion (Dr) in the rootzone. Following the FAO-2Kc formulations, RZSM ranges between SM_{WP} and SM_{FC}, which constrain the total available water (TAW) and readily available water (RAW = p TAW). The right plot represents the temporal variability of LST-derived RZSM, where is showed an unstressed period (shaded area) for which $RZSM_{LST}$ (equal to $SM_{threshold}$) is corrected for both LST-derived ET and precipitation through a daily water budget.

function of Ks during stressed periods (Ks < 1, Dr < RAW):

$$RZSM = SM_{WP} + Ks_{LST}(1-p)(SM_{FC}-SM_{WP}) \quad (11)$$

Note that for unstressed periods (Ks = 1), RZSM from Eq. (11) would be equal to the threshold from which the stressed conditions end ($SM_{Threshold}$). According to the values of SM_{WP}, SM_{FC} and p used in this study (0.17, 0.37 and 0.55, respectively), the $SM_{Threshold}$ is equal to 0.26. During unstressed periods, RZSM from Eq. (11) is thus corrected dynamically for both cumulated precipitation and cumulated ET_{LST} during this period through a daily water balance (shaded area in plot of Fig. 3). The RZSM is limited to a maximum of SM_{FC}. If this maximum is reached then the RZSM is reset to the $SM_{Threshold}$ and next the above correction is applied. For instance, in the Fig. 3, $RZSM_{LST,cor}$ would reach SM_{FC} if the unstressed period were longer and then it would be reset to the $SM_{Threshold}$ to carry on the correction in the unstressed period remaining.

3.2.5. Irrigation retrieval

Irrigation events are detected based on a significant increase in first-guess (LST-derived) RZSM, which cannot be attributed to precipitation. Only significant increases are considered with a RZSM change larger than a threshold value equal to 0.02 m^3m^{-3}, which represents a water supply greater than 10 mm for a 0.5 m root-zone depth. Note that such a threshold considers that ET and drainage are both negligible compared to the irrigation depth (during the irrigation event), and that the irrigation depth is larger than 10 mm. For the periods with steady increase in RZSM, the amount of retrieved/inverted irrigation (I_{inv}) is constrained through a water budget between the amounts of precipitation as inflow and the LST-derived ET as outflow, as well as the drainage if it is produced by precipitation.

The periods when a significant man-made water supply is observed are considered as probable dates for the retrieved irrigation events. If an irrigation is effectively detected for this period (with a minimum threshold of 10 mm), then the estimated date of irrigation is set as the last date of the period, in order to agree the maximum LST-based RZSM and the maximum RZSM simulated from FAO-56.

3.2.6. Re-analyzed RZSM and ET

Once irrigation has been retrieved from first-guess (LST-derived) RZSM, first-guess ET and observed precipitations, the standard FAO-2Kc is implemented by using the default (non-calibrated) parameters given by Allen et al. (1998), but with the difference that the retrieved irrigation (amounts and dates) is introduced as forcing. From the FAO-2Kc we obtained ET, E, T as well as Dr and TAW that allow us to calculate RZSM by using the Eq. (10) throughout the growing season. Note that Eq. (10) is valid to obtain the RZSM for both stressed and non-stresses periods, because Dr is calculated from the daily water balance implemented in FAO-2Kc for its full range ($0 \leq Dr \leq TAW$). To distinguish the simulated ET and RZSM from their first-guess (LST-derived) values, the former are referred to as re-analyzed RZSM and ET, respectively.

3.3. Validation strategy of irrigation, ET and RZSM estimates

In this study, the validation is carried out in terms of ET, RZSM and irrigation estimates by comparing them against ground-based ET, RZSM and actual irrigation on a daily basis. Two evaluations are performed for ET and RZSM estimates: 1) LST-derived (or first-guess) estimates and 2) derived from standard FAO-2Kc forced by retrieved irrigation. The irrigation is assessed in terms of dates and amounts. Regarding dates, the irrigation is compared in terms of 1) the numbers of retrieved irrigation events and 2) the agreement between probable dates on which the irrigation is detected and the actual date of the events. Regarding amounts, two scales are considered for the cumulated irrigation: the daily and seasonal time scales. However, taking into account that irrigation is estimated by assuming a negligible drainage (during irrigation periods), the retrieved irrigation is compared to the observed irrigation after subtracting the drainage. Since no measurement was available during the field experiment, drainage was estimated from the standard FAO-2Kc using observed irrigation as forcing.

4. Results

4.1. LST partitioning

In Fig. 4 is shown the series of soil (Ts, Ts_{min} and Ts_{max}) and vegetation (Tv, Tv_{min} and Tv_{max}) temperatures. According to the partition method, Ts and Tv are estimated within its corresponding endmembers and the ground-based LST (LST_{obs} in Fig. 4) is observed within the minimum and maximum temperatures (Tv_{min} and Ts_{max}, respectively) for practically the whole season. Thus temperature endmembers are suitably simulated, fully consistent with LST observations.

In order to validate quantitatively the partition of LST into its vegetation (Tv) and soil (Ts) components, Tv is compared against the mean vegetation temperature from the seven thermocouples set up in the vegetation apex. The RMSE and R^2 are equal to 3.27 °C and 0.92, respectively. Note that if the validation daytime period is restricted between 10 a.m. and 1 pm only (still consistent with the overpass time of thermal missions such as ASTER, Landsat and MODIS), the errors are improved reaching a RMSE of 2.98 °C. These results are similar to the errors obtained by Stefan et al. (2015) for the simulation of the soil temperature endmembers (Ts_{max}, Ts_{min}) over the same study area. It can be observed in Fig. 5 that Tv is overestimated for values larger than 30 °C, corresponding to the late season (after DAS 120). This is due to location (in the apex) of the Tv measurements. Indeed, the youngest leaves of the plant are expected to be colder (with a higher transpiration rate) than the adult and senescing leaves, whose temperature has not been measured. Another reason can be probably explained for the impact of water stress on surface roughness (vegetation height), which was neglected in the estimation of Tv_{max} and Tv_{min}. The four

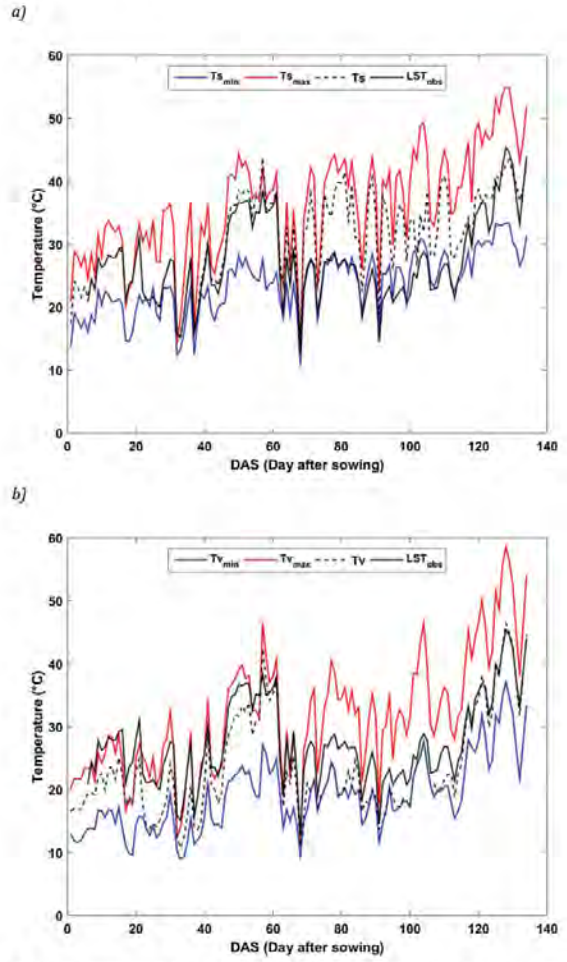


Fig. 4. Time series of (a) Ts_{min}, Ts_{max} and Ts estimates and (b) Tv_{min}, Tv_{max} and Tv estimates. Ground-based LST (LST_{obs}) is also shown on both plots for comparison.

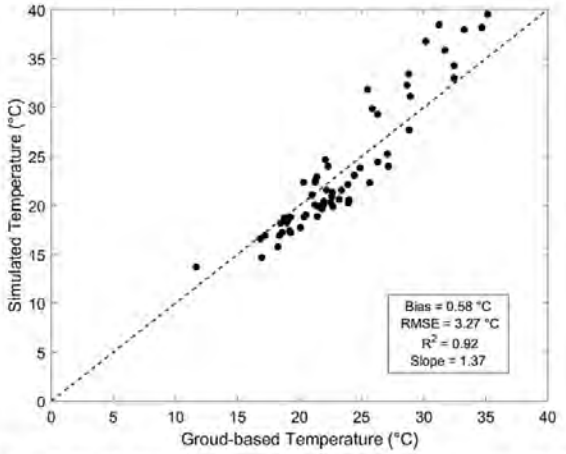


Fig. 5. Retrieved versus ground-based vegetation temperature (average of the 7 thermocouples between 10 a.m. and 2 pm) for the period with fc > 0.5 (between DAS 69 and 134).

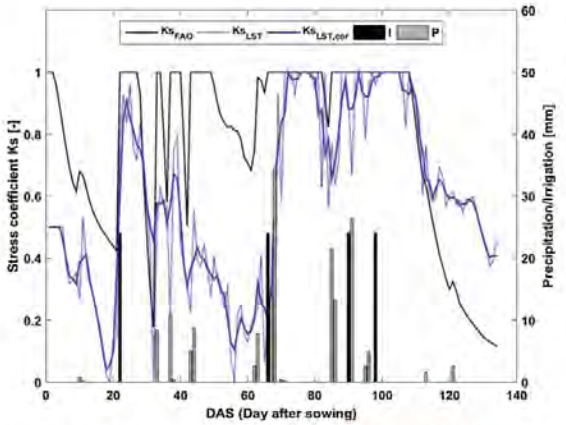


Fig. 6. Ks from FAO-2Kc method according to Allen et al., 1998 (Ks_{FAO}), LST-derived Ks from daily ground-based LST (Ks_{LST}) and the smoothed LST-derived Ks ($Ks_{LST,cor}$). Precipitation (P) and irrigation (I) amounts are also shown.

temperature endmembers and the decomposed temperatures (Tv, Ts) are then used in Eqs. (8)–(10) to estimate the E and T reduction factors (Kr_{LST} and Ks_{LST}, respectively).

4.2. LST-derived ET estimates

Two versions of the FAO-2Kc method are compared: the standard version by using the parameters given in Allen et al. (1998) forced by the observed irrigation, and the version proposed in this study by using the Kr_{LST} (Eq. (7)) and Ks_{LST} (Eq. (8)) coefficients derived from LST/VI data. Comparison between the time series of vegetation stress coefficient from standard FAO-2Kc (Ks_{FAO}) and from LST/VI (Ks_{LST}) is presented in Fig. 6. Overall, Ks_{LST} detects stress periods and responds well to the water inputs (see the significant increase just after irrigation events), even though its estimation is fully independent of the daily water balance. However, it shows day-to-day variability that could be associated with uncertainties in the LST partitioning method (errors in Tv estimates). For this reason, the LST-derived Ks is smoothed to reduce random uncertainties, by using the Ks_{LST} values estimated on the day before and the day after (Eq. (9)). It can be observed that LST-derived Ks simulates stress conditions in a more pronounced way than the standard FAO-2Kc, except for the late season. Such information can next be used to simulate the required water supply (see Section 4.3).

The evolution of ET during the growing season is simulated by both FAO-2Kc versions (Fig. 7). Results show that the performance of the FAO-2Kc by using coefficients based on LST/VI is superior to that of the standard version. The ET is estimated with an RMSE equal to 0.84 and 0.68 mm.day^{-1} by using the standard FAO-2Kc and the proposed method, respectively. The main discrepancies between both methods can be observed during the development (between DAS 40 and 70) and late (after DAS 110) stages due to great differences in Ks estimates and thus in T. Late in the season (after DAS 110) a difference in E estimates is also observed, according to daily water balance used in FAO-2Kc the water in surface evaporable layer is fully depleted (Kr_{FAO} = 0, E = 0), whereas the LST-derived E increases to about 1 mm day^{-1} because Ts is estimated between Ts_{max} and Ts_{min} from the partition of LST and thus Kr_{LST} is larger than 0. The increase in E can be explained by an increase of i) the sun-exposed soil due to the reduction of vegetation and ii) the capillary rise from the root zone, which can be detected from the LST-derived E estimates although the fc was assumed constant after the fc peak. A recent study about the E/T partitioning of winter wheat (Rafi

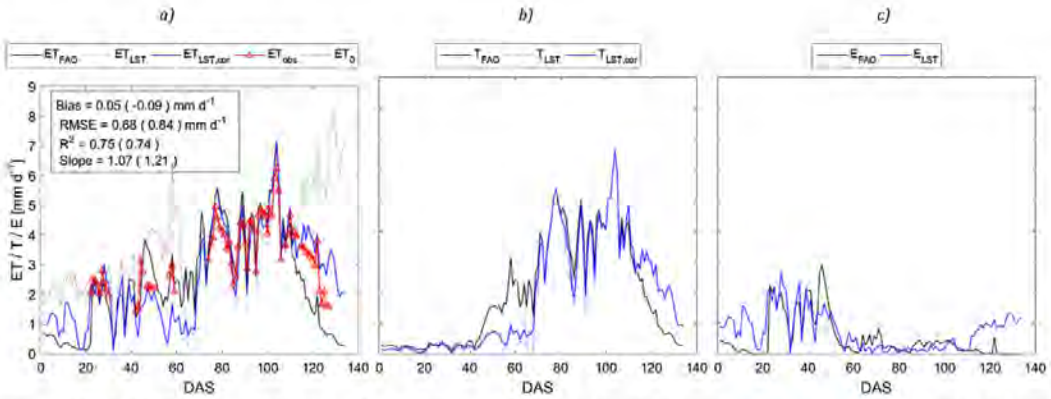


Fig. 7. Time series of daily (a) ET, (b) T and (c) E estimates from FAO-2Kc method using the parameters given by Allen et al (1998) forced by observed irrigation, and from LST-derived Ks (ET and T) and LST-derived Kr (E) and from the smoothed LST-derived Ks (ET_{cor} and T_{cor}, respectively). The statistical parameters of ET_{cor} (ET_{FAO}) versus EC observations are shown in the box of (a).

et al., 2018) noted an underestimation of E by FAO-56 especially during the senescence period, consistent with the thermal-derived E estimates of this study. In the same way, others differences in E is found in the initial stage (before DAS 20) that could not be evaluated due to the lack of in situ measurements. Discrepancies are also observed when comparing each method individually against the observed ET. During the first period (DAS 40–70), ET is overestimated with the standard FAO-2Kc while it is underestimated with FAO-2Kc constrained by LST/VI data, whereas the opposite situation is encountered during late season, although the errors for the modified FAO-2Kc are lower.

Note that the ET and T estimated by using the LST-derived Ks or the smoothed LST-derived one are almost the same (Fig. 7b). Also, the RMSE and slope for ET are slightly improved by using the smoothed LST-derived Ks from 0.70 to 0.68 mm day^{-1} and from 1.10 to 1.07, respectively. Nonetheless, it is worth noting that the smoothing is more useful in the estimation of RZSM from Eq. (11) by reducing the noisy temporal variability from thermal data (Ks_{LST}) and by obtaining a temporal variability more consistent with the temporal dynamic of the observed RZSM.

4.3. Irrigation estimates

The calculation of RZSM from Ks_{LST} (Eq. (11)) and its variations allowed the detection of the irrigation time. In Fig. 8 it can be observed that four probable irrigation events were identified, corresponding to significant increases in LST-derived RZSM. Note that the probable days for an irrigation supply are marked in cyan in Fig. 8. Every identified event is in good agreement with the observed irrigation. However, only three irrigation events were detected from the inversion of the water budget whereas four probable events were obtained from significant increases in $RZSM_{LST}$. The probable event detected on DAS 86–90 does not correspond to a retrieved irrigation event. This is due to the rainfall events on DAS 86–87, which resulted in relatively high RZSM values, so that the LST-derived RZSM was not sensitive enough to an additional (man-made) water supply on DAS 91. Given that the last two actual irrigation events were applied 8 days apart and because three rainfalls occurred between both events, it was difficult to differentiate both irrigation supplies. This may be the reason for the overestimation of the irrigation amount of the last event (irrigation is estimated as 39.6 mm compared to 24 mm for the assumed true value).

The total irrigation depth for the growing season was equal to 67 mm, that represents a relative error of 30.2% compared to the total irrigation applied by the farmer. Note that the retrieved irrigation amounts are only estimated considering the water required to produce the increase in LST-derived RZSM and thus the drainage from irrigation

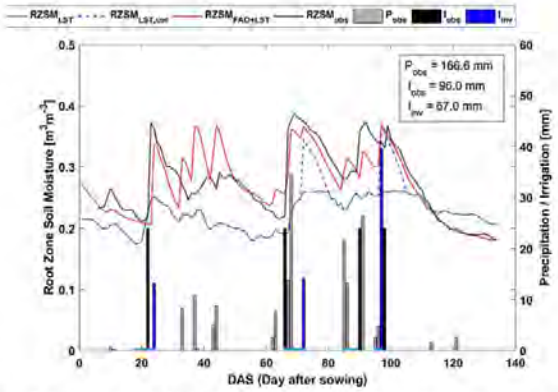


Fig. 8. Time series of LST-derived RZSM for stressed periods when Ks < 1 ($RZSM_{LST}$), corrected LST-derived RZSM ($RZSM_{LST,cor}$) through a water budget for unstressed periods when Ks = 1 and the RZSM simulated by the FAO-2Kc ($RZSM_{FAO+LST}$) by using precipitation (P_{obs}) and retrieved irrigation (I_{inv}) as input. The periods of significant increase in $RZSM_{LST,cor}$ are marked in the x axis (cyan). Observed precipitation, irrigation and RZSM are also shown for comparison. The observed cumulated precipitation (P_{obs}), irrigation (I_{obs}) and retrieved irrigation (I_{inv}) are shown.

is not taken into account. The total drainage of the irrigation periods simulated along the season by standard FAO-2Kc with observed irrigation as forcing is equal to 26.2 mm. If we subtract this quantity to the observed total irrigation water supply (24 mm x 4 irrigations = 96 mm) the effective irrigation would be equal to 69.8 mm, which is very close to the cumulated retrieved irrigation estimated as 67.0 mm.

4.4. RZSM estimates

The time series for daily first-guess (LST-derived) RZSM and re-analyzed RZSM (RZSM simulated by the FAO-2Kc forced by retrieved irrigation) are shown in Fig. 8, namely $RZSM_{LST}$ and $RZSM_{FAO+LST}$. Also, the time series of the observed RZSM is shown for comparison. The validation for each RZSM product is presented in Fig. 9. It can be observed in both Figs. 8 and 9 that the first-guess RZSM is systematically underestimated with an averaged bias equal to $-0.044\ m^3m^{-3}$. Although the first-guess RZSM shows a poor accuracy with a RMSE of $0.061\ m^3m^{-3}$, it is shown an acceptable representativeness of the temporal variability of RZSM that can be seen in the ability to detect the

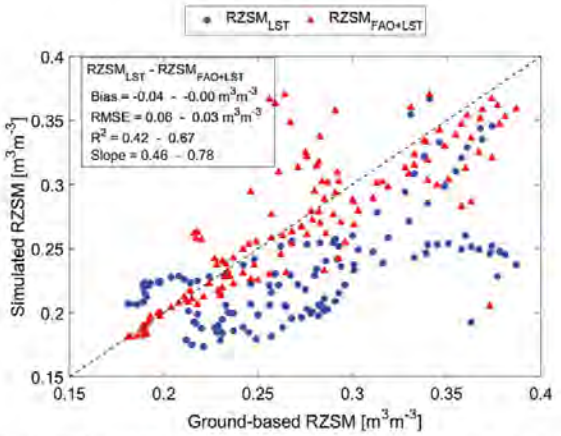


Fig. 9. LST-derived RZSM ($RZSM_{LST}$) and FAO-simulated RZSM by forcing the FAO-2Kc model using retrieved irrigation ($RZSM_{FAO+LST}$) versus ground-based RZSM.

irrigation dates and amounts, just as in previous section, and an acceptable R^2 equal to 0.42. $RZSM_{FAO+LST}$ is significantly improved (RMSE of 0.034 m^3m^{-3} and R^2 of 0.68) and the results are very close if the actual irrigation is used as forcing in the FAO-2Kc (RMSE equal to 0.032 m^3m^{-3} and R^2 equal to 0.73). Overall, standard FAO-2Kc is able to estimate the RZSM ($RZSM_{FAO+LST}$) through the Eq. (10), except during rainfall periods (without irrigation) when an overestimation can be observed (Figs. 8 and 9). Hence, the standard FAO-2Kc does not represent sufficiently well the response of RZSM to the precipitation. This could be an effect of the rain gauges, which generally provide a larger measurement than the effective precipitation due to canopy interception. It can also be assumed that the FAO-2Kc model responds differently to natural and man-made water supplies due to differences in water supply intensities.

Regarding the overestimation during the late season of first-guess RZSM from Eq. (11), and given the overestimation during the same period of LST-derived ET, which are both dependent on LST-derived Ks, we can affirm that the LST-derived Ks during this period is overestimated. This may be due to an overestimation of Tv_{max} (see Fig. 5) during this period with full-cover senescent vegetation. In fact, it is suspected that the assumption $Tv_{max} - Tv_{min} = Ts_{max} - Ts_{min}$ does not apply during senescence period.

5. Discussion

5.1. Utility of thermal data to help constrain the water budget and retrieving root zone soil moisture

Given the results of Ks_{LST} estimates in Fig. 6 it can be observed that Ks_{LST} responds well to water inputs and its dynamic is fully consistent with the water balance estimates (Ks_{FAO}). Moreover, the ET estimated from LST-derived coefficients (ET_{LST}) is more accurate in Fig. 7 than that of the standard FAO-2Kc (ET_{FAO}). The good performance of ET_{LST} can be explained by 1) the strong relationship between the LST and the coupled energy-water balance as recently reported in Diarra et al., (2017) when the TSEB model was used over the wheat field in the same area, 2) and the robustness of contextual models, which do not require accurate LST estimates to obtain satisfying results in ET retrievals (Kalma et al., 2008). In contrast with contextual methods, the standard FAO-2Kc requires local calibration to accurately estimate ET. This was notably demonstrated by Er-Raki et al. (2007) with the same wheat field. For instance, they found a significant difference between the locally calibrated and non-calibrated Kcb and then ET estimates, indicating that wheat was not growing in optimal conditions. Such conditions can be detected by the proposed approach based on LST-derived coefficients (Ks_{LST} and Kr_{LST}), thus avoiding both the use of parameters (e.g. SM_{FC}, SM_{WP}, Ze, Zr) and the local calibration of Kcb. However, if locally derived Kcb by Er-Raki et al. (2007) is used in the standard FAO-2Kc, better estimates of ET are obtained with a RMSE and R^2 equal to 0.65 mm day^{-1} and 0.81, respectively. Nonetheless, the use of EC measurements for calibration is a strong limitation for application of the methods to large areas. It should be noted that the performance of ET_{LST} is even better than the re-analyzed ET ($ET_{FAO+LST}$) since it is simulated from FAO-2Kc by using the retrieved irrigation and non-calibrated Kcb. In order to improve these estimates, the Kcb could be 1) forced by NDVI and 2) calibrated from ET_{LST} estimates since $ET_{FAO+LST}$ does not take into account the stress detected from LST-estimates (not only the water stress). In this sense the vegetation conditions can be included in the re-analyzed ET through the Kcb calibrated from LST/VI data accounting the ET_{LST} improvement.

LST-derived RZSM ($RZSM_{LST}$) responds well to stressed periods and water inputs, consistent with the control of RZSM on the vegetation stress detected from canopy temperature (Tv). Even though a significant bias is observed in the validation of $RZSM_{LST}$, its range of variability is enough to detect significant increases, which is the basis of the irrigation retrieval procedure. Finally, FAO-2Kc is implemented by using the retrieved irrigation and a re-analyzed RZSM is retrieved with a noticeable improvement. Such results confirm the utility of LST to help constrain the water budget components, and can be used in an irrigation scheduling program for deciding when and how much to irrigate.

5.2. Applicability to temporally sparse thermal data

As mentioned in Section 2, this study was undertaken by using ground-based radiometric LST. Therefore, the uncertainty and temporal sampling of remotely sensed LST are not taken into account. Regarding the uncertainty, many studies have demonstrated that contextual models, such as the LST/VI-based method used herein to partition LST, allow us to avoid accurate estimates of surface variables, since the extreme water conditions (stressed – well-watered) used as boundaries to estimate thermal-based evaporative indices are estimated from the variability captured within thermal imagery (Kalma et al., 2008; Li et al., 2009). With regard to temporal sampling, this issue becomes a key limitation of spaceborne thermal sensors due to the restriction of surface retrievals to sufficiently cloud-free days (Crow et al., 2008). In addition to the thermal data currently available at high spatial (100 m) resolution have a repeat cycle of 16 days only, and up to 8 days by combining Landsat-7 and -8. To assess the impact of the observation frequency on the proposed approach, a sensitivity analysis is carried out by decreasing the LST observation frequency. It should be noted that the smoothing of Ks_{LST} (Eq. (9)) to reduce the day-to-day variability is only applied for a daily revisit of LST observations. For a frequency between 2 and 16 days the Ks_{LST} from Eq. (8) is directly used without smoothing to LST-derived estimates. The assessment is undertaken in terms of RZSM, ET and total irrigation water supply simulated by FAO-2Kc.

Increasing the duration between LST observations, naturally leads to a decreasing the number of thermal-derived ET and RZSM retrievals (from Eqs. (4) and (11), respectively) available to constrain the irrigation from FAO-2Kc. However, given that irrigation can be estimated, it allows us to run FAO-2Kc for estimating RZSM and ET every day along the season. Fig. 10 shows the impact of the observation frequency every 2, 4, 8 and 16 days on estimating RZSM. One can observe the decreasing number of LST-derived RZSM estimates ($RZSM_{LST}$), its errors and the significant improvement after running FAO-2Kc model by using the retrieved irrigation. Such approach allows estimating the RZSM for all days during the growing season ($RZSM_{FAO+LST}$) irrespective of the observation frequency used.

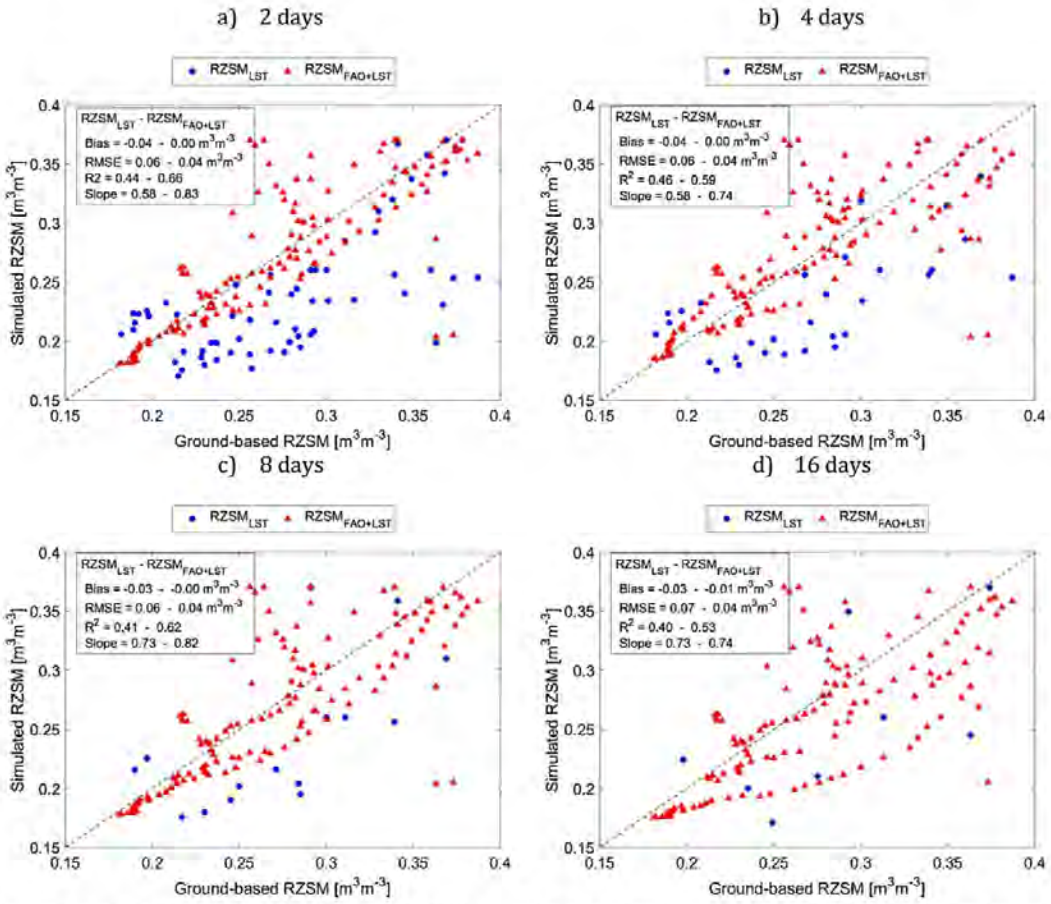


Fig. 10. Validation of the RZSM simulated by FAO-2Kc approach ($RZSM_{FAO+LST}$) by using observed precipitation and the irrigation retrieved from thermal observations available at a decreasing frequency (1 every 2, 4, 8 and 16 days). The statistical parameters of the LST-derived RZSM ($RZSM_{LST}$) are shown as a reference of the improvement of in $RZSM_{FAO+LST}$.

Fig. 11 shows the impact on RZSM and ET estimates of the availability of LST observations according to the time revisit frequency ranging from 1 to 16 days. Although even the errors are gradually increasing, the results demonstrate a relatively good performance and acceptable errors by increasing the revisit period. Fig. 12 shows the impact of the availability of LST observations on the retrieved total irrigation water amount and number of irrigation events. Acceptable errors in the total water supply are observed. The number of simulated irrigation events decreases as the time revisit frequency decreases, falling below 3 events with a revisit longer than 8 days. Overall, it might be noted that up to a 10-day revisit of LST observations, a good agreement is obtained with R^2 higher than 0.5 and 0.6 for RZSM and ET respectively, and a mean absolute error (MAE) of total irrigation water supply lower than 15 mm (corresponding to a relative MAE of 21%). According to these results, it could be considered the use of LST products with time revisit of 8 days such as i) the combination of Landsat-7 and -8 LST on cloud-free days and/or ii) the 1 km resolution MODIS LST product downscaled to 100 m resolution by using the Landsat LST (e.g. Anderson et al., 2012; Cammalleri et al., 2014; Olivera-Guerra et al., 2017; Weng et al., 2014).

The results show clearly the applicability to remote sensing data and the utility to the irrigation scheduling at regional scale. Given that Ks_{LST} and irrigation volumes and dates can be fully obtained from remotely sensed LST/VI data, this methodology could be implemented in an irrigation index to characterize the irrigation distribution, such as the irrigation index priority proposed by Belaqziz et al. (2013). This index takes into account the Ks and the irrigation volumes and dates and by using remote sensed-derived Ks and irrigation would allow evaluate the irrigation scheduling over broad irrigated agricultural areas poorly monitored.

6. Conclusions

A new approach in the calculation of water budget components and for irrigation scheduling (when and how much to irrigate) is developed by integrating LST data into the FAO-2Kc model. It relies on: 1) the estimation of first-guess (LST-derived) RZSM from Ks_{LST} ($Ks_{LST} < 1$) during stressed periods and its correction for both cumulated precipitation and cumulated ET during unstressed periods ($Ks_{LST} = 1$); 2) the estimation of irrigation amounts and dates along the season from (first-guess) LST-derived RZSM and ET estimates; and 3) the use of retrieved irrigations to force FAO-2Kc to simulate RZSM and ET on a daily basis. Statistical results indicate that first-guess (LST-derived) ET (ET_{LST}) is more accurate than the ET simulated by the standard version of FAO-2Kc while the first-guess RZSM is significantly improved when FAO-2Kc is implemented by using retrieved irrigation. Results show that the new methodology combining FAO-2Kc and LST/VI data is able to 1) accurately estimate the crop ET using the default (non-calibrated)

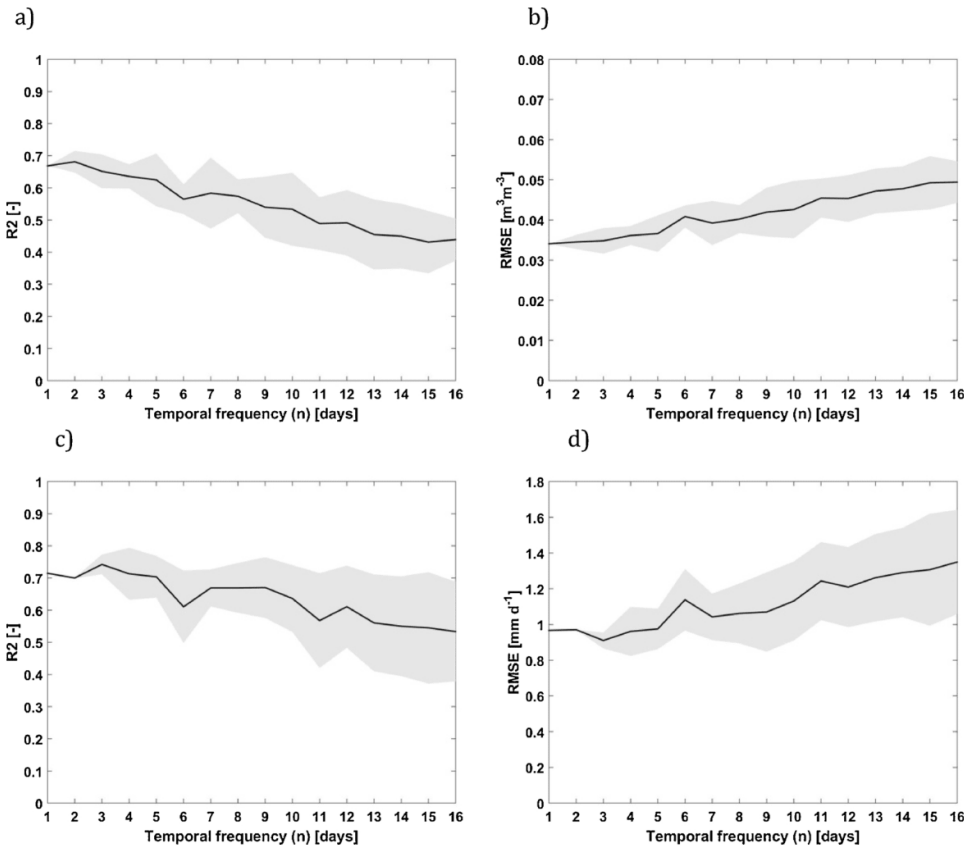


Fig. 11. Sensitivity of (a,b) $RZSM_{FAO+LST}$ and (c,d) re-analyzed ET (ET simulated from FAO-2Kc approach by using the input of precipitation and retrieved irrigation) to different frequency of thermal data observations. Average R^2 (a,c) and RMSE (b,d) are presented for each temporal frequency by running the model n times by changing the first day of observation from 1 to n. The shaded area represents its standard deviation.

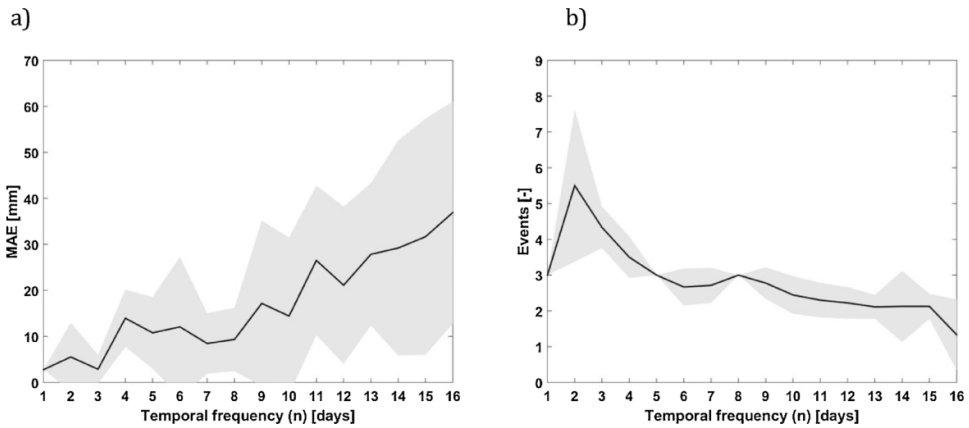


Fig. 12. Sensitivity of total irrigation water supply constrained from LST-derived ET and RZSM to different frequency of thermal data observations. (a) Average mean absolute error (MAE) of total irrigation water supply and (b) number of retrieved irrigation events are presented for each temporal frequency where the model is run n times by changing the start day from 1 to n. The shaded area represents its standard deviation. The observed total irrigation water supply is equal to 96 mm (69.8 mm without drainage) distributed in 4 events during the wheat growing season.

parameters given by Allen et al. (1998), 2) to estimate the irrigation amounts and dates and 3) to accurately simulate RZSM.

The impact of temporal sampling in LST observation is assessed by carrying out by decreasing the LST observation frequency from 1 to 16 days. It is demonstrated that the irrigation amounts and dates can be estimated, allowing us to run FAO-2Kc for estimating RZSM and ET along the season on a daily basis. Although errors are gradually increasing with the observation period, results demonstrate a relatively good performance and acceptable errors for an observation frequency of 1 per 8 days so it is recommended to use LST observations at a temporal resolution finer than 10 days. In order to take advantage of the high temporal resolution of MODIS LST and the high spatial resolution of Landsat LST, downscaling method could be included in the future for monitoring the RZSM at the field and daily scale. However, further research will be required to assess the impact of downscaling uncertainties in the proposed methodology.

Acknowledgements

This study was supported by the French Agence Nationale de la Recherche (MIXMOD-E project, ANR-13-JS06-003-01) and the European Commission Horizon 2020 Programme for Research and Innovation (H2020) in the context of the Marie Sklodowska-Curie Research and Innovation Staff Exchange (RISE) action (REC project, grant agreement no: 645642). The *in situ* data set was provided by the Joint International Laboratory TREMA http://trema.ucam.ac.ma. L. Olivera-Guerra acknowledges the support from CONICYT through the PhD fellowship "BecasChile de Doctorado en el Extranjero".

References

Allen, R.G., 2000. Using the FAO-56 dual crop coefficient method over an irrigated region as part of an evapotranspiration intercomparison study. J. Hydrol. 229, 27–41. http://dx.doi.org/10.1016/S0022-1694(99)00194-8.

Allen, R.G., Pereira, L.S., Raes, D., Smith, M., 1998. Crop Evapotranspiration - Guidlines for Computing Crop Water Requirements. Irrig. Drainage. Pap. 56, Food Agriciculture. Organ. United Nations, Rome, Italy.

Amazirh, A., Er-Raki, S., Chehbouni, A., Rivalland, V., Diarra, A., Khabba, S., Ezzahar, J., Merlin, O., 2017. Modified Penman–Monteith equation for monitoring evapotranspiration of wheat crop: relationship between the surface resistance and remotely sensed stress index. Biosyst. Eng. 164, 68–84. http://dx.doi.org/10.1016/j.biosystemseng.2017.09.015.

Anderson, M.C., Kustas, W.P., Alfieri, J.G., Gao, F., Hain, C., Prueger, J.H., Evett, S., Colaizzi, P., Howell, T., Chávez, J.L., 2012. Mapping daily evapotranspiration at landsat spatial scales during the BEAREX'08 field campaign. Adv. Water Resour. 50, 162–177. http://dx.doi.org/10.1016/j.advwatres.2012.06.005.

Bastiaanssen, W.G.M., Molden, D.J., Makin, I.W., 2000. Remote sensing for irrigated agriculture: examples from research and possible applications. Agric. Water Manag. 46, 137–155. http://dx.doi.org/10.1016/S0378-3774(00)00080-9.

Belaqziz, S., Khabba, S., Er-Raki, S., Jarlan, L., Le Page, M., Kharrou, M.H., Adnani, M.El, Chehbouni, A., 2013. A new irrigation priority index based on remote sensing data for assessing the networks irrigation scheduling. Agric. Water Manag. 119, 1–9. http://dx.doi.org/10.1016/j.agwat.2012.12.011.

Boulet, G., Chehbouni, A., Gentine, P., Duchemin, B., Ezzahar, J., Hadria, R., 2007. Monitoring water stress using time series of observed to unstressed surface temperature difference. Agric. For. Meteorol. 146, 159–172. http://dx.doi.org/10.1016/j.agrformet.2007.05.012.

Calvet, J.-C., Noilhan, J., Bessemoulin, P., 1998. Retrieving the root-zone soil moisture from surface soil moisture or temperature estimates: a feasibility study based on field measurements. J. Appl. Meteorol. 37, 371–386. http://dx.doi.org/10.1175/1520-0450(1998)037<0371:RTRZSM>2.0.CO;2.

Cammalleri, C., Anderson, M.C., Gao, F., Hain, C.R., Kustas, W.P., 2014. Mapping daily evapotranspiration at field scales over rainfed and irrigated agricultural areas using remote sensing data fusion. Agric. For. Meteorol. 186, 1–11. http://dx.doi.org/10.1016/j.agrformet.2013.11.001.

Chehbouni, A., Escadafal, R., Duchemin, B., Boulet, G., Simonneaux, V., Dedieu, G., Mougenot, B., Khabba, S., Kharrou, H., Maisongrande, P., Merlin, O., Chaponnière, A., Ezzahar, J., Er-Raki, S., Hoedjes, J., Hadria, R., Abourida, A., Cheggour, A., Raibi, F., Boudhar, A., Benhadj, I., Hanich, L., Benkaddour, A., Guemouria, N., Chehbouni, A.H., Lahrouni, A., Olioso, A., Jacob, F., Williams, D.G., Sobrino, J.A., 2008. An integrated modelling and remote sensing approach for hydrological study in arid and semi-arid regions: the SUDMED programme. Int. J. Remote Sens. 29, 5161–5181. http://dx.doi.org/10.1080/01431160802036417.

Crow, W., Kustas, W., Prueger, J., 2008. Monitoring root-zone soil moisture through the assimilation of a thermal remote sensing-based soil moisture proxy into a water balance model. Remote Sens. Environ. 112, 1268–1281. http://dx.doi.org/10.1016/j.rse.2006.11.033.

Dejonge, K.C., Taghvaeian, S., Trout, T.J., Comas, L.H., 2015. Comparison of canopy temperature-based water stress indices for maize. Agric. Water Manag. 156, 51–62. http://dx.doi.org/10.1016/j.agwat.2015.03.023.

Diarra, A., Jarlan, L., Er-Raki, S., Le Page, M., Aouade, G., Tavernier, A., Boulet, G., Ezzahar, J., Merlin, O., Khabba, S., 2017. Performance of the two-source energy budget (TSEB) model for the monitoring of evapotranspiration over irrigated annual crops in North Africa. Agric. Water Manag. 193, 71–88. http://dx.doi.org/10.1016/j.agwat.2017.08.007.

Duchemin, B., Hadria, R., Erraki, S., Boulet, G., Maisongrande, P., Chehbouni, A., Escadafal, R., Ezzahar, J., Hoedjes, J.C.B., Kharrou, M.H., Khabba, S., Mougenot, B., Olioso, A., Rodriguez, J.-C., Simonneaux, V., 2006. Monitoring wheat phenology and irrigation in Central Morocco: on the use of relationships between evapotranspiration, crops coefficients, leaf area index and remotely-sensed vegetation indices. Agric. Water Manag. 79, 1–27. http://dx.doi.org/10.1016/j.agwat.2005.02.013.

Duchemin, B., Hagolle, O., Mougenot, B., Benhadj, I., Hadria, R., Simonneaux, V., Ezzahar, J., Hoedjes, J., Khabba, S., Kharrou, M.H., Boulet, G., Dedieu, G., Er-Raki, S., Escadafal, R., Olioso, A., Chehbouni, A.G., 2008. Agrometeorological study of semi-arid areas: an experiment for analysing the potential of time series of FORMOSAT-2 images (Tensift-Marrakech plain). Int. J. Remote Sens. 29, 5291–5300. http://dx.doi.org/10.1080/01431160802036482.

Er-Raki, S., Chehbouni, A., Guemouria, N., Duchemin, B., Ezzahar, J., Hadria, R., 2007. Combining FAO-56 model and ground-based remote sensing to estimate water consumptions of wheat crops in a semi-arid region. Agric. Water Manag. 87, 41–54. http://dx.doi.org/10.1016/j.agwat.2006.02.004.

Er-Raki, S., Chehbouni, A., Hoedjes, J., Ezzahar, J., Duchemin, B., Jacob, F., 2008. Improvement of FAO-56 method for olive orchards through sequential assimilation of thermal infrared-based estimates of ET. Agric. Water Manag. 95, 309–321. http://dx.doi.org/10.1016/j.agwat.2007.10.013.

Er-Raki, S., Chehbouni, A., Duchemin, B., 2010. Combining satellite remote sensing data with the FAO-56 dual approach for water use mapping in irrigated wheat fields of a semi-arid region. Remote Sens. 2, 375–387. http://dx.doi.org/10.3390/rs2010375.

González-Dugo, M.P., Mateos, L., 2008. Spectral vegetation indices for benchmarking water productivity of irrigated cotton and sugarbeet crops. Agric. Water Manag. 95, 48–58. http://dx.doi.org/10.1016/j.agwat.2007.09.001.

Gutman, G., Ignatov, A., 1998. The derivation of the green vegetation fraction from NOAA / AVHRR. Int. J. Remote Sens. 19, 1533–1543.

Hain, C.R., Mecikalski, J.R., Anderson, M.C., 2009. Retrieval of an available water-based soil moisture proxy from thermal infrared remote sensing. Part I: Methodology and Validation. J. Hydrometeorol. 10, 665–683. http://dx.doi.org/10.1175/2008JHM1024.1.

Hain, C.R., Crow, W.T., Anderson, M.C., Mecikalski, J.R., 2012. An ensemble Kalman filter dual assimilation of thermal infrared and microwave satellite observations of soil moisture into the Noah land surface model. Water Resour. Res. 48. http://dx.doi.org/10.1029/2011WR011268.

Hunsaker, D.J., Pinter, P.J., Kimball, B.A., 2005. Wheat basal crop coefficients determined by normalized difference vegetation index. Irrig. Sci. 24, 1–14. http://dx.doi.org/10.1007/s00271-005-0001-0.

Ihuoma, S.O., Madramootoo, C.A., 2017. Recent advances in crop water stress detection. Comput. Electron. Agric. 141, 267–275. http://dx.doi.org/10.1016/j.compag.2017.07.026.

Jarlan, L., Khabba, S., Er-Raki, S., Le Page, M., Hanich, L., Fakir, Y., Merlin, O., Mangiarotti, S., Gascoin, S., Ezzahar, J., Kharrou, M.H., Berjamy, B., Saaïdi, A., Boudhar, A., Benkaddour, A., Laftouhi, N., Abaoui, J., Tavernier, A., Boulet, G., Simonneaux, V., Driouech, F., El Adnani, M., El Fazziki, A., Amenzou, N., Raibi, F., El Mandour, A., Ibouh, H., Le Dantec, V., Habets, F., Tramblay, Y., Mougenot, B., Leblanc, M., El Faïz, M., Drapeau, L., Coudert, B., Hagolle, O., Filali, N., Belaqziz, S., Marchane, A., Szczypta, C., Toumi, J., Diarra, A., Aouade, G., Hajhouji, Y., Nassah, H., Bigeard, G., Chirouze, J., Boukhari, K., Abourida, A., Richard, B., Fanise, P., Kasbani, M., Chakir, A., Zribi, M., Marah, H., Naimi, A., Mokssit, A., Kerr, Y., Escadafal, R., 2015. Remote sensing of Water resources in semi-arid Mediterranean areas: the joint international laboratory TREMA. Int. J. Remote Sens. 36, 4879–4917. http://dx.doi.org/10.1080/01431161.2015.1093198.

Kalma, J.D., McVicar, T.R., McCabe, M.F., 2008. Estimating land surface evaporation: a review of methods using remotely sensed surface temperature data. Surv. Geophys. 29, 421–469. http://dx.doi.org/10.1007/s10712-008-9037-z.

Kite, G.W., Droogers, P., 2000. Comparing evapotranspiration estimates from satellites, hydrological models and field data. J. Hydrol. 229, 3–18. http://dx.doi.org/10.1016/S0022-1694(99)00195-X.

Kullberg, E.G., DeJonge, K.C., Chávez, J.L., 2016. Evaluation of thermal remote sensing indices to estimate crop evapotranspiration coefficients. Agric. Water Manag. 179, 64–73. http://dx.doi.org/10.1016/j.agwat.2016.07.007.

Li, Z.-L., Tang, R., Wan, Z., Bi, Y., Zhou, C., Tang, B., Yan, G., Zhang, X., 2009. A review of current methodologies for regional evapotranspiration estimation from remotely sensed data. Sensors (Basel). 9, 3801–3853. http://dx.doi.org/10.3390/s90503801.

Li, F., Crow, W.T., Kustas, W.P., 2010. Towards the estimation root-zone soil moisture via the simultaneous assimilation of thermal and microwave soil moisture retrievals. Adv. Water Resour. 33, 201–214. http://dx.doi.org/10.1016/j.advwatres.2009.11.007.

Long, D., Singh, V.P., 2012. A Two-source trapezoid model for evapotranspiration (TTME) from satellite imagery. Remote Sens. Environ. 121, 370–388. http://dx.doi.org/10.1016/j.rse.2012.02.015.

Merlin, O., 2013. An original interpretation of the wet edge of the surface temperature-albedo space to estimate crop evapotranspiration (SEB-1S). Hydrol. Earth Syst. Sci. 17, 3623–3637. http://dx.doi.org/10.5194/hess-17-3623-2013.

Merlin, O., Rüdiger, C., Bitar, A.Al, Richaume, P., Walker, J.P., Kerr, Y.H., 2012.

Disaggregation of SMOS soil moisture in Southeastern Australia. IEEE Trans. Geosci. Remote Sens. 50, 1556–1571.
Merlin, O., Chirouze, J., Olioso, A., Jarlan, L., Chehbouni, G., Boulet, G., 2014. An image-based four-source surface energy balance model to estimate crop evapotranspiration from solar reflectance/thermal emission data (SEB-4S). Agric. For. Meteorol. 184, 188–203. http://dx.doi.org/10.1016/j.agrformet.2013.10.002.
Moran, M.S., Clarke, T.R., Inoue, Y., Vidal, A., 1994. Estimating crop water deficit using the relation between surface-air temperature and spectral vegetation index. Remote Sens. Environ. 49, 246–263.
Olioso, A., Sòria, G., Sobrino, J., Duchemin, B., 2007. Evidence of low land surface thermal infrared emissivity in the presence of dry vegetation. IEEE Geosci. Remote Sens. Lett. 4, 112–116.
Olivera-Guerra, L., Mattar, C., Merlin, O., Durán-Alarcón, C., Santamaría-Artigas, A., Fuster, R., 2017. An operational method for the disaggregation of land surface temperature to estimate actual evapotranspiration in the arid region of Chile. ISPRS J. Photogramm. Remote Sens. 128, 170–181. http://dx.doi.org/10.1016/j.isprsjprs.2017.03.014.
Rafi, Z., Merlin, O., Le Dantec, V., Khabba, S., Mordelet, P., Er-Raki, S., Amazirh, A., Olivera-Guerra, L., Ait Hssaine, B., Simonneaux, V., Ezzahar, J., Ferrer, F., 2018. Partitioning evapotranspiration of drip-irrigated wheat crop: a comparison study of FAO-56 dual crop coefficient model estimates with eddy covariance, sap flow and lysimeter measurements. Agric. For. Meteorol Under review.
Roerink, G.J., Su, Z., Menenti, M., 2000. S-SEBI: a simple remote sensing algorithm to estimate the surface energy balance. Phys. Chem. Earth Part B Hydrol. Ocean. Atmos. 25, 147–157. http://dx.doi.org/10.1016/S1464-1909(99)00128-8.
Sandholt, I., Rasmussen, K., Andersen, J., 2002. A simple interpretation of the surface temperature/vegetation index space for assessment of surface moisture status. Remote Sens. Environ. 79, 213–224. http://dx.doi.org/10.1016/S0034-4257(01)00274-7.
Sobrino, J.A., Jiménez-muñoz, J.C., Sòria, G., Romaguera, M., Guanter, L., Moreno, J., Plaza, A., Martínez, P., 2008. Land surface emissivity retrieval from different VNIR and TIR sensors. IEEE Trans. Geosci. Remote Sens. 46, 316–327.
Stefan, V.G., Merlin, O., Er-Raki, S., Escorihuela, M.J., Khabba, S., 2015. Consistency between In Situ, model-derived and high-resolution-image-based soil temperature endmembers: towards a robust data-based model for multi-resolution monitoring of crop evapotranspiration. Remote Sens. 7, 10444–10479. http://dx.doi.org/10.3390/rs70810444.
Toumi, J., Er-Raki, S., Ezzahar, J., Khabba, S., Jarlan, L., Chehbouni, A., 2016. Performance assessment of aqua crop model for estimating evapotranspiration, soil water content and grain yield of winter wheat in Tensift Al Haouz (Morocco): application to irrigation management. Agric. Water Manag. 163, 219–235. http://dx.doi.org/10.1016/j.agwat.2015.09.007.
Weng, Q., Fu, P., Gao, F., 2014. Generating daily land surface temperature at landsat resolution by fusing landsat and MODIS data. Remote Sens. Environ. 145, 55–67. http://dx.doi.org/10.1016/j.rse.2014.02.003.

Chapter 4. Real-life application of the irrigation retrieval approach

Contents

4.1. Introduction *90*

4.2. Issues for implementing the crop water balance modelling over large areas *91*

4.3. Contextual methods for detecting soil and crop water status *91*

4.4. Landsat-derived estimates integrated into a crop water balance model for irrigation retrieval *93*

4.5. From pixel-scale to field-scale irrigation *95*

4.6. Crop coefficients Kcb and Ke derived from contextual methods *97*

4.7. Main results of the spatial application to Haouz Plain *100*

4.8. Summary and conclusions *105*

4.9. ARTICLE: Irrigation retrieval from Landsat optical/thermal data integrated into a crop water balance model: A case study over winter wheat fields in a semi-arid region *106*

4.1. Introduction

The quantification of irrigation amounts and timing spatially distributed is one of the main issues to be overcome by the water balance model for the monitoring of the water budget components (ET, RZSM) over large areas. Irrigation is the main water supply in semi-arid to arid regions to force the FAO-2Kc model. Therefore, an operational implementation of the FAO-2Kc relies on the availability of irrigation amount and timing at field scale over the irrigated perimeter. This information is rarely available and at the same time it is critical for an efficient management of water resources.

Despite numerous methods that have been developed for estimating the crop water requirements and few others that have focused on the irrigation during the last years, no method is yet available to estimate irrigation at field scale. Some recent studies have demonstrated the potential of SSM estimates derived from remote sensing micro-wave data to quantify irrigation (Brocca et al., 2018, 2017; Escorihuela and Quintana-Seguí, 2016; Jalilvand et al., 2019; Kumar et al., 2015; Lawston et al., 2017b; Malbéteau et al., 2018; Zhang et al., 2018). However, the micro-wave-based methods to estimate SSM face two main issues: i) the very coarse (~40 km) spatial resolution of readily available satellite SSM data is unsuitable for monitoring crop fields, and ii) the sensing depth by micro-wave observations is too shallow (few centimeters) to be representative of the root-zone water storage and to reasonably solve the crop water balance.

This chapter presents an approach that aims to retrieve the irrigation at field scale over extended areas from readily available remote sensing optical/thermal data. This approach allows retrieving the irrigation amounts and timing along the agricultural season in order to estimate the daily RZSM and ET. For this purposes, the method presented in the previous chapter is adapted to be implemented with sparsely remote sensing optical/thermal data. Both Landsat-7 and -8 are combined to provide a revisit frequency of Landsat data up to 8 days when there are clear-sky conditions. The approach is implemented over three agricultural areas of 12 by 12 km in the semi-arid region of central Morocco. The approach is evaluated over five experimental sites covered by winter wheat during four growing seasons and under different irrigation systems (drip, flood and no-irrigation). One of the sites is not irrigated and is used as benchmark during four seasons. The validation is carried out in terms of irrigation amounts and dates as well as in terms of daily ET and RZSM. The proposed algorithm is also benchmarked with the standard non-stressed FAO-2Kc as well as the FAO-2Kc forced by actual irrigations (measured using flow meters).

4.2. Issues for implementing the crop water balance modelling over large areas

Given that the approach presented in the previous chapter was implemented with ground-based observations, three major issues must be addressed in order to apply the algorithm to remote sensing data from readily available LST observations. First, a contextual approach should be implemented from Landsat data to partition the LST into soil and canopy temperatures in order to detect the soil and crop water status, respectively. Results of the contextual method allow estimating a Landsat-derived crop stress coefficient (Ks) over large scales. Second, the estimation of daily RZSM from sparsely available Landsat data is not straightforward as it involves a greater complexity. That implies that the Landsat-derived Ks should be integrated into a crop water balance model in a pixel-by-pixel scheme in order to provide the RZSM temporal dynamics along the season. Third, the pixel-scale irrigation estimates can be aggregated to the crop field scale since irrigation is usually applied within a single day over the entire crop field.

In addition to the spatially distributed irrigation, the implementation of the FAO-2Kc at regional scale faces the issue that calibration is required in order to obtain accurate estimations. For instance, the use of EC measurements for calibration of crop-basal coefficient (Kcb) is a strong limitation for application of FAO-2Kc model to large areas.

In order to overcome the main issues exposed above for the implementation at large scales, the next sections present: i) crop water status from a contextual method, ii) the integration of Landsat-derived estimates into a crop water balance model, iii) the aggregation of pixel-scale irrigation to the crop field-scale, and iv) crop coefficients derived from a contextual method.

4.3. Contextual methods for detecting soil and crop water status

In the previous chapter, the conditions for applying a contextual method with ground-based data was to simulate temperature endmembers every day by a surface energy balance. From Landsat-7/8 data, a contextual method can be applied directly from every Landsat overpass in order to partition the LST and to derive the Ks and Kr following the Eq. 3.11 and Eq. 3.12, respectively.

The LST partitioning method is based on the LST-fv feature space as in several works (e.g. Long and Singh, 2012; Merlin et al., 2014; Sandholt et al., 2002), with the difference that the assumptions of the Two-source Surface Energy Balance (TSEB) formalisms (Norman et al., 1995) are adopted. The TSEB model assumes that the soil surface layer is fully

depleted before the vegetation stress begins; meaning that the water availability in the root zone decreases below SM_{crit} once the SSM reaches its minimal value (half the SM_{wp} according to the FAO-2Kc).

The main steps to partition the LST from the contextual method are described below. First, the LST-fv feature space is used to estimate the temperature endmembers (Tv_{min}, Tv_{max}, Ts_{min} and Tv_{max}) from the polygon constrained by a "wet edge" (defined as the line between Ts_{min} and Tv_{min}) and a "dry edge" (defined as the line between Ts_{max} and Tv_{max}). The "wet edge" and "dry edge" are determined from the linear regressions of the minimal and maximal LST, respectively, which are selected by *fv* classes with an interval of 0.01 (see Fig. 4.1.a). In such a way, the temperature endmembers can be determined only from the contextual information of LST-fv space. Second, the TSEB assumption solves the vegetation and soil fluxes components using an iterative procedure, where LST is partitioned into Ts and Tv by decomposing linearly the LST (Eq. 3.10). The procedure is initialized with a transpiration rate to its maximum value (potential transpiration), meaning that Tv is equal to Tv_{min}. The TSEB assumes that both flux components are positives, hence if soil evaporation is negative, the soil is likely dry so evaporation is set to zero ($Ts=Ts_{max}$) and a new transpiration value is calculated together with a new Tv from the Eq. 3.10 ($Tv>Tv_{min}$). Therefore, the TSEB assumption in the LST-fv feature space (see Fig. 4.1.b) makes Tv equal to Tv_{min} for every Ts below Ts_{max}, while Ts remains equal to Ts_{max} when Tv is larger than Tv_{min}. Consequently, two zones can be distinguished in the LST-fv space divided by the diagonal Ts_{max}-Tv_{min} of the polygon as is depicted in the Fig. 4.1.b. Below the diagonal corresponds to a well-watered/unstressed vegetation zone with maximum transpiration rate ($Tv=Tv_{min}$), while above the diagonal corresponds to a stressed vegetation and a fully dried surface top layer ($Ts=Ts_{max}$).

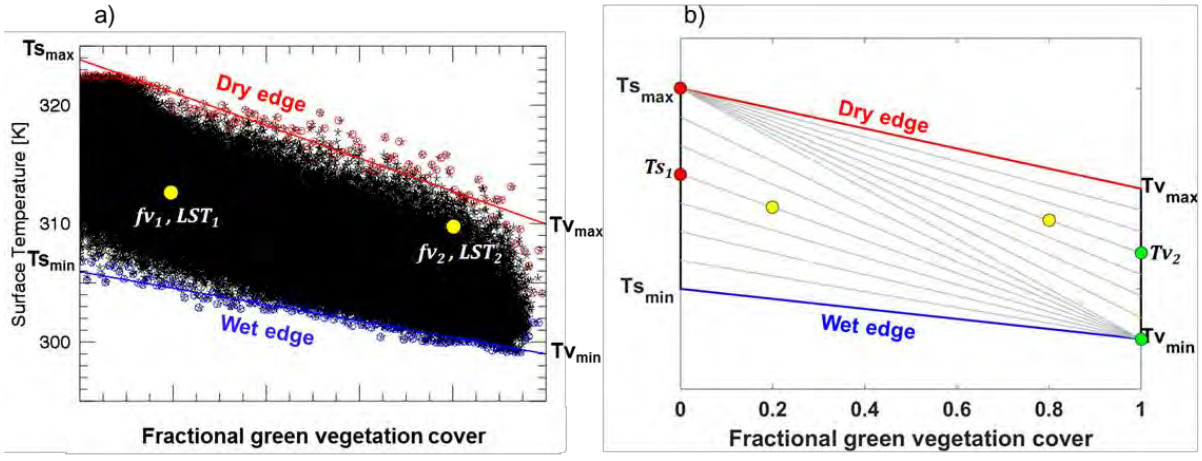


Fig. 4.1. In the right plot, an example of LST-fv feature space constrained by the polygon Ts_{min}-Tv_{min}-Tv_{max}-Ts_{max} from the linear regression of the minimum (blue circles) and maximum (red circles) LST by fv classes. A conceptual diagram (left plot) of the LST-fv polygon to partition LST for two pixels (fv,LST) (yellow points) showing its

corresponding Ts (red points, right plot) and Tv (green points, right plot) values following the TSEB assumptions.

Once the LST is partitioned into Tv and Ts, a Landsat-derived Ks and Kr can be estimated from the Eq. 3.11 and Eq. 3.12, as is proposed in the previous chapter. Ks corresponds basically to the normalization of Tv using minimum (Tv_{min}) and maximum (Tv_{max}) Tv values, while Kr is the normalization of Ts with regard to Ts_{min} and Ts_{max}. Finally, a Landsat-derived RZSM can be estimated from the Ks according to Eq. 3.14. Note that in the article in Section 4.9, Eq. 3.14 is expressed in terms of SM_{crit}, which is estimated from the fraction p (crop tolerance to the stress), and the soil parameters SM_{wp} and SM_{fc}.

4.4. Landsat-derived estimates integrated into a crop water balance model for irrigation retrieval

The approach to determine the irrigation consists basically in detecting the irrigation events and then estimating the amounts by the difference of RZSM. Therefore the RZSM dynamics is needed for all the agricultural season. As it was shown in the previous section, the FAO-2Kc model is used to translate thermal observations into RZSM diagnostic estimates and to propagate the RZSM information along the season. Unlike in Chapter 3 where ground-based optical/thermal data are available every day, in this chapter, the implementation of a crop water balance model basically based on FAO-2Kc is adapted to the temporal resolution of Landsat (8 to 16 days). For this purpose, the FAO-based model is initialized by Landsat-derived RZSM diagnostic estimates and then is run in recursive and/or forward mode between Landsat overpass dates, as is described below. That is carried out in order to estimate the RZSM dynamics used to detect irrigation date. Then the (daily) irrigation amount is estimated as a difference between the RZSM estimated on the irrigation date and the RZSM estimated on the day before as follows:

$$I_i = 1000(RZSM_i - RZSM_{i-1})Zr_i \qquad \text{Eq. 4.1}$$

where I_i is the irrigation amount (mm) on the irrigation date *i*, RZSM (m^3/m^3) is estimated on the irrigation day *i* ($RZSM_i$) and on the day before *i-1* ($RZSM_{i-1}$) and Zr_i is the effective root zone depth (m), which is used in the factor $1000Zr_i$ to convert the RZSM unit (m^3/m^3) to irrigation depth (mm).

In the Eq. 4.1, $RZSM_i$ is estimated from a daily crop water balance in a recursive mode (hereby referred to as RWB) by initializing it at date j (j > i) from a Landsat-derived RZSM ($RZSM_{landsat,j}$). In RWB, the water balance is applied backward at daily scale for every period between two (clear sky) successive Landsat overpass dates (j and *j-Pj,* with *Pj*

being the number of days between both successive Landsat dates) by starting from the last Landsat overpass date of the season to its previous date. Overall, an irrigation event is detected when the simulated $RZSM_{RWB,t}$ (for t=j-1,…,j-Pj) reaches SM_{fc}. However, four different cases need to be considered depending on the value of Landsat-derived Ks (and consequently $RZSM_{landsat,j}$) at date j-Pj. In addition, it may be needed the daily crop water balance in a forward mode (hereby referred to as FWB) by initializing it at date j-Pj (j < i) from $RZSM_{landsat,j-Pj}$. For clarity, each case is illustrated in Fig. 4.2 showing the water balance run in forward or recursive method. Here, the RZSM is estimated from the RWB (right dotted arrow) or the FBW (left dotted arrow) initialized by the $RZSM_{Landsat}$ at date *j* and *j-Pj*, respectively. An irrigation event is detected when $RZSM_{RWB}$ reaches SM_{fc} and its amount is estimated by the difference between the RZSM retrieved at date *i* and *i-1*.

During unstressed periods (Ks=1) the thermal data are not able to detect the variation of soil moisture between SM_{crit} and SM_{fc}, meaning that $RZSM_{Landsat,j-Pj}$ is kept constant to SM_{crit} when $Ks_{Landsat,j-Pj}$ is equal to 1. In this case, $RZSM_{Landsat,j-Pj}$ is updated by $RZSM_{RWB,j-Pj}$ when it is larger than SM_{crit}, as illustrated in Fig. 4.2 c) and d). The updated RZSM at j-Pj is then used to reinitialize the previous period (from date *j-Pj* to its previous Landsat overpass date). It should be noted that in cases c) and d) illustrated in Fig. 4.2, more than one irrigation event can be detected between two successive Landsat overpasses when $RZSM_{RWB}$ reaches SM_{fc} more than once in this period. In the computation of crop water balance based on FAO-2Kc, the capillarity rise and runoff are neglected due to flat surfaces and a water table significantly deep (>30 m) in the study area (Duchemin et al, 2006). The main components of the water balance actually are the ET and irrigation/precipitations. Precipitation is provided by meteorological stations while ET is estimated from the FAO-2Kc formalism. The basal crop coefficient (Kcb) and evaporation coefficient (Ke) are estimated from a generic expression from the daily *fv* interpolated from Landsat data. The generic expression for Kcb and Ke are analytically derived from contextual method as described in Section 4.6. While the Ks and Kr are computed from the crop water balance according to FAO-2Kc, initialized from the Landsat-derived estimates.

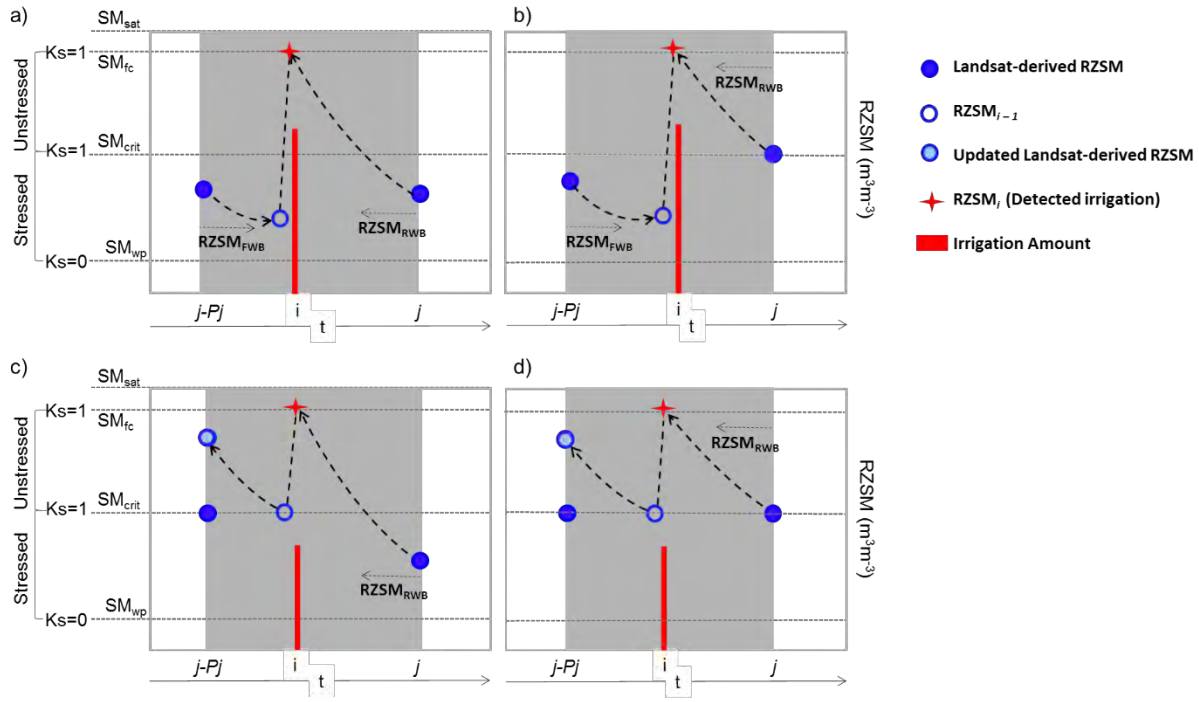


Fig. 4.2. Schematic representation of pixel-scale irrigation retrieval between two successive Landsat overpass dates in four different cases: stressed-stressed (a), stressed-unstressed (b), unstressed-stressed (c) and unstressed-unstressed (d).

4.5. From pixel-scale to field-scale irrigation

The irrigation retrieval at pixel-scale from the RZSM derived pixel-by-pixel is implemented regardless of its neighboring pixels. Consequently, the irrigation at pixel-scale within a given field crop might differ in its predicted dates and volumes. Given that irrigation is usually applied on the same day over the entire field crop we propose a procedure of aggregation to provide irrigation (dates and amounts) at crop field scale from the statistical distribution of pixel-scale irrigations within the given field crop.

The aggregation procedure involves three steps as illustrated in Fig. 4.3 for clarity. First, for each period P_j between two successive satellite overpasses, the number of irrigations within a given crop field ($N_{Ifield,Pj}$) is estimated as the total number of irrigations at pixel-scale divided by the number of pixels contained in the crop field (N_{pixel}). Then, the daily amounts of irrigation at pixel-scale are averaged within the crop field (I_i). The daily fraction of irrigated pixels (f_i) is also estimated as the number of pixels where irrigation is detected divided by N_{pixel}. Finally, the irrigation volume applied over the crop field (I_{field}) is estimated by integrating the amounts of irrigation in the $N_{Ifield,Pj}$ sub-periods of period P_j, as well as the most probable date ($Date_{Ifield}$) of the irrigation event within each sub-period is estimated as:

$$I_{field} = \frac{\int_{ini}^{end} I_i f_i d_i}{\int_{ini}^{end} f_i d_i} \qquad \text{Eq. 4.2}$$

$$Date_{Ifield} = \frac{\int_{ini}^{end} i\, I_i f_i d_i}{\int_{ini}^{end} I_i f_i d_i} \qquad \text{Eq. 4.3}$$

where I_i is the averaged irrigation within the crop field on the day i and f_i is its frequency (number of pixels where an irrigation is detected divided the total pixels of the field crop). The limits of integration *ini* and *end* are set to the first day before and the last day after the peak with f_i is equal to zero, respectively, when irrigation is not detected in any pixel of the field.

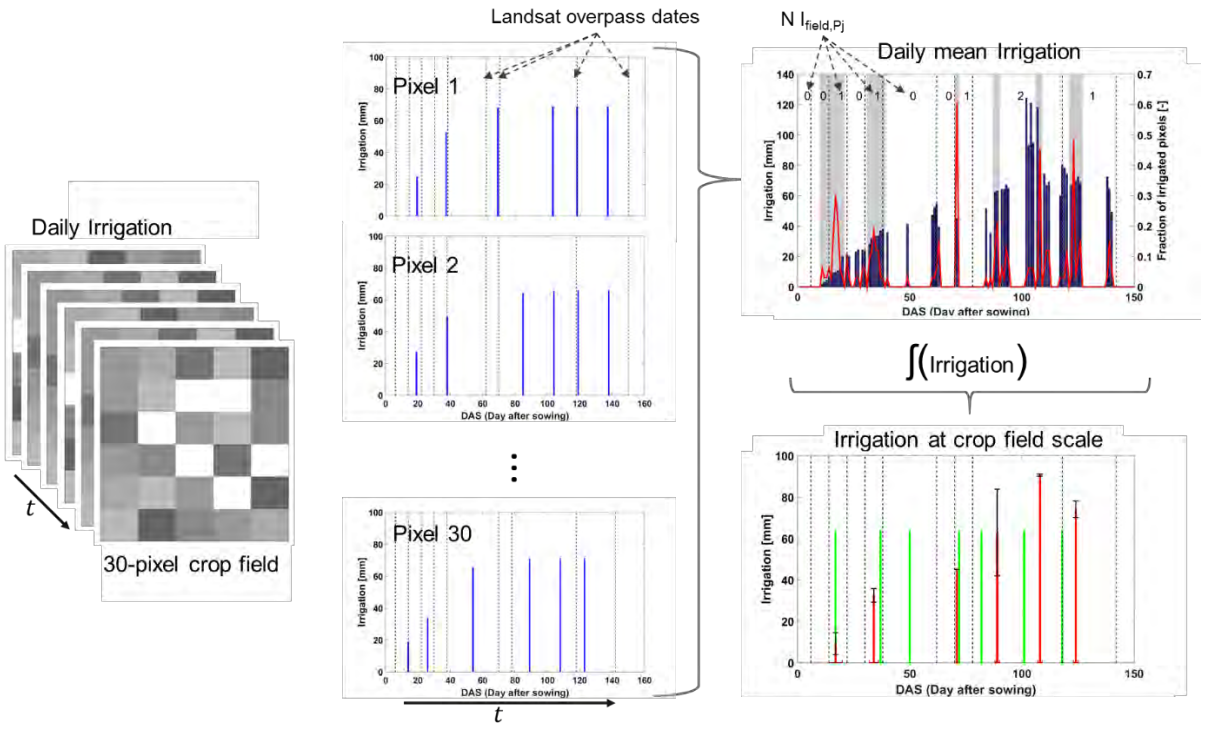


Fig. 4.3. Schematic diagram presenting the plot-scale irrigation retrieval from pixel-scale irrigation for an example of a 30-pixel field crop.

In the Fig. 4.3, the daily pixel-scale irrigation within the crop field (left) is represented along the season for every pixel (middle plots).The daily irrigation of all pixels within the field crop are daily averaged (blue bar in top right plot) and its fraction of irrigated pixels is also estimated (red line in top right plot). The daily mean irrigations are integrated according to its fractional irrigated pixels to obtain the plot-scale irrigation (red bar in bottom right plot) with its standard deviation for amounts (black error bar) and days (red error bar). In this example, the actual irrigation (green bar) is showed as reference as well as the Landsat overpass dates available (vertical dotted line). Note that in the schematic diagram is represented the case when two irrigation events at pixel scale are

detected between two successive Landsat overpasses (around DAS 100), which can be detected by the case c) and d) in Fig. 4.2. These two irrigation events are then aggregated at crop field scale by taking into account the two sub-periods of integration around the two picks in f_i for the corresponding period P_j.

4.6. Crop coefficients Kcb and Ke derived from contextual methods

The contextual model has been extensively implemented with one-source surface energy balance models, meaning that the ET is estimated as a whole without distinguishing between soil evaporation and plant transpiration. Instead, the FAO-2Kc works like a two-source model that estimates separately the soil evaporation and plant transpiration. In order to take advantage of satellite data for generic implementations, we link the FAO-2Kc formalism with a contextual model to derive the main coefficients for transpiration (Kcb) and evaporation (Ke). In practice, we use the Operational Simplified Surface Energy Balance formalism (SSEBop, Senay et al., 2013) as contextual model given that it presents some points of comparison with the FAO-56 model: the actual ET is based on reference evapotranspiration (ET_0) scaled by a coefficient to represent the maximum ET reached by a certain crop (Kc_{max}). The ET formalism is expressed as follows:

$$ET = EF \cdot Kc_{max} \cdot ET_0 \qquad \text{Eq. 4.4}$$

Here, Kc_{max} is modulated by the evaporative fraction EF as a single crop coefficient containing the transpiration and evaporation coefficients. EF is estimated as follows:

$$EF = \frac{LST_{max} - LST}{LST_{max} - LST_{min}} \qquad \text{Eq. 4.5}$$

where LST_{min} and LST_{max} are the minimum and maximum LST representing the wet/unstressed and dry/stressed conditions (see Fig. 4.1), respectively. It should be noted that EF in the original SSEBop is estimated pixel-by-pixel, meaning that the boundary conditions of LST_{min} and LST_{max} are not estimated from the contextual information contained in remote sensed optical/thermal data. However, the expression in Eq. 4.5 is the same as that used in several contextual methods where EF is retrieved from the LST – fv and/or LST – albedo spaces (e.g. Roerink et al., 2000; Merlin et al., 2013; Merlin et al., 2014). Therefore, we considered the EF obtained from contextual method in SSEBop model, to be made equal to FAO-2Kc as:

$$(Ks \cdot Kcb + Ke)ET_0 = ET = EF \cdot Kc_{max} \cdot ET_0 \qquad \text{Eq. 4.6}$$

In the FAO-2Kc model (on the left-hand side of the equation), the transpiration component (Kcb ET_0) is controlled by the Ks and the evaporation (Ke ET_0) is controlled

by the Kr. While in SSEBop (on the right-hand side of the equation), the ET is controlled by the Kc_{max} and EF as a single crop coefficient containing the transpiration and evaporation coefficients. By simplifying the Eq. 4.6 by ET_0, the crop coefficient can be expressed as:

$$(Ks \cdot Kcb + Ke) = EF \cdot Kc_{max} \quad \text{Eq. 4.7}$$

As EF is obtained from Eq. 4.5, in this thesis Kr (contained in Ke) and Ks are estimated from thermal and fv once LST has been partitioned according to Eq. 3.11 and Eq. 3.12, respectively. Thus, every term used in Eq. 4.5 is partitioned into its vegetation and soil components in such a way that Ke and Kcb formulations can be analytically derived from the equality in Eq. 4.7. LST_{min} and LST_{max} are linearly partitioned as:

$$LST_{max} = fvTv_{max} + (1 - fv)Ts_{max} \quad \text{Eq. 4.8}$$

$$LST_{min} = fvTv_{min} + (1 - fv)Ts_{min} \quad \text{Eq. 4.9}$$

Then by inserting the equations above in Eq. 4.5, EF can be expressed as:

$$EF = \frac{[fvTv_{max} + (1 - fv)Ts_{max}] - [fvTv + (1 - fv)Ts]}{[fvTv_{max} + (1 - fv)Ts_{max}] - [fvTv_{min} + (1 - fv)Ts_{min}]} \quad \text{Eq. 4.10}$$

And by re-arranging the equation:

$$EF = \frac{fv(Tv_{max} - Tv) + (1 - fv)(Ts_{max} - Ts)}{fv(Tv_{max} - Tv_{min}) + (1 - fv)(Ts_{max} - Ts_{min})} \quad \text{Eq. 4.11}$$

The differences (Tv_{max} – Tv) and (Ts_{max} – Ts) can be expressed as function of the thermal-derived Ks and Kr, respectively, and the Eq. 4.11 can be rewritten as:

$$EF = \frac{fv(Tv_{max} - Tv_{min})Ks + (1 - fv)(Ts_{max} - Ts_{min})Kr}{fv(Tv_{max} - Tv_{min}) + (1 - fv)(Ts_{max} - Ts_{min})} \quad \text{Eq. 4.12}$$

For clarity we set $\Delta Tv = Tv_{max} - Tv_{min}$ and $\Delta Ts = Ts_{max} - Ts_{min}$ in Eq. 4.12. By inserting Eq. 4.12 into the right-side of Eq. 4.7, we obtain:

$$EF \cdot Kc_{max} = \frac{fv(\Delta Tv)Ks + (1 - fv)(\Delta Ts)Kr}{fv(\Delta Tv) + (1 - fv)(\Delta Ts)} \cdot Kc_{max} \quad \text{Eq. 4.13}$$

Then by re-arranging the equation, two terms related to the vegetation and soil components are highlighted, as it is shown on the left-side of Eq. 4.7:

$$(Ks \cdot Kcb + Ke) = \left[\frac{fv(\Delta Tv)Ks}{fv(\Delta Tv) + (1-fv)(\Delta Ts)} Kc_{max} + \frac{(1-fv)(\Delta Ts)Kr}{fv(\Delta Tv) + (1-fv)(\Delta Ts)} Kc_{max}\right] \quad \text{Eq. 4.14}$$

where the first term in parentheses can be considered as the transpiration coefficient (Ks Kcb) and the second as Ke, as they are depicted in the FAO-2Kc formalism (Eq. 4.6). To simplify Kcb and Ke formulations, ΔTv is assumed close to ΔTs in A.8 as was used in previous chapter as well as in Stefan et al. (2015). Hence the following simple expressions are derived, which can be implemented from remote sensing data only:

$$Kcb = fvKc_{max} \quad \text{Eq. 4.15}$$

$$Ke = (1-fv)KrKc_{max} \quad \text{Eq. 4.16}$$

where Kcb depends on fv while Ke depends on the soil fraction (1 – fv) weighted by Kr and Kc_{max}. These expressions are consistent with the FAO-2Kc calibrated with vegetation index proposed in the literature (e.g. Er-Raki et al., 2010; Kullberg et al., 2016; Simonneaux et al., 2008). In this study, Kc_{max} is set to 1.2 as a typical recommended value (Allen et al., 2011; Senay et al., 2013; Senay et al., 2016).

The generic coefficients Kcb and Ke were evaluated over the winter wheat field R3-4ha during the 2002-2003 growing season and compared against the Kcb formulations from in-situ calibration that were used as comparison in the previous chapter. The Fig. 4.4 shows the validation of the FAO-2Kc applied with the generic Kcb and Ke, which obtains a good performance very close to that obtained by the FAO-2Kc locally calibrated. The RMSE is equal to 0.63 mm/d, the R^2 is equal to 0.81 and the slope of the linear regression is equal to 1.01. With regard to the other FAO-2Kc versions, only the bias is slightly worsened (equal to -0.31 mm/d) while the other statistical parameters are very close or even improved.

The validation demonstrates the applicability of the generic Kcb and Ke with remote sensing data over extended areas, although it is only validated over winter wheat. A comprehensive validation over other crop types should be carried out in order to demonstrate the reliability of these derived coefficients. However, the generic Kcb and Ke were derived analytically from the link with the SSEBop formalism, which has been validated over several land covers in addition to crops (Chen et al., 2016; Senay et al., 2016, 2014, 2013b; Singh et al., 2014; Velpuri et al., 2013). That might mean that the generic coefficients Kcb and Ke are suitable for the land cover where the SSEBop has obtained good performances. Although generic Kcb and Ke are not calibrated, only one parameter (Kc_{max}) should be calibrated over other crop types if the generic coefficients do not obtain good performances. Moreover, the calibration should be reduced only to

one parameter (Kc_{max}) and no longer to a value of Kcb for every stage of the growing season as well as the length of the every stage.

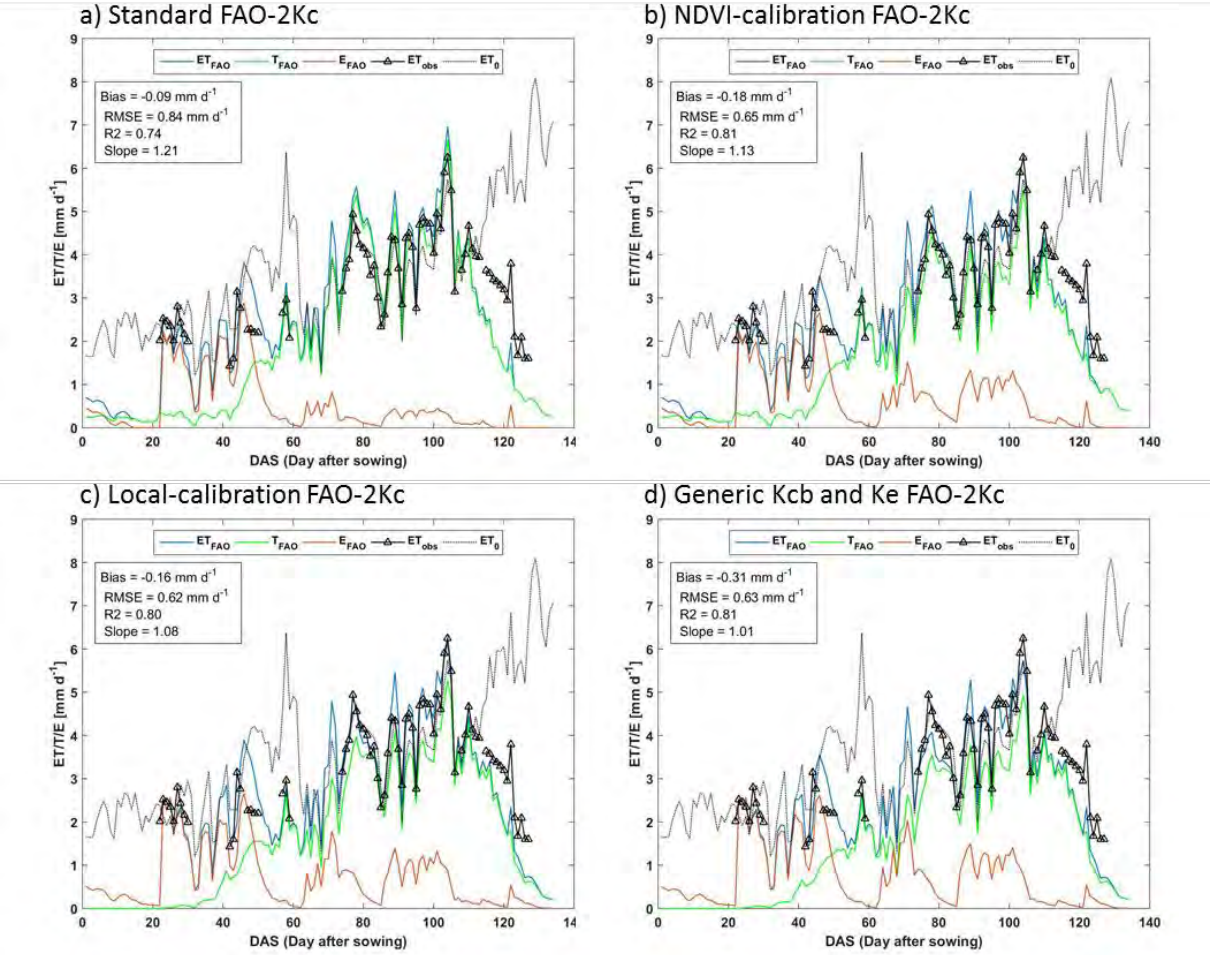


Fig. 4.4. Comparison of evapotranspiration (ET), transpiration (T) and evaporation (E) temporal series over the R3-4ha site (winter wheat field) for the 2002-2003 season estimated from the a) standard, b) NDVI-calibration, c) Local-calibration and d) generic Kcb and Ke FAO-2Kc. The ground-based ET (ET_{obs}) and ET_0 are depicted for reference. The validation of ET from every method against ET_{obs} is shown by means of bias, RMSE, R^2 and slope of the linear regression.

4.7. Main results of the spatial application to Haouz Plain

The approach for irrigation retrieval is implemented over three agricultural areas of 12 by 12 km in the Haouz Plain in central Morocco. The forcing meteorological variables for

the approach are provided by the automated stations installed in each area. The approach is validated over: two drip-irrigated fields in Chichaoua area, two (1 flood- and 1 drip-irrigated) fields in R3 area and one rainfed field in Sidi-Rahal area.

In this section is presented the main results of the work available in the article in Section 4.9 as well as detailed and complementary results over the R3 area where drip- and flood-irrigated winter wheat fields are available. Before implementing the approach, a land use map is used to extract wheat fields and bare soil. The bare soil is also used as benchmark, as was validated in the Bour site during the 2015-2016 season in Sidi Rahal area. The Fig. 4.5 shows the spatial distribution of daily ET on five selected dates every 30 days. The five images depict the temporal dynamics during the different growing stages. The image on January 10 during the initial stage shows low ET rates proper of colder days in winter when most of the fields are under bare soil conditions or low fractional vegetation cover. The image on February 9 during the development stage illustrates that the ET increases over some parcels where an effective full cover is reached, while ET is kept low over non-cultivated parcels or where the sowing date was later. The images on March 10 and April 9 during the beginning and ending of the mid-season, respectively, show higher ET rates mainly due to the atmospheric demand. The image on May 9 during the late stage shows that ET rates decrease with the beginning of the senescence period.

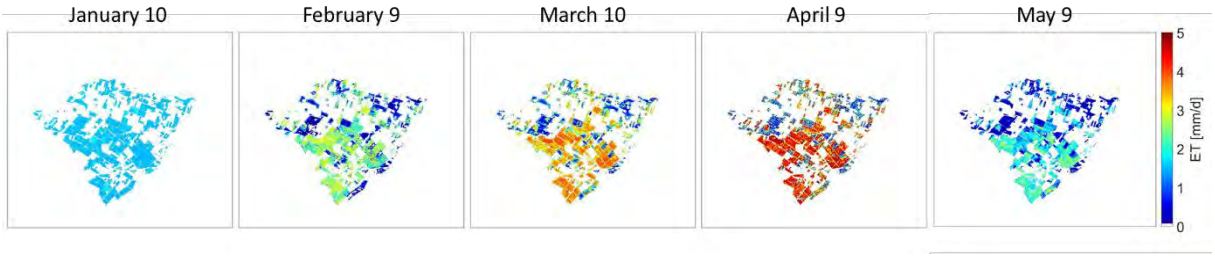


Fig. 4.5. Spatial distribution of daily ET showing the temporal dynamics on five selected dates along the 2016 growing season over R3 area.

The Fig. 4.6 shows the temporal series of ET, the partition into plant transpiration and soil evaporation compared against ground-based ET (ET_{obs}) over the R3-4ha (flood-irrigated) and R3-2ha (drip-irrigated) sites. The validation shows that the ET is estimated with a RMSE of 0.88 (RRMSE of 26.9%) and 0.78 (RRMSE of 31.5%) mm/d and a correlation coefficient of 0.88 and 0.72 for the R3-4ha and R3-2ha sites, respectively. The comparison against the ET estimated from the FAO-2Kc forced by actual irrigations (FAO-2Kc_{Iobs}) shows that the accuracy is close to that estimated by using retrieved irrigations. While the relative RMSE (RRMSE) in the ET from FAO-2Kc_{Iobs} is almost equal in both sites (RRMSE~26%), some differences are depicted in the errors from FAO-2$Kc_{Landsat}$ in the sites. While in R3-4ha the errors from FAO-2$Kc_{Landsat}$ are kept almost constants with regard to FAO-2Kc_{Iobs} in terms of RMSE and R^2, in R3-2ha the errors are slightly worsened with a RRMSE increasing from 25.6% to 31.5% and a R^2 dropping from 0.85 to 0.72. These differences can be partially explained by the irrigation techniques, obtaining better performance over the flood irrigated field (R3-4ha).

In the R3-4ha field, the ET from either FAO-2Kc$_{Iobs}$ or FAO-2Kc$_{Landsat}$ is underestimated with a bias of -0.61 mm/d and -0.55 mm/d, respectively. This underestimation might come from an overestimation in ET$_{obs}$ when the Bowen correction is applied since the ratio between ET$_{obs}$ and ET$_0$ would suppose a Kc above 1.3, which is too high for the study area (Duchemin et al., 2006; Er-Raki et al., 2007; Le Page et al., 2014). Instead, the validation against the ET$_{obs}$ without applying the Bowen correction (Fig. 4.7) would lead to a bias equal to 0.05 and 0.11 mm/d from FAO-2Kc$_{Iobs}$ and FAO-2Kc$_{Landsat}$, respectively, while the accuracy would be increased with a RMSE equal to 0.58 and 0.55 mm/d keeping the R^2 almost constant for both FAO-2Kc$_{Iobs}$ and FAO-2Kc$_{Landsat}$, respectively.

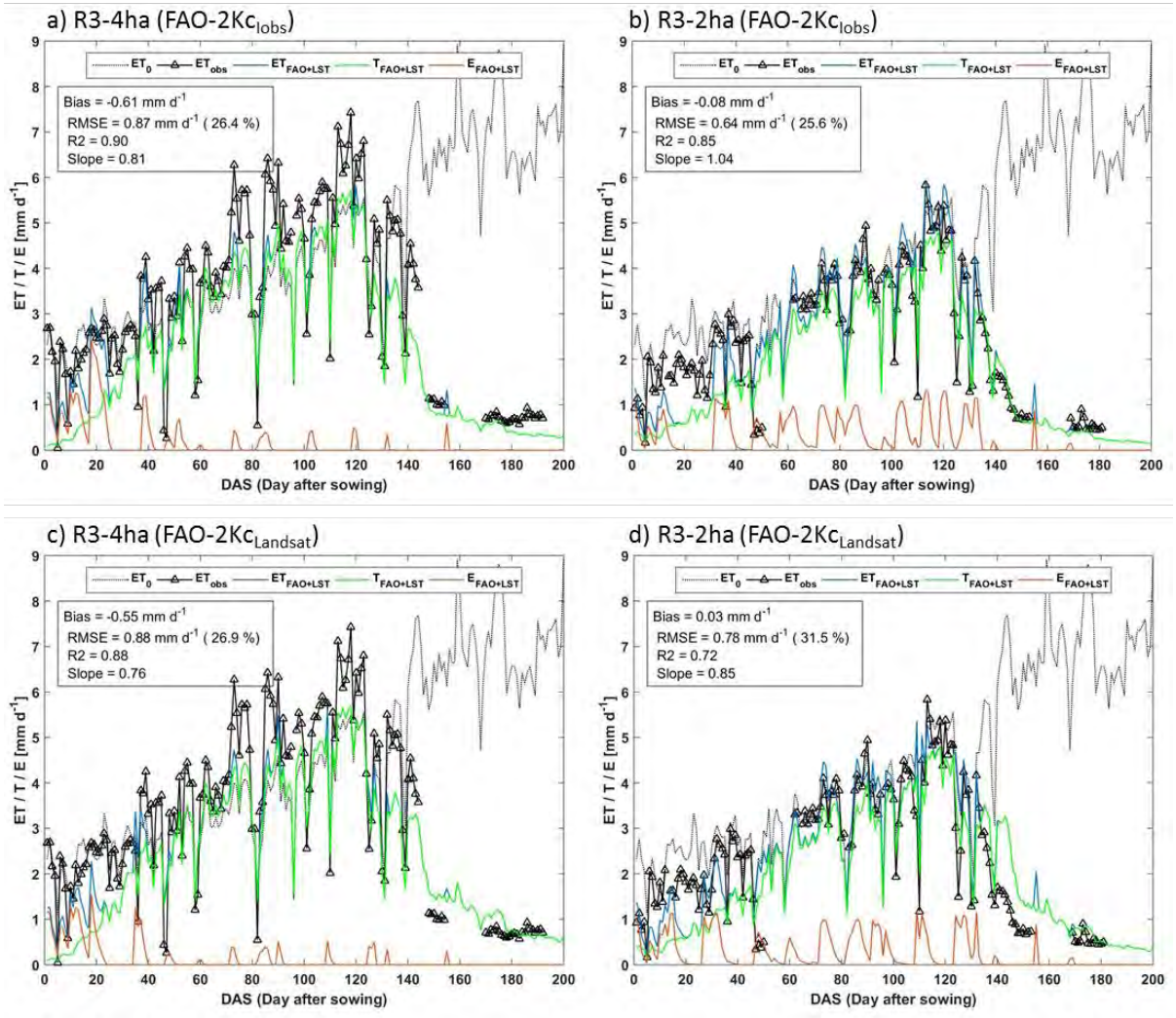


Fig. 4.6. Temporal series of ET and its partition into transpiration (T) and evaporation (E) forced by the actual irrigations (FAO-2Kc$_{Iobs}$ in top plots) and retrieved irrigations (FAO-2Kc$_{Landsat}$ in bottom plots) over the R3-4ha (left plots) and R3-2ha winter wheat field (right plots) along the 2016 growing season. Observed ET (ET$_{obs}$) and ET$_0$ are shown as reference.

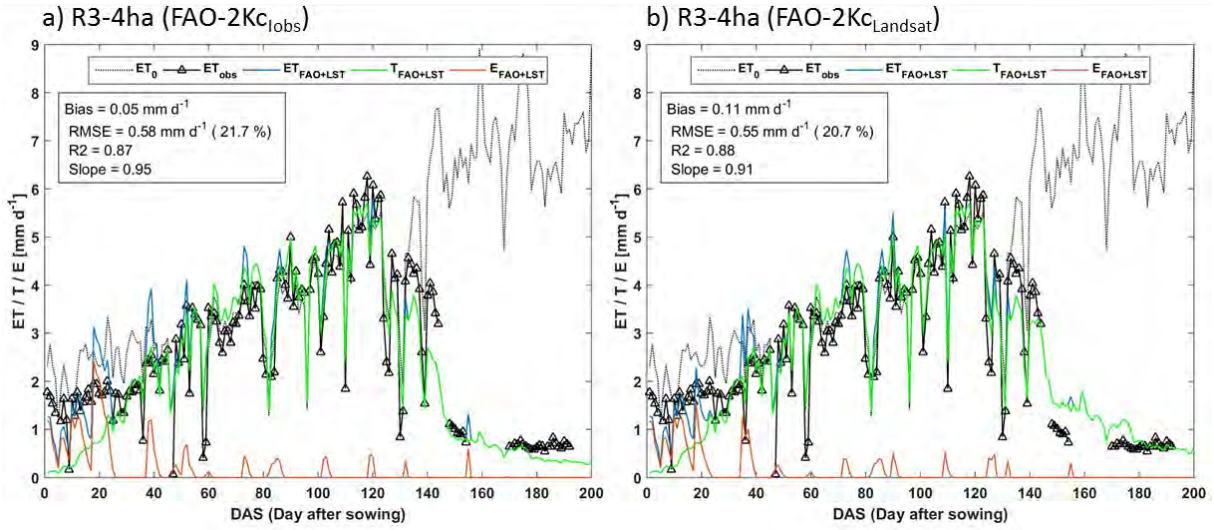


Fig. 4.7. Comparison of ET forced by the actual irrigations (FAO-2Kc$_{Iobs}$) and retrieved irrigations (FAO-2Kc$_{Landsat}$) against the observed ET without applying the Bowen correction (ET$_{obs}$) over the R3-4ha site along the 2016 growing season.

The Fig. 4.8 shows the cumulated monthly ET throughout the growing season. The minimum ET rates are cumulated during the initial stages when most of the fields have low vegetation cover, while maximum ET rates are cumulated during the mid-season when the crops are completely developed.

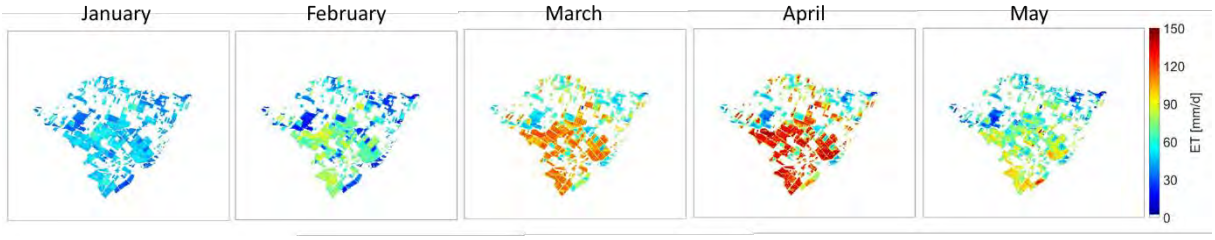


Fig. 4.8. Spatial distribution of monthly ET from January to May 2016 along the growing season over R3 area.

The Fig. 4.9 shows the spatial distribution of daily RZSM on the same five selected dates as in Fig. 4.5. The five images depict the temporal dynamics during the different growing stages. The image on January 10 shows that RZSM is close to the SM$_{fc}$ over all the area because the day before there was an important precipitation of 10 mm sufficient to fulfill the water storage capacity of the initial stage. It should be noted that during the initial stage the root-zone is set to a minimum value equal to 10 cm, meaning that the water storage capacity is fully filled up with 15 mm considering a SM$_{wp}$ and SM$_{fc}$ equal to 0.17 and 0.32 m^3/ m^3, respectively. The images on the other dates show the spatial variability in RZSM without significant precipitation during the previous days.

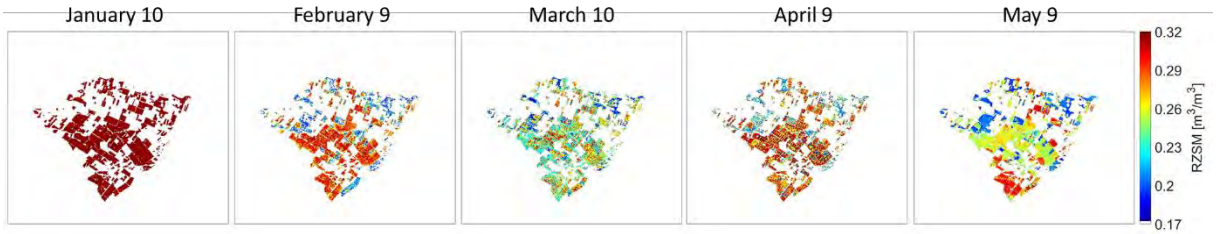


Fig. 4.9. Spatial distribution of daily RZSM showing the temporal dynamics on five selected dates along the 2016 growing season over R3 area.

From the daily and spatially distributed RZSM, as is shown in the Fig. 4.9 for five selected dates, the daily irrigation is retrieved at pixel-scale over the agricultural area. To evaluate the performance of the irrigation retrieval method over a range of time periods, the daily estimated and observed irrigations are cumulated from 1 to 90 days, whose results are shown in the article of the Section 4.9. The Fig. 4.10 shows the spatial distribution of the irrigation cumulated over 15 days. The images on the first 15-day periods (January 1 and 16) show low irrigation amounts estimated during initial stages mainly due to the fact that the root-zone is too small and this approach estimates the effective irrigation without taking into account the water lost by deep percolation. The periods beginning on March 31 and April 15 show the highest irrigation amounts, corresponding to the maximum water requirements of crops typical of mid-season stages. Finally in the senescent periods the water requirements are diminished and the irrigation amounts are minimal as is shown on the image of May 15. That can be also observed in the cumulated monthly irrigation in the Fig. 4.11.

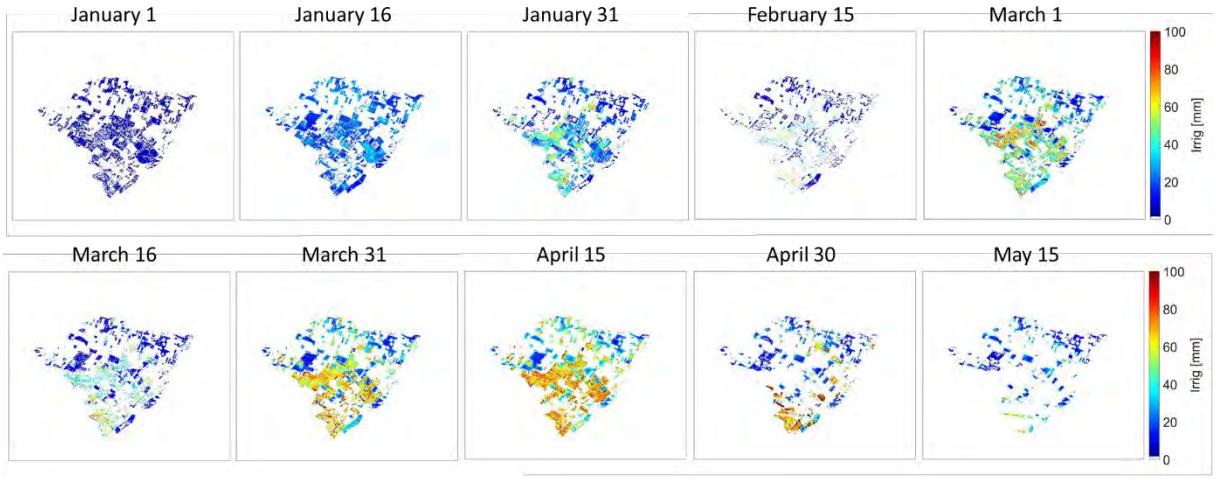


Fig. 4.10. Spatial distribution of cumulated irrigation over 15 days along the 2016 growing season over R3 area. The dates indicate the first day of the 15-days period.

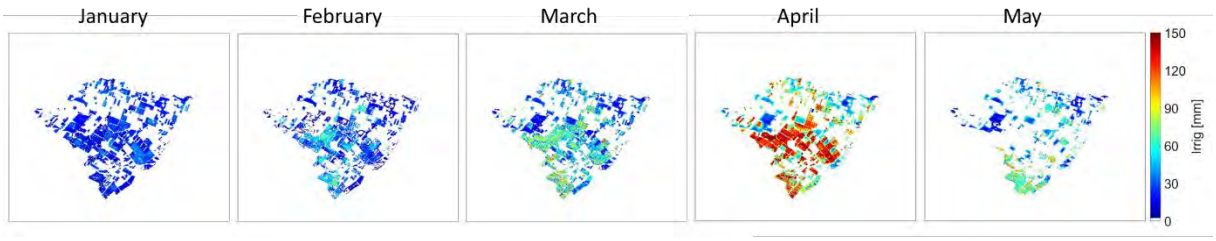


Fig. 4.11. Spatial distribution of monthly irrigation from January to May 2016 along the growing season over R3 area.

Finally, the total (seasonal) irrigation amount spatilly distributed is depicted in the Fig. 4.12. It is observed that the irrigation is estimated between 200 and 300 mm over most of the winter wheat fields. It can be also observed that low irrigation amounts have been estimated over several non-cultivated fields (lower than 100 mm). The irrigations detected over non-cultivated fields are part of the errors of the approach, but at least are not confused with the cultivaded and irrigated fields.

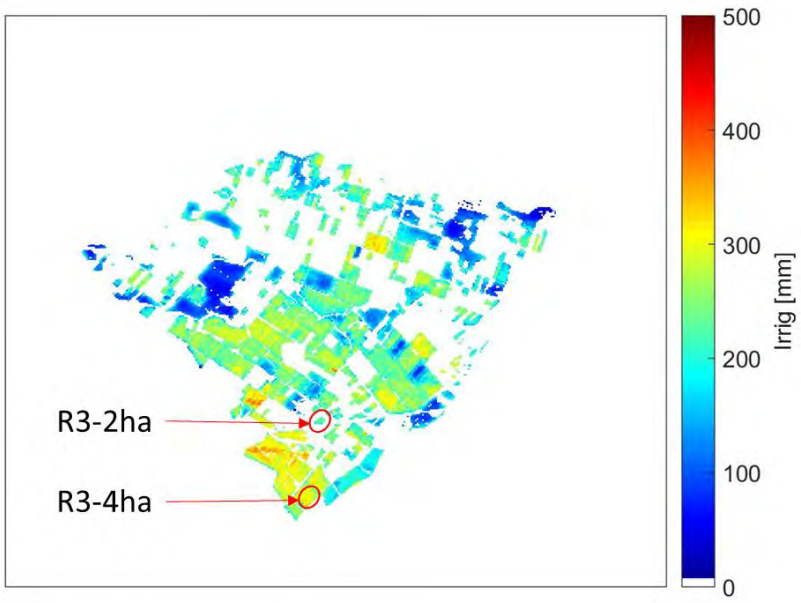


Fig. 4.12. Spatial distribution of the total irrigation depth for the 2016 growing season over R3 area.

4.8. Summary and conclusions

The implementation of crop water balance modelling over irrigated areas faces the main issue that the quantification of irrigation spatially distributed is often unknown. In particular, the application of FAO-2Kc model over extended areas (like irrigated districts) would need calibration and irrigation at field scale to be forced. In order to overcome these issues, we proposed a novel approach to estimate the irrigation amounts and timing by integrating remotely sensed optical/thermal data into a crop water balance model that is basically based on the FAO-2Kc formalism. The main idea behind the algorithm is

retrieving the RZSM dynamics in order to detect the irrigation date first and then the irrigation amount as the difference between the RZSM on the irrigation date and that on the day before. Like an assimilation procedure, the remote sensing information is integrated as a crop water status (Ks) into the crop water balance model, by initializing the model at every satellite overpass date. Landsat-7 and -8 data were used to apply the approach, which four general procedures to be implemented in order to retrieve the irrigation at field scale: i) partitioning the Landsat LST to derive the crop water stress coefficient Ks, ii) estimating the daily RZSM from the integration of Landsat-derived Ks into a crop water balance model, iii) retrieving irrigation at Landsat pixel scale and iv) aggregating pixel-scale irrigation estimates at the crop field scale.

The approach is implemented over three agricultural areas of 12 by 12 km in Haouz Plain in central Morocco during four seasons and validated over five winter wheat fields under different irrigation techniques (drip, flood and no-irrigation). The approach is validated in terms of irrigation estimates as well as daily RZSM and ET as intermediate variables linked to the crop water balance model. The results show that the total (seasonal) irrigation amounts over all the sites and seasons is accurately estimated (RMSE=44 mm and R=0.95), regardless of the irrigation techniques. Irrigation is also validated over different accumulation periods, in which acceptable errors (R = 0.52 and RMSE = 27 mm) are obtained for irrigations cumulated over 15 days and the performance gradually improves by increasing the accumulation period. As it is presented in the article (Section 4.9), these results are however strongly related to the frequency of Landsat overpasses (one image every 8 or 16 days or more in cloudy conditions). Poor agreements at daily to weekly scales are found in terms of irrigation, however the daily RZSM and ET simulated from the retrieved irrigations are estimated accurately and are very close to those estimated from actual irrigations.

Therefore, the approach obtains acceptable errors in irrigation amount and timing in order to simulate the dynamics of water budget components (ET and RZSM) along the season at daily and field crop scale. Regarding the accuracy of ET estimates over the sites, it is demonstrated that the formulation of generic coefficients Kcb and Ke allows generic implementations by using satellite data, avoiding calibration with in situ data that are usually unavailable over extended areas. Finally, this study demonstrates the utility of high spatial resolution optical/thermal data for estimating irrigation and consequently for better closing the water budget over agricultural areas.

4.9. ARTICLE: *Irrigation retrieval from Landsat optical/thermal data integrated into a crop water balance model: A case study* over winter wheat fields in a semi-arid region

Remote Sensing of Environment 239 (2020) 111627

Contents lists available at ScienceDirect

Remote Sensing of Environment

journal homepage: www.elsevier.com/locate/rse

Irrigation retrieval from Landsat optical/thermal data integrated into a crop water balance model: A case study over winter wheat fields in a semi-arid region

Luis Olivera-Guerra[a,*], Olivier Merlin[a], Salah Er-Raki[b,c]

[a] Centre d'Etudes Spatiales de la Biosphère (CESBIO), Université de Toulouse, CNES, CNRS, IRD, UPS, Toulouse, France
[b] LP2M2E, Département de Physique Appliquée, Faculté des Sciences et Techniques, Université Cadi Ayyad, Marrakech, Morocco
[c] Center for Remote Sensing Application (CRSA), University Mohammed VI Polytechnic (UM6P), Benguerir, Morocco

ARTICLE INFO

Edited by Jing M. Chen

Keywords:
Irrigation
Land surface temperature
FAO-56 model
Landsat
Root-zone soil moisture
Evapotranspiration

ABSTRACT

Monitoring irrigation is essential for an efficient management of water resources in arid and semi-arid regions. We propose to estimate the timing and the amount of irrigation throughout the agricultural season using optical and thermal Landsat-7/8 data. The approach is implemented in four steps: i) partitioning the Landsat land surface temperature (LST) to derive the crop water stress coefficient (Ks), ii) estimating the daily root zone soil moisture (RZSM) from the integration of Landsat-derived Ks into a crop water balance model, iii) retrieving irrigation at the Landsat pixel scale and iv) aggregating pixel-scale irrigation estimates at the crop field scale. The new irrigation retrieval method is tested over three agricultural areas during four seasons and is evaluated over five winter wheat fields under different irrigation techniques (drip, flood and no-irrigation). The model is very accurate for the seasonal accumulated amounts ($R \sim 0.95$ and RMSE ~ 44 mm). However, lower agreements with observed irrigations are obtained at the daily scale. To assess the performance of the irrigation retrieval method over a range of time periods, the daily predicted and observed irrigations are cumulated from 1 to 90 days. Generally, acceptable errors ($R = 0.52$ and RMSE = 27 mm) are obtained for irrigations cumulated over 15 days and the performance gradually improves by increasing the accumulation period, depicting a strong link to the frequency of Landsat overpasses (16 days or 8 days by combining Landsat-7 and -8). Despite the uncertainties in retrieved irrigations at daily to weekly scales, the daily RZSM and evapotranspiration simulated from the retrieved daily irrigations are estimated accurately and are very close to those estimated from actual irrigations. This research demonstrates the utility of high spatial resolution optical and thermal data for estimating irrigation and consequently for better closing the water budget over agricultural areas. We also show that significant improvements can be expected at daily to weekly time scales by reducing the revisit time of high-spatial resolution thermal data, as included in the TRISHNA future mission requirements.

1. Introduction

Irrigated agriculture consumes > 70% of freshwater at global scale (Foley et al., 2011) and > 80% in semi-arid and arid regions (Chehbouni et al., 2008; Garrido et al., 2010). The water scarcity issue is particularly acute in the Mediterranean, which is and will continue to be a hot spot of climate change with an observed trend towards warmer conditions and a greater irregularity in seasonal and annual precipitations (Giorgi, 2006; IPCC, 2013). Increasing the water use efficiency in agriculture is essential for the sustainability of water resources and hence has been identified as one key topic related to water scarcity and droughts (Werner et al., 2012). Despite the important pressure of agriculture on water resources, information on the amount of irrigated water is often unavailable. Therefore, monitoring and quantifying irrigation over extended areas is critical for an efficient management of water resources.

In an attempt to estimate the irrigation volumes from remote sensing data, some recent studies have explored the utility of surface soil moisture estimates from micro-wave sensors (Brocca et al., 2018, 2017; Escorihuela and Quintana-Seguí, 2016; Jalilvand et al., 2019; Kumar et al., 2015; Lawston et al., 2017; Malbéteau et al., 2018; Zhang et al., 2018). In particular, Brocca et al. (2018) developed an approach to quantify the irrigation amounts by combining the currently available coarse resolution satellite soil moisture products (e.g. SMAP, SMOS,

* Corresponding author.
E-mail address: olivera-guerrale@cesbio.cnes.fr (L. Olivera-Guerra).

https://doi.org/10.1016/j.rse.2019.111627
Received 19 June 2019; Received in revised form 25 November 2019; Accepted 21 December 2019
Available online 10 January 2020
0034-4257/ © 2020 Elsevier Inc. All rights reserved.

ASCAT, AMSR-2) and a soil water balance. This work was applied over various semi-arid and semi-humid regions worldwide but could not be quantitatively assessed due to the unavailability of reliable in situ observations of irrigation over corresponding irrigated perimeters. However, this approach was quantitatively assessed at ~50 km resolution over a semi-arid region (Jalilvand et al., 2019). Some deficiencies were obtained over periods with sustained rainfalls and the method was not implemented in winter because the method fails in correctly separating irrigation from precipitation (Brocca et al., 2018). This makes the approach unsuitable for winter crops, which are especially important in the Mediterranean. Nevertheless, the ability to quantify monthly irrigations was demonstrated under specific conditions: during prolonged periods of low rainfall and using satellite soil moisture data with a low uncertainty and a frequency higher than 3 days.

There are two main issues with the use of microwave-based soil moisture for retrieving irrigation. The first limitation is the very coarse resolution (~40 km) of readily available satellite soil moisture data sets. The spatial resolution can be improved to 1 km resolution using disaggregation methods (e.g. Molero et al., 2016; Peng et al., 2017), but this enhanced resolution is still unsuitable for monitoring the water management at the crop field scale, i.e. about 100 m or 1 ha (Anderson et al., 2012). Furthermore, recent methods to obtain soil moisture data at suitable resolution (~100 m) have not reached an operational maturity yet (e.g. Amazirh et al., 2018; Merlin et al., 2013; Peng et al., 2017). The second limitation is related to the sensing depth (several cm or so) of microwave observations. The dynamics of the top soil moisture is likely to be used to detect irrigation events. However the volume sensed is much smaller than the root zone water storage, which weakens the capability of microwave-based approaches to solve the crop water budget.

Alternatively to microwave-based approaches, optical/thermal data have demonstrated to be valuable for monitoring the crop water requirements by means of evapotranspiration (ET) estimates (Gowda et al., 2008; Kalma et al., 2008; Li et al., 2009). Thermal data have the advantage over microwave data of providing information on the vegetation water status, even within individual fields, in order to improve the water use efficiency (Anderson et al., 2012). In this vein, different methods have been developed in the last decades to estimate ET from LST data (Gowda et al., 2008; Kalma et al., 2008; Li et al., 2009). Despite the large variety of existing approaches to estimate crop water requirements by means of ET estimates, irrigation is generally simulated from the modeled water needs (e.g. Allen et al., 1998; Bastiaanssen et al., 2007; Battude et al., 2017; Corbari et al., 2019; Duchemin et al., 2008). Those models are based either on the water balance or on the coupled energy-water balance, but in both cases, the simulated irrigation may differ considerably from actual irrigation amounts. The reason is that the modeling of soil moisture dynamics and its interaction with the crop consumption through ET is prone to significant uncertainties, especially when no information is available on the actual crop water status over time. Other approaches based on ET estimates from remote sensing surface energy balance (SEB) models (e.g. SEBS, SEBAL, METRIC) have the advantage of estimating the crop water requirement without the calculation of the water balance. This is feasible using daily optical/thermal data. The point is that the remotely sensed variables for operating SEB models at daily scale generally have a spatial resolution of 1 km or more (e.g. Romaguera et al., 2014; van Eekelen et al., 2015), which is unsuitable at crop field scale. When using high-spatial resolution optical/thermal data, the low temporal resolution has to be taken into account. In Droogers et al. (2010), a water balance model was calibrated to minimize the difference between simulated and remotely sensing Landsat-derived ET over an irrigated cotton crop field. The calibration involved adjusting the irrigation amount and a stress threshold below which irrigation is triggered. The stress threshold f_1 was defined as the actual to potential transpiration and ranged from 0.95 to 0.98 in that study. However, due to compensation effects between irrigation amounts and dates, the authors had to further constrain the inverse problem by fixing the irrigation dates during the first half of the season (from March to end of June) and to assume that there is no stress during the second half of the season (from July). Therefore, during the first stage, irrigation events are supposed to be known, while during the second stage, the approach in Droogers et al. (2010) is very similar to the application of the classical FAO-56 model (Allen et al., 1998) that triggers irrigation as soon as the root zone soil moisture gets below 0.95–0.98 times the critical soil moisture below which the crop stress starts. The retrieved irrigation amounts were assessed at the seasonal time scale but, due to the lack of validation data, they were not compared to actual irrigations at shorter time scales. Recently, Corbari et al. (2019) developed a system to predict the water needs (irrigation) from the coupling of remote sensing data, soil water-energy hydrological modeling and meteorological forecasts. Landsat-derived vegetation and albedo parameters, as well as land surface temperature (LST) data were used to initialize and calibrate the energy-water balance. However, this approach required observed data of the previous days (especially soil moisture) to simulate the soil moisture and irrigation water needs for up to 3 days, which is not currently possible over large scales because there is no method that allows obtaining operationally soil moisture data at suitable resolution (~100 m). Another approach was proposed by Chen et al. (2018) to detect the timing of irrigation from a vegetation index by using Landsat and MODIS reflectance data. The method was demonstrated to be promising in detecting irrigation events during the first half of the growing season only. Actually, vegetation index presents great fluctuation and is insensitive to water supplement during the second half of the growing season. In addition, the method does not allow retrieving irrigation amounts.

Among the thermal-based ET models, the contextual approaches have had an especial interest in the scientific community for its simplicity and operationality over large areas, by estimating ET as a fraction of either potential ET (Moran et al., 1994), or available energy (Long and Singh, 2012; Roerink et al., 2000). The evaporative fraction (EF, defined as the ratio of ET to available energy, i.e., the difference between net radiation and soil heat flux) can be estimated from the contextual information of remotely sensed optical and thermal images, where dry and wet conditions are identified from the LST – fv (e.g. Long and Singh, 2012; Moran et al., 1994) space, the LST – albedo (e.g. Roerink et al., 2000) space or even from their combination (Merlin, 2013; Merlin et al., 2014). According to a number of thermal-based methods, LST can be related to the root-zone soil moisture (RZSM) by means of the canopy temperature and its associated transpiration (Boulet et al., 2007; Hain et al., 2009; Moran et al., 1994). Hence, one key step to estimate thermal-derived RZSM is the partitioning of LST into soil and canopy temperatures (Merlin et al., 2014, 2012; Moran et al., 1994). In dry and wet regimes where a thermal-based EF (or canopy temperature-based water stress index) is 0 and 1, respectively, LST is no more sensitive to RZSM. LST is hence useful only in a transitional regime where RZSM is strongly related to LST. In the transitional regime, the soil moisture ranges between a given critical soil moisture (SM_{crit}, below which vegetation is under stress condition) and the soil moisture at permanent wilting point (SM_{wp}, below which water is not accessible to plants). SM_{crit} is thus defined between SM_{wp} and the soil moisture at field capacity (SM_{fc}, above which water cannot be held against gravitational drainage). Therefore, the nonlinear response of LST for different RZSM levels/regimes is a big issue when trying to develop a RZSM retrieval approach from LST data. Olivera-Guerra et al. (2018) developed an approach to derive a first guess RZSM from a LST-derived water stress coefficient, while under unstressed conditions (i.e. when LST is no more sensitive to RZSM) the RZSM was estimated from a crop water balance model. The temporal dynamics of RZSM were hence obtained along the season under stressed and unstressed condition, by making an optimal use of both the water budget model and sequential LST observations. However, the method in Olivera-Guerra et al. (2018) was not applied to remote sensing data and its application

to readily available LST observations requires to account for three major issues that are addressed in the present work. First, a contextual approach should be implemented from Landsat data to partition the LST into canopy and soil temperatures by detecting the wet and dry conditions from the LST – fv space. This would allow for estimating a Landsat-derived crop stress coefficient (Ks) over large scales. Second, a serious complexity is introduced when trying to estimate the daily RZSM from sparsely available Landsat data. Especially the Landsat-derived Ks should be integrated into a crop water balance model in both recursive and forward modes, in order to provide the temporal dynamics of RZSM along the season at pixel scale over large areas. Third, given that irrigation is usually applied within a single day over the entire crop field, the pixel-scale irrigation estimates can be aggregated (following a strategy to be defined) to provide the irrigation dates and amounts at the crop field scale.

Therefore, this study aims, for the first time, to develop an original approach to retrieve the crop field scale irrigation timing and amounts on a daily basis all along the agricultural season from readily available remote sensing data. For this purpose, a key and novel step in the approach is to estimate the daily RZSM by combining a forward and recursive crop water balance initialized by temporally-sparse Landsat data. To our knowledge it is the first remote sensing-based approach to estimate irrigation at such high spatio-temporal resolution from readily available optical/thermal data and without relying on ad hoc assumptions on irrigation regimes (e.g. no stress) and/or dates. The approach is implemented with Landsat-7 and -8 data over three 12 km by 12 km areas in central Morocco and is validated over five sites with different irrigation techniques (drip, flood and no-irrigation) during four agricultural seasons. The paper is presented as follows. Data sets are first described (Section 2). Next, the irrigation retrieval method is presented: i) partitioning the Landsat LST to derive the crop water stress coefficient Ks, ii) estimating the daily RZSM from the integration of Landsat-derived Ks into a crop water balance model, iii) retrieving irrigation at the Landsat pixel scale and iv) aggregating pixel-scale irrigation estimates at the crop field scale (Section 3). Then, the approach is tested over three agricultural areas and validated against in situ measurements in terms of irrigation as well as daily RZSM and ET (Section 4). Finally, the conclusions and perspectives are presented (Section 5).

2. Data collection and pre-processing

The study focuses on three 12 km by 12 km agricultural areas located in the semi-arid Haouz plain in central Morocco (Fig. 1). Each agricultural area is mainly covered by winter wheat crops. Five experimental sites comprising two drip irrigation, two flood irrigation and one rainfed wheat fields were monitored during four agricultural seasons. Details about irrigation systems, crop field area and monitoring period per area, named Chichaoua, R3 and Sidi Rahal are showed in Table 1. The soil texture are predominantly clay loam, clay and silt loam for Chichaoua, R3 and Sidi Rahal areas, respectively. The site of Sidi Rahal (Bour) was maintained under bare soil conditions during the 2015–2016 season due to the dry winter of 2015. However, the four seasons between 2015 and 2018 are used as benchmark. More details about the field campaigns can be found in Ait Hssaine et al. (2018), Amazirh et al. (2018, 2017), Merlin et al. (2018) and Rafi et al. (2019).

2.1. Ground-based data

2.1.1. Irrigation data

In the Chichaoua area, flowmeters were used to monitor the irrigation of the two drip-irrigated fields. Irrigation was applied every 3–4 days during the 2016–2017 season until mid-April. Nevertheless, one field (EC1) was voluntarily stressed during specific periods along the season (controlled stress). Irrigations were stopped at mid-March and at the beginning of February of the 2017–2018 season over the reference (EC2) and controlled stress (EC1) field, respectively. The mean irrigation was 13 mm over 2 h.

In the R3 area, the flood-irrigated fields were irrigated every 1 to 3 weeks from January to April. Irrigation of the 2 ha field was precisely measured with a mean irrigation of 33 mm distributed in 8 events, while the 4 ha field was irrigated 7 times with an estimated volume of 64 mm each. No irrigation was applied to the Sidi Rahal rainfed (Bour) wheat field.

2.1.2. Meteorological and flux stations

Automatic meteorological stations were installed in each experimental area: two over alfalfa fields close to the monitored wheat fields in the Chichaoua and R3 areas and one over the monitored rainfed wheat field in Sidi Rahal. Meteorological data including air temperature, solar radiation, relative humidity and wind speed were collected continuously every 30 min. Likewise, five micro-meteorological stations equipped with eddy-covariance systems were installed in each site. Here, net radiation was measured by NR01 (Hukseflux) or CNR (Kipp & Zonen) radiometers, depending on the station. Soil heat fluxes were estimated from two HFP-01 heat flux plates (Hukseflux) per site buried at 5 cm. Finally, latent and sensible heat fluxes were acquired with krypton KH2O hygrometers (Campbell) and CSAT3 3D Sonic Anemometers at a frequency of 10 Hz and averaged over 30 min. The reliability and quality of the eddy covariance measurements over each field have been assessed through the energy balance closure (Ait Hssaine et al., 2018; Amazirh et al., 2017; Rafi et al., 2019).

2.1.3. Soil moisture data

Time Domain Reflectometry (TDR) probes (CS615 and CS655) were installed near the flux stations in each site to measure the soil moisture at different depths. The TDR probes were installed at 5, 15, 25, 35, 50, 80 cm in the stress controlled drip-irrigated (Chichaoua) and in the 4 ha flood-irrigated field (R3). Meanwhile, the TDR probes were installed at 5, 15, 30, 50, 80 cm in the reference drip-irrigated field and in the 2 ha R3 flood-irrigated field. In the rainfed wheat field, the TDR probes were installed only at the soil surface layer (at 5 and 10 cm). The measurements at different depths were used to estimate the soil moisture integrated over the root zone by means of linear interpolations. In situ RZSM estimates were then normalized by using the soil moisture values at wilting point (SM_{wp}) and at field capacity (SM_{fc}) estimated from pedo-transfer functions (Wosten et al., 1999).

2.2. Remote sensing data

Landsat-7 and -8 data collected for the agricultural seasons from 2014 to 2018 are used. Images with < 30% of cloud cover are considered for the analysis, giving an average of 20 images per agricultural season. We combine Landsat-7 and 8 to increase the frequency of the thermal data since it is one main critical issue for monitoring crop water use together with its high spatial resolution. We estimate LST and *fv* using both optical and thermal data (see below). We maintain the 30 m spatial resolution for all data, even when the thermal bands are resampled from their original 60 m and 100 m resolution for Landsat-7 and -8, respectively.

2.2.1. Land surface temperature

LST is estimated using the single-channel algorithm described in Jiménez-Muñoz et al. (2009); Jiménez-Muñoz et al. (2014), which uses as input the thermal band of Landsat, the atmospheric water vapor content, and the spectral surface emissivity. The thermal data are acquired from bands 6 and 10 of Landsat-7 and -8 Level-1, respectively, while the atmospheric water vapor content is obtained from the daily MODIS MOD05 v6.0 product. The spectral surface emissivity is estimated using the simplified NDVI thresholds method proposed by Sobrino et al. (2008), which weights the spectral soil and vegetation emissivity (here set to 0.985) through the *fv*. Similarly, the spectral soil emissivity is obtained from the ASTER GED product by using bands 13

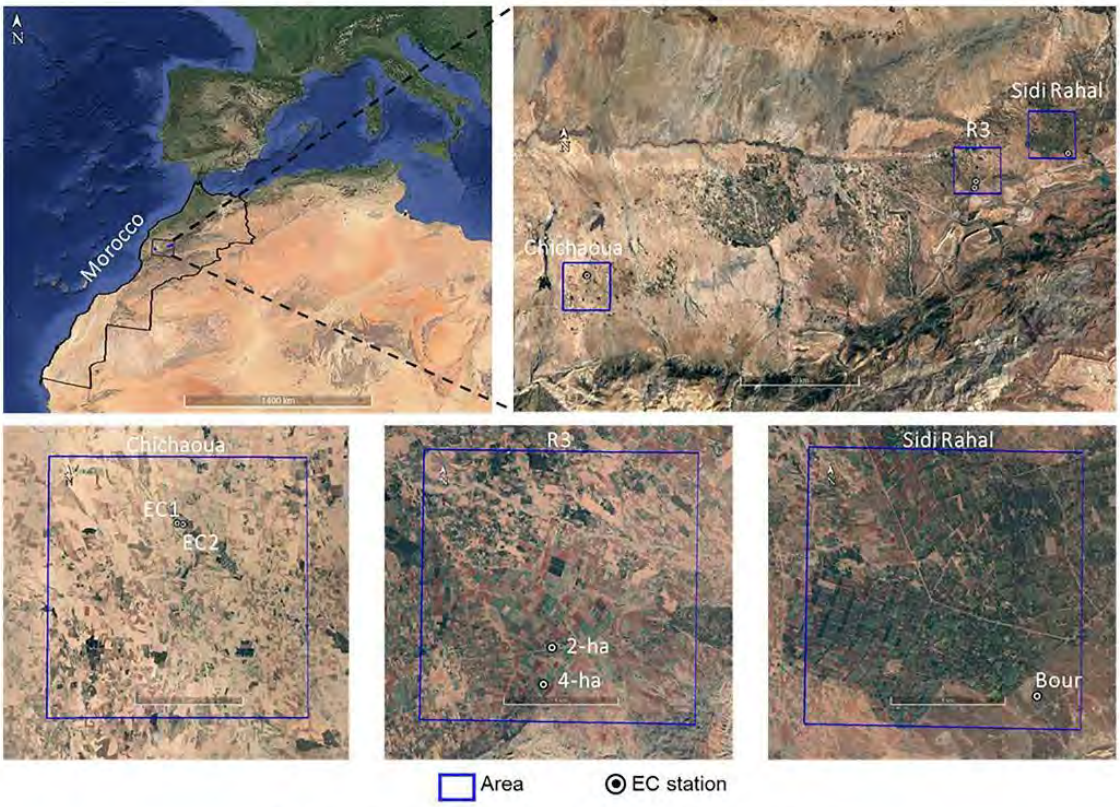


Fig. 1. Study areas and field crops where the developed approach is evaluated.

and 14 with the above-mentioned simplified NDVI method. Then, the ASTER spectral soil emissivities are adjusted to the Landsat thermal bands using the broadband regression approach (Ogawa and Schmugge, 2004) as in Malakar et al. (2018) and Duan et al. (2018). The regression coefficients between the emissivities for Landsat and ASTER bands were derived by convoluting the soil emissivity spectra of all soil types available in the ASTER spectral library for every thermal band (Baldridge et al., 2009). Accuracies resulted in root mean square error (RMSE) of 0.0007 and 0.0005, and R^2 of 0.96 and 0.99 for Landsat-7 and -8 thermal band, respectively. The reliability of LST estimates was assessed in Amazirh et al. (2019, 2017), which found a relatively good agreement between satellite and ground-based LST over the sites of the study area with a RMSE lower than 2.4 K.

2.2.2. *Fractional green vegetation cover*

The fractional green vegetation cover *fv* is estimated linearly between a minimum and maximum of the Normalized Difference Vegetation Index (NDVI), which often represent bare soil (NDVIs) and fully vegetated surface (NDVIv) values, respectively (Gutman and Ignatov, 1998). NDVIs and NDVIv are set to 0.14 and 0.93 (Duchemin et al., 2006). NDVI values are estimated using the red and near-infrared bands of Level-2 Landsat products.

Table 1
Main characteristics of experimental winter wheat fields by agricultural area.

Area	Site name	Crop field area	Soil texture (%clay, %sand	Irrigation system	Monitoring period (mm/yyyy)	Total Irrigation applied	# events	Mean irrigation (mm)
Chichaoua	EC1	~1.5 ha	Clay loam (32.5%, 37.5%)	Drip-irrigated	11/2016–5/2017	374	25	15.0 (± 5.6)
					11/2017–5/2018	327	26	12.6 (± 11.2)
	EC2	~1.5 ha			11/2016–5/2017	504	37	13.6 (± 5.7)
					11/2017–5/2018	528	38	13.9 (± 11.4)
R3	4ha	4 ha	Clay (47%, 18%)	Flood-irrigated	12/2015–5/2016	448	7	64.0 (−)
	2ha[a]	2 ha		Drip-irrigated	12/2015–5/2016	268	8	29.3 (± 7.6)
Sidi Rahal	Bour	~1 ha	Loam (18%, 41%)	Rainfed	10/2014–5/2015	0	0	0
					10/2015–5/2016	0	0	0
					10/2016–5/2017	0	0	0
					10/2017–5/2018	0	0	0

[a] R3-2ha field is actually irrigated by drip system with amounts and quantities according to a flood irrigation system. Thus, R3-2ha is considered as flood-irrigated site.

3. Method

The method to retrieve irrigation dates and volumes from Landsat LST/NDVI time series is described below. The basic idea behind the retrieval approach is first to determine the irrigation date and then to estimate the (daily) irrigation amount as the difference between the RZSM estimated on the irrigation date and that estimated on the day before. As in Olivera-Guerra et al. (2018), thermal-derived crop stress coefficient (Ks) is translated into RZSM diagnostic by means of the dual crop coefficient FAO (FAO-2Kc) formalism. In this former work, irrigation was estimated from the variability in daily first guess RZSM by using optical/thermal in situ observations. Given that the method proposed herein uses temporally sparse Landsat data, the Landsat-derived RZSM diagnostic is propagated in a recursive and forward water balance mode to estimate the daily RZSM along the season. Therefore, this method significantly differs from the study in Olivera-Guerra et al. (2018) in several major aspects. For clarity, the main assumptions are listed (Section 3.1) and each original component is described separately: the irrigation retrieval at the pixel scale using Landsat-derived Ks (Section 3.2), the use of a contextual method to derive RZSM from Landsat data (Section 3.3), the implementation of a crop water balance model (WB) in recursive and forward modes to estimate the daily RZSM between two successive Landsat overpass dates (separated by 8 to 16 days in clear sky conditions) (Section 3.4), the aggregation of pixel-scale irrigation estimates at the crop field scale (Section 3.5), and the definition of a validation strategy of the field-scale retrieved irrigation dates/volumes (Section 3.6).

3.1. Model assumptions

The approach is based on several assumptions, some of which relate to the FAO-2Kc modeling approach, while others are specific to the proposed irrigation retrieval method. The assumptions deriving from the FAO-2Kc model are:

- The daily RZSM varies within a range defined by a minimum value set to the soil moisture at wilting point (SM_{wp}) and by a maximum value set to the soil moisture at field capacity (SM_{fc}). Both extreme soil moisture values are estimated using pedo-transfer functions (Wosten et al., 1999). SM_{wp} and SM_{fc} were equal to 0.17 and 0.32 $m^3\ m^{-3}$, respectively. Uniform soil parameters were used to test the genericity of the irrigation retrieval approach.
- When RZSM reaches SM_{fc}, any additional water supply is considered as water excess and is therefore drained from the soil bucket by deep percolation (occurring simultaneously to the water excess supply).
- The RZSM is linearly related to Ks between SM_{wp} and the critical RZSM (SM_{crit} = 0.24 $m^3\ m^{-3}$), which is estimated as a fraction of the total available water (i.d. difference between SM_{fc} and SM_{wp}) according to the water stress tolerance of crops (Allen et al., 1998).
- The rooting depth is estimated from the vegetation cover and varies linearly between a minimum value (set to 0.1 m) and a maximum value depending on the crop type.

The assumptions specific to the irrigation retrieval approach are:

- The retrieved irrigation is the effective irrigation (irrigation minus drainage), meaning that the irrigation excess which triggers deep percolation is not taken into account.
- An irrigation event is detected on the day when the RZSM estimated recursively from the FAO-2Kc water budget reaches SM_{fc} and it is not due to rainfall.
- The field-scale retrieved irrigation occurs on the same day over the entire field crop.
- Due to the saturation of Landsat-derived Ks (equal to 1) for soil moisture values between SM_{crit} and SM_{fc}, the Landsat-derived RZSM ranges between SM_{wp} and SM_{crit}.
- If two successive Landsat overpass dates both indicate unstressed conditions (Ks = 1), it is assumed that the crop does not undergo water stress during that period. It is also assumed that Ks = 1 between a Landsat date indicating unstressed conditions and an irrigation event detected before the next Landsat overpass date.
- In our study, the capillarity rise and runoff are neglected due to flat surfaces and a water table significant deep (> 30 m) in the study area (Duchemin et al., 2006).

3.2. Pixel-scale irrigation retrieval

Irrigation is first estimated at the Landsat pixel scale as:

$$I_i = 1000(RZSM_i - RZSM_{i-1})Zr_i \quad (1)$$

where I_i is the irrigation amount (mm) on the irrigation date *i* and $RZSM_i$ and $RZSM_{i-1}$ (m^3/m^3) the RZSM estimated on the irrigation day and on the day before, respectively. The RZSM unit (m^3/m^3) is converted to irrigation depth (mm) by the factor $1000Zr_i$, with Zr_i being the effective root zone depth (m) at the irrigation date. Zr_i is estimated according to the Appendix A.2

To estimate $RZSM_i$ in Eq. (1), the WB is applied in the recursive mode (here-after referred to as RWB) at daily scale for every period between two consecutive clear sky Landsat overpass dates (*j* and *j-Pj*, with *Pj* being the number of days between both successive Landsat dates). The RWB is applied from the last Landsat overpass date of the season to its previous dates. Therefore, the RWB is initialized at date j (j > i) from a Landsat-derived RZSM ($RZSM_{Landsat,j}$), and an irrigation event is detected at date i when the simulated $RZSM_{RWB,t}$ (for t = j-1, …,i) reaches SM_{fc}. However, four different cases need to be considered depending on the value (equal or smaller than 1) of Landsat-derived Ks at dates *j-Pj* and *j*. For clarity, each case is illustrated in Fig. 2.

Case 1. stressed-stressed (Fig. 2.a). The crop is under stress (Ks < 1) on both Landsat overpass dates j and j-Pj. Hence both $RZSM_{Landsat,j}$ and $RZSM_{Landsat,j\text{-}Pj}$ are smaller than SM_{crit}. In this case, if an irrigation event at date *i* > *j-Pj* (i.e. $RZSM_{RWB,t} = SM_{fc}$) is detected, the WB model is used in the forward mode (referred to as FWB) to estimate the RZSM at day *i-1* from an initial value set to $RZSM_{Landsat,j\text{-}Pj}$. The irrigation amount at date *i* is estimated as:

$$I_i = 1000(SM_{FC} - RZSM_{FWB,t=i-1})Zr_i \quad (2)$$

Case 2. stressed-unstressed (Fig. 2.b). The crop is under stress (Ks < 1) on Landsat overpass date j-Pj and is unstressed (Ks = 1) on Landsat overpass date j. In this case, the RWB is initialized to SM_{crit} at Landsat overpass date j and if $RZSM_{RWB,t=i}$ reaches SM_{fc} for i > $j\text{-}P_j$, then $RZSM_{t=i-1}$ is estimated from the FWB initialized by $RZSM_{landsat,j\text{-}Pj}$ at Landsat overpass date j-Pj. The irrigation amount is then estimated as in Eq. (2).

For cases 1 and 2, two other specific conditions need to be considered:

i) $RZSM_{FWB,t}$ might reach its minimum value (SM_{wp}) before the detected irrigation event from $RZSM_{RWB,t=i}$. In that situation, another irrigation event is triggered in such a way that the simulated $RZSM_{FWB}$ is set to SM_{fc} and the FWB is used to propagate RZSM until *i-1* in the Eq. (2).

ii) $RZSM_{RWB,t}$ does not reach SM_{fc} for *t* > *j-Pj*. In that case, an irrigation is detected at date j-Pj + 1 provided that the difference between $RZSM_{RWB,j\text{-}Pj+1}$ and $RZSM_{Landsat,j\text{-}Pj}$ is positive and significant (larger than a given threshold to be set). In this case, the irrigation amount is calculated as:

$$I_{i=j-Pj+1} = 1000(RZSM_{RWB,i} - RZSM_{Landsat,j-P_j})Zr_i \quad (3)$$

Note that the threshold is determined as the uncertainty associated to $RZSM_{Landsat,j\text{-}Pj}$ estimate by using the propagation of uncertainty

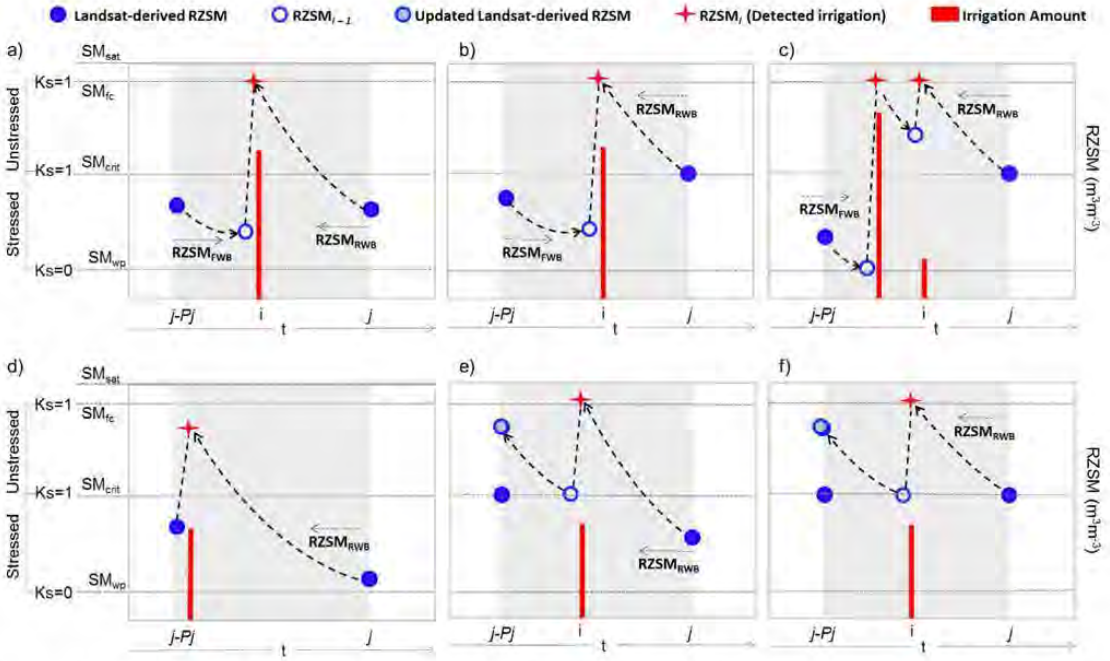


Fig. 2. Schematic representation of pixel-scale irrigation retrieval between two successive Landsat overpass dates in four different cases: stressed-stressed (a), stressed-unstressed (b), unstressed-stressed (e) and unstressed-unstressed (f). The specific conditions c) and d) can be found in the stressed-(un)stressed cases (a,b). The RZSM is estimated from the FWB (right dotted arrow) or the RBW (left dotted arrow) initialized by the $RZSM_{Landsat}$ at date *j* and *j-Pj*, respectively. An irrigation event is detected when $RZSM_{RWB}$ reaches SM_{fc} and its amount is estimated by the difference between the RZSM retrieved at date *i* and *i-1*.

method from the partial derivatives of every independent variable (see Appendix A.3).

Case 3. unstressed-stressed (Fig. 2.c). The crop is unstressed (Ks = 1) on Landsat overpass date j-Pj and is under stress (Ks < 1) on Landsat overpass date j. In this case, if an irrigation event at date $i > j\text{-}Pj$ (i.e. $RZSM_{RWB,t} = SM_{fc}$) is detected, then $RZSM_{t=i-1}$ is set to SM_{crit} at date *i-1*. The irrigation amount at date *i* is thus determined as follows:

$$I_i = 1000(SM_{fc} - SM_{crit})Zr_i \quad (4)$$

Case 4. unstressed-unstressed (Fig. 2.d). The crop is unstressed (Ks = 1) on both Landsat overpass dates j-Pj and j. In this case, an irrigation is detected (date) and estimated (amount) as in the Case 3.

For cases 3 and 4, $RZSM_{Landsat,j\text{-}Pj}$ is updated by $RZSM_{RWB,j\text{-}Pj}$. The updated RZSM at j-Pj is then used to reinitialize the previous period (from date *j-Pj* to its previous Landsat overpass date).

3.3. Landsat-derived RZSM

The Landsat-derived RZSM ($RZSM_{landsat,j}$) is estimated as:

$$RZSM_{landsat,j} = SM_{wp} + Ks_{Landsat,j}(SM_{crit} - SM_{wp}) \quad (5)$$

where $Ks_{Landsat,j}$ is the Landsat-derived Ks, estimated from a normalization of the Landsat-derived vegetation temperature (Tv), using minimum (Tv_{min}) and maximum (Tv_{max}) Tv values. Hence, Ks values range between 0 and 1, where 1 corresponds to well-watered/unstressed vegetation ($Tv = Tv_{min}$) and 0 to non-transpiring or senescent vegetation ($Tv = Tv_{max}$). Landsat-derived Tv is obtained from a partitioning method of LST:

$$Tv = \frac{LST - (1 - fv)Ts}{fv} \quad (6)$$

with Ts being the soil temperature and fv the fractional vegetation cover. This partitioning method is based on the LST-fv feature space (e.g. Jiang and Islam, 2003; Long and Singh, 2012; Merlin et al., 2014; Sandholt et al., 2002), by incorporating the assumptions of the two-source surface energy balance (TSEB) formalisms (Norman et al., 1995). First, the LST-fv feature space is used to estimate the temperature endmembers (Tv_{min}, Tv_{max}, Ts_{min} and Tv_{max}) from a polygon constrained by a "dry edge" (defined as the line between Ts_{min} and Tv_{min}) and a "wet edge" (defined as the line between Ts_{max} and Tv_{max}). The "wet edge" and "dry edge" are determined from the linear regressions of the minimal and maximal LST, respectively, which are selected by *fv* classes with an interval of 0.01 (see Fig. 3.a). Second, the TSEB assumption for solving the vegetation and soil fluxes components and their corresponding Tv and Ts is only used for the partitioning of LST by applying Eq. (6). The procedure is initialized with Tv being equal to Tv_{min} and the corresponding initial Ts by decomposing linearly the LST from Eq. (6). This is consistent with the TSEB approach when the transpiration rate is initialized to its potential rate (corresponding to $Tv = Tv_{min}$). If Ts is above the Ts_{max}, Ts is then set to Ts_{max} and a new Tv is calculated from Eq. (6). In that case, the vegetation undergoes water stress ($Tv > Tv_{min}$). Therefore, the TSEB assumption in the LST-fv feature space (see Fig. 3.b) makes Tv equal to Tv_{min} for every Ts below Ts_{max}, while Ts remains equal to Ts_{max} when Tv is larger than Tv_{min}.

3.4. Water balance-derived RZSM

The daily RZSM between Landsat overpass dates is estimated by solving the crop WB in forward and recursive modes, named FWB and RWB respectively. According to the FAO-2Kc formalism, the general expression of the crop WB model is:

$$Dr_i = Dr_{i-1} + ET_i - P_i - I_i + DP_i - CR_i + RO_i \quad (7)$$

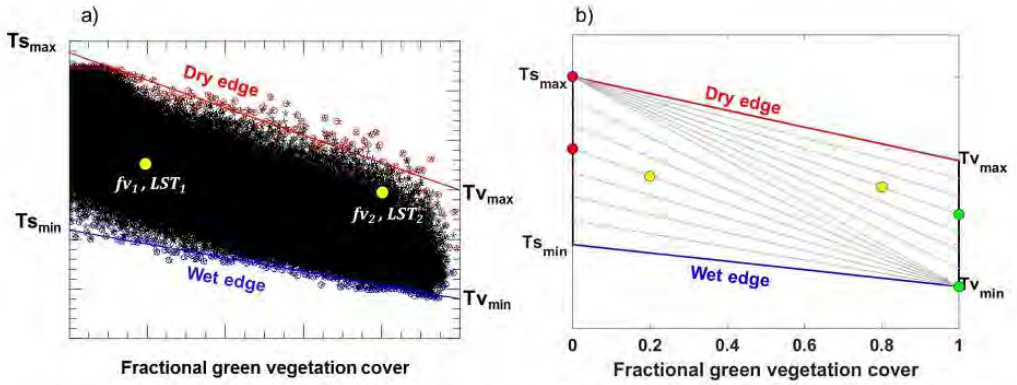


Fig. 3. In a), example of LST-fv feature space constrained by the polygon Ts_{min}-Tv_{min}-Tv_{max}-Ts_{max} from the linear regression of the minimum and maximum LST by fv classes. In b), a conceptual diagram of the LST-fv polygon for partitioning LST for two pixels (*fv,LST*) (yellow points) showing its Ts (red points) and Tv (green points) values corresponding to the TSEB assumptions. (For interpretation of the references to colour in this figure legend, the reader is referred to the web version of this article.)

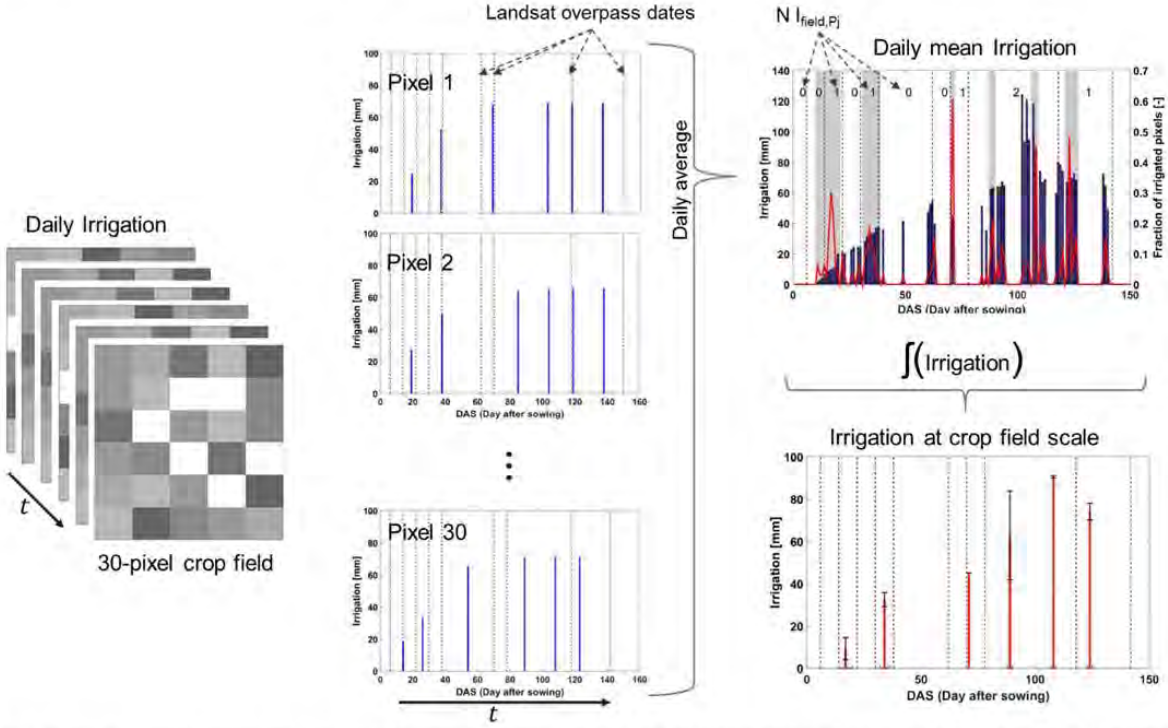


Fig. 4. Schematic diagram presenting the crop field scale irrigation retrieval from pixel-scale irrigation estimates for an example of a 30-pixel crop field. The daily pixel-scale irrigation is represented for every pixel (middle plots), from which are estimated the daily averaged irrigation (blue bar in top right plot) and the fraction of irrigated pixels (red line). Between two successive Landsat overpass dates in top right plot, the daily mean irrigation is integrated in the periods (shaded areas) according to its fractional irrigated pixels. The crop field scale irrigation (red bar in bottom right plot) is obtained by deriving the most probable irrigation date and is provided with its standard deviation for amount (black error bar) and date (red error bar). (For interpretation of the references to colour in this figure legend, the reader is referred to the web version of this article.)

where Dr. is the root zone depletion, ET the evapotranspiration, P the precipitation, DP the deep percolation, CR the capillarity rise, RO the surface runoff and I the irrigation. Every term is expressed in mm for the day *t* (and *t-1* for Dr). According to the assumptions used in this study, CR and RO are neglected while I is the variable to be estimated. Therefore, the FWB and RWB models can be expressed in Eqs. (8) and (9), respectively as:

$$Dr_t = Dr_{t-1} + ET_t - P_t \quad (8)$$

$$Dr_{t-1} = Dr_t - ET_t + P_t \quad (9)$$

Note that in the above equations, the DP resulting from heavy rainfall is not computed since Dr_t or Dr_{t-1} are set to 0 when $P_t > Dr_t$.

$_1$ + ET_t or P_t > Dr_t–ET_t for FWB and RWB, respectively. For both RWB and FWB models, the Landsat-derived RZSM (either $RZSM_{Landsat,j\text{-}Pj}$ or $RZSM_{Landsat,t}$) is used to initialize the root zone depletion.

$$Dr_t = 1000(SM_{fc} - RZSM_t)Zr_t \quad (10)$$

In Eqs. (8) and (9), ET_t is estimated from the FAO-2Kc formalism, where its basal crop coefficient (Kcb) and evaporation coefficient (Ke) are estimated from a generic expression from the daily *fv* interpolated from Landsat data. More details about the generic expressions to estimate Kcb and Ke are described in Appendix A.3. Kcb and Ke are first adjusted using Ks and an evaporation reduction coefficient (Kr), which are initialized from their Landsat-derived estimates (at date *j-Pj* or *j* for forward or recursive mode, respectively). Then Ks and Kr are computed from the crop WB according to FAO-2Kc. Similarly to Ks, Kr is estimated as the normalization of Ts between Ts_{min} and Ts_{max}. Finally, RZSM in forward ($RZSM_{FWB,t}$) and recursive ($RZSM_{RWB,t}$) modes are obtained from the root zone depletion by inverting Eq. (10).

3.5. Crop field scale irrigation retrieval

The irrigation was previously retrieved from the RZSM derived at the pixel level regardless of its neighboring context. Hence the within-field variability in terms of predicted irrigation dates and amounts can be further constrained. Given that irrigations usually occur on the same day over the entire crop field, we propose a procedure of aggregation to provide the irrigation dates and amounts at the crop field scale. The three-step procedure is described below.

First, for each period P_j between two successive satellite overpasses, the number of irrigations within a given crop field ($N_{Ifield,Pj}$) is estimated as the total number of irrigations at pixel-scale divided by the number of pixels contained in the crop field (N_{pixel}). Then, the daily amounts of irrigation at pixel-scale are averaged within the crop field (I_i). The daily fraction of irrigated pixels (f_i) is also estimated as the number of pixels where irrigation is detected divided by N_{pixel} (Fig. 4). Finally, the irrigation volume applied over the crop field (I_{field}) is estimated by integrating the amounts of irrigation in the $N_{Ifield,Pj}$ sub-periods of period P_j (Eq. (11)). The most probable date ($Date_{Ifield}$) of the irrigation event within each sub-period is estimated similarly according to Eq. (12).

$$I_{field} = \frac{\int_{ini}^{end} I_i f_i \, d_i}{\int_{ini}^{end} f_i \, d_i} \quad (11)$$

$$Date_{Ifield} = \frac{\int_{ini}^{end} i I_i f_i \, d_i}{\int_{ini}^{end} I_i f_i \, d_i} \quad (12)$$

with I_i and f_i being the areal averaged irrigation and the fraction of irrigated pixels within the field crop on day *i*, respectively. d_i is the time differential in the integral equations. The limits of integration *ini* and *end* are set according to f_i and $N_{Ifield,Pj}$ in period P_j. $N_{Ifield,Pj}$ is equal to the number of local maxima (peaks) of f_i detected for each sub-period. The limits *ini* and *end* are set to the first day before and the last day after the peak with f_i is equal to zero (i.e. the days when irrigation is not detected in any pixel of the field), respectively. For clarity, different integration periods are illustrated in Fig. 4.

3.6. Validation strategy

3.6.1. Irrigation

The performance of the irrigation retrieval method is evaluated at various time scales. In order to do that, the irrigation amounts are accumulated in overlapping windows throughout the seasons by increasing sequentially the windows from 1 day to 3 months (90 days). This strategy is implemented for every site. It allows the performance of the approach to be assessed for different accumulation periods, to be compared with the temporal resolution of Landsat data. The total irrigation applied during the entire season is also evaluated for all the sites.

The retrieved irrigation is also compared against the classical approach, which assumes no stress, meaning that irrigation is triggered when the RZSM reaches SM_{crit} in order to maintain Ks at 1. For this purpose, FAO-2Kc is run to simulate irrigation events along the season in order to maintain the crop under unstressed conditions (here-after referred to as $FAO\text{-}2Kc_{Ks=1}$). Note that the coefficients used in the FAO-2Kc (Kcb and Ke) are also averaged within the crop field, consistent with the irrigation retrieval method. The deep percolation resulting from the actual irrigation (I_{obs}) is removed from the comparison because our approach and $FAO\text{-}2Kc_{Ks=1}$ both estimate the effective irrigation only (i.e. without deep percolation resulting from irrigation). For this purpose, the deep percolation is estimated according to the FAO-2Kc forced by actual irrigation (here-after referred to as $FAO\text{-}2Kc_{Iobs}$).

3.6.2. RZSM and ET

The irrigation retrieval method is also assessed in terms of RZSM and ET estimates. Indeed, RZSM is an intermediate variable from which irrigation is retrieved, and ET is indirectly related to the irrigation through the RWB and the FWB. For this purpose, the retrieved irrigation is used to force FAO-2Kc to simulate RZSM and ET on a daily basis, and the RZSM and ET estimates are compared with in situ observations. The results are notably compared with those obtained for the $FAO\text{-}2Kc_{Iobs}$ (in situ irrigation) and $FAO\text{-}2Kc_{Ks=1}$ (no stress) approaches. In summary, the validation strategy implies running the FAO-2Kc by using the water balance driven by i) the actual irrigation, ii) the irrigation simulated without stress (Ks = 1) and iii) the retrieved irrigation from our approach.

4. Results and discussions

The irrigation retrieval is applied to the four irrigated sites and to the rainfed site. Results are assessed in terms of the retrieved irrigation amount and timing, and in terms of the intermediate variables (RZSM and ET) needed in the irrigation retrieval algorithm.

4.1. Irrigation

Fig. 5 shows the comparison between the irrigation retrieved by the proposed methodology ($I_{FAO\text{-}2Kc_Landsat}$), the irrigation simulated by FAO-2Kc by avoiding stress ($I_{FAO\text{-}2Kc_Ks=1}$) and the actual irrigation (I_{obs}). The comparison is carried out for each site and season separately. Over flood-irrigated wheat fields in R3 area, six and five irrigation events are correctly estimated in the R3-4ha and R3-2ha field, respectively, against the seven and eight irrigations that were actually applied by the farmer. Note that the irrigation applied at the end of the development stage (equal to 64 and 36 mm in R3-4ha and -2ha, respectively) is missing over both sites. It could not be detected by the retrieval approach due to a virtual increase in the WB model of the root zone storage associated with the root growth. Thus, according to the WB model, no irrigation is needed in this period to supply the crop water needs. In R3-2ha field, three irrigation events are retrieved during the mid-season stage instead of the five irrigations applied by the farmer in the same period. That is because of i) the cloud-free Landsat data are widely separated (by 16 and 24 days) during this period and ii) the approach assumes a maximum irrigation amount by fully filling up the water storage capacity while the actual irrigations possibly do not reach this threshold and hence the number of retrieved irrigation events is generally reduced. The latter also explains the overestimation of irrigation amounts by event during the mid-season stage over both R3-4ha and R3-2ha fields. Indeed, in both sites, the irrigation amount estimated in the initial stage (i.e. beginning of the growing season) was much underestimated compared to the irrigation really applied by farmers. Regarding the irrigation dates in R3-4ha field, three first irrigation events are accurately detected with a time

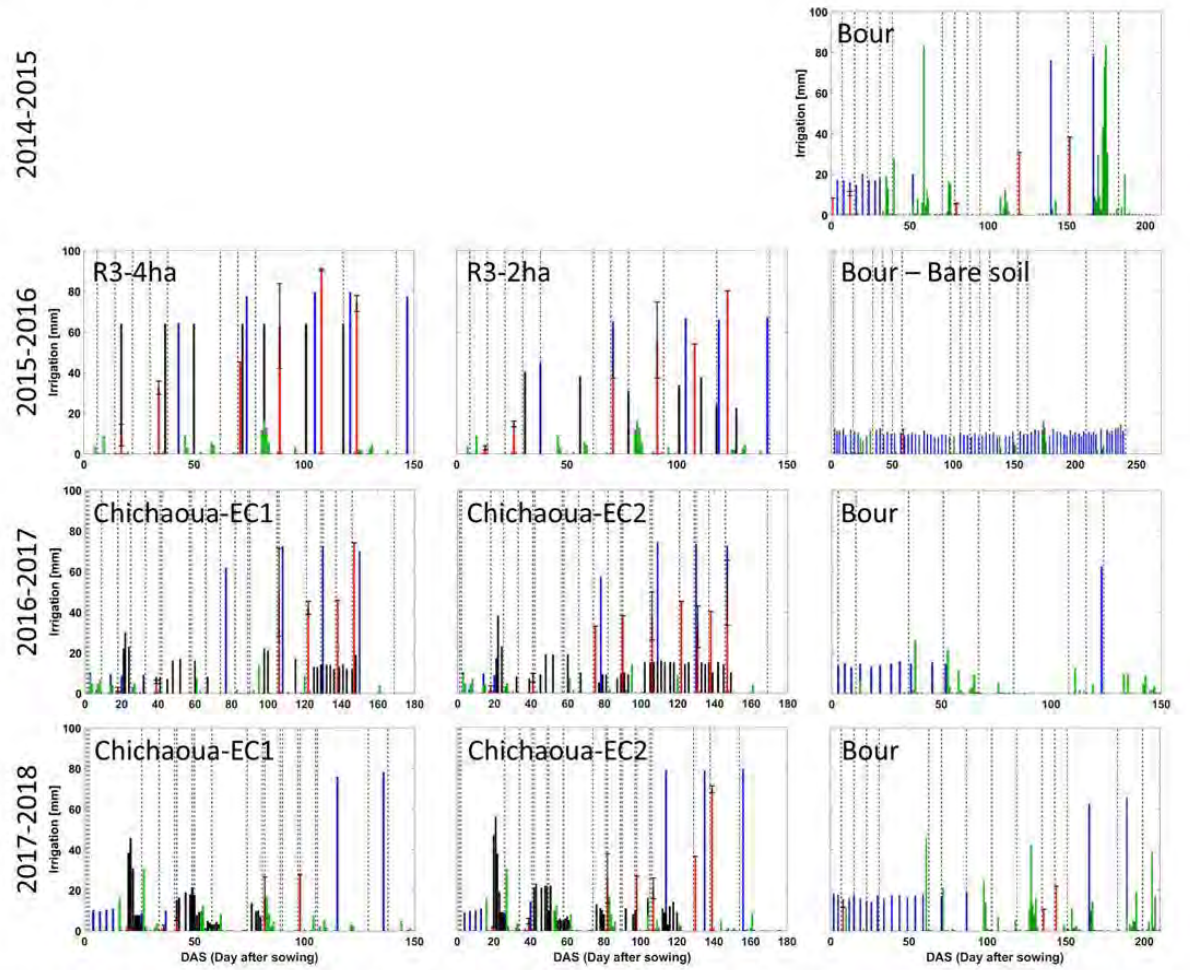


Fig. 5. Comparison between volumes and timing of the observed irrigation (black), irrigation triggered by avoiding stress (blue) and irrigation retrieved from the proposed approach (red) along the season for each site. The horizontal and vertical error bars represent the standard deviation of the retrieved irrigation dates and amounts, respectively. The green bar indicates the precipitation and the vertical dotted lines indicate the Landsat overpass dates. (For interpretation of the references to colour in this figure legend, the reader is referred to the web version of this article.)

difference about the actual events shorter than 3 days, while the last three irrigation events are poorly estimated with a time difference of about one week. The precision in the timing of retrieved irrigations is also closely linked to the frequency of cloud-free Landsat data over the crop field since the first irrigations are detected with an availability of Landsat data every 8 days, while the last irrigations are detected by using cloud-free images separated by 40 and 24 days. The difference between observed and retrieved irrigation (date and amount) may be also related to the inadequate amount and planning of irrigation by the farmer. In fact, irrigation amounts and timing are planned only by the understanding and perception of the farmer without using any guideline for scheduling the amount and timing of irrigation water applications. Consequently, some irrigations are missing and some are unnecessary.

Similarly, in Chichaoua area over both sites (EC-1 and EC-2) and seasons (2016–2018), the irrigations in the initial stage are underestimated while in the mid-season stage the amount by irrigation event is much overestimated. As it was mentioned for R3 fields, the fact that the FAO-based approach simulates water supplies by filling up the water storage capacity makes the amounts be modulated by the water storage capacity, which depends on the rooting depth Zr and the parameterization for soil properties and vegetation type (i.d. SM_{wp}, SM_{fc} and SM_{crit}). Consequently, during the initial stage when Zr is equal or close to its minimum value (set to 0.1 m) the water supplies to fill up the root zone are smaller while they are larger during the mid-season stage when Zr is close to 1 m. Moreover, as it is observed in all irrigated fields, applying large amounts of water supplies during initial stages is a common irrigation practice applied by the farmers, on the one hand, in order to store water in layers deeper than the actual root zone at the initial stage and, on the other hand, to avoid the appearance of soil crusting thus facilitating the plant emergence (Le Page et al., 2014). This is not taken into account in the proposed approach. Specifically over the drip-irrigated fields, the overestimation in irrigation amounts is partially explained by i) the irrigation frequency operated by the farmer (1–3 days), which is much higher than the Landsat temporal resolution (> 8 days) and ii) the small amounts applied without completely fill up the reservoir storage capacity (i.e. the RZSM does not necessarily reach the SM_{fc} after each irrigation). Regarding the stressed periods in EC1 site during the growing season 2016–2017, no irrigation was applied during the periods from DAS 68 to 97 and from DAS 101 to

114. In coherence, no irrigation is detected by our approach during the period DAS 68 to 97. However, an irrigation event of 49 mm is detected on DAS 106, which might represent two irrigations of 43 mm applied by the farmer one week before. Conversely in the EC2 field during the growing season 2016–2017, the farmer applied 8 irrigation events with amounts smaller than 10 mm every 2 days during two periods from DAS 77 to 81 and from DAS 87 to 95. During these two periods, our approach was able to detect one irrigation per period with amounts of 33 and 38 mm, respectively. These amounts are much larger than those applied by the farmer but they are together very close to the irrigation accumulated during both periods (68 mm).

In Sidi Rahal area, the rainfed wheat field is used as benchmark to evaluate where no irrigation should be retrieved. Only three significant irrigation events are detected in the 2014–2015 and 2017–2018 seasons while in the other seasons some irrigation events are estimated but with very small amounts lower than 15 mm. In the mid-season stage of the 2014–2015 season, two important irrigation events (31 and 38 mm) are retrieved from a significant difference between $RZSM_{RWB,j\text{-}Pj+1}$ and $RZSM_{Landsat,j\text{-}Pj}$ at date *j-Pj + 1* (situation (ii) of case 1 or 2). In this period between Landsat overpass dates, the water depleted from the crop consumption through ET minus the precipitation (according to the WB) is much larger than the difference of $RZSM_{Landsat}$ between dates *j* and *j-Pj*, which is thus translated in the retrieved irrigation amounts. That is partially explained by uncertainties in the estimation of ET, the water storage capacity (from SM_{wp}, SM_{fc} and Zr) or capillarity rises from deeper layers that are neglected in the approach.

Despite the differences between daily retrieved and actual irrigation, the proposed approach is able to accurately estimate the total irrigation amount applied at the seasonal time scale (see Fig. 6) with a correlation coefficient (R) equal to 0.95, a RMSE of 44 mm and a bias lower than 15 mm. Fig. 6 shows also the comparison with the classical approach FAO-$2Kc_{Ks=1}$, which provides poor estimates of irrigations due to a large overestimation (bias = 252 mm). Such an overestimation is explained by that fact that the FAO-$2Kc_{Ks=1}$ approach avoids the water stress, regardless of the crop water status. Following FAO-$2Kc_{Ks=1}$, the winter wheat fields would need between 300 and 400 mm by season, while both the irrigation applied by farmers and the retrieved irrigation were very different by field and by season. It should

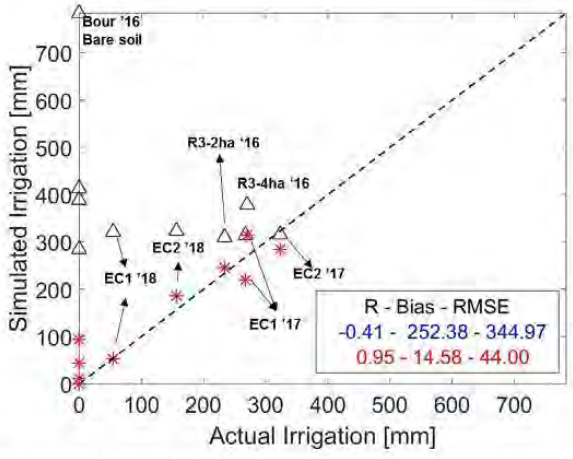


Fig. 6. Total irrigation depth applied by the farmer in the season is plotted versus the irrigation simulated by the FAO-2kc in order to avoid the water stress (blue, $I_{FAO\text{-}2Kc_Ks=1}$) and the irrigation retrieved by the proposed approach (red, $I_{FAO\text{-}2Kc_Landsat}$). The correlation coefficient (R), bias and root mean square error (RMSE) are shown for $I_{FAO\text{-}2Kc_Ks=1}$ and $I_{FAO\text{-}2Kc_Landsat}$. (For interpretation of the references to colour in this figure legend, the reader is referred to the web version of this article.)

be noted that in bare soil conditions (Bour 2015–2016), FAO-$2Kc_{Ks=1}$ estimates several irrigation events of small amounts. This is due to the top surface soil layer (set to 10 cm) that is quickly depleted by evaporation and needs to be re-filled frequently to maintain the Ks equal to 1. Note that the FAO-based approach assumes a minimum rooting depth (Zr_{min} set to 10 cm) even if there is no vegetation along the season. The root zone depletion and Ks are thus estimated in such conditions. As result, the total irrigation depth for Bour 2015–2016 season simulated by FAO-$2Kc_{Ks=1}$ is almost twice the wheat water requirements. The large simulated irrigation is also partly due to the low rainfall during this season and, consequently, the water balance requires larger water supply to maintain the Ks equal to 1. Over EC1 and EC2 fields in the 2016–2017 season, FAO-$2Kc_{Ks=1}$ obtained a total irrigation very close to that applied by the farmer because these sites were maintained unstressed during almost all the season.

A more comprehensive comparison at different time scales between the irrigation estimates from the classical approach FAO-$2Kc_{Ks=1}$ and the proposed approach FAO-$2Kc_{Landsat}$ is shown in Fig. 7. The irrigation amounts throughout the seasons are cumulated in overlapping windows of 1 day to 3 months (90 days). Overall, the proposed approach obtains a better performance than that of FAO-$2Kc_{Ks=1}$ with higher accuracies in term of R, bias and relative RMSE (RRMSE). With exception of two fields in Chichaoua area for 2017–2018 season, good agreements are reached over 15 days (R = 0.52 and RMSE = 27 mm) and then the agreements are further improved by increasing the accumulation period. Results for the fields in Chichaoua area for 2017–2018 season are relatively poor. This is mainly due to the stopping of irrigations early in the season (beginning of February for EC1 and mid-March for EC2) so that the water requirements were fulfilled mainly from the water stored in the soil or capillarity rise while the approach estimates significant irrigation amounts during that period. This problem can be partially explained by uncertainties and biases in the parameter values used to estimate the water storage capacity (SM_{wp}, SM_{fc} and Zr) and the capillarity rises from deeper layers that are neglected in the approach. Nevertheless, in spite of difficulties with monitoring drip irrigation, our approach has a better performance than the classical approach at every time scale, especially in terms of bias and RRMSE.

The results at different time scales indicate that the Landsat-based retrieval approach is robust for time intervals equal of longer than 2 weeks, which is the time period of Landsat acquisitions (~16 days). On the contrary, the approach generally fails in retrieving reliable cumulated irrigation for time periods shorter than 10 days by using the Landsat frequency. Therefore, we can expect significant improvements in the irrigation estimates at daily to weekly time scale by increasing the revisit frequency of LST data. Such high spatio-temporal resolution will be achieved by future thermal missions like TRISHNA (Lagouarde and Bhattacharya, 2018).

4.2. Daily RZSM and ET

Fig. 8 and Table 2 report the results of the irrigation retrieval approach in terms of daily RZSM in comparison with the classical approach FAO-$2Kc_{Ks=1}$ and the FAO-2Kc forced by actual irrigations (FAO-$2Kc_{Iobs}$). The daily RZSM simulated from FAO-$2Kc_{Iobs}$ obtains an overall R equal to 0.75 and a RMSE equal to 0.04 m^3/m^3, while the proposed approach obtains an R slightly lower (0.66) and the same RMSE value. FAO-$2Kc_{Ks=1}$ obtains a low R equal to 0.25 and a RMSE of 0.07 m^3/m^3, meaning a deterioration of about 65% with regard FAO-$2Kc_{Iobs}$. The similar performance between the proposed approach and FAO-$2Kc_{Iobs}$ demonstrates that the retrieved irrigation is correctly estimated in order to simulate the RZSM temporal dynamics similar to that retrieved from the FAO-2Kc forced by actual irrigations.

Similarly, Fig. 9 and Table 3 show the comparison between the proposed approach, FAO-$2Kc_{Iobs}$ and FAO-$2Kc_{Ks=1}$ in terms of daily ET. Overall, the proposed approach provides better performance than FAO-$2Kc_{Ks=1}$ and is very close to the FAO-$2Kc_{Iobs}$. However, particular

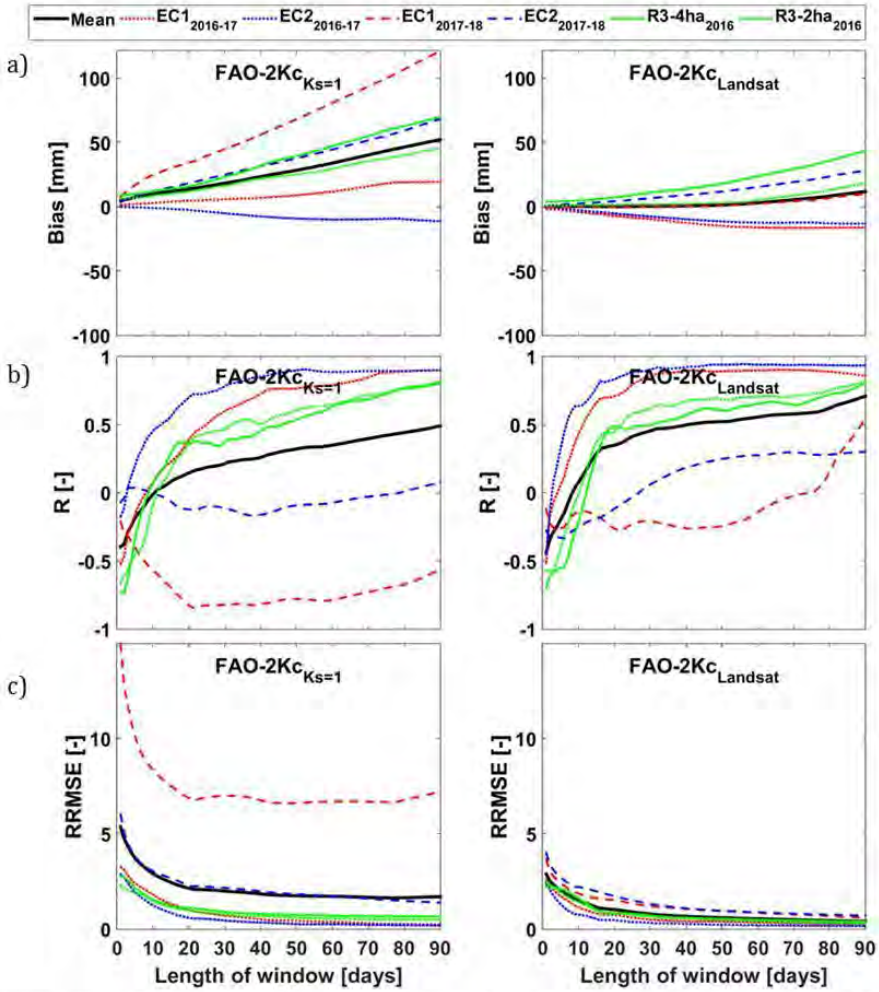


Fig. 7. Bias (a), correlation coefficient (R, b) and relative root mean square error (RRMSE, c) between observed and retrieved irrigation cumulated from 1 to 90 days through a moving window for site and season. The irrigation is retrieved by the proposed approach (FAO-2Kc$_{Landsat}$) and is also simulated by the FAO-2Kc in order to avoid water stress (FAO-2Kc$_{Ks=1}$).

results were obtained in the Chichaoua fields (EC1 and EC2). For 2016–2017 season, the FAO-2Kc$_{Ks=1}$ obtains better results than the proposed approach due to the Ks simulated from actual irrigations is equal to 1 during almost all the season while the Landsat-derived Ks detects stressed conditions (Ks$_{Landsat}$ < 1) during a large period in mid-season. In the 2017–2018 season, the proposed approach provides the best performance while results from FAO-2Kc$_{Iobs}$ are worse than the others. Since the three FAO-based models differ only in the irrigation to force the WB by using the same parameterization, the fact that FAO-2Kc$_{Iobs}$ obtains worse results confirms that over both sites the estimation of the water storage capacity and the capillarity rise is wrongly considered. This is also revealed during the mid-season stage when actual irrigation was stopped. Hence the irrigation retrieved by the proposed approach and by FAO-2Kc$_{Ks=1}$ during the mid-season stage compensates a too large water storage capacity or the (neglected) input of water from capillarity rise.

Note that FAO-2Kc$_{Ks=1}$ tends to overestimate the low ET rates typical of initial stages when the low vegetation cover makes the surface layer be quickly depleted by evaporation. In this stage, the top surface soil layer (set to 10 cm) is equal or very close to the root zone. The water storage after being depleted by evaporation, needs to be frequently re-filled to maintain the RZSM above the SM$_{crit}$ (Ks = 1) by triggering irrigations and the evaporation is thus maintained at maximum rate. This can be clearly observed in Bour site, with longer initial stages and particularly throughout the 2015–2016 season, when soil remained bare all the season.

Finally, the high accuracy in ET estimates from the proposed approach and from FAO-2Kc$_{Iobs}$ demonstrate the reliability of generic coefficients Kcb and Ke to be implemented with satellite data to estimate accurately ET at field scale over extended areas. The formulation of generic coefficients derived analytically (see Appendix A.3) from the link between the FAO-2Kc and a one source image-based model (SSEBop) allows avoiding calibration from in situ data that are rarely available over extended areas. Those generic coefficients would allow this implementation over different crop types although an extensive evaluation would be recommended.

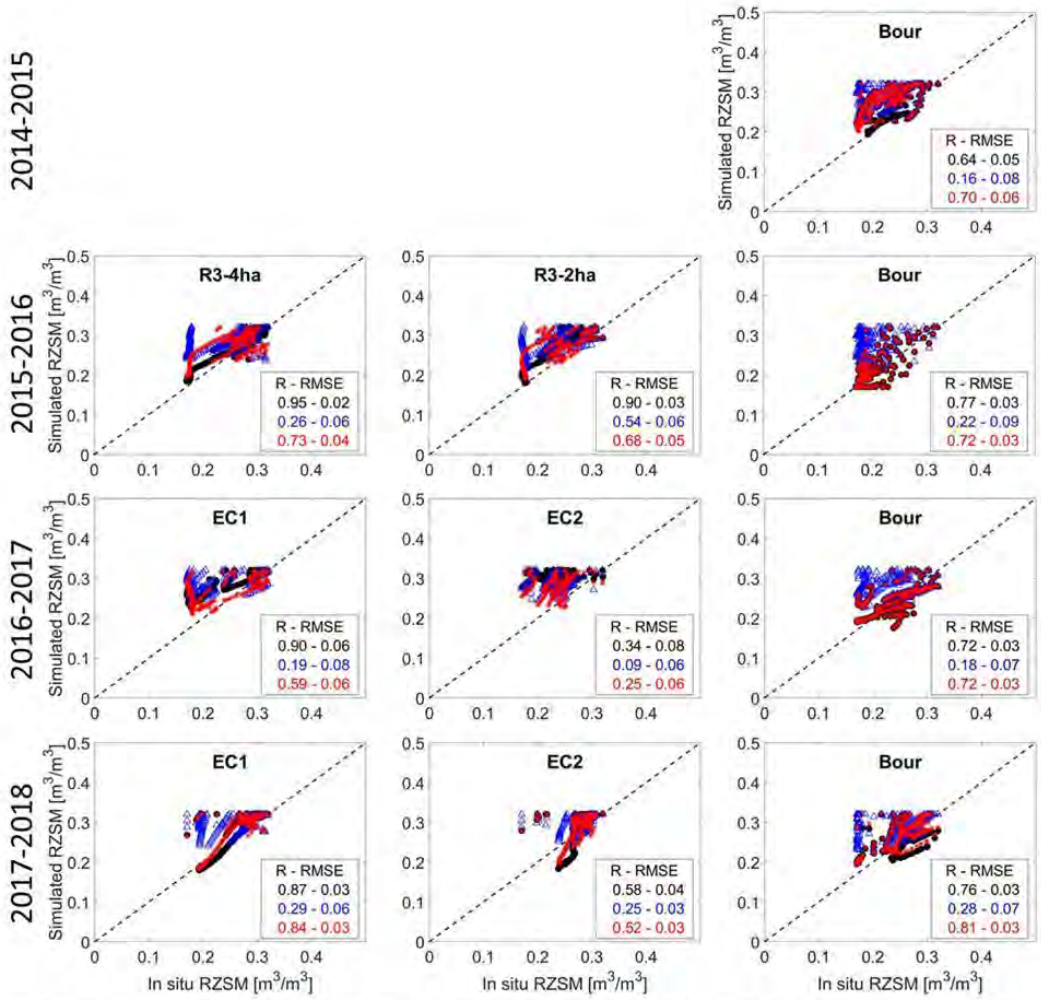


Fig. 8. Ground-based RZSM is plotted versus the RZSM simulated by the FAO-2Kc forced by observed irrigation (black), irrigation triggered by avoiding stress (blue) and irrigation retrieved from the proposed methodology (red). The correlation coefficient (R), bias and root mean square error (RMSE) are shown for RZSM from FAO-based models forced by the three different irrigation data sets. (For interpretation of the references to colour in this figure legend, the reader is referred to the web version of this article.)

Table 2
Correlation coefficient (R) and root mean square error (RMSE) between observed and simulated RZSM from FAO-2Kc forced by observed irrigation (FAO-2Kc$_{Iobs}$), irrigation triggered avoiding stress (FAO-2Kc$_{Ks=1}$) and irrigation retrieved from the proposed methodology (FAO-2Kc$_{Landsat}$).

Area	Site-season	R (−)			RMSE (m^3/m^3)		
		FAO-2Kc$_{Iobs}$	FAO-2Kc$_{Ks=1}$	FAO-2Kc$_{Landsat}$	FAO-2Kc$_{Iobs}$	FAO-2Kc$_{Ks=1}$	FAO-2Kc$_{Landsat}$
R3	R3-4ha-2016	0.95	0.26	0.73	0.02	0.06	0.04
	R3-2ha-2016	0.90	0.54	0.68	0.03	0.06	0.05
Chichaoua	EC1–2017	0.91	0.19	0.59	0.06	0.08	0.06
	EC2–2017	0.39	0.09	0.25	0.08	0.06	0.06
	EC1–2018	0.87	0.29	0.84	0.03	0.06	0.03
	EC2–2018	0.58	0.25	0.52	0.04	0.03	0.03
Sidi Rahal	Bour-2015	0.64	0.16	0.70	0.05	0.08	0.06
	Bour-2016	0.77	0.22	0.72	0.03	0.09	0.03
	Bour-2017	0.72	0.18	0.72	0.03	0.07	0.03
	Bour-2018	0.76	0.28	0.81	0.03	0.07	0.03
	All	0.75	0.25	0.66	0.04	0.07	0.04

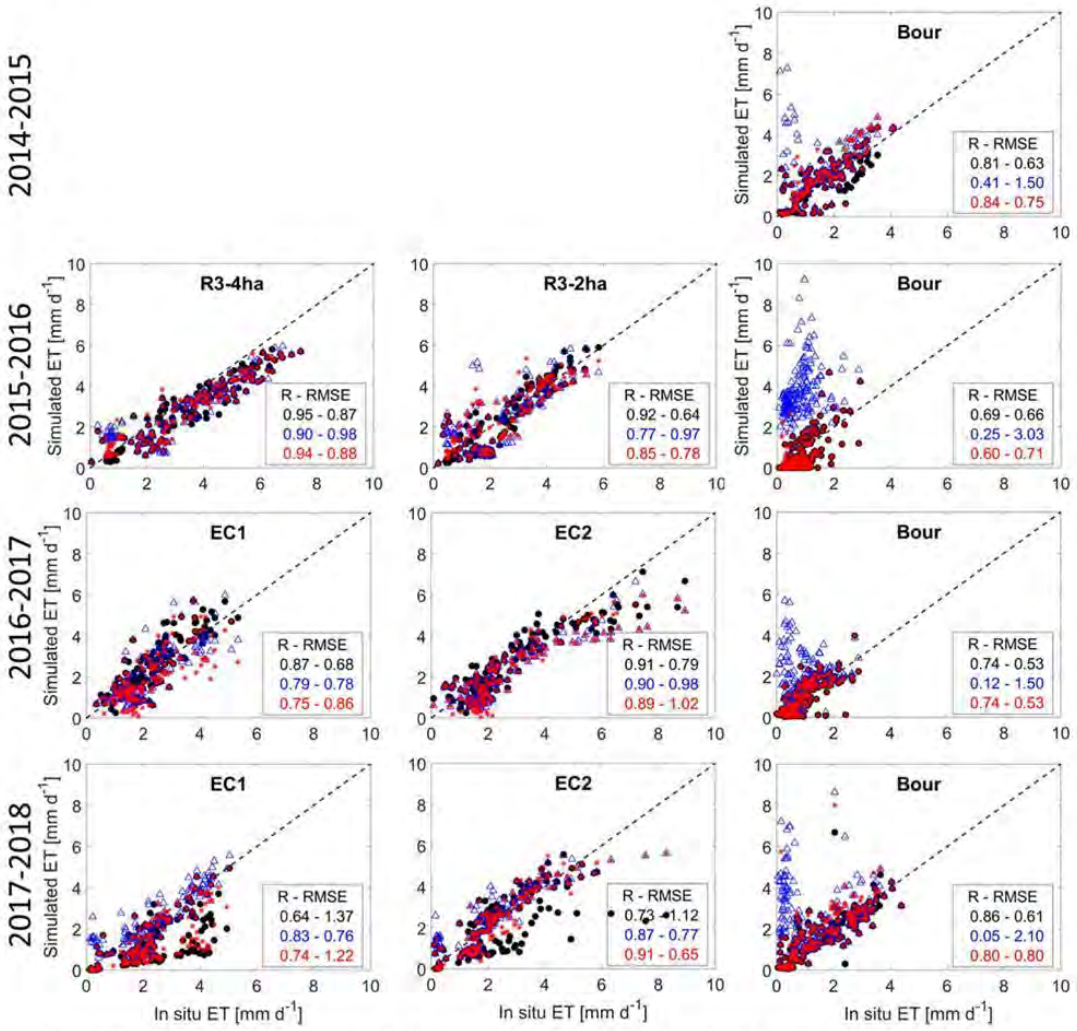


Fig. 9. Ground-based ET is plotted versus the ET simulated by from FAO-2Kc forced by observed irrigation (black, $ET_{FAO\text{-}2Kc_Iobs}$), irrigation triggered by avoiding stress (blue, $ET_{FAO\text{-}2Kc_Ks=1}$) and irrigation retrieved from the proposed methodology (red, $ET_{FAO\text{-}2Kc_Landsat}$). The correlation coefficient (R), bias and root mean square error (RMSE) are shown for $ET_{FAO\text{-}2Kc_Iobs}$, ET $ET_{FAO\text{-}2Kc_Ks=1}$ and $ET_{FAO\text{-}2Kc_Landsat}$. (For interpretation of the references to colour in this figure legend, the reader is referred to the web version of this article.)

Table 3
Correlation coefficient (R) and root mean square error (RMSE) between observed and simulated ET from FAO-2Kc forced by observed irrigation ($FAO\text{-}2Kc_{Iobs}$), irrigation triggered avoiding stress ($FAO\text{-}2Kc_{Ks=1}$) and irrigation retrieved from the proposed methodology ($FAO\text{-}2Kc_{Landsat}$).

Area	Site-season	R (−)			RMSE (mm/d)		
		$FAO\text{-}2Kc_{Iobs}$	$FAO\text{-}2Kc_{Ks=1}$	$FAO\text{-}2Kc_{Landsat}$	$FAO\text{-}2Kc_{Iobs}$	$FAO\text{-}2Kc_{Ks=1}$	$FAO\text{-}2Kc_{Landsat}$
R3	R3-4ha–2016	0.95	0.90	0.94	0.87	0.98	0.88
	R3-2ha–2016	0.92	0.77	0.85	0.68	0.97	0.78
Chichaoua	EC1–2017	0.87	0.79	0.75	0.89	0.88	0.94
	EC2–2017	0.91	0.90	0.89	0.85	1.00	1.06
	EC1–2018	0.64	0.83	0.74	1.37	0.76	1.22
	EC2–2018	0.73	0.87	0.91	1.12	0.77	0.65
Sidi Rahal	Bour–2015	0.81	0.41	0.84	0.63	1.50	0.75
	Bour–2016	0.69	0.25	0.60	0.66	3.03	0.71
	Bour–2017	0.74	0.12	0.74	0.53	1.50	0.53
	Bour–2018	0.86	0.05	0.80	0.61	2.10	0.80
	All	0.81	0.59	0.81	0.82	1.35	0.83

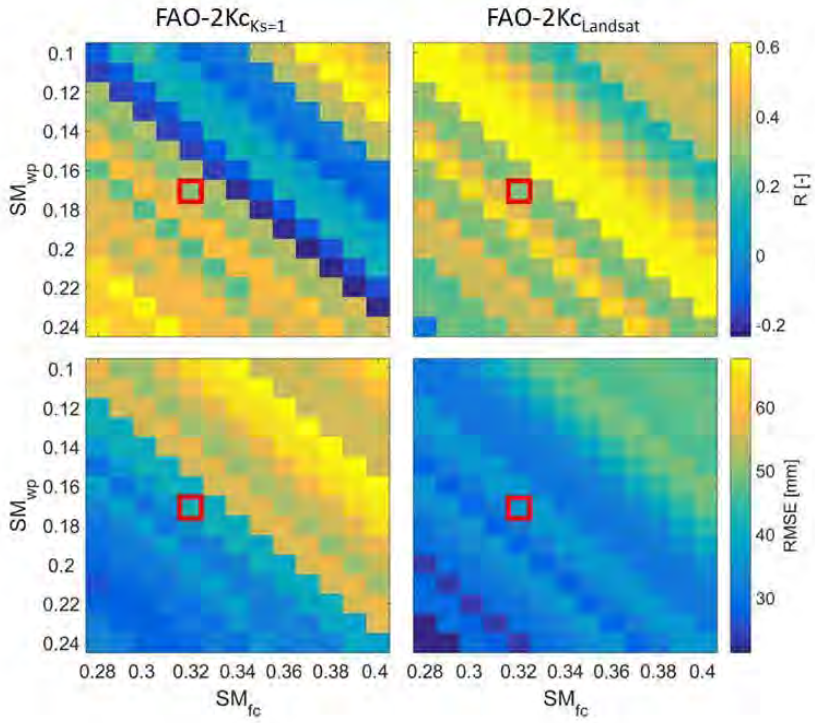


Fig. 10. Sensitivity analysis results for the soil parameters SM_{fc} and SM_{wp} by setting Zr_{max} set to 1.0 m. The irrigations are estimated by using SM_{fc} ranging between 0.28 and 0.40 m^3 m^{-3} and SM_{wp} ranging between 0.10 and 0.24 m^3 m^{-3}. The statistical parameter R (top) and RMSE (bottom) for actual irrigation accumulated over 15 days are estimated by using FAO-2Kc$_{Ks=1}$ (left) and FAO-2Kc$_{Landsat}$ (right) models. The red square indicates the SM_{fc} and SM_{wp} used in the approach. (For interpretation of the references to colour in this figure legend, the reader is referred to the web version of this article.)

4.3. Sensitivity analysis for soil parameters

The three main soil parameters (SM_{fc}, SM_{wp}, Zr) directly affect the water storage capacity and hence the estimation of the irrigation amount and timing. Note that SM_{crit} also affects the detection of irrigations and their amount particularly during unstressed periods (see Fig. 2). However, SM_{crit} is estimated from SM_{fc} and SM_{wp} and thus its impact is indirectly taken into account with SM_{fc} and SM_{wp}. SM_{crit} also depends on the crop tolerance to stress (fraction p) but as in Olivera-Guerra et al. (2018), the fraction p was considered constant for simplicity and because there is no significant difference for when using a constant or variable p (the variation in the overall RMSE and R^2 of simulated versus observed ET was found to be lower than 1%). Consequently, the sensitivity analysis is conducted for SM_{fc}, SM_{wp} and Zr only to assess the impact of uncertainties in soil parameters.

Fig. 10 depicts the sensitivity analysis for SM_{fc} and SM_{wp} in terms of retrieved irrigation by using the FAO-2Kc$_{Ks=1}$ and FAO-2Kc$_{Landsat}$ models over the site R3-4ha. The irrigation at daily scale are cumulated over 15 days and compared against cumulated actual irrigations. When looking at the variability of R and RMSE for irrigations from FAO-2Kc$_{Ks=1}$ and FAO-2Kc$_{Landsat}$, the later model is less sensitive to the soil parameters. The plots indicate that several optimal values can be found. This is due to the difference between SM_{fc} and SM_{wp} rather than the absolute value of each. Thus, the approach is sensitive to the water storage capacity defined by the difference between SM_{fc} and SM_{wp}, weighted by the root zone depth or in other words to the total available water (TAW = $Zr(SM_{fc} - SM_{wp})$). The higher R values of irrigation retrieved from FAO-2Kc$_{Landsat}$ suggest that the optimal difference ($SM_{fc} - SM_{wp}$) is between 0.17 and 0.19 m^3 m^{-3}, consistent with the values proposed by Allen et al. (1998) for clayey soils. However in this study, SM_{fc} and SM_{wp} are set to 0.32 and 0.17 m^3 m^{-3} respectively. Therefore, the approach can obtain a better performance by using optimal SM_{fc} and SM_{wp} values.

The root zone depth, which is estimated following the Appendix A.2, is also an important parameter in the water storage capacity. In the Eq. (A.1), the main parameter to be calibrated is Zr_{max}. Therefore, the same sensitivity analysis as for SM_{fc} and SM_{wp} was performed by using a Zr_{max} ranging from 0.5 to 1.5 m. These Zr_{max} values are typical for wheat fields, keeping in mind that 0.52 m was measured over a winter wheat field in the study area during the growing season 2002–2003 (Er-Raki et al., 2007), while Allen et al. (1998) propose values between 1 and 1.8 m for wheat fields. For Zr_{max} set to 0.5 m, optimal results in terms of irrigation accuracy are obtained for a difference ($SM_{fc} - SM_{wp}$) ranging from 0.25 to 0.27 m^3 m^{-3}, while by setting Zr_{max} to 1.5 m, optimal results are obtained for a difference ($SM_{fc} - SM_{wp}$) ranging from 0.12 to 0.13 m^3 m^{-3}. It is found that the optimal SM_{fc} and SM_{wp} values for Zr_{max} equal to 0.5 m and 1.5 m are not realistic for soils present in the study area. Indeed the difference 0.25–0.27 m^3 m^{-3} (Zr_{max} = 0.5 m) is much larger than that for clayey soils, and the difference of 0.12–0.13 m^3 m^{-3} (Zr_{max} = 1.5 m) is typical for sandy soils. Therefore, the sensitivity analysis shows that 1 m is a deemed acceptable value for Zr_{max} that allows obtaining both optimal and realistic SM_{fc} and SM_{wp} values for the main soils present in the study area.

Although good accuracies were found using uniform parameters, Fig. 10 indicates that the performance can still be improved if optimal values are used by properly adjusting them to the actual soil texture of the crop field.

5. Conclusion

A new approach to estimate the field-scale irrigation amounts and timing along the agricultural season is developed by integrating the Landsat optical and thermal data into a crop water balance (FAO-based) model. The main idea behind the approach is first to determine the irrigation date and then to estimate the irrigation amount as the difference between the RZSM estimated on the irrigation date and that estimated on the day before. In order to integrate the Landsat data into a crop water balance model and then to retrieve the irrigation at field

scale, four general procedures are implemented: i) partitioning the Landsat LST to derive the crop water stress coefficient Ks, ii) estimating the daily RZSM from the integration of Landsat-derived Ks into a crop water balance model, iii) retrieving irrigation at the Landsat pixel scale and iv) aggregating pixel-scale irrigation estimates at the crop field scale. The approach is assessed over three agricultural areas during four seasons and validated specifically on five winter wheat fields under different irrigation techniques (drip, flood and no-irrigation). The approach is validated in terms of irrigation estimates as well as daily RZSM and ET as intermediate variables linked to the crop water balance model. The approach is compared against the classical approach FAO-2Kc that simulates irrigations to avoid stressed conditions (FAO-$2Kc_{Ks=1}$) and the FAO-2Kc forced by actual irrigations (FAO-$2Kc_{Iobs}$).

The results depict that the proposed approach estimates accurately the total irrigation amounts over all the fields and seasons with a RMSE equal to 44 mm and an R of 0.95. To assess the performance of the irrigation retrieval method at different time scales along the seasons, the daily irrigations are cumulated over overlapping periods of 1 to 90 days (3 months). This analysis shows that acceptable errors are obtained for irrigations cumulated over 15 days and the performance is gradually improved by increasing the accumulation period. This period is closely linked to the revisit time of Landsat data that is 16 days or 8 day when combining Landsat-7 and Landsat-8 data, and often longer in cloudy conditions.

Although the approach does not allow obtaining good performances at daily to weekly scale in terms of irrigation amounts and timing, the daily RZSM and ET simulated from the retrieved irrigations are estimated accurately and are very close to those estimated from actual irrigations (FAO-$2Kc_{Iobs}$). Based on these results, we can conclude that:

i) The approach obtains acceptable errors in irrigation amount and timing in order to simulate the dynamic of water budget components along the season at daily and crop field scale.
ii) The formulation of generic coefficients Kcb and Ke, which are derived analytically from the link between the FAO-2Kc and the image-based model (SSEBop) formalisms allows its implementation to estimate ET accurately at field scale over extended areas by using satellite data. Hence, the Kcb and Ke allow generic implementations avoiding calibration, which usually needs in situ data that are rarely available over extended areas.

This new approach demonstrates the utility of optical and thermal data for estimating the irrigation and then for retrieving the water budget components of crops. However, significant improvements can be expected if the revisit time is reduced with a similar or even improved spatial resolution. In this vein, the advent of the TRISHNA mission at high spatio-temporal resolution in the thermal infrared (Lagouarde and Bhattacharya, 2018), will lead to substantial improvements in the estimation of irrigation at daily to weekly scale. Such an improvement will come not only from a shorter revisit cycles (~3 days), but also from a higher spatial resolution (~50 m), being more suitable for monitoring water consumption at crop field scale. Additionally, some improvements are foreseen to better estimate irrigation timing and the soil coefficients. Better constraining the topsoil layer (soil moisture) would improve the estimation of Kr and Ke coefficients. This issue will be addressed in future studies by integrating the surface soil moisture through a soil evaporative efficiency model (Merlin et al., 2016), which can be derived from active C-band Sentinel-1 data (Amazirh et al., 2018).

Author contributions

Conceptualization: L. Olivera-Guerra and O. Merlin;
Methodology: L. Olivera-Guerra and O. Merlin.
Validation: L. Olivera-Guerra.
Supervision: O. Merlin and S. Er-Raki.
Investigation: L. Olivera-Guerra.
Resources: O. Merlin and S. Er-Raki.
Data curation, L. Olivera-Guerra.
Visualization: L. Olivera-Guerra.
Writing—original draft preparation: L. Olivera-Guerra and O. Merlin.
Writing—review and editing: L. Olivera-Guerra, O. Merlin and S. Er-Raki.

Declaration of competing interest

The authors declare that they have no known competing financial interests or personal relationships that could have appeared to influence the work reported in this paper.

Acknowledgement

This study was supported by the European Commission Horizon 2020 Programme for Research and Innovation (H2020) in the context of the Marie Sklodowska-Curie Research and Innovation Staff Exchange (RISE) action (REC project, grant agreement no: 645642 followed by ACCWA project, grant agreement no: 823965). L. Olivera-Guerra acknowledges the support from CONICYT-Chile through the PhD fellowship "BecasChile de Doctorado en el Extranjero" (grant agreement no: 4721/2016).

Appendix A

A.1. Rooting depth Zr

Zr varies according to the vegetation cover between a minimum value (Zr_{min} set to 0.1 m) and a maximum value (Zr_{max} set to 1 m at fv = 1) and is expressed as:

$$Zr_t = Zr_{min} + fv_t\,(Zr_{max} - Zr_{min}) \quad (A.1)$$

where fv_t is the daily fv interpolated from the Landsat fv estimates. Note that once Zr_t reaches its maximum value at the maximum fv_t it is maintained constant until the end of the season.

A.2. Uncertainty in Landsat-derived RZSM

The Landsat-derived $RZSM_{Landsat,j}$ at date j in the Eq. (5) can be expressed as:

$$RZSM_{Landsat,j} = SM_{wp} + Ks_{Landsat,j}\,(1-p)(SM_{fc} - SM_{wp}) \quad (A.2)$$

with p being the tolerance of crop to water stress as a fraction of the total available water. The uncertainty in $RZSM_{Landsat,j}$ is estimated from the propagation of uncertainty method, which takes into account a relative error of every independent variable in the Eq. (A.2) through its partial derivatives. We consider an error of 10% ($\varepsilon = 0.1$) for every variable and therefore the uncertainty in $RZSM_{Landsat,j}$ can be analytically written as:

$$e_{RZSM_{Landsat,j}} = \{SM_{wp} + Ks_{Landsat,j}(2 - 3p)(SM_{fc} - SM_{wp})\}\varepsilon \quad (A.3)$$

A.3. Landsat-derived Kcb and Ke

In order to take advantage of satellite data for generic implementations, we link the FAO-2Kc formalism with a contextual model to estimate the main parameters Kcb and Ke. As it is expressed in Eq. (A.4), the dual crop coefficient FAO-2Kc ET is made equal to the single source Operational Simplified Surface Energy Balance (SSEBop, Senay et al., 2013) formalism in order to derive the coefficients required in FAO-2Kc.

$$(Ks \cdot Kcb + Ke)ET_0 = ET = EF \cdot Kc_{max} \cdot ET_0 \quad (A.4)$$

where ET0 is the reference evapotranspiration, EF the evaporative fraction (defined as the ratio of ET to available energy) and Kc_{max} the coefficient to scale the ET_0 down to the maximum ET reached by a crop. On the left-hand side of the equation, FAO-2Kc model estimates the ET from a crop basal coefficient (Kcb) and an evaporation coefficient (Ke), respectively, weighted by ET_0. The transpiration component (Kcb ET_0) is controlled by the crop stress coefficient (Ks) and the evaporation (Ke ET_0) is controlled by the evaporation reduction coefficient (Kr). On the right-hand side of the equation, SSEBop uses Kc_{max} modulated by EF as a single crop coefficient containing the transpiration and evaporation coefficients. EF can be estimated as:

$$EF = \frac{LST_{max} - LST}{LST_{max} - LST_{min}} \quad (A.5)$$

where LST_{min} and LST_{max} are the minimum and maximum LST representing the wet/unstressed and dry/stressed conditions (see Fig. 3), respectively, as has been used in several contextual methods (e.g. Roerink et al., 2000; Merlin et al., 2013; Merlin et al., 2014). Given that Kr, Ks and EF are estimated from thermal and fv data in our study, every term used in (A.5) is partitioned into its vegetation and soil components in such a way that Ke and Kcb formulations can be analytically derived from the equality in Eq. (A.4), as it is described below.

By partitioning every term in A.5, EF can be expressed as:

$$EF = \frac{[fvTv_{max} + (1 - fv)Ts_{max}] - [fvTv + (1 - fv)Ts]}{[fvTv_{max} + (1 - fv)Ts_{max}] - [fvTv_{min} + (1 - fv)Ts_{min}]} \quad (A.6)$$

By introducing the Landsat-derived Ks and Kr into A.6, SSEBop ET in Eq. (A.4) can be rewritten as:

$$ET = \left[\frac{fv(Tv_{max} - Tv_{min})Ks + (1 - fv)(Ts_{max} - Ts_{min})Kr}{fv(Tv_{max} - Tv_{min}) + (1 - fv)(Ts_{max} - Ts_{min})} \cdot Kc_{max}\right] \cdot ET_0 \quad (A.7)$$

For clarity we set $\Delta Tv = Tv_{max} - Tv_{min}$ and $\Delta Ts = Ts_{max} - Ts_{min}$ in A.7. By re-arranging, two terms related to the vegetation and soil components are highlighted:

$$ET = \left[\frac{fv(\Delta Tv)Ks}{fv(\Delta Tv) + (1 - fv)(\Delta Ts)}Kc_{max} + \frac{(1 - fv)(\Delta Ts)Kr}{fv(\Delta Tv) + (1 - fv)(\Delta Ts)}Kc_{max}\right] \cdot ET_0 \quad (A.8)$$

where the first term in parentheses can be considered as the transpiration coefficient (Ks Kcb) and the second as Ke, as they are depicted in the FAO-2Kc formalism (Eq. (A.4)). To simplify Kcb and Ke formulations, ΔTv is assumed close to ΔTs in A.8 as in previous works (Olivera-Guerra et al., 2018; Stefan et al., 2015). Hence the following simple expressions are derived:

$$Kcb = fvKc_{max} \quad (A.9)$$

$$Ke = (1 - fv)KrKc_{max} \quad (A.10)$$

where Kcb depends on *fv* while Ke depends on the soil fraction (*1 – fv*) weighted by Kr and Kc_{max}. These expressions are consistent with the FAO-2kc calibrated with vegetation index proposed in the literature (e.g. Er-Raki et al., 2010; Kullberg et al., 2016; Simonneaux et al., 2008). In this study, Kc_{max} is set to 1.2 as a typical recommended value (Allen et al., 2011; Senay et al., 2013; Senay et al., 2016).

References

Ait Hssaine, B., Merlin, O., Rafi, Z., Ezzahar, J., Jarlan, L., Khabba, S., Er-Raki, S., 2018. Calibrating an evapotranspiration model using radiometric surface temperature, vegetation cover fraction and near-surface soil moisture data. Agric. For. Meteorol. 256–257, 104–115. https://doi.org/10.1016/J.AGRFORMET.2018.02.033.

Allen, R.G., Pereira, L.S., Raes, D., Smith, M., 1998. Crop Evapotranspiration - Guidlines for Computing Crop Water Requirements. Irrig. Drainage. Pap 56 Food Agriculture. Organ. United Nations, Rome, Italy.

Allen, R.G., Pereira, L.S., Howell, T., Jensen, M.E., 2011. Evapotranspiration information reporting: I. factors governing measurement accuracy. Agric. Water Manag. 98, 899–920. https://doi.org/10.1016/j.agwat.2010.12.015.

Amazirh, A., Er-Raki, S., Chehbouni, A., Rivalland, V., Diarra, A., Khabba, S., Ezzahar, J., Merlin, O., 2017. Modified penman–Monteith equation for monitoring evapotranspiration of wheat crop: relationship between the surface resistance and remotely sensed stress index. Biosyst. Eng. 164, 68–84. https://doi.org/10.1016/j.biosystemseng.2017.09.015.

Amazirh, A., Merlin, O., Er-Raki, S., Gao, Q., Rivalland, V., Malbeteau, Y., Khabba, S., Escorihuela, M.J., 2018. Retrieving surface soil moisture at high spatio-temporal resolution from a synergy between Sentinel-1 radar and Landsat thermal data: a study case over bare soil. Remote Sens. Environ. 211, 321–337. https://doi.org/10.1016/j.rse.2018.04.013.

Amazirh, A., Merlin, O., Er-Raki, S., 2019. Including Sentinel-1 radar data to improve the disaggregation of MODIS land surface temperature data. ISPRS J. Photogramm. Remote Sens. 150, 11–26. https://doi.org/10.1016/j.isprsjprs.2019.02.004.

Anderson, M.C., Allen, R.G., Morse, A., Kustas, W.P., 2012. Use of Landsat thermal imagery in monitoring evapotranspiration and managing water resources. Remote Sens. Environ. 122, 50–65. https://doi.org/10.1016/j.rse.2011.08.025.

Baldridge, A.M., Hook, S.J., Grove, C.I., Rivera, G., 2009. The ASTER spectral library version 2.0. Remote Sens. Environ. 113, 711–715. https://doi.org/10.1016/j.rse.2008.11.007.

Bastiaanssen, W.G.M., Allen, R.G., Droogers, P., D'Urso, G., Steduto, P., 2007. Twenty-five years modeling irrigated and drained soils: state of the art. Agric. Water Manag. 92, 111–125. https://doi.org/10.1016/j.agwat.2007.05.013.

Battude, M., Al, A., Brut, A., Tallec, T., Huc, M., Cros, J., Weber, J., Lhuissier, L., Simonneaux, V., 2017. Modeling water needs and total irrigation depths of maize crop in the south west of France using high spatial and temporal resolution satellite imagery. Agric. Water Manag. 189, 123–136. https://doi.org/10.1016/j.agwat.2017.04.018.

Boulet, G., Chehbouni, A., Gentine, P., Duchemin, B., Ezzahar, J., Hadria, R., 2007. Monitoring water stress using time series of observed to unstressed surface temperature difference. Agric. For. Meteorol. 146, 159–172. https://doi.org/10.1016/j.agrformet.2007.05.012.

Brocca, L., Ciabatta, L., Massari, C., Camici, S., Tarpanelli, A., 2017. Soil moisture for hydrological applications: open questions and new opportunities. Water (Switzerland) 9. https://doi.org/10.3390/w9020140.

Brocca, L., Tarpanelli, A., Filippucci, P., Dorigo, W., Zaussinger, F., Gruber, A., Fernández-Prieto, D., 2018. How much water is used for irrigation? A new approach exploiting coarse resolution satellite soil moisture products. Int. J. Appl. Earth Obs. Geoinf. 73,

752–766. https://doi.org/10.1016/j.jag.2018.08.023.
Chehbouni, A., Escadafal, R., Duchemin, B., Boulet, G., Simonneaux, V., Dedieu, G., Mougenot, B., Khabba, S., Kharrou, H., Maisongrande, P., Merlin, O., Chaponnière, A., Ezzahar, J., Er-Raki, S., Hoedjes, J., Hadria, R., Abourida, A., Cheggour, A., Raibi, F., Boudhar, A., Benhadj, I., Hanich, L., Benkaddour, A., Guemouria, N., Chehbouni, A.H., Lahrouni, A., Olioso, A., Jacob, F., Williams, D.G., Sobrino, J.A., 2008. An integrated modelling and remote sensing approach for hydrological study in arid and semi-arid regions: the SUDMED programme. Int. J. Remote Sens. 29, 5161–5181. https://doi.org/10.1080/01431160802036417.
Chen, Y., Lu, D., Luo, L., Pokhrel, Y., Deb, K., Huang, J., Ran, Y., 2018. Detecting irrigation extent, frequency, and timing in a heterogeneous arid agricultural region using MODIS time series, Landsat imagery, and ancillary data. Remote Sens. Environ. 204, 197–211. https://doi.org/10.1016/j.rse.2017.10.020.
Corbari, C., Ceppi, A., Telesca, V., Mancini, M., 2019. Smart irrigation forecast using satellite LANDSAT data and meteo- hydrological modeling. Agric. Water Manag. 212, 283–294. https://doi.org/10.1016/j.agwat.2018.09.005.
Droogers, P., Immerzeel, W.W., Lorite, I.J., 2010. Estimating actual irrigation application by remotely sensed evapotranspiration observations. Agric. Water Manag. 97, 1351–1359. https://doi.org/10.1016/j.agwat.2010.03.017.
Duan, S.B., Li, Z.L., Wang, C., Zhang, S., Tang, B.H., Leng, P., Gao, M.F., 2018. Land-surface temperature retrieval from Landsat 8 single-channel thermal infrared data in combination with NCEP reanalysis data and ASTER GED product. Int. J. Remote Sens. 00, 1–16. https://doi.org/10.1080/01431161.2018.1460513.
Duchemin, B., Hadria, R., Er-Raki, S., Boulet, G., Maisongrande, P., Chehbouni, A., Escadafal, R., Ezzahar, J., Hoedjes, J.C.B., Kharrou, M.H., Khabba, S., Mougenot, B., Olioso, A., Rodriguez, J.-C., Simonneaux, V., 2006. Monitoring wheat phenology and irrigation in Central Morocco: On the use of relationships between evapotranspiration, crops coefficients, leaf area index and remotely-sensed vegetation indices. Agric. Water Manag. 79, 1–27. https://doi.org/10.1016/j.agwat.2005.02.013.
Duchemin, B., Maisongrande, P., Boulet, G., Benhadj, I., 2008. A simple algorithm for yield estimates: evaluation for semi-arid irrigated winter wheat monitored with green leaf area index. Environ. Model. Softw. 23, 876–892. https://doi.org/10.1016/j.envsoft.2007.10.003.
Er-Raki, S., Chehbouni, A., Duchemin, B., 2010. Combining satellite remote sensing data with the FAO-56 dual approach for water use mapping in irrigated wheat fields of a semi-arid region. Remote Sens. 2, 375–387. https://doi.org/10.3390/rs2010375.
Er-Raki, S., Chehbouni, A., Guemouria, N., Duchemin, B., Ezzahar, J., Hadria, R., 2007. Combining FAO-56 model and ground-based remote sensing to estimate water consumptions of wheat crops in a semi-arid region. Agric. Water Manag. 87. 41–54. https://doi.org/10.1016/j.agwat.2006.02.004.
Escorihuela, M.J., Quintana-Seguí, P., 2016. Comparison of remote sensing and simulated soil moisture datasets in Mediterranean landscapes. Remote Sens. Environ. 180, 99–114. https://doi.org/10.1016/j.rse.2016.02.046.
Foley, J.A., Ramankutty, N., Brauman, K.A., Cassidy, E.S., Gerber, J.S., Johnston, M., Mueller, N.D., O'Connell, C., Ray, D.K., West, P.C., Balzer, C., Bennett, E.M., Carpenter, S.R., Hill, J., Monfreda, C., Polasky, S., Rockström, J., Sheehan, J., Siebert, S., Tilman, D., Zaks, D.P.M., 2011. Solutions for a cultivated planet. Nature 478, 337–342. https://doi.org/10.1038/nature10452.
Garrido, A., Llamas, M.R., Varela-Ortega, C., Novo, P., Rodríguez-Casado, R., Aldaya, M.M., 2010. Water Footprint and Virtual Water Trade in Spain. Policy Implications. Series: Natural Resource Management and Policy 35. pp. 150. https://doi.org/10.1007/978-1-4419-5741-2. IX.
Giorgi, F., 2006. Climate change hot-spots. Geophys. Res. Lett. 33, 1–4. https://doi.org/10.1029/2006GL025734.
Gowda, P.H., Chavez, J.L., Colaizzi, P.D., Evett, S.R., Howell, T.A., Tolk, J.A., 2008. ET mapping for agricultural water management: present status and challenges. Irrig. Sci. 26, 223–237. https://doi.org/10.1007/s00271-007-0088-6.
Gutman, G., Ignatov, A., 1998. The derivation of the green vegetation fraction from NOAA/AVHRR. Int. J. Remote Sens. 19 (8), 1533–1543. https://doi.org/10.1080/014311698215333.
Hain, C.R., Mecikalski, J.R., Anderson, M.C., 2009. Retrieval of an available water-based soil moisture proxy from thermal infrared remote sensing. Part I: methodology and validation. J. Hydrometeorol. 10, 665–683. https://doi.org/10.1175/2008JHM1024.1.
IPCC, 2013. Climate change 2013: The physical science basis. In: Stocker, T.F. (Ed.), Contribution of Working Group I to the Fifth Assessment Report of the Intergovernmental Panel on Climate Change. Cambridge University Press, Cambridge, United Kingdom and New York, NY, USA, pp. 1535.0.
Jalilvand, E., Tajrishy, M., Ghazi Zadeh Hashemi, S.A., Brocca, L., 2019. Quantification of irrigation water using remote sensing of soil moisture in a semi-arid region. Remote Sens. Environ. 231, 111226. https://doi.org/10.1016/j.rse.2019.111226.
Jiang, L., Islam, S., 2003. An intercomparison of regional latent heat flux estimation using remote sensing data. Int. J. Remote Sens. 24, 2221–2236. https://doi.org/10.1080/0143116021015482l.
Jiménez-Munoz, J.C., Sobrino, J.A., Sòria, G., Cristobal, J., Pons, X., Ninyerola, M., 2009. Revision of the single-channel algorithm for land surface temperature retrieval from landsat thermal-infrared data. IEEE Trans. Geosci. Remote Sens. 47, 339–349. https://doi.org/10.1109/TGRS.2008.2007125.
Jiménez-Muñoz, J.C., Sobrino, J.A., Skoković, D., Mattar, C., Cristóbal, J., 2014. Land surface temperature retrieval methods from Landsat-8 thermal infrared sensor data. Geosci. Remote Sens. Lett. IEEE 11, 1840–1843. https://doi.org/10.1109/LGRS.2014.2312032.
Kalma, J.D., McVicar, T.R., McCabe, M.F., 2008. Estimating land surface evaporation: a review of methods using remotely sensed surface temperature data. Surv. Geophys. 29, 421–469. https://doi.org/10.1007/s10712-008-9037-z.
Kullberg, E.G., DeJonge, K.C., Chávez, J.L., 2016. Evaluation of thermal remote sensing indices to estimate crop evapotranspiration coefficients. Agric. Water Manag. 179, 64–73. https://doi.org/10.1016/j.agwat.2016.07.007.
Kumar, S.V., Peters-Lidard, C.D., Santanello, J.A., Reichle, R.H., Draper, C.S., Koster, R.D., Nearing, G., Jasinski, M.F., 2015. Evaluating the utility of satellite soil moisture retrievals over irrigated areas and the ability of land data assimilation methods to correct for unmodeled processes. Hydrol. Earth Syst. Sci. 19, 4463–4478. https://doi.org/10.5194/hess-19-4463-2015.
Lagouarde, J., Bhattacharya, B.K., 2018. TRISHNA: A new high spatio-temporal resolution Indian-French mission in the thermal infrared. In: Remote Sensing and Hydrology Symposium (ICRS-IAHS).
Lawston, P.M., Santanello, J.A., Kumar, S.V., 2017. Irrigation signals detected from SMAP soil moisture retrievals. Geophys. Res. Lett. 44, 11,860–11,867. https://doi.org/10.1002/2017GL075733.
Le Page, M., Toumi, J., Khabba, S., Hagolle, O., Tavernier, A., Hakim Kharrou, M., Er-Raki, S., Huc, M., Kasbani, M., Moutamanni, A.E., Yousfi, M., Jarlan, L., 2014. A life-size and near real-time test of irrigation scheduling with a sentinel-2 like time series (SPOT4-Take5) in Morocco. Remote Sens. 6, 11182–11203. https://doi.org/10.3390/rs61111182.
Li, Z.-L., Tang, R., Wan, Z., Bi, Y., Zhou, C., Tang, B., Yan, G., Zhang, X., 2009. A review of current methodologies for regional evapotranspiration estimation from remotely sensed data. Sensors (Basel) 9, 3801–3853. https://doi.org/10.3390/s90503801.
Long, D., Singh, V.P., 2012. A two-source trapezoid model for evapotranspiration (TTME) from satellite imagery. Remote Sens. Environ. 121, 370–388. https://doi.org/10.1016/j.rse.2012.02.015.
Malakar, N.K., Hulley, G.C., Hook, S.J., Laraby, K., Cook, M., Schott, J.R., 2018. An operational land surface temperature product for Landsat thermal data: methodology and validation. IEEE Trans. Geosci. Remote Sens. 5717–5735. https://doi.org/10.1109/TGRS.2018.2824828.
Malbéteau, Y., Merlin, O., Balsamo, G., Er-Raki, S., Khabba, S., Walker, J.P., Jarlan, L., 2018. Toward a surface soil moisture product at high spatiotemporal resolution: temporally interpolated, spatially disaggregated SMOS data. J. Hydrometeorol. 19. 183–200. https://doi.org/10.1175/jhm-d-16-0280.1.
Merlin, O., 2013. An original interpretation of the wet edge of the surface temperature-albedo space to estimate crop evapotranspiration (SEB-1S), and its validation over an irrigated area in northwestern Mexico. Hydrol. Earth Syst. Sci. 17, 3623–3637. https://doi.org/10.5194/hess-17-3623-2013.
Merlin, O., Rüdiger, C., Bitar, A.A., Richaume, P., Walker, J.P., Kerr, Y.H., 2012. Disaggregation of SMOS soil moisture in southeastern Australia. IEEE Trans. Geosci. Remote Sens. 50, 1556–1571.
Merlin, O., Escorihuela, M.J., Mayoral, M.A., Hagolle, O., Al Bitar, A., Kerr, Y., 2013. Self-calibrated evaporation-based disaggregation of SMOS soil moisture: an evaluation study at 3km and 100m resolution in Catalunya, Spain. Remote Sens. Environ. 130, 25–38. https://doi.org/10.1016/j.rse.2012.11.008.
Merlin, O., Chirouze, J., Olioso, A., Jarlan, L., Chehbouni, G., Boulet, G., 2014. An image-based four-source surface energy balance model to estimate crop evapotranspiration from solar reflectance/thermal emission data (SEB-4S). Agric. For. Meteorol. 184, 188–203. https://doi.org/10.1016/j.agrformet.2013.10.002.
Merlin, O., Stefan, V.G., Amazirh, A., Chanzy, A., Ceschia, E., Tallec, T., Beringer, J., Gentine, P., Er-Raki, S., Bircher, S., Khabba, S., 2016. Modeling soil evaporation efficiency in a range of soil and atmospheric conditions: a downward approach based on multi-site data. Water Resour. Res. 52, 3663–3684. https://doi.org/10.1002/2015WR018233.
Merlin, O., Olivera-guerra, L., Aït, B., Amazirh, A., Ra, Z., Ezzahar, J., Gentine, P., Khabba, S., Gascoin, S., Er-raki, S., 2018. A phenomenological model of soil evaporative efficiency using surface soil moisture and temperature data. Agric. For. Meteorol. 256–257, 501–515. https://doi.org/10.1016/j.agrformet.2018.04.010.
Molero, B., Merlin, O., Malbéteau, Y., Al Bitar, A., Cabot, F., Stefan, V., Kerr, Y., Bacon, S., Cosh, M.H., Bindlish, R., Jackson, T.J., 2016. SMOS disaggregated soil moisture product at 1 km resolution: processor overview and first validation results. Remote Sens. Environ. 180, 361–376. https://doi.org/10.1016/j.rse.2016.02.045.
Moran, M.S., Clarke, T.R., Inoue, Y., Vidal, A., 1994. Estimating crop water deficit using the relation between surface-air temperature and spectral vegetation index. Remote Sens. Environ. 49, 246–263. https://doi.org/10.1016/0034-4257(94)90020-5.
Norman, J.M., Kustas, W.P., Humes, K.S., 1995. A two-source approach for estimating soil and vegetation energy fluxes in observations of directional radiometric surface temperature. Agric. For. Meteorol. 77, 263–293. https://doi.org/10.1016/0168-1923(95)02265-Y.
Ogawa, K., Schmugge, T., 2004. Mapping surface broadband emissivity of the Sahara Desert using ASTER and MODIS data. Earth Interact. 8, 1–14. https://doi.org/10.1175/1087-3562(2004)008<0001:MSBEOT>2.0.CO;2.
Olivera-Guerra, L., Merlin, O., Er-raki, S., Khabba, S., Escorihuela, M.-J., 2018. Estimating the water budget components of irrigated crops: combining the FAO-56 dual crop coefficient with surface temperature and vegetation index data. Agric. Water Manag. 208, 120–131. https://doi.org/10.1016/j.agwat.2018.06.014.
Peng, J., Loew, A., Merlin, O., Verhoest, N.E.C., 2017. A review of spatial downscaling of satellite remotely sensed soil moisture. Rev. Geophys. 55, 341–366. https://doi.org/10.1002/2016RG000543.
Rafi, Z., Merlin, O., Le Dantec, V., Khabba, S., Mordelet, P., Er-raki, S., Amazirh, A., Olivera-guerra, L., Ait Hssaine, B., 2019. Partitioning evapotranspiration of a drip-irrigated wheat crop: inter- comparing eddy covariance-, sap flow-, lysimeter- and FAO-based methods. Agric. For. Meteorol. 265, 310–326. https://doi.org/10.1016/j.agrformet.2018.11.031.
Roerink, G.J., Su, Z., Menenti, M., 2000. S-SEBI: a simple remote sensing algorithm to estimate the surface energy balance. Phys. Chem. Earth, Part B Hydrol. Ocean. Atmos. 25, 147–157. https://doi.org/10.1016/S1464-1909(99)00128-8.
Romaguera, M., Krol, M.S., Salama, M.S., Su, Z., Hoekstra, A.Y., 2014. Application of a

remote sensing method for estimating monthly blue water evapotranspiration in irrigated agriculture. Remote Sens. 6, 10033–10050. https://doi.org/10.3390/rs61010033.

Sandholt, I., Rasmussen, K., Andersen, J., 2002. A simple interpretation of the surface temperature/vegetation index space for assessment of surface moisture status. Remote Sens. Environ. 79, 213–224. https://doi.org/10.1016/S0034-4257(01)00274-7.

Senay, G.B., Bohms, S., Singh, R.K., Gowda, P.H., Velpuri, N.M., Alemu, H., Verdin, J.P., 2013. Operational evapotranspiration mapping using remote sensing and weather datasets: a new parameterization for the SSEB approach. JAWRA J. Am. Water Resour. Assoc. 49, 577–591. https://doi.org/10.1111/jawr.12057.

Senay, G.B., Friedrichs, M., Singh, R.K., Velpuri, N.M., et al., 2016. Evaluating Landsat 8 evapotranspiration for water use mapping in the Colorado River Basin. Remote Sens. Environ. 185, 171–185. https://doi.org/10.1016/j.rse.2015.12.043.

Simonneaux, V., Duchemin, B., Helson, D., Er-Raki, S., Olioso, A., Chehbouni, A.G., 2008. The use of high-resolution image time series for crop classification and evapotranspiration estimate over an irrigated area in Central Morocco. Int. J. Remote Sens. 29, 95–116. https://doi.org/10.1080/01431160701250390.

Sobrino, J.A., Jiménez-muñoz, J.C., Sòria, G., Romaguera, M., Guanter, L., Moreno, J., Plaza, A., Martínez, P., 2008. Land surface emissivity retrieval from different VNIR and TIR sensors. IEEE Trans. Geosci. Remote Sens. 46, 316–327.

Stefan, V., Merlin, O., Er-Raki, S., Escorihuela, M.J., Khabba, S., 2015. Consistency between In Situ, model-derived and high-resolution-image-based soil temperature endmembers: Towards a robust data-based model for multi-resolution monitoring of crop evapotranspiration. Remote Sens. 7, 10444–10479. https://doi.org/10.3390/rs70810444.

van Eekelen, M.W., Bastiaanssen, W.G.M., Jarmain, C., Jackson, B., Ferreira, F., 2015. A novel approach to estimate direct and indirect water withdrawals from satellite measurements: a case study from the Incomati basin. Agric. Ecosyst. Environ. 200, 126–142. https://doi.org/10.1016/j.agee.2014.10.023.

Werner, B., Collins, R., et al., 2012. Towards Efficient Use of Water Resources in Europe. EEA Report | no 1/2012. European Environment Agency, Copenhagen. https://doi.org/10.2800/95096.

Wosten, J.H.M., Lilly, A., Nemes, A., Le Bas, C., 1999. Development and use of a database of hydraulic properties of European soils. Geoderma 90, 169–218.

Zhang, X., Qiu, J., Leng, G., Yang, Y., Gao, Q., 2018. The potential utility of satellite soil moisture retrievals for detecting irrigation patterns in China. Water 10, 1–19. https://doi.org/10.3390/w10111505.

Chapter 5. Disaggregation of thermal data for improving the water budget components estimation

Contents

5.1. Introduction *126*

5.2. Disaggregation of LST data *127*

5.2.1. Operational method for disaggregating LST data *128*

5.3. Application in Copiapo River Basin – Chile: main results *131*

5.3.1. Disaggregated LST product *132*

5.3.2. Operational estimation of ET every 8 days *134*

5.4. Application over a winter-wheat field (R3) in Haouz Plain – Morocco *136*

5.4.1. Disaggregated LST *137*

5.4.2. Irrigation retrieval by using disaggregated LST *138*

5.4.3. Daily RZSM and ET *141*

5.5. Summary and conclusions *143*

5.6. ARTICLE: An operational method for the disaggregation of land surface temperature to estimate actual evapotranspiration in the arid region of Chile *144*

5.1. Introduction

The approach developed in this thesis relies on thermal-derived RZSM that is assimilated into a water balance to estimate the temporal dynamic of RZSM and then the irrigation. In the previous chapter, it has been showed how the results are sensitive to the time revisit of LST data, worsened by cloudy days. Thus, the quantification of irrigation spatially distributed can be retrieved from remote sensed LST during the agricultural season. In fact, the LST is highly variable over a range of spatial and temporal scales due to different factors such as climatic conditions, soil properties, vegetation cover and soil moisture from surface to deeper layer. LST from thermal data has proven to be a valuable diagnostic for detecting information on the vegetation water status, serving to study the variability in water consumption in individual fields or even within the field (Anderson et al., 2012a). Consequently, several approaches based on thermal data have been developed for monitoring the crop water requirements by means of ET estimates (Gowda et al., 2008; Kalma et al., 2008; Li et al., 2009).

Several satellite sensors provide thermal data, however, at present the Landsat satellites are the only satellites that provide routine and global thermal imagery at scales that resolve water use patterns over heterogeneous agricultural areas – at about 100 m resolution. Nevertheless, the overpass frequency of Landsat (16 days for a single system or 8 days by combining Landsat-7 and -8 under clear sky conditions but more in cloudy conditions) is not optimal for ET monitoring given the soil surface drying time and the quick hydric status change, especially over irrigated areas. On other side, coarser-scale thermal sensor, such as the 1-km resolution MODIS can provide LST data for ET mapping on a near-daily basis. However, these data are too coarse to resolve water use at the scale of individual users in most irrigation districts (Anderson et al., 2012b). Therefore, the disaggregation methods to enhance at high temporal resolution the low spatial resolution LST data present a solution to overcome the issue of availability of LST data at a suitable resolution for the monitoring of crops.

This chapter aims to present an operational method for disaggregating LST data by using the fusion between Landsat and MODIS data in order to take advantage of the high spatial and temporal resolution from both sensors, respectively. This approach allows providing the main and key input data for thermal-based methods to estimate the water budget components. First, a brief state-of-the-art of disaggregation methods of LST data is presented. We focus mainly on methods based on the relationship between LST and vegetation indices relationship with potential to operational application compared to other methods that include additional land surface variables to better constrain the subpixel variation in coarser LST, but they are more difficult to implement. Second, we present the implementation of an approach over Copiapo valley in an arid region of Chile for estimating operationally the ET from the simplified surface energy balance model SSEBop. Finally, we present the implementation of the irrigation retrieval approach by

using disaggregated thermal data provided by the operational approach presented in this chapter. This procedure is carried out to enhance and ensure the availability of the main input data every 8 days, evaluating if disaggregated LST data can help better estimate the water budget components. The approach is implemented over R3 area in Haouz Plain, Morocco, where the irrigation retrieval method was implemented and presented in the previous chapter by using LST from the combined Landsat-7/-8 data.

5.2. Disaggregation of LST data

The disaggregation of LST data focuses on decomposing pixel-based temperatures providing a better dataset of LST with finer temporal and spatial resolutions. Given that satellite data in the VNIR wavelengths, used for computing vegetation indices, are provided at higher resolution than the thermal, resolution information on vegetation cover conditions are available at resolutions an order of magnitude smaller than LST. Consequently, most common methods to disaggregate remotely sensed LST have been based on a scale invariant relationship between LST and vegetation indices (VI), largely related to fractional vegetation cover. The VI-based methods are still the most used operational approaches due to the availability of data at high spatial and temporal resolution, such as DisTrad, TsHarp, among other algorithms (Agam et al., 2007a; Bindhu et al., 2013; Kustas et al., 2003; Mukherjee et al., 2014; Zhan et al., 2013).

In addition to use the LST-NDVI relation only, other studies have proposed to use the LST-NDVI feature space to derive soil water status indices that could improve the disaggregation accuracy over agricultural areas with high moisture content (Chen et al., 2010; Sandholt et al., 2002; Yang et al., 2010). This procedure has been further extended by using additional factors that modulate the LST, reflecting the soil moisture content and vegetation type (Amazirh et al., 2019; Merlin et al., 2012a, 2010; Yang et al., 2011). For instance, Merlin et al. (2010) distinguished between photosynthetically and non-photosynthetically active vegetation from time series of optical shortwave data to be included in the disaggregation procedure. Then, Merlin et al. (2012a) and Amazirh et al., (2019) included microwave data to better take into account the soil moisture effects on the disaggregation of LST. Although these latter methods can provide better accuracies than using only the LST-NDVI relationship, they require additional parameters such as soil moisture, albedo, soil and vegetation temperatures, among others, which make it difficult to implement in an operational structure.

5.2.1. Operational method for disaggregating LST data

An operational disaggregation method is developed and presented in this section in order to ensure the availability of LST data at high spatial resolution every 8 days to be used in the monitoring of crop water requirements by means of ET estimates. In the Section 5.6, the article presents in details the method and its implementation over the Copiapo Valley, Chile. This approach is developed by using time series of MODIS LST from the MOD11A2 product and Landsat-8 LST. MOD11A2 product provides routinely LST at coarse spatial resolution (1 km) per-pixel averaged over 8 days from daily LST.

The disaggregation method is mainly based on the LST-NDVI relationship by taking into account three essential points: i) the spatial relationship between *LST* and *NDVI* at high spatial resolution (Landsat-8), ii) the spatial relationship between Landsat-8 and MODIS *LST* across scales and iii) the temporal variations along the year of both relationships aforementioned. The main steps to merge these relationships and then to obtain the disaggregated LST at Landsat spatial resolution and at higher temporal resolution representative of the 8-day compositing period are described below.

5.2.1.1. Relationship between LST and NDVI

The first step involves representing the strong seasonality of LST and NDVI, through the variability of the relationship between *LST* and *NDVI* along the year by using the seasonal behavior of the linear regression parameters derived from Landsat 8 imagery. The seasonality of LST-NDVI is given by its individual temporal variability in terms of the annual temperature cycle approximated by a sinusoidal function (Bechtel, 2012) and phenological cycles of different ecosystems (Cheema and Bastiaanssen, 2010; Duchemin et al., 1999; Li et al., 2010; Liu et al., 2017). This seasonality is taken into account by using the seasonal behavior of the linear regression parameters (slope and offset) derived from Landsat-8 imagery at 100 m resolution. The regression parameters could be fitted to a sinusoidal function due mainly to the annual temperature cycle and phenological changes. For this purpose, the clear-sky Landsat images available along two years were used as calibration period. The intercept and slope (*a, b* respectively) of the linear relationship between NDVI and LST for every Landsat image are estimated and then adjusted to a sinusoidal model in function of the day of year in order to estimate *a* and *b* every 8 days (a_{8day} and b_{8day}, respectively) along the year. The linear coefficients are modelled every 8 days to be applied to the composite 16-day MODIS *NDVI* product ($NDVI_{MOD,250m_16day}$) in order to obtain a disaggregated *LST* averaged every 8 days at 250 m as follows:

$$LST_{250m_8day} = a_{8day} + b_{8day} \cdot NDVI_{MOD_{250m_16day}} + \langle error_{100m_8day} \rangle_{250m} \quad \text{Eq. 5.1}$$

where the subscripts 250m and 8day denote the spatial and temporal resolution, respectively; and $error_{100m_8day}$ is an error pixel-by-pixel modeled every 8 days between Landsat-8 LST and LST modeled from the linear relationship by using a_{8day} and b_{8day}. This error is obtained every 8 days from a second order fit applied on a pixel-by-pixel by using the Landsat-8 images available in the calibration period. It should be noted that the Eq. 5.1 accounts for the seasonal vegetation behavior by using the invariant spatial scale between 100 m and 250 m mentioned previously.

The Fig. 5.1 shows an example of the LST-NDVI relation over Copiapo Valley for a selected date in winter (9th August 2013) and summer (29th November 2013). It also shows how the intercepts and slopes are adjusted to a sinusoidal fit. The intercepts and slopes are well adjusted with a RMSE of 2.63 and 1.39 K, respectively, and a R^2 equal to 0.93 and 0.90, respectively. The adjustment of the linear regression parameters as a function of day of year allows retrieving a representation of the LST-NDVI relationships along the year with an acceptable accuracy.

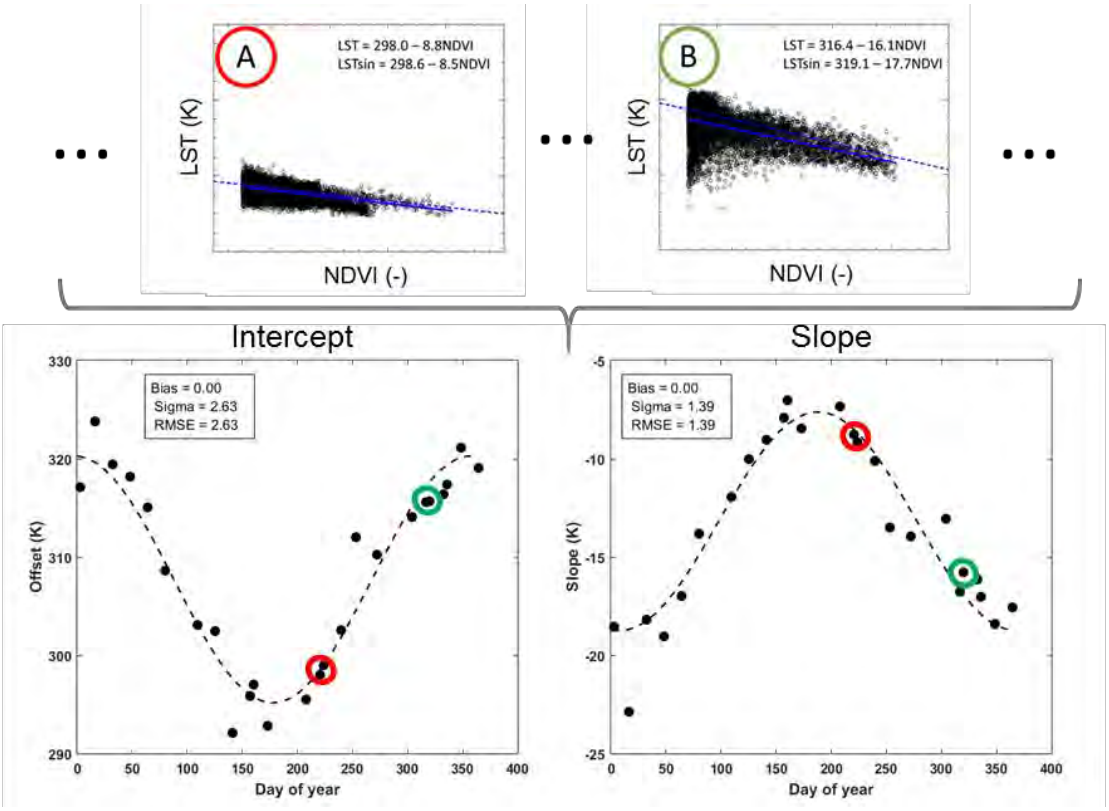


Fig. 5.1. In the top plots, linear relationship between *LST* and *NDVI* from Landsat-8 image for a selected date on winter (Plot A) and summer (Plot B). In the bottom plots, sinusoidal functions (dashed line) are adjusted to intercepts and slopes of the linear relationship *LST-NDVI* from the Landsat images for the years 2013 and 2014 according to the day of year. The intercept and slope for Plot A and B are highlighted in red and green, respectively. The statistical parameters of the sinusoidal fit for intercept and slope are shown in the box of every plot.

5.2.1.2. Relationship between MODIS and Landsat-8 LST

The second step involves representing the relationship between LST observed by Landsat and MODIS at finer and coarser resolution, respectively. For this purpose, the ratio between MODIS LST at 1 km resolution and Landsat-8 LST at 100 m resolution is calculated for every available Landsat image. This ratio is estimated pixel-by-pixel for every Landsat image during 2013 and 2014 in order to detect the seasonal pattern at 100 m Landsat-pixel resolution. This ratio, hereby referred to as ω, varies according to differences of the annual temperature cycle at coarse and fine scale, which is modulated by the specific LST temporal dynamics at both scales. These differences can be mainly due to the different land cover at Landsat spatial-resolution (100 m) and a coarser spatial-resolution (1 km). For instance, for heterogeneous land cover such as agricultural areas, several phenological stages will be evidenced and therefore, a high impact on the proportion of vegetation cover can be observed in MODIS or Landsat-8 pixel. Consequently, ω estimated along the year demonstrates a crop seasonal behavior that modulates the *LST* differences between Landsat-8 and MODIS (see Fig. 5.2 for an example over the pixel corresponding to the monitored vineyard in Copiapo Valley). It should be noted that ω is calculated by assuming a constant proportion of land cover types contained in a given pixel (finer or coarser). Once the factor ω is estimated for the whole calibration period, it can be interpolated as function of the day of year every 8 days (ω_{8day_100m}) in order to obtain *LST* at Landsat-pixel resolution from MODIS at 1 km resolution as follows:

$$LST_{8day_100m} = \omega_{8day_100m} \cdot \langle LST_{MOD_8day_1km} \rangle_{100m} \qquad \text{Eq. 5.2}$$

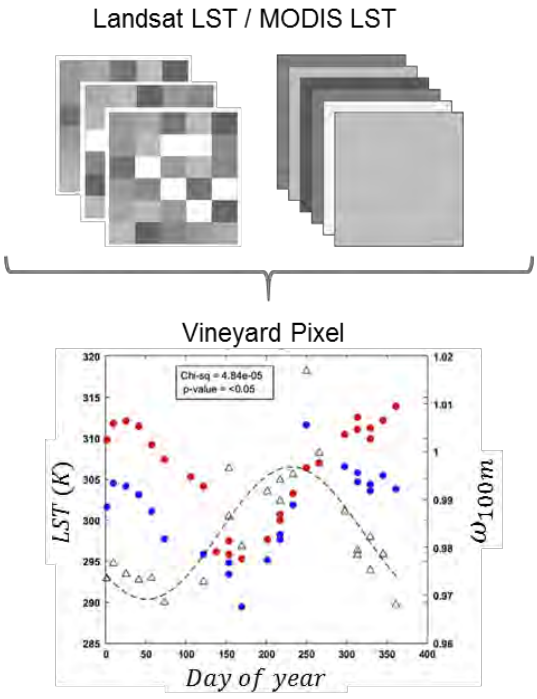


Fig. 5.2. Landsat-8 LST (blue circle), 8-day composite MODIS LST (red circle) over a vineyard pixel and the ratio between Landsat-8 and MODIS LST (ω_{100m}, triangle) for all Landsat image dates during 2013 and 2014. The sinusoidal functions of ω_{100m} according to the day of the year (ω_{8day_100m}, dashed line).

5.2.1.3. Combining the LST–NDVI and Landsat–MODIS relationships

Finally, both relationships found in the previous sections to estimate two 'first-guess' disaggregated LST are combined in order to estimate the final disaggregated LST product at 100 m resolution every 8 days. A combination of *LST* at 250 m and 100 m resolution from the LST-NDVI and Landsat-MODIS relationships, respectively, is adopted to generate a final and robust disaggregated *LST* product ($DLST_{8day_100m}$) as follow:

$$DLST_{8day_100m} = LST_{8day_100m} + \langle LST_{250m_8day} - \langle LST_{8day_100m} \rangle_{250m} \rangle_{100m} \quad \text{Eq. 5.3}$$

With $\langle LST_{8day_100m} \rangle_{250m}$ being the average of LST_{8day_100m} within each 250 m pixel resolution and $\langle \ \ \rangle_{100m}$ being the resampling from 250 m to 100 m resolution by using nearest neighbors in order to correct the product LST_{8day_100m} by the difference between LST_{8day_250m} and $\langle LST_{8day_100m} \rangle_{250m}$.

The final $DLST_{8day_100m}$ retrieval can be implemented operationally from a time series of Landsat and MODIS data, extending the usefulness of thermal data in applications for monitoring the water resources in agricultural areas.

5.3. Application in Copiapo River Basin – Chile: main results

The approach for disaggregating LST is implemented over the agricultural area of the Copiapó Valley located in south of Atacama Desert, Chile. The approach is validated over two drip-irrigated vineyard and olive orchards of about 28 and 17 hectares, respectively. The disaggregated LST (DLST) is produced as an average over 8 days at 100 m resolution. Then, DLST is used to estimate the cumulated ET every 8 days at 100 m of spatial resolution. For this purpose, it is used the simplified operational surface energy balance model (SSEBop: Senay et al., 2013a) that uses LST as main input to estimate the ET from a thermal-derived evaporative fraction, ET_0 and a crop coefficient. Before implementing the approach, a land use map is used to extract the agricultural area and mask the

surrounding desert. This approach is validated in terms of LST and ET, whose main results are presented in this section below. More details are presented in the article available in Section 5.6.

5.3.1. Disaggregated LST product

Fig. 5.5 shows a comparison of spatial distribution between LST at coarse resolution from MODIS (LST_1km), the intermediate disaggregated LST from the NDVI-LST relationship (LST_250m), the intermediate disaggregated LST from the MODIS-Landsat LST relationship (LST_100m) and the final disaggregated LST product (DLST_100m). These figures are representative of a compositing 8-day period, showing the averaged LST at the MODIS day-time overpass over 8 days, such as the 8-day MODIS LST product (MOD11A2). In the figure, LSTs are shown for an 8-day period during summer (January) and winter (July). The LST_250m product is able to distinguish the main crops such as vineyards and olives orchards in terms of low magnitudes of LST. This is given by large fields presented in the area, which may cover even more than 10 ha. Additionally in January, the LST depicts the impact of bare soils from the surrounding desert. However, when using the DLST_100m based on both MODIS and Landsat data, the border reveals a high LST difference in comparison to the crops and orchards (about 20 and 10 K for summer and winter, respectively). These differences can be observed also during winter, with olive orchards temperatures noticeably lower than on the boundary. The use of both disaggregated LST from LST-NDVI and Landsat-MODIS relationships, resulted in a good characterization of olive orchards, vineyards and crops, which are distinguished from the rest of surfaces. Furthermore, the maximum LST values in the boundary of the area detected in the LST_100m and LST_250m products are smoothed in the DLST_100m product marking out the crop areas along the valley.

The approach is validated in terms of averaged LST at MODIS overpass time over the vineyards and olive fields. In Fig. 5.3 is shown the validation of DLST that is estimated with a RMSE and R^2 of 3.55 K and 0.72 for both fields, respectively, which are very close to the errors obtained in Landsat-8 LST with a RMSE of 3.16 K (Fig. 5.4). The DLST during summer is overestimated for about 4 and 6 K in olives and vineyards, respectively. This overestimation could be attributed to the high complexity of surface temperature over the study area where more dense measurements would be required with detailed spatial sampling. In addition, differences in temperature during summer might be attributed to misleading in surface emissivity values that can cause errors of up to 4 K over arid and sparsely vegetated areas (Guillevic et al., 2014). It should be noted that the surface emissivity over this area was estimated according to the simplified NDVI thresholds method proposed by Sobrino et al. (2008) using a fixed soil emissivity calculated from the ASTER spectral library (Baldridge et al., 2009) according to soil types presented in

the area. Such a emissivity classification method may lead to uncertainties of more than 4 K under dry and warm conditions because the surface has a much larger contribution to the observed radiance than the atmosphere, hence increasing the sensitivity to emissivity error (Malakar et al., 2018). Despite the differences observed between DLST and ground-based LST, a consistent agreement with Landsat-8 LST is observed, being also overestimated during the season.

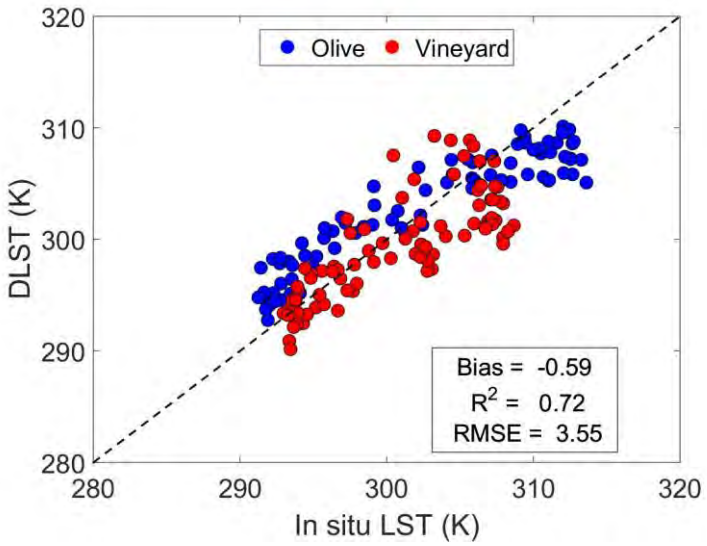


Fig. 5.3. Scatterplot between disaggregated LST at 100 m (DLST) from Eq. 5.3 and the averaged in situ LST over 8 days at MODIS overpass time over the olive and vineyard stations.

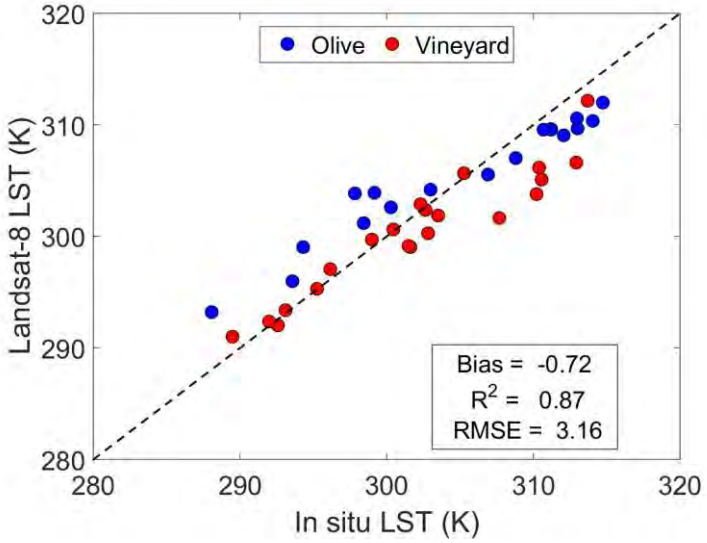


Fig. 5.4. Scatterplot between Landsat-8 LST at 100 m and in situ LST over the olive and vineyard stations.

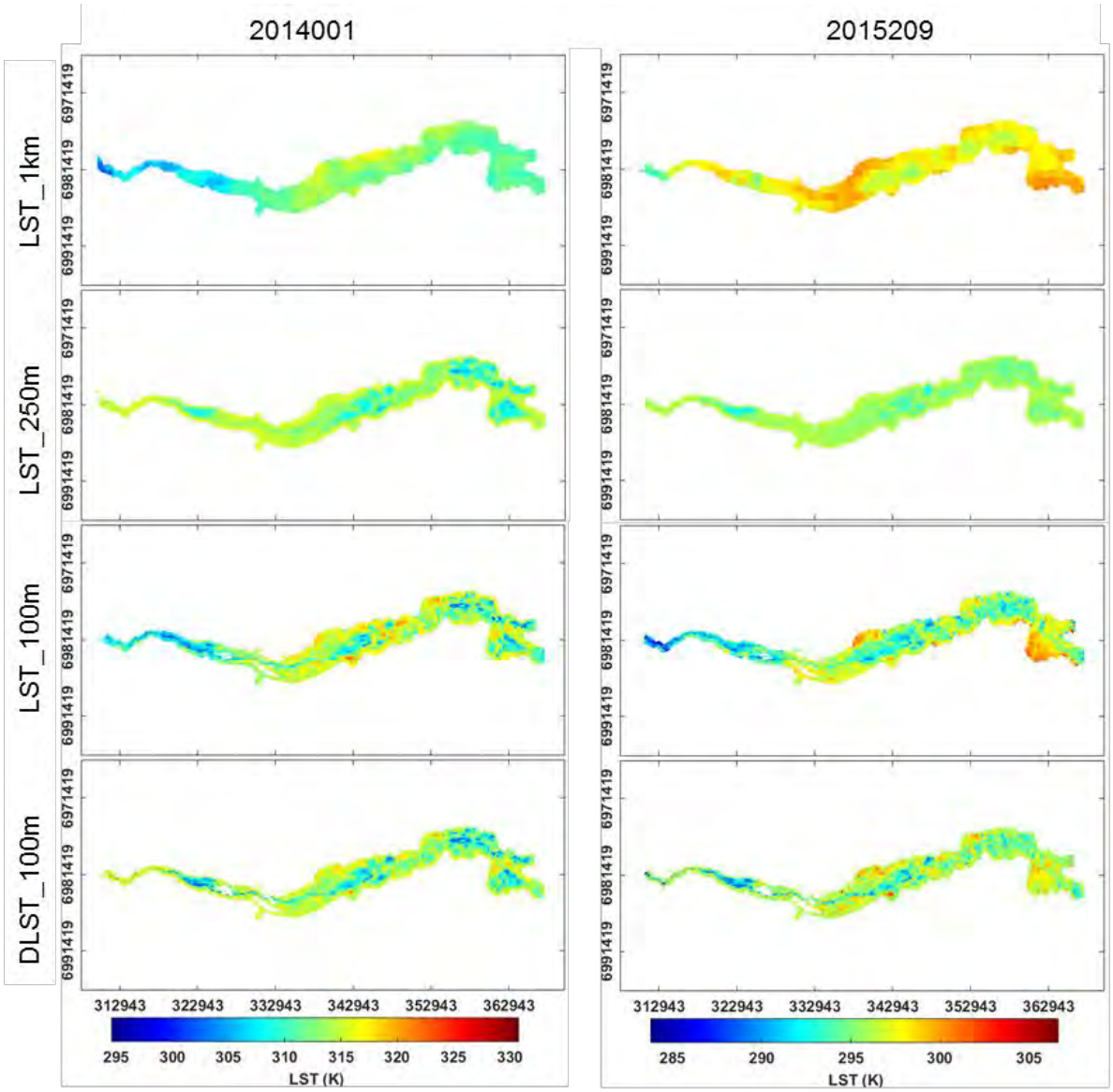


Fig. 5.5. Comparison between the composite 8-day MODIS *LST* (*LST_1km*), the disaggregated *LST* at 250 m from MODIS NDVI (*LST_250m*) using Eq. 5.1, the disaggregated *LST* at 100 m from MODIS *LST* (*LST_100m*) using Eq. 5.2 and the final disaggregated *LST* at 100 m (*DLST_100m*) from Eq. 5.3.

5.3.2. Operational estimation of ET every 8 days

Fig. 5.6 shows a comparison of the 8-day ET estimated from the SSEBop model by using LST at coarse resolution from MODIS (ET_1km) and the final disaggregated LST product (ET_100m) for the same 8-day periods as in Fig. 5.5. Large differences in the spatial variability can be observed between ET at coarse and high resolution. ET differences can exceed 10 mm/8 days over crop fields in summer, especially over vineyards. Although the differences in ET between spatial resolutions are lower over olive orchards, these are

constantly observed along the year regardless of the season. Instead, the vineyards show a seasonal pattern in terms of differences between ET_1km and ET_100m, which is strongly related to phenological changes.

During summer and winter, the ET estimated by using MODIS LST 1 km is quite homogeneous. Otherwise, the ET estimated by using *DLST_100m* targeted the maximum values in summer and the minimum in winter, showing heterogeneous ET maps that can be used to characterize areas with different crop water status, which is useful for crop water management.

Given that ground-based ET were not available over the study area, the FAO-56 model is implemented at field scale to estimate ET, which is used as comparison as partial assessment. The ET obtained from SSEBop by using DLST_100m and Landsat LST are compared against the ET at field scale. A good agreement is obtained for ET by using DLST_100m with an overall RMSE equal to 0.61 mm/day, while the ET by using Landsat LST obtained a RMSE equal to 0.75 mm/day. The ET from Landsat LST is slightly underestimated with a bias of -0.15 mm/day in average for both crops. These results demonstrate the utility of the operational method for estimating reliable ET estimates over an arid region with a complex heterogeneity. The *SSEBop* method is based on the differences between the dry and hot surface and air temperatures and in this context, the proposed *DLST* method is a valuable approach to characterize the *LST* spatial variability over arid regions. This approach provides routinely LST useful to retrieve reliable ETa maps, being of great value for the optimization of irrigation scheduling and water use efficiency.

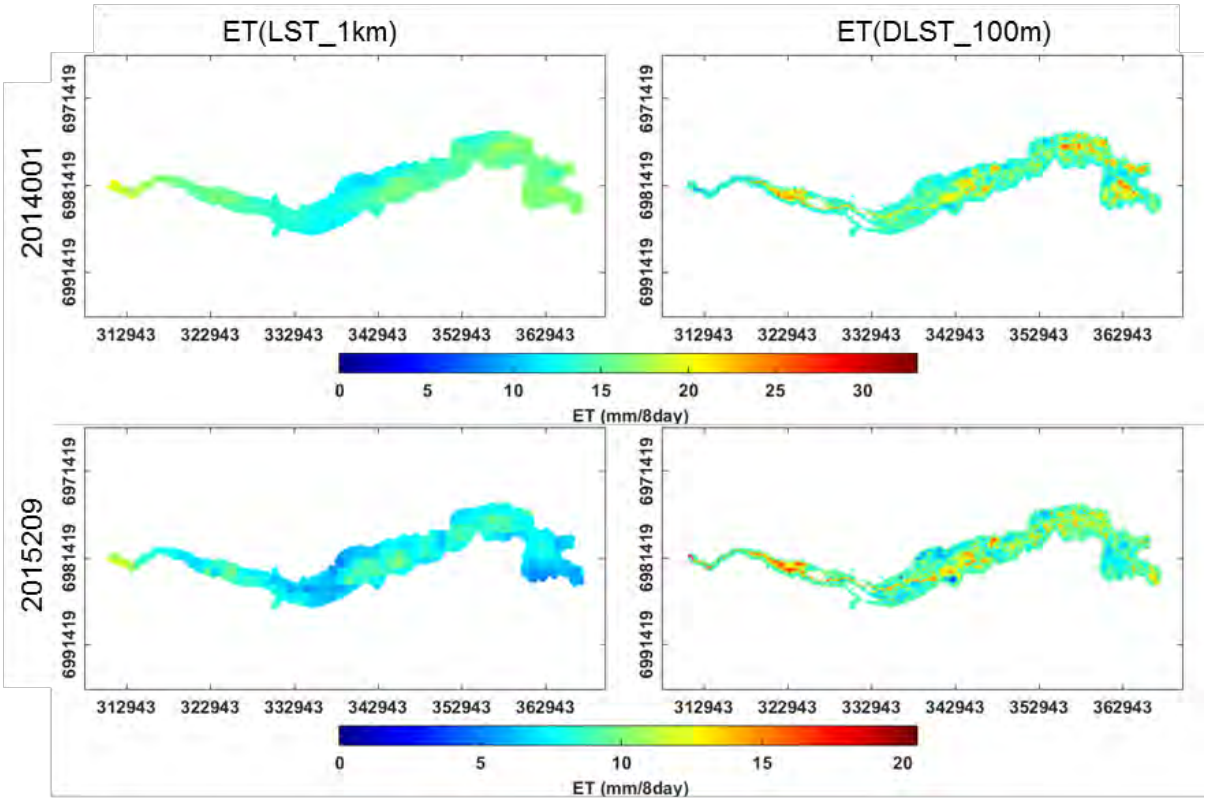


Fig. 5.6. Comparison between the cumulated *ET* over 8 days from the MODIS LST at 1km (left figures) and from the disaggregated LST at 100 m (right figures) for two selected dates in summer (2014001) and winter (2015209).

5.4. Application over a winter-wheat field (R3) in Haouz Plain – Morocco

The disaggregation approach presented in Section 5.2.1 is implemented over the R3 area in Haouz Plain in order to improve the revisit time of LST data to be integrated into the irrigation retrieval method. In the previous Section 5.3, the approach is applied to obtain averaged LST over 8-day periods at 100 m in order to retrieve cumulated ET over same periods by using the SSEBop model. Unlike the application over Copiapo Valley in Chile (Section 5.3), in this section the method is applied to obtain daily LST data every 8 days at high spatial resolution by using the combination of Landsat-7 and -8 together with daily MODIS LST at 1 km (MOD11A1). Thus, the objective of this section is to implement the retrieval irrigation approach presented in Chapter 4 by using disaggregated LST data from MODIS LST at the same Landsat-pixel resolution with an enhanced temporal resolution.

It should be noted that the disaggregation method is only based on optical Landsat and MODIS data, meaning that the disaggregation method is not able to provide LST data during Landsat overpasses dates under cloudy conditions. Keeping in mind that an availability of LST data every 8 days can be achieved by combining Landsat-7 and -8 under clear-sky conditions, the disaggregation approach is implemented every 8 days twice separately: i) coinciding with the Landsat overpass dates in order to assess the disaggregated LST against Landsat LST and ii) with an interface of 4 days with respect to Landsat overpass dates in order to complement the availability of Landsat-7 and -8 LST. Therefore, the first implementation will not be able to complement the Landsat-7 and -8 LST because of cloudy conditions. Otherwise, the second implementation allows complement the Landsat-7 and -8 LST, achieving an availability up to 4 days when successive Landsat-7, disaggregated and Landsat-8 LST are under clear-sky conditions. Consequently, the combined LST dataset between Landsat-7/-8 and disaggregated LST is used for applying the irrigation retrieval approach.

In the following sections, the results are presented in terms of disaggregated LST as well as daily water budget components (irrigation, RZSM and ET) retrieved spatially over the R3 area from the irrigation retrieval approach. In addition, it is presented a comparison between disaggregated LST and Landsat LST as well as the water budget components retrieved by using Landsat LST only and including disaggregated LST data.

5.4.1. Disaggregated LST

Fig. 5.7 presents the scatterplots of Landsat LST versus disaggregated LST over the R3 area for five selected dates (one per month) along the growing season from January to May 2016 corresponding to winter wheat crops. It is depicted that the scatter in disaggregated data is smaller during winter as shown in the first 3 scatterplots from January to March. This can be explained by more homogeneous surfaces in the area during winter, especially in terms of water status conditions. For instance, the lowest scatter is observed in January 6 when most of the fields are under bare soil conditions or low fractional vegetation cover, while larger scatters are observed in April and May when the full the range of vegetation cover and water status conditions can be found in the area. That is demonstrated in the quantitative results presented in Table 5.1.

Table 5.1 presents quantitative results in terms of bias, RMSE and correlation coefficient between disaggregated LST and Landsat LST. The disaggregation approach obtains good performance with regard to Landsat LST, with an overall bias equal to 1.01 K (ranging between -0.9 and 3.6 K), RMSE of 2.6 K (ranging between 0.55 and 4.6 K) and R of 0.87 (ranging between 0.72 and 0.96). With regard to both Landsat-7 and -8, no difference in DLST is found in the comparison between both sensors, with a mean RMSE equal to 2.8 and 2.5 K and R equal to 0.89 and 0.85 for Landsat-7 and -8, respectively.

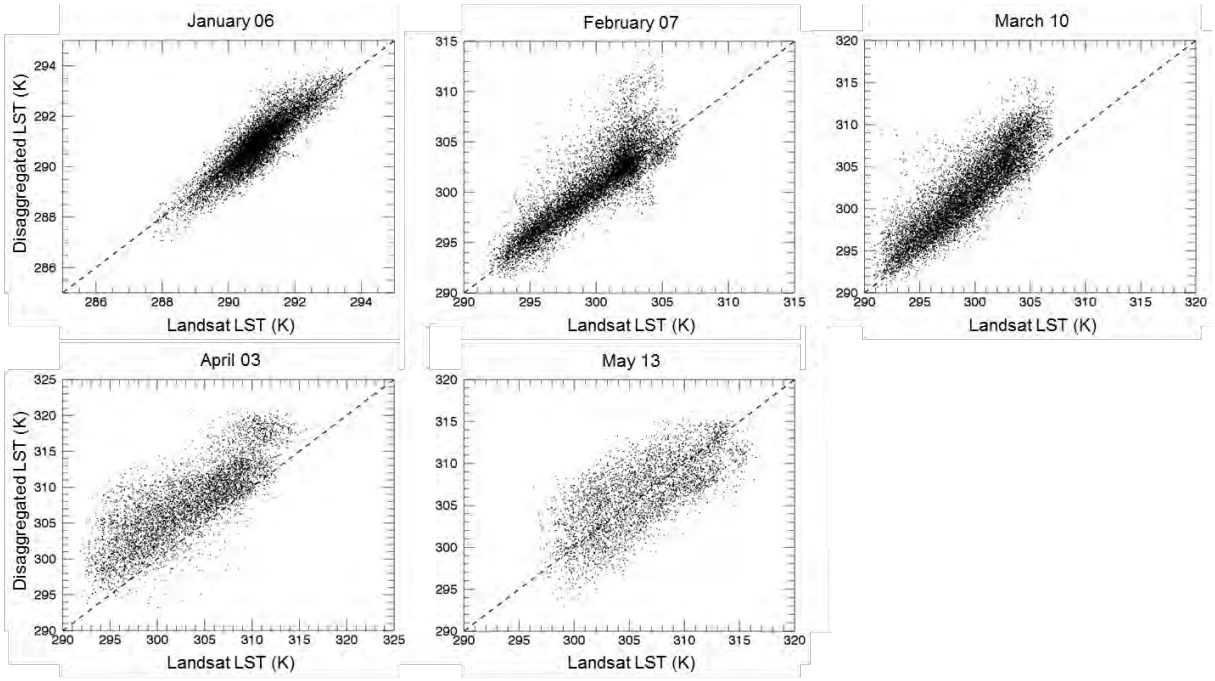


Fig. 5.7. Comparison between disaggregated LST (DLST) against Landsat LST for five selected dates along the growing season over R3 area.

Table 5.1. Statistical parameters between disaggregated LST against Landsat LST for all the dates available during the growing season 2016 over R3.

Landsat-	Date	Bias (K)	RMSE (K)	R (-)
8	Jan 6	0.17	0.55	0.88
7	Jan 14	-0.89	1.27	0.95
8	Jan 22	1.29	1.53	0.95
7	Jan 30	-1.13	1.45	0.96
8	Feb 7	0.59	1.42	0.92
7	Mar 2	0.78	2.31	0.88
8	Mar 10	1.81	2.75	0.89
7	Mar 18	2.50	3.48	0.91
7	Apr 3	3.59	4.59	0.86
8	Apr 27	1.54	3.55	0.82
8	May 13	0.60	3.27	0.72
7	May 21	-1.09	3.57	0.80
8	May 29	3.39	4.23	0.80
All		1.01	2.61	0.87

The highest accuracies in terms of bias and RMSE are obtained on January 6 with values lower than 1 K. Overall, higher accuracies are found during January and February with RMSE lower than 1.5 K and R above 0.88, while the lowest accuracies are found during April and May with RMSE between 3.2 and 4.6 K. In spite of high errors obtained during April and May, the performance of the approach is quite acceptable and very close to the performance obtained by other more complex algorithms, such as that proposed by Amazirh et al. (2019). Amazirh et al. (2019) included SAR data from Sentinel-1 in addition to LST and fv data to disaggregate MODIS LST data in the same R3 area and growing season, obtaining an overall RMSE equal to 3.35 K and R equal to 0.75 by using six Landsat LST images for comparison. However, we used Landsat and MODIS data for the calibration during the same period of comparison, whereas Amazirh et al. (2019) used only SAR and MODIS data to disaggregate and compare against Landsat LST. Consequently, a better performance can be obtained by a simpler and operational method.

5.4.2. Irrigation retrieval by using disaggregated LST

The LST data are first estimated at Landsat-pixel resolution every 8 days (under clear-sky conditions) from the disaggregation approach and then combined with Landsat-7 and -8 LST. Here, it is reminded that the disaggregation approach is implemented with an interface of 4 days with respect to Landsat overpass dates. The irrigation retrieval

approach is applied by using this combined LST dataset with an enhanced temporal resolution over R3 area. Fig. 5.8 shows the comparison of irrigation estimated by using only Landsat LST data against those estimated by using the combined Landsat and disaggregated LST over both R3-4ha and R3-2ha sites. In the plots of Fig. 5.8, vertical dashed lines depict LST data that are actually available over every site, showing how the disaggregated LST data complement the Landsat LST. Both combined LST products achieve an availability of LST data up to 4 days as observed at the beginning of both development and late seasons.

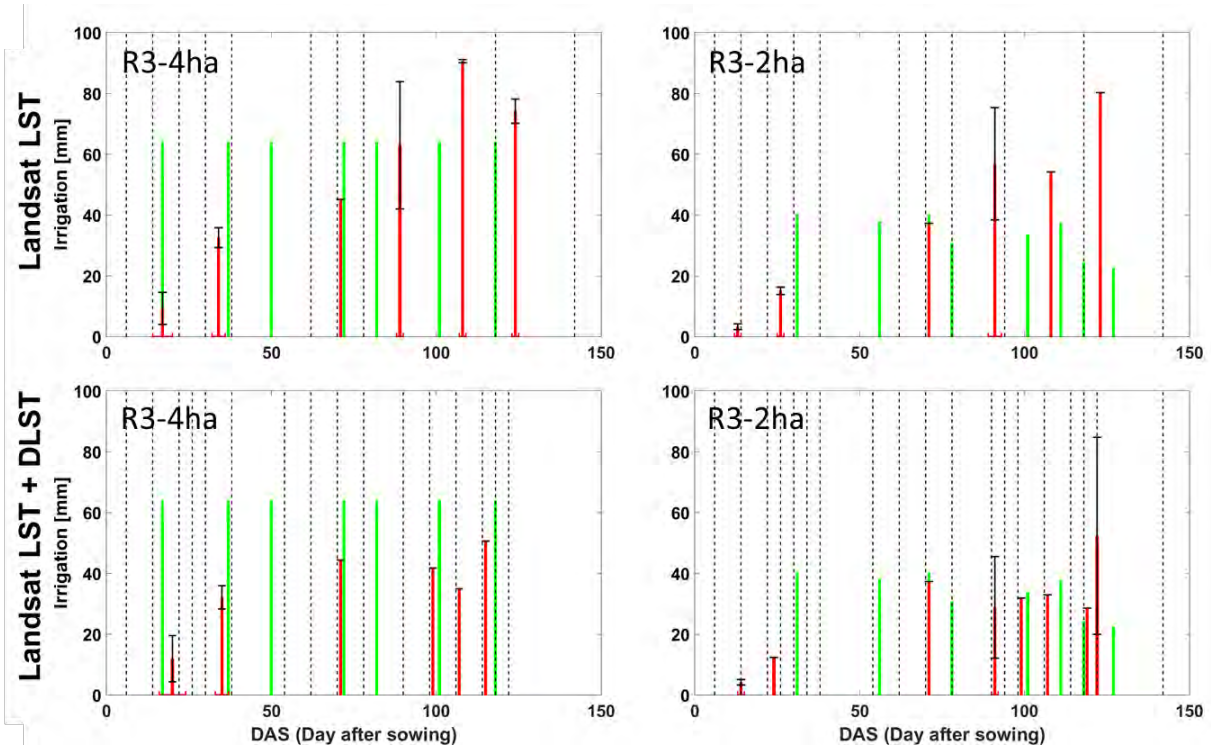


Fig. 5.8. Comparison between irrigation applied by the farmer (green) and retrieved irrigation (red) by using only Landsat LST (top plots) and the combined Landsat and disaggregated LST data (bottom plots) along the season 2016 for both monitored sites in R3 area. The horizontal and vertical error bars represent the standard deviation of the retrieved irrigation in dates and amounts, respectively. The dashed lines represent the availability of LST data.

The irrigation applied at the end of the development stage is missing over both sites and by using both LST dataset. It could not be detected by the retrieval approach due to: i) a virtual increase in the WB model of the root zone storage associated with the root growth and ii) cloudy condition near the day after sowing (DAS) 50 that does not allow providing a frequency revisit of LST data higher than 16 days. In R3-4ha site, the number of irrigation events does not change by using either Landsat only or Landsat and disaggregated LST data. However, the amounts and dates change from the mid-season stage. The last three irrigation events over R3-4ha are no longer overestimated by using the combined Landsat and disaggregated LST data. While the effective actual irrigation (i.e. water applied by the farmer minus the deep percolation) during the period of the last

three events is equal to 140 mm, the retrieved irrigation is 209 and 127 mm by using Landsat only and combined with disaggregated LST, respectively. Similarly over R3-2ha, the last irrigations events are overestimated by using Landsat LST only, and also three irrigation events are detected instead of the five applied by the farmer. Otherwise using the combined Landsat and disaggregated LST, the five irrigation events are detected and their amounts are closer to those of the actual irrigations.

As a more comprehensive comparison at different time scales, the performance of the irrigation retrieval method is evaluated at various time scales. As in the article presented in the previous Chapter (Section 4.9), the irrigation amounts are accumulated in overlapping windows throughout the seasons by increasing sequentially the windows from 1 day to 3 months (90 days). This strategy is implemented for every site by assessing the performance of the approach for different accumulation periods. Fig. 5.9 shows this assessment by comparing the irrigation estimates from the proposed approach by using Landsat LST only against those by using both Landsat LST and disaggregated LST data. Fig. 5.9 depicts the improvement achieved over both sites by using an enhanced LST dataset at every accumulation period, with higher accuracies in terms of R, RMSE and bias. The overall accuracy of cumulated irrigations at different time scales (between 1 to 90 days) is better with respect to those retrieved using only Landsat LST. In terms of correlation coefficient, it is improved by 47% (from 0.46 to 0.67) and 12% (from 0.53 to 0.60) over R3-4ha and R3-2ha, respectively, while the RMSE is improved by 35% (from 52 to 34 mm) and 13% (from 40 to 35 mm) over the same sites.

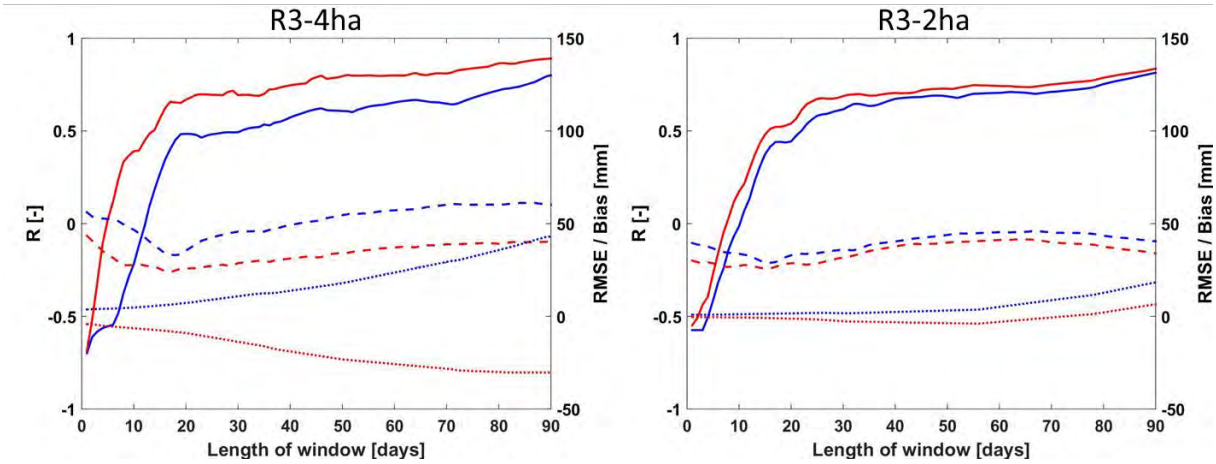


Fig. 5.9. Comparison of statistical parameters R (solid line), RMSE (dashed line) and bias (dotted line) between observed and retrieved irrigation by using Landsat LST only (blue lines) and both Landsat and disaggregated LST data (red lines) cumulated from 1 to 90 days through a moving window over both R3-4ha and R3-2ha sites during 2016 season.

Even though the performance of the approach is improved by using an enhanced LST dataset in terms of frequency revisit of LST data, the approach with both LST datasets is found to be reliable for time intervals equal or longer than 2 weeks. On the contrary, the

approach generally fails in retrieving reliable cumulated irrigation for time periods shorter than 10 days either by using Landsat only or the enhanced with disaggregated LST data. Despite the revisit time shorter than 16 days (up to 4 days) no significant improvement is achieved at daily to weekly time scale. This might be explained by the errors associated with the disaggregation method. Therefore, a sensitivity analysis of errors associated to LST data should be carried out in order to differentiate the errors coming only from the revisit time. That would allow discerning the expected improvements in the irrigation estimates (at daily to weekly time scale) by using LST data at enhanced spatio-temporal resolution directly achieved by future thermal missions like TRISHNA (Lagouarde and Bhattacharya, 2018) .

5.4.3. Daily RZSM and ET

The irrigation retrieval method by using the combined Landsat-7/8 and disaggregated LST is also assessed in terms of RZSM and ET estimates. For this purpose, the retrieved irrigation in the previous section is used to force FAO-2Kc to simulate RZSM ($RZSM_{FAO\text{-}2Kc_DLST}$) and ET ($ET_{FAO\text{-}2Kc_DLST}$) on a daily basis at Landsat-pixel resolution, which are compared with in situ observations along the 2016 growing season. $RZSM_{FAO\text{-}2Kc_DLST}$ and $ET_{FAO\text{-}2Kc_DLST}$ estimates are notably compared with those obtained from the FAO-2Kc model forced by: i) the actual irrigation ($ET_{FAO\text{-}2Kc_Iobs}$ and $RZSM_{FAO\text{-}2Kc_Iobs}$) and ii) the irrigation retrieved from our approach by using Landsat-7/8 LST only ($ET_{FAO\text{-}2Kc_Landsat}$ and $RZSM_{FAO\text{-}2Kc_Landsat}$), as are estimated in the Chapter 4.

Fig. 5.10 shows the validation of daily RZSM estimates over both R3-4ha and R3-2ha sites compared against in situ observations as well as the comparison between $RZSM_{FAO\text{-}2Kc_Iobs}$, $RZSM_{FAO\text{-}2Kc_Landsat}$ and $RZSM_{FAO\text{-}2Kc_DLST}$ estimates. Fig. 5.10 depicts the improvement achieved by including disaggregated LST data for enhancing the temporal resolution of LST. Over both sites, the accuracy of $RZSM_{FAO\text{-}2Kc_DLST}$ estimates is significantly improved with respect to that of $RZSM_{FAO\text{-}2Kc_Landsat}$. In terms of correlation coefficient, it is improved by 12% (from 0.73 to 0.82) and 17% (from 0.68 to 0.79) over R3-4ha and R3-2ha, respectively, while the RMSE is improved by 29% (from 0.04 to 0.03 m^3m^{-3}) and 23% (from 0.05 to 0.04 m^3m^{-3}) over the same sites.

As in Fig. 5.10, Fig. 5.11 presents the validation of daily ET estimates over both R3-4ha and R3-2ha sites compared against in situ observations as well as the comparison between $ET_{FAO\text{-}2Kc_Iobs}$, $ET_{FAO\text{-}2Kc_Landsat}$ and $ET_{FAO\text{-}2Kc_DLST}$ estimates. Unlike the RZSM estimates, combining the disaggregated LST with Landsat LST data does not achieve an improvement. On the contrary, the RMSE obtained in $ET_{FAO\text{-}2Kc_DLST}$ estimates is worsened by 27% with respect to $ET_{FAO\text{-}2Kc_Landsat}$ over the R3-4ha site, while over the R3-2ha site, the accuracy keeps almost constant. The fact that ET estimates are not improved like RZSM, might be because the errors in disaggregated LST are translated into errors in the stress coefficient that is directly used to estimate ET. In the case of RZSM estimates, it is

reminded that the stress coefficient is used as an indicator of the RZSM dynamics and hence of the irrigation events. Consequently, RZSM is less sensitive to absolute values of stress coefficient than ET.

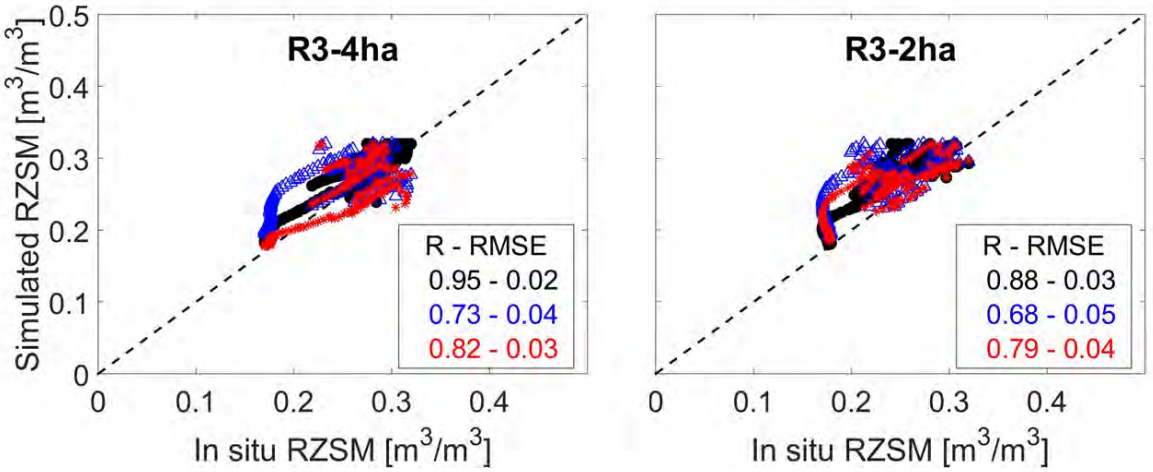


Fig. 5.10. Ground-based RZSM is plotted versus the RZSM simulated by the FAO-2Kc forced by: observed irrigation (black), irrigation retrieved from our approach by using Landsat LST only (blue) and irrigation retrieved from our approach by using Landsat LST together with disaggregated LST (red). The correlation coefficient (R) and root mean square error (RMSE) are shown for RZSM from FAO-based models forced by the three different irrigation data sets.

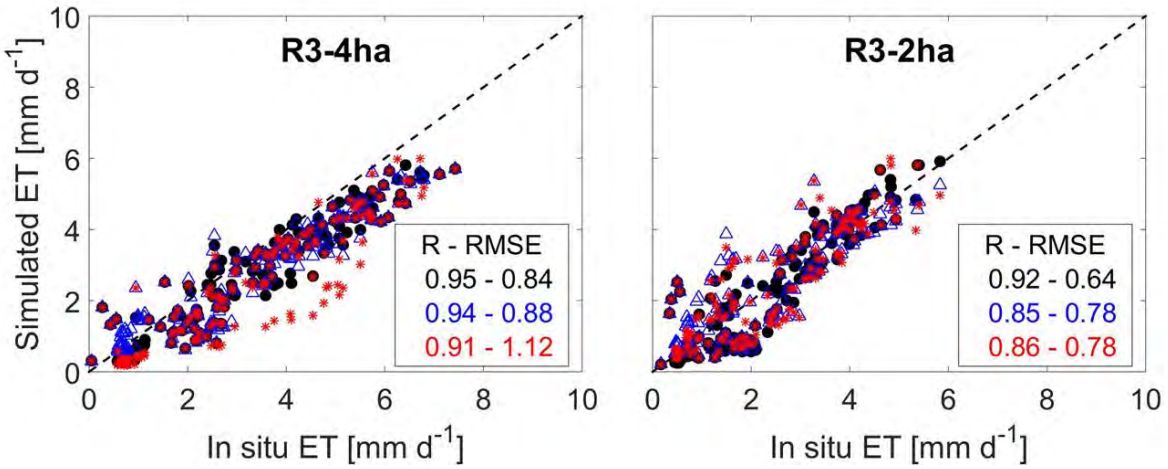


Fig. 5.11. Ground-based ET is plotted versus the ET simulated by the FAO-2Kc forced by: observed irrigation (black), irrigation retrieved from our approach by using Landsat LST only (blue) and irrigation retrieved from our approach by using Landsat LST together with disaggregated LST (red). The correlation coefficient (R) and root mean square error (RMSE) are shown for ET from FAO-based models forced by the three different irrigation data sets.

5.5. Summary and conclusions

LST is an important variable in surface energy and water balance and is an invaluable asset to better detect the crop water status at high (~100 m) spatial resolution. This information has served to monitor crop water needs in individual fields as well as the variability within larger fields. However, the main issue of LST derived from readily available satellite thermal data is the temporal resolution (~16-day revisit interval) for monitoring the rapid changes of soil water status. In order to address this issue, we proposed an operational method for disaggregating the LST by combining MODIS data at high-temporal resolution with Landsat data at high-spatial resolution. The method combines the LST-NDVI relationship at fine resolution from Landsat with the Landsat-MODIS LST relationship. This method is implemented over the narrow Copiapo Valley, Chile, covered mainly by tree crops as well as over the R3 area in Haouz Plain, Morocco, covered mainly by winter wheat crops.

In Copiapo Valley, the disaggregation method is applied by using MOD11A2 LST product to provide LST data at Landsat spatial resolution and every 8 days representative of the 8-day compositing period. The disaggregated LST is integrated into the operational surface energy balance method (SSEBop) for estimating cumulated ET over 8 days at high spatial resolution. The approach is evaluated over a vineyard fields and olive orchards, where the disaggregated LST is estimated with a RMSE of 3.55 K for both fields. This result is very close to the accuracy obtained for Landsat-8 LST data (RMSE=3.16 K) over both fields. ET estimates are estimated with a RMSE equal to 0.70 and 0.50 mm/day over vineyards and olive orchard, respectively.

In R3 area, the disaggregation method is applied by using MOD11A1 LST product to provide LST data at Landsat spatial resolution and every 8 days. The disaggregated LST is estimated with an overall RMSE of 2.6 K with regard Landsat LST. The disaggregated LST is combined with Landsat-7/8 LST data to achieve an availability of LST up to 4 days under clear-sky conditions. The combined LST dataset is integrated into the FAO-based water balance model for applying the irrigation retrieval approach as proposed in Chapter 4. Then, the irrigation amounts and timing as well as daily RZSM and ET are estimated over R3 area at field scale on a daily basis. These water budget components are evaluated against in situ measurements over two winter wheat fields during the 2016 growing season (R3-4ha and R3-2ha). They are also compared against those estimated by using Landsat LST only. Enhancing the revisit time of LST by including disaggregated LST data improves the performance of the irrigation retrieval approach. Irrigations are also cumulated to carry out an assessment by comparing the irrigation estimates from the proposed approach by using Landsat LST only against those by using both Landsat LST and disaggregated LST data. The results depict an improvement in the accuracies achieved by using the enhanced LST dataset at every accumulation period. The overall RMSE of cumulated irrigation at different time scales is decreased from 46 to 34 mm

(meaning an improvement of 25%), while the correlation is increased from 0.50 to 0.64 (meaning an improvement of 29%).

However, this improvement is not enough to provide reliable irrigation estimates at time scale shorter than 2 weeks. That might be explained by the errors associated to the disaggregated LST data. Nevertheless, the improvement in irrigation amount and timing is useful to better estimate the daily RZSM, whose RMSE is decreased from 0.04 to 0.03 m^3m^3 and from 0.05 to 0.04 m^3m^3 in R3-4ha and R3-2ha, respectively.

In spite of the differences between the areas (i.e. narrow Copiapo valley covered by tree crops under arid climate versus the extended agricultural R3 area covered mainly by winter wheat crops), the use of disaggregated LST from the proposed method was relevant to better constrain the water budget components. That was demonstrated by implementing different approaches: the SSEBop for estimating ET over Copiapo Valley and the proposed irrigation retrieval method for irrigation, RZSM and ET. Consequently, the proposed approaches have potential to contribute to the agricultural water management in semi-arid to arid regions affected by scarcity of water resources, providing reliable maps of water budget components for optimizing irrigation scheduling and water use efficiency.

5.6. ARTICLE: *An operational method for the disaggregation of land surface temperature to estimate actual evapotranspiration in the arid region of Chile*

ISPRS Journal of Photogrammetry and Remote Sensing 128 (2017) 170–181

Contents lists available at ScienceDirect

ISPRS Journal of Photogrammetry and Remote Sensing

journal homepage: www.elsevier.com/locate/isprsjprs

An operational method for the disaggregation of land surface temperature to estimate actual evapotranspiration in the arid region of Chile

L. Olivera-Guerra [a,b,*], C. Mattar [a], O. Merlin [b], C. Durán-Alarcón [a,c], A. Santamaría-Artigas [a,d], R. Fuster [e]

[a] Laboratory for Analysis of the Biosphere (LAB), University of Chile, Santiago, Chile
[b] Centre d'Etudes Spatiales de la Biosphère (CESBIO), Toulouse, France
[c] Institut des Géosciences de l'Environnement (IGE), CNRS, Université Grenoble Alpes, 38400 Saint-Martin-d'Hères, France
[d] Department of Geographical Sciences, University of Maryland, College Park, MD 20742, USA
[e] Dept. Environmental Sciences, School of Agronomic Sciences, University of Chile, Santiago, Chile

ARTICLE INFO

Article history:
Received 24 September 2016
Received in revised form 15 March 2017
Accepted 27 March 2017

Keywords:
LST
Disaggregation
Evapotranspiration
Arid region
Landsat-8
MODIS

ABSTRACT

Monitoring evapotranspiration in arid and semi-arid environments plays a key role in water irrigation scheduling for water use efficiency. This work presents an operational method for evapotranspiration retrievals based on disaggregated Land Surface Temperature (*LST*). The retrieved *LST*s from Landsat-8 and MODIS data were merged in order to provide an 8-day composite *LST* product at 100 × 100 m resolution. The method was tested in the arid region of Copiapó, Chile using data from years 2013–2014 and validated using data from years 2015–2016. In-situ measurements from agrometeorological stations such as air temperature and potential evapotranspiration (*ET0*) estimated at the location were used in the ET estimation method. The disaggregation method was developed by taking into account (1) the spatial relationship between Landsat-8 and MODIS *LST*, (2) the spatial relationship between *LST* and the Normalized Difference Vegetation Index (*NDVI*) at high spatial resolution (Landsat-8), and (3) the temporal variations along the year of both relationships aforementioned. The comparison between disaggregated *LST* at 100 m resolution and in situ *LST* measurements presents a coefficient of determination (r^2), in average, equal to 0.70 and a RMSE equal to 3.6 K. The disaggregated *LST* was used in an operational model to estimate the actual evapotranspiration (*ETa*). The *ETa* shows good results in terms of seasonal variations and in comparison to the evapotranspiration estimated by using crop coefficients (*kc*). The comparison between remotely sensed and in situ *ETa* presents an overall r^2 close to 0.67 and a RMSE equal to 0.6 mm day^{-1} for both crops. These results are important for further improvements in water use sustainability in the Copiapó valley, which is currently affected by high water demand.
© 2017 International Society for Photogrammetry and Remote Sensing, Inc. (ISPRS). Published by Elsevier B.V. All rights reserved.

1. Introduction

Evapotranspiration (*ET*) is one of the most important parameters of the hydrological cycle affecting water availability on the Earth's surface. During the last decades, several works have been documented the critical importance of ET for agricultural irrigation scheduling (Porter et al., 2012; Senay et al., 2013), water resource availability (Oki and Kanae, 2006), hydrologic and meteorological forecasts (Findell et al., 2011) and climate change scenarios related to drought indexes (Gao et al., 2011). ET estimations are also crucial for management of water resource in areas of water scarcity since the actual rate of water use by vegetation can deviate significantly from potential ET rates (as regulated by atmospheric demand for water vapor) (Anderson et al., 2012). Thus, detailed spatial and temporal maps of ET provide power tools for decision makers and enable managers to more judiciously allocate available water for agricultural, urban, and environmental uses.

To estimate and quantify ET, it is necessary to account for diverse meteorological observations and land surface parameters such as the land surface temperature (LST). LST modulates the surface energy fluxes and it is key to estimating ET for monitoring crop water demand (Kalma et al., 2008; Li et al., 2009; Zhan

* Corresponding author at: Laboratory for Analysis of the Biosphere (LAB), University of Chile, Santiago, Chile.
E-mail address: olivera-guerrale@cesbio.cnes.fr (L. Olivera-Guerra).

http://dx.doi.org/10.1016/j.isprsjprs.2017.03.014
0924-2716/© 2017 International Society for Photogrammetry and Remote Sensing, Inc. (ISPRS). Published by Elsevier B.V. All rights reserved.

et al., 2013; Cammalleri et al., 2014). In agricultural and heterogeneous natural systems, high variability of ET and LST can occur at scales of hundreds of meters or less. Thus, moderate-resolution satellite Thermal Infra Red (TIR) imagery is therefore required and essential to identify and fully understand water use and water availability at the field scale associated with specific crop types (Anderson et al., 2012; Senay et al., 2016).

The combination of *LST* and vegetation indexes at several time and spatial scales has been proven as a potential technique to disaggregate *LST* (DLST) to determine crop *ET*. Several *DLST* methods have been proposed in recent decades using various information sources available at low, medium or high spatial resolution, which are widely detailed in Zhan et al. (2013). Nevertheless, the Normalized Difference Vegetation Index (NDVI) based methods are still the most used operational approaches due to the availability of data at high spatio-temporal resolution. For instance, ALEXI, DisALEXI, DisTrad, TsHarp, among other algorithms (Kustas et al., 2003; Anderson et al., 2004; Agam et al., 2007; Bindhu et al., 2013; Cammalleri et al., 2014; Mukherjee et al., 2014).

Some variations of the NDVI based methods including phenology such as the robust disaggregation procedure proposed by Merlin et al. (2010, 2012) which account for the senescent vegetation fraction and soil moisture in addition to *NDVI*. These methods require additional parameters such as soil moisture, albedo, soil and vegetation temperatures, among others, which might be difficult to implement in an operational structure. There are other simple methods based on a subtraction approach that merge the spatial detail of higher-resolution imagery with the temporal change observed in coarser or moderate-resolution imagery (Hong et al., 2011; Kim and Hogue, 2012). The methods mentioned above can be applied to *ET* or soil moisture retrievals in order to estimate the surface energy balance (*SEB*) at better spatial resolutions, as well as to crop water management (Sobrino et al., 2012; Mattar et al., 2014). However, DLST method must be adapted over arid zones where high seasonal phenology in addition to thermal amplitude is evidenced in large areas.

Remote Sensing monitoring of semi-arid or arid regions target cultivated areas surrounded by barren conditions (e.g. deserts) which can impact on *DLST* and therefore in *ET* quantification. The proportion of bare soil observed in a given pixel during a year can affect the crop vegetated fraction increasing the *LST* and affecting *ET* and water requirements. Hence, *DLST* approaches concerning the spatial resolution over arid or semi-arid regions by using operational methods should be capable to monitor crop water consumption and usage accounting the seasonal variations. Despite the fact that there are some works on complex heterogeneous and semi-arid regions (Zhu et al., 2010; Weng et al., 2014), these methods are not simple in their application and present shortcomings in the operational mode such as the use of search windows to select similar pixels and to perform a sensitivity analysis before modeling (Weng et al., 2014).

In Chile, a persistent rainfall deficit has prevailed in the central zone since 2010 leading with a decline in water reservoirs generating a megadrought without precedents (Boisier et al., 2016). In the arid region of Chile, such as the Copiapó valley, the water resources availability has declined in addition to the water demand owing to agricultural and mining activities. The arid region of Copiapó is one of the most important agricultural areas of Chile and demands large amounts of water (4856 L/s equal to 59% of the total demand in the Copiapó; Bravo, 2013). Thus, it is of crucial importance that the water demand be determined and monitored and the water use efficiency be improved in this zone. Therefore, the main objective of this work is to present an operational *DLST* approach for estimating the actual evapotranspiration (*ETa*) over an arid or semi-arid region in Chile. This manuscript is structured as follows: Section 2 presents the study area and data. Section 3 describes the method proposed in this work. Section 4 presents the results and analysis and finally, Sections 5 and 6 provide the discussion and conclusions, respectively.

2. Study area and data sets

2.1. Study area

The study area belongs to the Copiapó Valley located in the arid region of Atacama, Chile. The whole valley has an area of about 18538 km^2 divided in longitudinal sectors from the Los Andes Highlands (sector 1) to the coast (sector 6) (Fig. 1). The study area has a surface of about 1670 km^2, and is located in the flat lands of sectors 5 and 6. It is an agricultural area mainly covered by olives, vineyards, pomegranates and natural vegetation (Fig. 1). The climate is semi-arid to arid with low mean annual precipitation (28 mm) and hot and dry summers (December, January and February), which coincide with the vineyard's growing season, and cold and dry winters (June, July and August). Despite the Copiapó Valley's proximity to the Atacama Desert, the zone located in sector 5 and 6 is highly covered with clouds for several days per year, which might affect the *ETa* measurements and the availability of optical remote sensing imagery. In terms of water resources, the Copiapó Valley is characterized by acute water scarcity mainly attributed to the low annual precipitation and the systematic stress put onto the aquifer by water consumers, mainly agriculture and mining (Oyarzún and Oyarzún, 2011; Valdés-Pineda et al., 2014; Suarez et al., 2014). This situation has brought about the Copiapó Valley's current critical situation, resulting from the extraction of water in recent decades, which has risen to rates greater than the natural replenishing of the aquifer (demand equal to 8222 L/s over a replenishing equal to 6347 L/s; Bravo, 2013), thus increasing the pressure for water resources and generating a new regional scenario for water use efficiency.

2.2. In situ data

In this work, in situ data derived from meteorological stations generated by the "Grupo de Estudios del Agua (GEA)" (www.agroclima.cl), in addition to LAB-network (here in-after LAB-net) (Mattar et al., 2016) data sets, were used. The GEA meteorological data sets were provided by 12 meteorological stations in the Copiapó Valley, four of which are located in the study area of this work. These stations were located in vineyards and olives orchards, and they provide basic meteorological parameters. The reference evapotranspiration (*ET0*) from ASCE standardized of a short crop and air temperature (*Ta*) between January 2013 and December 2014 were processed from the GEA network and used in this work.

In addition, in order to complement the GEA meteorological stations, data from two meteorological and radiative flux stations from LAB-net were also used. To this end, *ET0*, *Ta*, *infrared thermal*, *global and net radiation* (*Rg*, *Rn*) provided at olive orchards and vineyards crops were processed between July 2014 to December 2014, totaling 6 stations in the study area. These stations were used to generate the calibration and the partial evaluation of the *ETa* retrieval approach. On the other hand, LAB-net data from years of 2015 and 2016 was used to validate the *DLST* and *ETa*. The LAB-net station over olives orchards is located in a plot of land measuring about 17 hectares with a fraction vegetation cover of 25% distributed uniformly. Whereas the LAB-net station over vineyards is located in an area of 28 hectares with a homogeneous fraction vegetation cover.

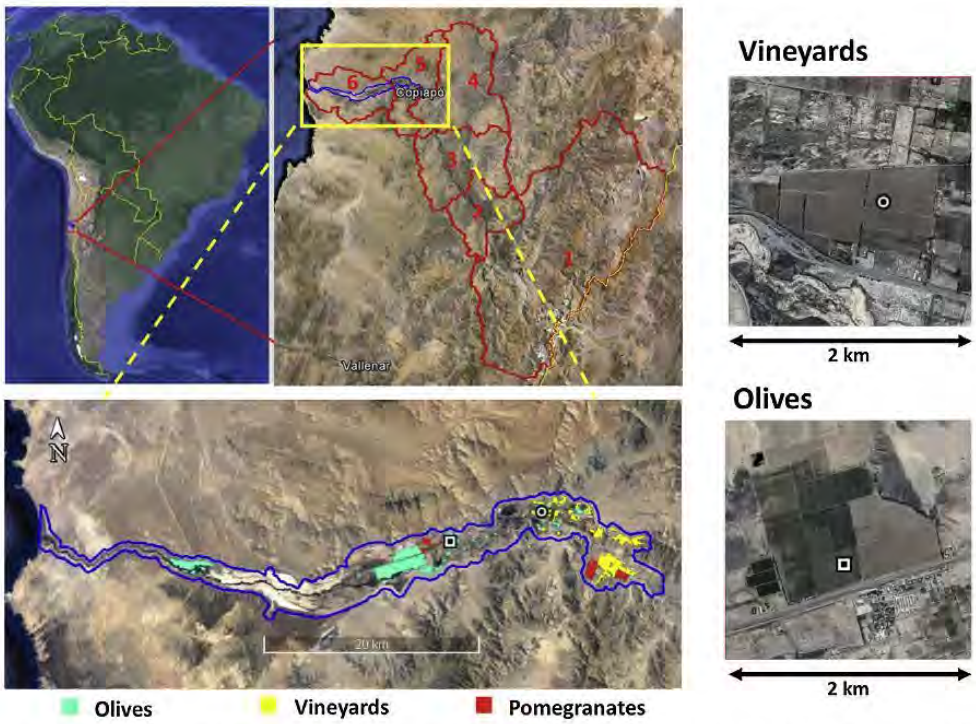


Fig. 1. Copiapó Valley divided in 6 sectors (red line) over which the study area (blue line) and the meteorological station over olive and vineyard crops (square and circle, respectively) are located in the sectors 5 and 6. In the figure the land cover of the main crops are shown: olives, vineyards and pomegranates. (For interpretation of the references to colour in this figure legend, the reader is referred to the web version of this article.)

2.3. Remote sensing data

To generate an operational approach, Landsat-8 and MODIS data products were used. In the case of Landsat-8, 25 clear sky images for Path 1 and Row 79 acquired for years 2013 (11 images) and 2014 (14 images) were used to develop and calibrate the proposed methodology. In addition, 21 clear sky images for years 2015 (9) and 2016 (12) for validation of Landsat-8 LST and for comparison of the DLST estimates. For the case of MODIS, water vapor content from the MOD05 and MOD07 product V5.0 was used in the estimation of the *LST* from Landsat-8. Moreover, the MODIS/Terra composite 8-day *LST* product (MOD11A2 V5.0) at 1 km spatial resolution and the MODIS/Terra composite 16-day normalized difference vegetation index *NDVI* (MOD13Q1 V5.0) at 250 m spatial resolution were also used in the *DLST* approach for the calibration (2013–2014) and validation (2015–2016) of *DLST* and *ETa* estimates.

3. Methodology

3.1. Disaggregation LST (DLST)

First of all, the *LST* from Landsat-8 was estimated by using the band 10 through the Single-channel (SC) algorithm described in Jiménez-Muñoz et al. (2014) and based on the work proposed by Sobrino et al. (1996) and is represented as follows:

$$LST = \gamma\left[\frac{1}{\varepsilon}(\varphi_1 \cdot L_{sen} + \varphi_2) + \varphi_3\right] + \delta \quad (1)$$

where ε is the surface emissivity, (φ, δ) are two parameters which depend of the at-sensor brightness temperature and the thermal band, and φ_1, φ_2 and φ_3 are approximation of the atmospheric functions versus the atmospheric water vapor content W from a second-order polynomial fit, whose coefficients are obtained from radiative transfer simulation using the GAPRI database (Mattar et al., 2015) and the W was derived from the daily MOD05 product. The emissivity ε was estimated according to the simplified *NDVI* thresholds method proposed by Sobrino et al. (2008), which requires *NDVI* and knowledge of the soil-emissivity spectrum corresponding to the soils of the study area. The soil emissivity was calculated by using the soil types from the ASTER spectral library (Baldridge et al., 2009), which belong to aridisol and entisol and were convoluted by using the relative spectral response for the Landsat-8 thermal band 10 using the RSR calculator (Durán-Alarcón et al., 2014). Finally, the *NDVI* threshold was 0.15 and 0.80 for the minimum and maximum, respectively. Both MODIS and Landsat-8 *LST* data were filtered by cloud mask using the Quality Control (QC) of both MODIS and Landsat-8. Both Landsat-8 and MODIS were spatially matched in order to extract the study area from both images and for the study period between 2013 and 2014.

The disaggregation method was developed by taking into account (1) the spatial relationship between *LST* and the Normalized Difference Vegetation Index (*NDVI*) at high spatial resolution (Landsat-8), (2) the spatial relationship between Landsat-8 and MODIS *LST*, and (3) the temporal variations along the year of both relationships aforementioned. The following sections describe these relationships and the methodology to merge them to obtain

the disaggregation LST product at Landsat spatial resolution and at higher temporal frequency of MODIS.

3.2. Relationship between LST and NDVI

The temporal variability of LST shows a strong seasonality (Weng et al., 2008) which its seasonal change can be modeled using the annual temperature cycle approximated by a sinusoidal function (Bechtel, 2012). In a similar way, the vegetation indices as NDVI present a strong seasonality which have been widely used to describe the phenological cycles of different ecosystems at different spatial resolution (Cheema and Bastiaanssen, 2010; Duchemin et al., 1999; Li et al., 2010; Liu et al., 2017). The annual variability of both NDVI and LST can be evidenced at both field and watershed scale and can be monitored at the high spatial resolution of Landsat. Based on the strong seasonality of LST and NDVI, the variability of the relationship between *LST* and *NDVI* throughout the year was considered by using the seasonal behavior of the linear regression parameters derived from Landsat 8 imagery. The intercept and the slope of the *LST–NDVI* relationship are controlled by a wide range of factors, such as the fractional vegetation cover, surface soil moisture variability and meteorological factors (Nemani et al., 1993). The regression parameters could be fitted to a sinusoidal function due mainly to the annual temperature cycle and the seasonal changes of differences of temperature between soil and vegetation. The cloud-free images available to two years (2013–2014) were used in order to provide information of a complete annual cycle and taking into account the low temporal frequency of sensors as Landsat-8. The Landsat-8 *NDVI* was resampled to the same spatial resolution of Landast-8 *LST*.

Because an ordinary least square regression algorithm lacks robustness and is sensitive to outliers (Rousseeuw, 1984), some authors have proposed overcoming this problem by using subpixel variability based sampling (co-efficient of variation <25%) (Agam et al., 2007; Kustas et al., 2003) or using least median square (LMS) regression and Projection Adjustment by Contribution Estimation (PACE) regression for more heterogeneous landscapes because these methods are less sensitive to outliers (Mukherjee et al., 2014). In this work, we propose a new method to describe the linear regression between LST and NDVI. This was carried out using the mean LST values derived from NDVI classes separated by 0.01 step forward. This technique was used to overcome the sensitive to extreme value or outliers in a robust and efficient way and in order to obtain a seasonal behavior of regression parameter, which would be not possible observe by using all the scatter data in the feature space plot. The latter is due to the influence of different factors (mentioned above) that often results in a wide range of LST for a given value of NDVI, thus leading to an imprecise quantification of the slope of the NDVI–LST relationship (Bindhu et al., 2013).

The intercept and the slope (a, b respectively) obtained for the calibration period (2013–2014) were adjusted by using a sinusoidal function to estimate a and b every 8 days (a_{8day} and b_{8day}, respectively) throughout the year. An invariant spatial scale between 100 m and 250 m was assumed for modeling the linear coefficients in order to obtain a disaggregated *LST* every 8 days at 250 m from the composite 16-day MODIS *NDVI* product, accounting for the seasonal vegetation behavior described as follows:

$$LST_{250m_8day} = a_{8day} + b_{8day} \cdot NDVI_{MOD_{250m_16day}} + error_{100m_8day} \quad (2)$$

where the subscripts 250 m and 8 day denotes the spatial and temporal resolution, respectively; a_{8day} and b_{8day} are the coefficients of the linear regression interpolated each 8 days for the whole image. *NDVI* 16-day composite was used for two corresponding 8-day period. To estimate LST using the LST – NDVI relationship the error pixel-by-pixel between the LST observed by Landsat 8 and the LST modeled were linear fitted. This error was obtained for each Landsat 8 image and then a second order polynomial fit was applied on a pixel-by-pixel basis to estimate an error each 8 days ($error_{100m_8day}$).

3.3. Relationship between MODIS and Landsat-8 LST

On the other hand, the MODIS *LST* was resampled from 1 km to 100 m resolution by using nearest neighbors in order to estimate a seasonal factor which considers the relationship pixel by pixel between MODIS resampled image and Landsat-8 (4). This factor has a seasonal pattern and can be used as a partial disaggregation between Landsat-8 and MODIS following the size of the most representative crops in the study area.

$$\omega_{8day_100m}(x,y,t) = \frac{LST_{L8_100m}(x,y,t)}{LST_{MOD_8day_1km}(x,y,t)} \quad (3)$$

The seasonal factor $\omega_{8day_100m}(x,y,t)$ varies according to differences of annual temperature cycle at coarse and fine scale, which is modulated by the specific LST temporal profiles at both scales. These differences can be mainly due to the different land cover at Landsat spatial-resolution (~100 m) and a coarser spatial-resolution (~1 km). For instance, homogeneous land covers, such as bare soil, will show low temporal differences at MODIS or Landsat-8 spatial resolution since the land cover is the same during the whole year, and the seasonal pattern will show a slow temporal variation. However, for heterogeneous land cover such as crops, several phenology stages will be evidenced and therefore, a high impact on the proportion of vegetation cover can be observed in MODIS or Landsat-8 pixel. In this case, $\omega_{8day_100m}(x,y,t)$ demonstrates a crop seasonal behavior which modulates the *LST* between Landsat-8 and MODIS. The $\omega_{8day_100m}(x,y,t)$ was calculated assuming a constant proportion of the land cover types contained in a given pixel. Once the factor $\omega_{8day_100m}(x,y,t)$ was estimated for the whole calibration period, it was interpolated every 8 days for the whole year in order to process the *LST* from MODIS at 1 km resolution to Landsat-8 for 8 days (4).

$$LST_{8day_100m} = \omega_{8day_100m} \cdot LST_{MOD_8day_1km} \quad (4)$$

Once the relationship between LST – NDVI and Landsat-8 – MODIS was determined to estimate a product of *LST* at 250 m and 100 m each 8 days (LST_{8day_100m} and LST_{8day_250m} respectively), a combination of them were applied to generate a final and robust disaggregated *LST* at 100 m and 8 days ($DLST_{8day_100m}$) as follow:

$$DLST_{8day_100m} = LST_{8day_100m} + \langle LST_{250m_8day} - \langle LST_{8day_100m} \rangle_{250m} \rangle_{100m} \quad (5)$$

with $\langle LST_{8day_100m} \rangle_{250m}$ being the average of LST_{8day_100m} within each 250 m pixel resolution and $\langle\ \rangle_{100m}$ being the resampling from 250 m to 100 m resolution by using nearest neighbors in order to correct the product LST_{8day_100m} by the difference between LST_{8day_250m} and $\langle LST_{8day_100m} \rangle_{250m}$. The final $DLST_{8day_100m}$ retrieval can be performed operationally that can be very useful as application to surface energy budget. In this work, the $DLST_{8day_100m}$ was used in an operational surface energy balance method to estimate the *ETa*, which is described below.

3.4. Estimation of actual evapotranspiration

The *ETa* was estimated by using the *Operational Simplified Surface Energy Balance* (*SSEBop*) developed by Senay et al. (2013) and evaluated in this study area by Olivera-Guerra et al. (2014). The *SSEBop* approach estimates the pixel-by-pixel evaporative fraction (*EF*) by using "hot/dry" and "cold/wet" reference values. To

estimate *ETa* routinely, the only data needed for this method are *LST*, daily maximum air temperature (*Ta*), and *ET0*.

This model relies on the simplification of the surface energy balance process which is mainly driven by the available net radiation (*Rn*). Since thermal remote sensing is conducted under clear-sky conditions, the *SSEBop* method assumes a location- and date-specific constant temperature difference (*dT*) between the hot/dry and cold/wet boundary reference points. *ETa* can be estimated using Eq. (6) as a fraction of the *ET0* as follows:

$$ET_a = EF \cdot k \cdot ET0 \tag{6}$$

where *ET0* is the green grass reference for the location; *k* is a coefficient that scales the *ET0* into the level of a maximum *ET* experienced by an aerodynamically rougher crop and *EF* is the evaporative fraction. Although a value of *k* between 1.0 – 1.25 is recommended (Allen et al., 2011; Senay et al., 2013; Senay et al., 2016), a value equal to 0.65 was used in this study, which was determined by Olivera-Guerra et al. (2014) to this domain area. This value is due to cover type mainly corresponding to vineyards and olive orchards, which often have a low fractional cover vegetation and whose maximum values of crop coefficient (*kc*) are equal to 0.70 and 0.65, respectively (Allen et al., 1998). The *EF* was estimated pixel-by-pixel according to the following equation:

$$EF = \frac{T_H - T_s}{T_H - T_C} = \frac{T_H - T_s}{dT} \tag{7}$$

where *Ts* is the *LST* downscaled at 100 m spatial resolution every 8 days. T_H is the estimated *Ts* at the idealized reference hot/dry condition of the pixel for the same time period, *Tc* is the estimated *Ts* at the idealized cold/wet reference point and the *dT* is the difference between *Th* and *Tc*. The cold boundary condition is derived as a correction of the *Ta*, whose correction coefficient was determined as a seasonal average between *Ts* and *Ta* on all pixels where *NDVI* is greater or equal to 0.75. A correction factor of 0.993 was established by using all Landsat imagery.

The predefined *dT* is solved from the *Rn* equation for a bare, dry soil where *ETa* is assumed 0 and sensible heat is assumed maximum (Bastiaanssen et al., 1998). It is calculated by using Eq. (8) and the assumptions of Senay et al., (2013).

$$dT = \frac{R_n r_{ah}}{\rho_a C_p} \tag{8}$$

where *Rn* is clear-sky net radiation (W m^{-2}); r_{ah} is the aerodynamic resistance to heat from a hypothetical bare and dry surface (sm^{-1}); ρ_a is the density of air (kg m^{-3}), estimated as a function of air pressure and temperature (Allen et al., 1998); *Cp* is the specific heat of air at constant pressure (1.013 kJ kg^{-1}K^{-1}). The r_{ah} was theoretically estimated through an iterative computation by implementing an energy budget for bare soil for the whole year according to Bastiaanssen (1995). According to this procedure, the average r_{ah} was equal to 113 sm^{-1}, which is very close to the value of 110 sm^{-1} determined by Senay et al. (2013).

3.5. Validation of LST and ETa

The validation of remotely sensed *LST* was carried out by comparing the *DLST* every 8 days and the *LST* measured in situ at LABnet stations. In order to compare the in-situ and the DLST at the 100 m scale, the thermal infrared sensor (Apogee SI-111®) was located at a height of 5 m and inclined to measure an area with the same fraction vegetation cover as the plot of land where the station is localized. To estimate the in situ *LST*, the radiometric temperature measured, by a step of 5 min, was converted to *LST* by using the following equation:

$$B(LST) = \frac{Lrad - (1-\varepsilon)Ldown}{\varepsilon} \tag{9}$$

where *Lrad* is the land leaving radiance (W m^{-2}) measured by a thermal radiometer, ε is the land surface emissivity, *Ldown* is the long-wave downwelling irradiance (W m^{-2}) and *B(LST)* is Planck's law for the *LST* (W m^{-2}sr^{-1}μm^{-1}). The *Ldown* was estimated using the methodology proposed by Jiménez-Muñoz et al. (2010), by processing a MOD07 profile into MODTRAN radiative transfer code and convoluting the downwelling irradiance spectra by using the Apogee SI-111® relative spectral response. The surface emissivity was acquired from the ASTER Global Emissivity Data Base (Hulley and Hook 2013) and the emissivity was converted from narrow band to a broad band by using the method proposed by Ogawa et al. (2003). Finally, the *LST* (K) was estimated by inverting Planck's law.

For the validation of *ETa*, the in situ *ET0* measured at the station located over the olive orchard and vineyard by a step of one hour were used. These *ET0* values were estimated at daily level and weighted by the *kc* estimated by the Direccion General de Aguas (2007) and Martínez and Tapia (2002) based on the FAO crop coefficient. The values of *kc* were estimated for the arid region of Atacama, changing during the seasons of the year. The mean *kc* values are presented in Table 1 for olives and vineyards and are crop site dependent which cannot be directly assimilated for the same crops in other regions of Chile. Finally, for the case of olives, the *kc* was weighted for fraction vegetation cover, which is equivalent to 25% during the whole year and the *kc* values were estimated to a vegetation cover equal to 50%.

To estimate the accuracy of the proposed *DLST* method and its application to *ETa* retrieval, the bias, standard deviation, RMSE and determination coefficient (r^2) were calculated for each station (olive and vineyards) between January 2015 and December 2016. This period was defined following the overflooding that occurred on 27th March 2015, which caused some damage to the irrigation system of the vineyards, as can be consequently seen in the crop growth after September 2015.

4. Results

4.1. Statistical relationship for LST – NDVI and Landsat-8 – MODIS

The *NDVI* and *LST* relationship was estimated to the 24 scenes available to the calibration period between 2013 and 2014. Fig. 2 represents the variability of scatterplot during a Landsat scene during winter and summer of 2013. In terms of seasonal variation, during winter the amplitude of *LST* is between 285 and 305 K, whereas in summer it varies between 290 K and 330 K. Meanwhile, the *NDVI* values mainly fall between 0.1–0.6 and 0.1–0.8 during winter and summer respectively. In summer, steeper slopes can be observed due to the greater temperature differences between soil and vegetation surface, as it is showed in Figs. 3 and 4.

The slope and intercept parameters were statistically adjusted for a sinusoidal shape (r^2 equal to 0.904 and 0.931, RMSE equal to 1.39 K and 2.63 K for slope and intercept, respectively). The estimated linear regression by the observed Landsat 8 and the simulated regression by the sinusoidal fit of slope and intercept match in terms of each statistical coefficient for each scene. This sinusoidal shape can be interpolated in order to obtain the parameters regression for the sinusoidal function to represent the whole year of *NDVI* and *LST* relationship for a Landsat scene. Indeed, Fig. 3 shows the scatter plots for the linear correlation between *NDVI* and *LST*.

In terms of the Landsat-8 and MODIS LST relationship, the fraction ω between both sensors can be fitted by a sinusoidal equation (Fig. 2), thus this parameter can be modeled for each day of the

Table 1
Vineyards and olives *kc* values.

	Jan	Feb	Mar	Apr	May	Jun	Jul	Aug	Sep	Oct	Nov	Dec
Vineyards	0.70	0.65	0.60	0.50	0.40	0.40	0.40	0.40	0.40	0.60	0.65	0.70
Olives	0.65	0.65	0.65	0.65	0.6	0.5	0.5	0.5	0.6	0.6	0.65	0.65

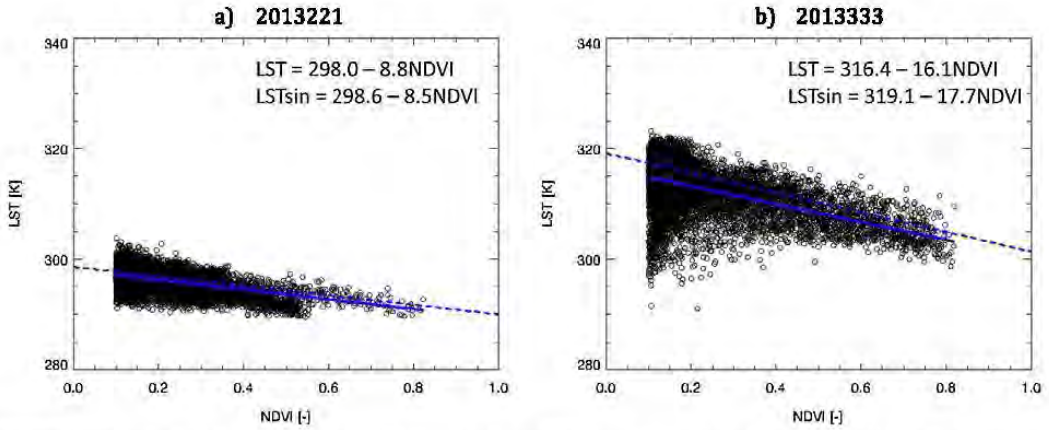


Fig. 2. Linear relationship between *LST* and *NDVI* by Landsat-8 image acquisition to winter (a) and summer (b). The equations are included for the linear regression from the observed Landsat-8 data (LST: solid line) and for the linear regression from the slope and intercept fitted to a sinusoidal function (LSTsin: dashed line).

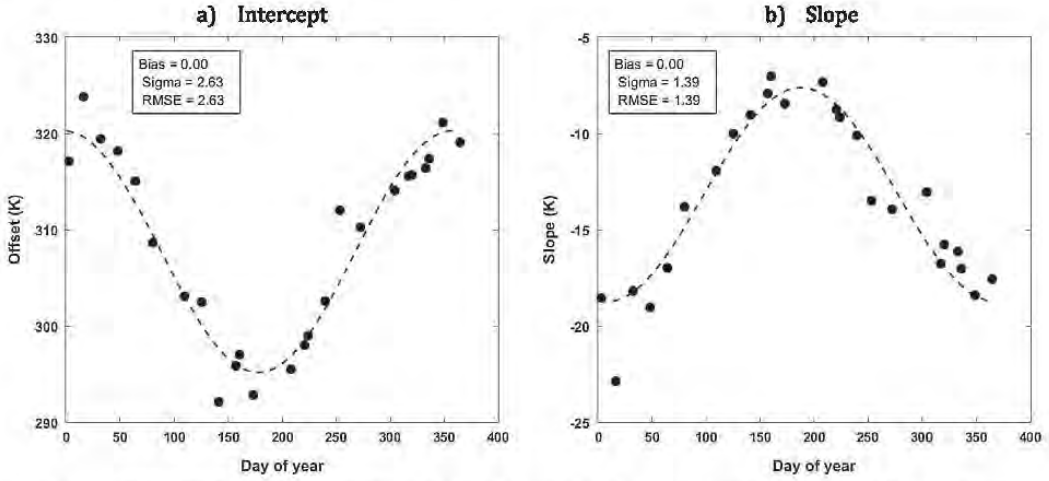


Fig. 3. Slope and intercept of the linear relationship between *LST* and *NDVI* from all Landsat image acquisition dates between 2013 and 2014 and its sinusoidal functions according to the day of year (dashed line).

year and the ω values for any obtained *DLST*. The ω can be obtained for each pixel according to the land cover type and the fraction of vegetation cover given in the Landsat-8 pixel at 100 m and in MODIS at 1 km spatial resolution. The difference of the fraction of vegetation cover between Landsat-8 and MODIS affects the annual amplitude of the ω, generating low amplitude for similar vegetation cover and high amplitude for a high difference of the vegetation cover between both Landsat-8 and MODIS pixels as presented in the case of olives and vineyards, respectively. This annual effect on ω can be also related to the land cover types variability within a MODIS pixel and its different phenological stages since the relationship between a fine and coarse resolution was revealed in terms of *LST* through the factor ω. The ω values can be closer to 1 in the case of olives and lower than 1 for vineyards because of during summer, during the maximum crop growth rate, the vegetation cover presents the highest values at Landsat-8 spatial resolution.

4.2. Disaggregation of LST (DLST)

Fig. 5 shows the disaggregated *LST* retrievals for a day on January (summer) and July (winter) used to obtain the *ETa* by using

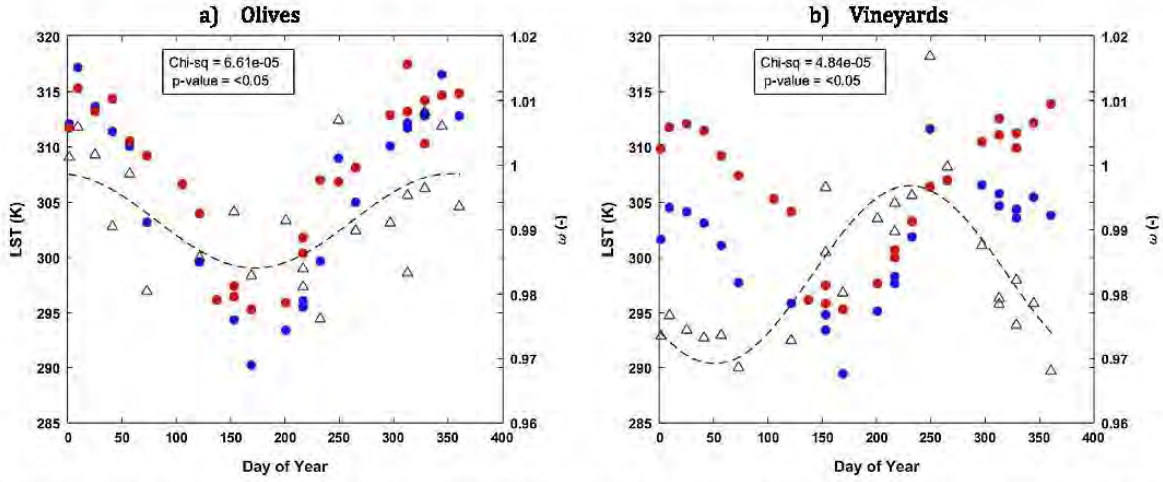


Fig. 4. *LST* from Landsat-8 overpass (blue circle), 8-day composite MODIS LST (red circle) and the ratio between Landsat-8 and *MODIS LST* (ω: triangle) for all Landsat image dates between 2013 and 2014. The sinusoidal functions of the ratio according to the day of the year (ω_{8day_100m}: dashed line). The graphs are shown for the pixel corresponding to the station located in olives (a) and vineyards (b). (For interpretation of the references to colour in this figure legend, the reader is referred to the web version of this article.)

MODIS and Landsat-8. The coarse (1 km) resolution MODIS *LST* can be used for a general characterization of the study area, where the most common feature is the bare soil surrounding the naturally vegetated and agricultural areas. For the case of *LST* retrieved at 250 m, the main vegetation orchards such as olives and vineyards can be distinguished in terms of low magnitudes of *LST*. Additionally, for January, the *LST* highlights the impact of the bare soil located on the boundary of the study area. However, when using the direct 1 km resolution *DLST* based on both MODIS and Landsat-8, the border reveals a high *LST* difference in comparison to the crops and orchards (±20 K and ±10 K for summer and winter, respectively). This can be also noticed for winter, where the vegetation of olive orchards located in the middle of the study area showed a *LST* noticeably lower than on the boundary. The use of both disaggregated *LST* from *NDVI* and by using the ω factor, resulted in a good characterization of olives orchards, vineyards and crops as they can be distinguished as the lower values. It is important to note that the riverbed of the Copiapó River can be also distinguished during winter since it gives the lowest *LST* values. Furthermore, the boundary's maximum *LST* values shown in the *NDVI–LST* relationship or by using the ω factor are smoothed in terms of the combination of both methodologies marking out the crop areas along the study area.

4.3. Evapotranspiration retrievals

The *ETa* estimated at 1 km and 100 m resolution for January and July is presented in Fig. 6. Over vineyards, a difference of about 10 mm 8 day^{-1} between the coarse and the fine pixel can be obtained during summer when using the *DLST* proposed method in comparison to MODIS. Other differences, though somewhat lower, are also obtained for Olives (±5 mm 8 day^{-1}) that are located in the central and western part of the study area. On the other hand, during July, the minimum threshold of *ETa* is evidenced over the riverbed, representing the lowest values of *ETa* in the whole study area (i.e. <2 mm 8 day^{-1}). The maximum values of *ETa* correspond to the vegetation orchards with partial vegetation cover such as olives or pomegranates. Vineyards did not show the maximum *ETa*, which seems to be consistent with the phenological stage of this crop. The *ETa* retrieved by MODIS is partially homogeneous during summer and winter, although the *ETa* retrieved by the *DLST* targeted the maximum values in summer and the minimum in winter, generating a heterogeneous *ETa* map which can be used to characterize the areas which need to be irrigated and useful for water requirements. However, for vineyards, there are significant differences when comparing seasonal periods such as summer and winter. For instance, during summer, a big difference in *ETa* can be seen by the influences of spatial resolution. These differences are close to 10 mm 8 day^{-1} when using MODIS or *ETa* from the *DLST* algorithm, although these differences are non-significative during winter.

As a partial evaluation with in situ measurements, Fig. 7 shows the times series for the *ETa* derived from *DLST* and 8-day composite MODIS LST over vineyards and olive orchards pixel at 100 m and 1 km resolution, respectively, and the *ET0* obtained from in situ measurements in the whole study area. It is important to note that maximum values are explained by the *ET0*, which seems to be lower when applying a *kc* in order to obtain *ETa*. For Olives, the vegetation cover fraction in addition to the proportions of land cover type at both 100 m pixel of DLST and 1 km pixel of MODIS are very close, thus the bare soil proportion is constant during all years and the vegetation fraction in both 100 m and 1 km pixel are very close. So, in the case of olives, when comparing the 1 km or 100 m resolution *ETa* with in situ measurements, there is no statistically significant differences ($p < 0.05$). The *ETa* from DLST and Landsat-8 overpass were compared show a good agreement in both olives and vineyards (r^2 equal to 0.67 in average for both crops), where the DLST is slightly underestimated in relation to Landsat-8 (bias equal to −0.05 mm day^{-1} and RMSE of 0.3 mm day^{-1} in average for both crops). It is important to note that *ETa* from DLST represent the average over 8 days whereas *ETa* from Landsat-8 overpass represent a clear-sky day, at least at the Landsat overpass. Therefore, this underestimation can be expected due to *ETa* from DLST can be represent the average over cloudy and clear-sky days.

4.4. Evaluation of LST and ETa

LST and *ETa* at 100 m and 8-days spatio-temporal resolution were simulated to the time series of 2015 and 2016 from the

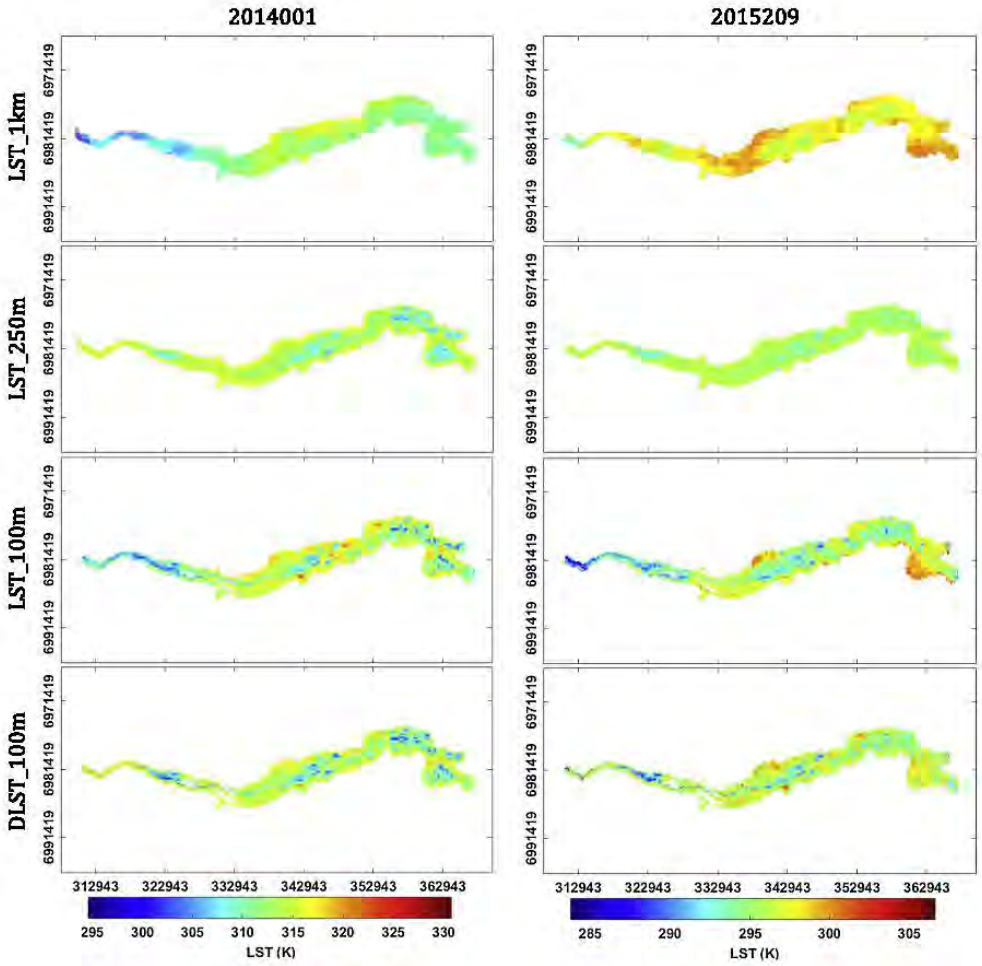


Fig. 5. Comparison between the composite 8-day MODIS *LST* (*LST* _1 km), the first product of disaggregated *LST* at 250 m from MODIS NDVI (*LST_250* m), the second product of *LST* at 100 m from MODIS *LST* (*LST_100* m) and the final disaggregated *LST* at 100 m (*DLST_100* m).

Eqs. (2), (3) and (5) by using the NDVI and LST MODIS composited product at 250 m and 1 km resolution, respectively. Note that Landsat imagery were used in the calibration period (2013–2014) and the evaluation period for 2015–2016. The time series of *LST* and *ETa* simulated from the operational approach and the in situ retrievals are presented in Fig. 8. The RMSE for *ETa* was estimated in 0.5 and 0.7 mm day^{-1} for olives and vineyards, respectively (Table 2). Meanwhile, the RMSE for *LST* was estimated lower than 3.6 K for both vineyards and olives. The *LST* during summer is overestimated closed to 4 and 6 K in olives and vineyards, respectively. The overestimation of LST could be attributed to the fraction vegetation cover which could generate rapidly changes in space as well as in time (Prata et al., 1995; Vauclin et al., 1982). This effect is related to the high complexity of surface temperature over the study area where more dense measurements are required with detailed spatial sampling (Li et al., 2013). On the other hand, high differences in *LST* over vineyards were observed during the summer 2015–2016 (December and January) corresponding to the maximum plant development to the vineyards. This was mainly attributed to the impact of irrigation on the crop since the drip system was damaged by the floods and it decreased the amount of water for the same period in the last years (2013 and 2014), which also explains the significant increase of LST in the plant development stage (September–November). The effect of the change in the irrigation can be evidenced by observing the NDVI that reached a value of 0.5 in summer 2015–2016 meanwhile the last years it was greater 0.7 for the same period. The differences in temperature retrieved during the summer season over vineyards might be attributed to misleading in surface emissivity values that can provoke errors of up to 4 K over arid and sparsely vegetated areas as described in Guillevic et al. (2014). Over olive orchards the fraction of vegetation cover is almost the same during the whole year, impacting on the amplitude of the *LST* between summer and winter and also in the comparison between in situ and *DLST*. Meanwhile in summer LST is overestimated, in winter is underestimated.

In spite of the differences observed between DLST and ground-based LST, a consistent agreement with Landsat-8 LST is observed, being also overestimated in summer season. Moreover, the statistics errors from DLST and Landsat-8 are very close for both olives and vineyards.

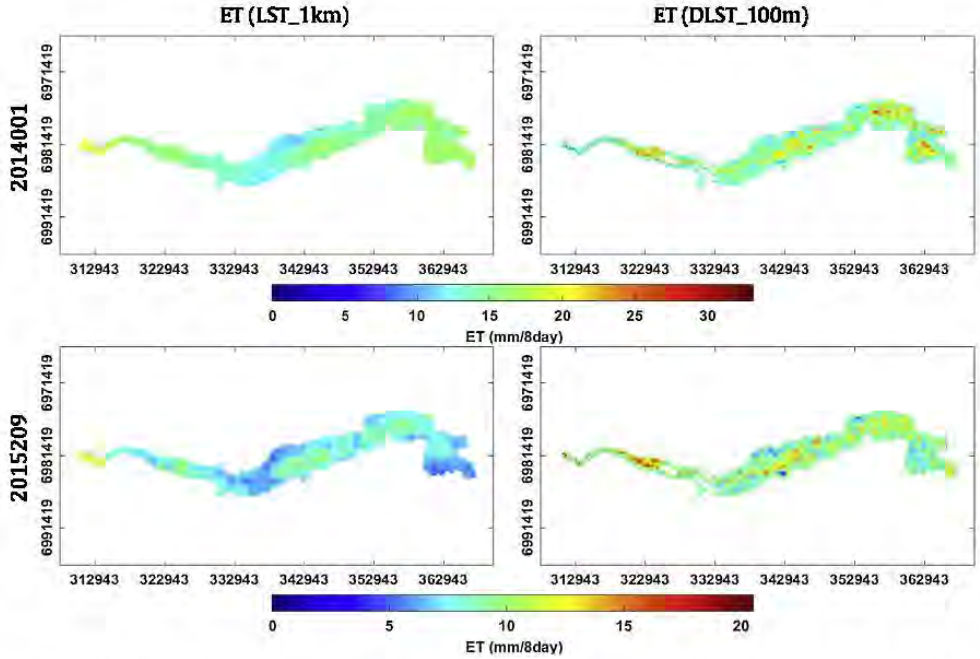


Fig. 6. Comparison between the composite 8-day *ETa* at 1 km and the disaggregated product at 100 m from MODIS *LST* at 1 km and the disaggregated *LST* product at 100 m, respectively.

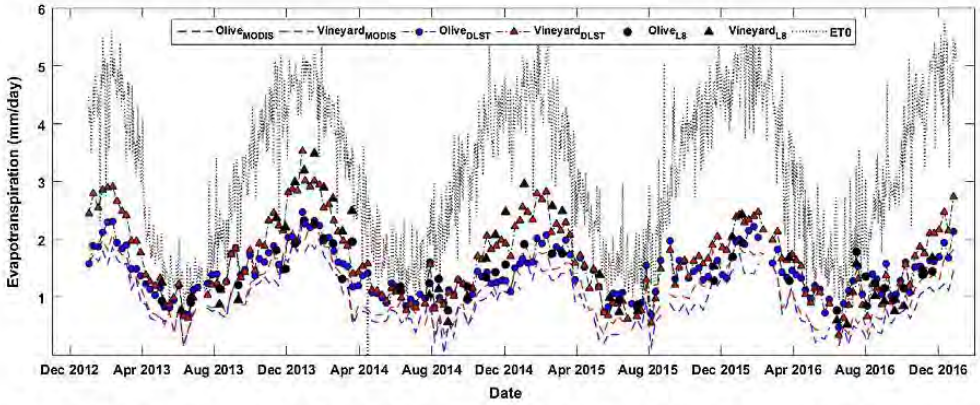


Fig. 7. *ETa* estimated over olive and vineyard station from different LST products. Subscript *MODIS* is for *ETa* from 8-day composite MODIS LST at 1 km, subscript *DLST* is for *ETa* from DLST proposed at 8-day and 100 m and *L8* is for *ETa* from Landsat-8 LST overpass at 100 m. *ETa* from DLST and MODIS are represented as the daily average over 8 days.

In terms of *ETa*, an important overestimation is evidenced during summer for vineyards showing the highest differences of the validation period reaching up to 1.4 mm day^{-1}. This difference could be attributed to the use of a *kc* for in situ *ETa* estimates under crop optimal conditions instead of the current crop which show some problems of water management (system irrigation) impacting the growing season and therefore lower NDVI values than the previous years. Therefore, it is possible that the *kc*-based *ETa* can be overestimated in vineyards for the summer periods after 2015. Another important result is the comparison between *ET0* and *ETa*, there is a high difference when comparing to *ET* in the arid zone, which shows an average difference greater than 1 mm day^{-1} during summer season accumulating 10 mm after 8 days. This is a key factor because in the study area, water irrigation scheduling programs are based on the *ET0*, which might overestimate the amount of water and therefore cause inefficiency in water usage.

5. Discussion

The sinusoidal annual relationship for *DLST* presented in this work performs well in terms of operational modes and applications

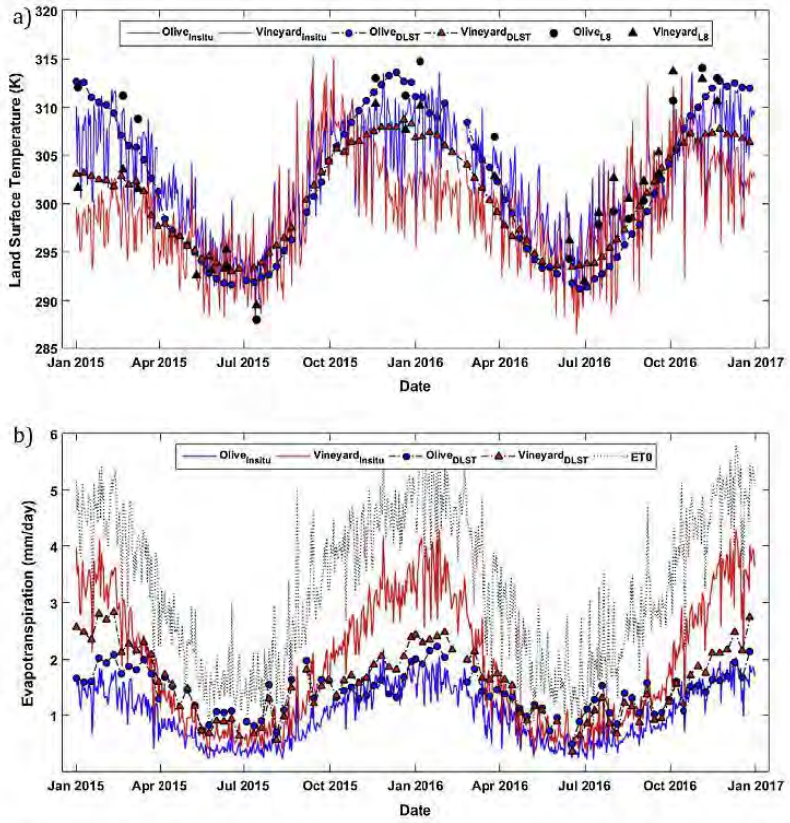


Fig. 8. Comparison between *DLST* and the in situ *LST* from LAB-net stations (top). LST from Landsat-8 overpass is shown for comparison for olives ($Olive_{L8}$) and vineyards ($Vineyard_{L8}$). Comparison between *ETa* from SSEBop and *DLST* and Kc-based ET (in situ) for olives orchards and vineyards (bottom).

Table 2
Coefficient of determination (r^2), mean bias error (Bias), standard deviation (Sigma) and root mean square error (RMSE) for *DLST* proposed and *ETa* from *DLST* and SSEBop method over olives orchards and vineyards. The values correspond to mean every 8 days at 100 m for the period 2015 to 2016. The same statistical parameters of LST and *ETa* from Landsat-8 are shown for comparison in the same period.

		Bias	Sigma	RMSE	r^2
DLST [K]	Olives	−0.30	3.56	3.57	0.87
	Vineyards	1.46	3.24	3.55	0.62
	Overall	0.59	3.50	3.55	0.72
LST Landsat-8 K	Olives	−0.37	3.29	3.31	0.95
	Vineyards	1.66	2.61	3.09	0.90
	Overall	0.72	3.08	3.16	0.87
ETa (DLST) [mm/day]	Olives	0.41	0.29	0.50	0.63
	Vineyards	−0.37	0.60	0.70	0.80
	Overall	0.02	0.61	0.61	0.67
ETa (Landsat-8) [mm/day]	Olives	0.27	0.41	0.49	0.44
	Vineyards	−0.52	0.77	0.93	0.63
	Overall	−0.15	0.74	0.75	0.49

to surface energy balance. These results are related to previous works which also demonstrate that the sinusoidal model can be used to obtain daily *LST* maps at medium spatial resolution (Weng et al., 2014). Moreover, based on the linear relationship derived from the interpolated sinusoidal regression coefficients, the *LST* can be obtained based on the *NDVI*, thus resulting in good seasonal performance over the arid area used here.

The *ETa* method for arid regions seems to be consistent with the results in terms of the operational algorithm and its retrievals. The *SSEBop* method is based on the differences between the dry and hot surface and air temperatures and in this context, the *DLST* method proposed here will be an excellent approach in terms of a good characterization of the *LST* over arid regions. This good characterization based on the combined ω fraction and *NDVI–LST* relationship represents the maximum and minimum of temperature used in the *dT* equation, a parameter which highly affects *ETa* retrievals during summer.

The *ETa* retrieved by the *DLST* obtained from the proposed method is consistent with the results when showing lower *ETa* than *ET0* values and is also influenced by the vegetation cover.

The phenology is a key parameter for a reliable *DLST* method and therefore the operation in terms of *ETa* maps. The validation was partially applied since the flooding that occurred in this area deserved more analysis to validate the *DLST* and *ETa* approach after September 2015, when the vineyards started the growing season. Nevertheless, the partial validation presented in this work demonstrates solid performance of the operational method in terms of *LST* and *ETa*.

Finally, several agricultural practices consider the *ET0* in this region in order to develop accurate water irrigation scheduling, which has overestimated the crop water requirements. Further efforts need to be applied to improve water use efficiency in the Copiapó Valley and should be accompanied by better knowledge of the crop spatial heterogeneity and a suitable strategy for an in situ monitoring network.

6. Conclusions

This work presents an operational method for disaggregating *LST* over an arid to semi-arid region that take into account (1) the spatial relationship between Landsat-8 and MODIS *LST*, (2) the spatial relationship between *LST* and the Normalized Difference Vegetation Index (*NDVI*) at high resolution (Landsat-8), and (3) the combination of both relationships. The disaggregated *LST* is integrated into an operational surface energy balance method (*SSEBop*) in order to estimate *ETa* at high temporal and spatial resolution. Results show that the developed approach gives an RMSE in *LST*, in average, lower than 3.6 K and an mean 8-day *ETa* lower than 0.7 mm/day. This approach is useful for generating better knowledge of water requirements in arid region which could be especially important in Chile where irrigation scheduling needs to be improved based on the current water usage and scarcity scenarios. Moreover, the proposed method modulates the contribution of vegetation by using two disaggregation methods based on temperature and *NDVI*. The simple use of *NDVI* and meteorologically-based equation could provide biased results since the values of *NDVI* need to be adapted to the high surface temperature derived from the soil/vegetation proportion. So, the use of integrated and operational method to extract surface information of surface and air temperature in addition to vegetation index could improve the surface energy balance in the arid region of Copiapó. Finally, this work contributes to determine and optimize the water demand in arid regions affected by the current drought in Chile, providing reliable *ETa* maps for irrigation scheduling and water use efficiency.

Acknowledgements

This work was partially funded by the projects Fondecyt-Initial (CONICYT/ref-11130359) and Fondef IDeA (CONICYT/ref-CA13I10102). The authors also wish to thank the NASA/MODIS and USGS/Landsat-8 teams for the data used in this work and also to Karina Palacios and Valentina Saavedra for their invaluable support in this work.

References

Agam, N., Kustas, W.P., Anderson, M.C., Li, F., Neale, C.M.U., 2007. A vegetation index based technique for spatial sharpening of thermal imagery. Remote Sens. Environ. 107, 545–558.

Allen, R.G., Pereira, L.S., Raes, D., Smith, M., 1998. Crop Evapotranspiration - Guidlines for Computing Crop Water Requirements. Irrig. Drainage. Pap. 56. Food Agricilculture. Organ., United Nations, Rome, Italy.

Allen, R.G., Pereira, L.S., Howell, T.a, Jensen, M.E., 2011. Evapotranspiration information reporting: I. Factors governing measurement accuracy. Agric. Water Manag. 98, 899–920. http://dx.doi.org/10.1016/j.agwat.2010.12.015.

Anderson, M.C., Norman, J.M., Mecikalski, J.R., Torn, R.D., Kustas, W.P., Basara, J.B., 2004. A multiscale remote sensing model for disaggregating regional fluxes to micrometeorological scales. J. Hydrometeorol. 5, 343–363. http://dx.doi.org/10.1175/1525-7541(2004)005<0343:AMRSMF>2.0.CO;2.

Anderson, M.C., Allen, R.G., Morse, A., Kustas, W.P., 2012. Use of Landsat thermal imagery in monitoring evapotranspiration and managing water resources. Remote Sens. Environ. 122, 50–65. http://dx.doi.org/10.1016/j.rse.2011.08.025.

Baldridge, A.M., Hook, S.J., Grove, C.I., Rivera, G., 2009. The ASTER spectral library version 2.0. Remote Sens. Environ 113, 711–715. http://dx.doi.org/10.1016/j.rse.2008.11.007.

Bastiaanssen, W.G.M., 1995. Regionalization of Surface Flux Densities and Moisture Indicators in Composite Terrain.

Bastiaanssen, W.G.M., Pelgrum, H., Wang, J., Ma, Y., Moreno, J.F., Roerink, G.J., van der Wal, T., 1998. A remote sensing surface energy balance algorithm for land (SEBAL). J. Hydrol. 212–213, 213–229. http://dx.doi.org/10.1016/S0022-1694(98)00254-6.

Bechtel, B., 2012. Robustness of annual cycle parameters to characterize the urban thermal landscapes. IEEE Geosci. Remote Sens. Lett. 9, 876–880. http://dx.doi.org/10.1109/LGRS.2012.2185034.

Bindhu, V.M., Narasimhan, B., Sudheer, K.P., 2013. Development and verification of a non-linear disaggregation method (NL-DisTrad) to downscale MODIS land surface temperature to the spatial scale of Landsat thermal data to estimate evapotranspiration. Remote Sens. Environ. 135, 118–129. http://dx.doi.org/10.1016/j.rse.2013.03.023.

Boisier, J.P., Rondanelli, R., Garreaud, R., Muñoz, F., 2016. Anthropogenic and natural contributions to the Southeast Pacific precipitation decline and recent megadrought in central Chile. Geophys. Res. Lett. http://dx.doi.org/10.1002/2015GL067265.

Bravo, D., 2013. Análisis de la incorporación de agua desalada al sistema hídrico en la cuenca del Río Copiapó. Memoria de Título. Universidad de Chile, Santiago, Chile, p. 60.

Cammalleri, C., Anderson, M.C., Gao, F., Hain, C.R., Kustas, W.P., 2014. Mapping daily evapotranspiration at field scales over rainfed and irrigated agricultural areas using remote sensing data fusion. Agric. For. Meteorol. 186, 1–11. http://dx.doi.org/10.1016/j.agrformet.2013.11.001.

Cheema, M.J.M., Bastiaanssen, W.G.M., 2010. Land use and land cover classification in the irrigated Indus Basin using growth phenology information from satellite data to support water management analysis. Agric. Water Manag. 97, 1541–1552. http://dx.doi.org/10.1016/j.agwat.2010.05.009.

Direccion General de Aguas, D., 2007. Estimaciones De Demanda De Agua Y Proyecciones Futuras. Zona II. Regiones V a XII y Región Metropolitana S.I.T. N° 122 571.

Duchemin, B., Goubier, J., Courrier, G., 1999. Monitoring phenological key stages and cycle duration of temperate deciduous forest ecosystems with NOAA/AVHRR data. Remote Sens. Environ. 67, 68–82. http://dx.doi.org/10.1016/S0034-4257(98)00067-4.

Durán-Alarcón, C., Santamaría-Artigas, A., Valenzuela, N., Mattar, C., 2014. RSR Calculator, una herramienta para el proceso de Calibración/Validación. Rev. Española Teledetec. 42, 111–117. http://dx.doi.org/10.4995/raet.2014.3230.

Findell, K.L., Gentine, P., Lintner, B.R., Kerr, C., 2011. Probability of afternoon precipitation in eastern United States and Mexico enhanced by high evaporation. Nat. Geosci. 4, 434–439. http://dx.doi.org/10.1038/ngeo1174.

Gao, Z., Gao, W., Chang, N.-B., 2011. Integrating temperature vegetation dryness index (TVDI) and regional water stress index (RWSI) for drought assessment with the aid of LANDSAT TM/ETM+ images. Int. J. Appl. Earth Obs. Geoinf. 13, 495–503. http://dx.doi.org/10.1016/j.jag.2010.10.005.

Guillevic, P.C., Biard, J.C., Hulley, G.C., Privette, J.L., Hook, S.J., Olioso, A., Göttsche, F. M., Radocinski, R., Román, M.O., Yu, Y., Csiszar, I., 2014. Validation of Land Surface Temperature products derived from the Visible Infrared Imaging Radiometer Suite (VIIRS) using ground-based and heritage satellite measurements. Remote Sens. Environ. 154, 19–37. http://dx.doi.org/10.1016/j.rse.2014.08.013.

Hong, S., Hendrickx, J.M.H., Borchers, B., Science, E., 2011. Down-scaling of SEBAL derived evapotranspiration maps from MODIS (250 m) to Landsat (30 m) scales. Earth 32, 1–37. http://dx.doi.org/10.1080/01431161.2010.512929.

Hulley, G., Hook, S., 2013. The ASTER Global Emissivity Database (ASTER GED) Collection.

Jiménez-Muñoz, J.C., Sobrino, J.A., Mattar, C., Franch, B., 2010. Atmospheric correction of optical imagery from MODIS and Reanalysis atmospheric products. Remote Sens. Environ. 114, 2195–2210. http://dx.doi.org/10.1016/j.rse.2010.04.022.

Jiménez-Muñoz, J.C., Sobrino, J.A., Skokovi, D., Mattar, C., Cristóbal, J., 2014. Land surface temperature retrieval methods from Landsat-8 thermal infrared sensor data. Geosci. Remote Sens. Lett. IEEE 11, 1840–1843. http://dx.doi.org/10.1109/LGRS.2014.2312032.

Kalma, J.D., McVicar, T.R., McCabe, M.F., 2008. Estimating land surface evaporation: a review of methods using remotely sensed surface temperature data. Surv. Geophys. 29, 421–469. http://dx.doi.org/10.1007/s10712-008-9037-z.

Kim, J., Hogue, T.S., 2012. Evaluation and sensitivity testing of a coupled Landsat-MODIS downscaling method for land surface temperature and vegetation indices in semi-arid regions. J. Appl. Remote Sens. 6, 63517–63569. http://dx.doi.org/10.1117/1.JRS.6.063569.

Kustas, W.P., Norman, J.M., Anderson, M.C., French, A.N., 2003. Estimating subpixel surface temperatures and energy fluxes from the vegetation index–radiometric temperature relationship. Remote Sens. Environ. 85, 429–440. http://dx.doi.org/10.1016/S0034-4257(03)00036-1.

Li, Z.-L., Tang, R., Wan, Z., Bi, Y., Zhou, C., Tang, B., Yan, G., Zhang, X., 2009. A review of current methodologies for regional evapotranspiration estimation from

remotely sensed data. Sensors (Basel) 9, 3801–3853. http://dx.doi.org/10.3390/s90503801.
Li, M., Qu, J.J., Hao, X., 2010. Investigating phenological changes using MODIS vegetation indices in deciduous broadleaf forest over continental U.S. during 2000–2008. Ecol. Inform. 5, 410–417. http://dx.doi.org/10.1016/j.ecoinf.2010.04.002.
Li, Z.-L., Tang, B.-H., Wu, H., Ren, H., Yan, G., Wan, Z., Trigo, I.F., Sobrino, J.A., 2013. Satellite-derived land surface temperature: current status and perspectives. Remote Sens. Environ. 131, 14–37. http://dx.doi.org/10.1016/j.rse.2012.12.008.
Liu, Y., Hill, M.J., Zhang, X., Wang, Z., Richardson, A.D., Hufkens, K., Filippa, G., Baldocchi, D.D., Ma, S., Verfaillie, J., Schaaf, C.B., 2017. Using data from Landsat, MODIS, VIIRS and PhenoCams to monitor the phenology of California oak/grass savanna and open grassland across spatial scales. Agric. For. Meteorol. 237–238, 311–325. http://dx.doi.org/10.1016/j.agrformet.2017.02.026.
Martínez, L., Tapia, F., 2002. Riego del Olivar Proyecto: Manejo Moderno de Huertos de Olivos en el Valle de Huasco Bol. INIA N°72 34.
Mattar, C., Franch, B., Sobrino, J.A., Corbari, C., Jiménez-Muñoz, J.C., Olivera-Guerra, L., Skokovic, D., Sória, G., Oltra-Carrió, R., Julien, Y., Mancini, M., 2014. Impacts of the broadband albedo on actual evapotranspiration estimated by S-SEBI model over an agricultural area. Remote Sens. Environ. 147, 23–42. http://dx.doi.org/10.1016/j.rse.2014.02.011.
Mattar, C., Durán-Alarcón, C., Jimenez-Munoz, J.C., Santamaría-Artigas, A., Olivera-Guerra, L., Sobrino, J.A., 2015. Global Atmospheric Profiles from Reanalysis Information (GAPRI): a new database for earth surface temperature retrieval. Int. J. Remote Sens. 37–41. http://dx.doi.org/10.1080/01431161.2015.1054965.
Mattar, C., Santamaría-artigas, A., Durán-alarcón, C., Olivera-guerra, L., Fuster, R., Borvarán, D., 2016. The LAB-net soil moisture network : application to thermal remote sensing and surface energy balance. Data 1, 1–14. http://dx.doi.org/10.3390/data1010006.
Merlin, O., Duchemin, B., Hagolle, O., Jacob, F., Coudert, B., Chehbouni, G., Dedieu, G., Garatuza, J., Kerr, Y., 2010. Disaggregation of MODIS surface temperature over an agricultural area using a time series of Formosat-2 images. Remote Sens. Environ. 114, 2500–2512. http://dx.doi.org/10.1016/j.rse.2010.05.025.
Merlin, O., Jacob, F., Wigneron, J.P., Walker, J., Chehbouni, G., 2012. Multidimensional disaggregation of land surface temperature using high-resolution red, near-infrared, shortwave-infrared, and microwave-L bands. IEEE Trans. Geosci. Remote Sens. 50, 1864–1880. http://dx.doi.org/10.1109/TGRS.2011.2169802.
Mukherjee, S., Joshi, P.K., Garg, R.D., 2014. A comparison of different regression models for downscaling Landsat and MODIS land surface temperature images over heterogeneous landscape. Adv. Sp. Res. 54, 655–669. http://dx.doi.org/10.1016/j.asr.2014.04.013.
Nemani, R.R., Pierce, L., Running, S.W., Goward, S., 1993. Developing satellite-derived estimates of surface moisture stress. J. Applied Met. 32, 548–557. http://dx.doi.org/10.1175/1520-0450.
Ogawa, K., Schmugge, T., Jacob, F., 2003. Estimation of land surface window (8–12 μm) emissivity from multi-spectral thermal infrared remote sensing — a case study in a part of Sahara Desert. Geophys. Res. Lett. 30 (2), 12–15. http://dx.doi.org/10.1029/2002GL016354.
Oki, T., Kanae, S., 2006. Global hydrological cycles and world water resources. Science 313, 1068–1072. http://dx.doi.org/10.1126/science.1128845 (80-.).
Olivera-Guerra, L., Mattar, C., Durán-Alarcón, C., Santamaría-Artigas, A., Fuster, R., 2014. A first evaluation of an operational method to estimate actual evapotranspiration by using MODIS data over the semi-arid region of Chile. In: Procd. IV Recent Advances in Quantitative Remote Sensing Symposium (RAQRS). 22–25 September, Valencia, Spain.
Oyarzún, J., Oyarzún, R., 2011. Sustainable development threats, inter-sector conflicts and environmental policy requirements in the arid, mining rich, Northern Chile territory. Sustain. Dev. 19, 263–274. http://dx.doi.org/10.1002/sd.441.
Porter, D.O., Gowda, P.H., Marek, T.H., Howell, T.A., Irmak, S., Moorhead, J., 2012. Sensitivity of grass and alfalfa reference evapotranspiration to sensor accuracy. Appl. Eng. Agric. 28, 543–549. http://dx.doi.org/10.1007/s00382-007-0340-z.
Prata, A.J., Caselles, V., Coll, C., Sobrino, J.A., Ottle, C., 1995. Thermal remote sensing of land surface temperature from satellites: current status and future prospects. Remote Sens. Rev. 12 (3–4), 175–224. http://dx.doi.org/10.1080/02757259509532285.
Rousseeuw, P.J., 1984. Least median of squares regression. J. Am. Stat. Assoc. 79, 871–880.
Senay, G.B., Bohms, S., Singh, R.K., Gowda, P.H., Velpuri, N.M., Alemu, H., Verdin, J.P., 2013. Operational evapotranspiration mapping using remote sensing and weather datasets: a new parameterization for the SSEB approach. JAWRA J. Am. Water Resour. Assoc. 49, 577–591. http://dx.doi.org/10.1111/jawr.12057.
Senay, G.B., Friedrichs, M., Singh, R.K., Velpuri, N.M., 2016. Evaluating Landsat 8 evapotranspiration for water use mapping in the Colorado River Basin. Remote Sens. Environ. 185, 171–185. http://dx.doi.org/10.1016/j.rse.2015.12.043.
Sobrino, J.A., Li, Z.L., Stoll, M.P., Becker, F., 1996. Multi-channel and multi-angle algorithms for estimating sea and land surface temper- ature with ATSR data. Int. J. Remote Sens. 17 (11), 2089–2114.
Sobrino, J.A., Jiménez-muñoz, J.C., Sòria, G., Romaguera, M., Guanter, L., Moreno, J., Member, A., Plaza, A., Member, S., Martínez, P., 2008. Land surface emissivity retrieval from different VNIR and TIR sensors. IEEE Trans. Geosci. Remote Sens. 46, 316–327.
Sobrino, J.A., Franch, B., Mattar, C., Jiménez-Muñoz, J.C., Corbari, C., 2012. A method to estimate soil moisture from Airborne Hyperspectral Scanner (AHS) and ASTER data: application to SEN2FLEX and SEN3EXP campaigns. Remote Sens. Environ. 117, 415–428. http://dx.doi.org/10.1016/j.rse.2011.10.018.
Suarez, F., Muñoz, J.F., Fernández, B., Dorsaz, J.-M., Hunter, Ch., Karavitis, C.A., Gironás, J., 2014. Integrated water resource management and energy requirements for water supply in the Copiapó River Basin, Chile. Water 6, 2590–2613.
Valdés-Pineda, R., Pizarro, R., García-Chevesich, P., Valdés, J., Olivares, C., Vera, M., Balocchi, F., Pérez, F., Vallejos, C., Fuentes, R., Abarza, A., Helwig, B., 2014. Water governance in Chile: availability, management and climate change, J. Hydrol. 519 (Part C), 2538–2567.
Vaculin, M., Vieira, R., Bernard, R., Hatfield, J.L., 1982. Spatial variability of surface tem- perature along two transects of a bare. Water Resour. Res. 18, 1677–1686.
Weng, Q., Fu, P., Gao, F., 2014. Generating daily land surface temperature at Landsat resolution by fusing Landsat and MODIS data. Remote Sens. Environ. 145, 55–67. http://dx.doi.org/10.1016/j.rse.2014.02.003.
Weng, Q., Liu, H., Liang, B., Lu, D., 2008. The spatial variations of urban land surface temperatures: pertinent factors, zoning effect, and seasonal variability. IEEE J. Sel. Top. Appl. Earth Obs. Remote Sens. 1, 154–166. http://dx.doi.org/10.1109/JSTARS.2008.917869.
Zhan, W., Chen, Y., Zhou, J., Wang, J., Liu, W., Voogt, J., Zhu, X., Quan, J., Li, J., 2013. Disaggregation of remotely sensed land surface temperature: literature survey, taxonomy, issues, and caveats. Remote Sens. Environ. 131, 119–139. http://dx.doi.org/10.1016/j.rse.2012.12.014.
Zhu, X., Chen, J., Gao, F., Chen, X., Masek, J.G., 2010. An enhanced spatial and temporal adaptive reflectance fusion model for complex heterogeneous regions. Remote Sens. Environ. 114, 2610–2623. http://dx.doi.org/10.1016/j.rse.2010.05.032.

Chapter 6. Conclusions and Perspectives

Contents

6.1. Summary of results *158*

6.2. Identifying the main limitations of the methods *160*

6.2.1. Irrigation retrieval approach *161*

6.2.2. LST disaggregation method *162*

6.3. Perspectives *163*

6.3.1. Towards the improvement in spatial and temporal resolution *163*

6.3.2. Towards the use of radar data for a better representation of hydrological processes *164*

6.3.3. Partitioning soil/vegetation components *165*

This PhD thesis entitled "**Monitoring the water budget of irrigated crops from multi-spectral optical/thermal remote sensing data**" is focused on monitoring the main water budget components (such as the ET, RZSM and irrigation) of agricultural areas at crop field scale (100 m resolution) on a daily basis over extended areas (e.g. irrigation districts of few kilometers of extension). For this purpose, novel approaches are proposed based on the coupling between readily available remote sensing optical/thermal data and a FAO-based model. An important part of this work has been devoted to develop an innovative strategy to take advantage of: i) the availability of optical/thermal data at a suited spatial resolution for monitoring crops, ii) the simplicity of contextual methods from optical/thermal data in the estimation of soil/vegetation water status, iii) the utility of optical/thermal data as proxy of soil moisture and RZSM, and iv) enhancing the temporal resolution of high-spatial resolution thermal data to better constrain the dynamics of water budget components.

6.1. Summary of results

Despite irrigation being the main water supply in semi-arid to arid regions, information on spatially distributed irrigation is rarely available. This lack of knowledge is therefore one of the main issues to be overcome by water balance models that need water inputs as an essential forcing. The first part of this thesis is devoted to developing and evaluating a novel retrieval approach of irrigation and the associated variables (ET and RZSM) from the integration of optical/thermal data into the FAO-based water balance model. The estimation of irrigation is a key step on the development of the approach since no method is yet available to retrieve the timing and amounts of irrigation at both crop field and daily scales.

A feasibility study of the proposed approach is carried out using ground-based optical/thermal measurements over a winter wheat field in the R3 area of the Haouz Plain, Morocco. The approach adapts the thermal-based contextual models implemented with remote sensing data to ground-based measurements by simulating from a surface energy balance the extreme conditions in terms of both soil/vegetation cover and water status. This procedure is adopted with a twofold purpose: i) taking advantage of the simplicity and robustness of contextual methods and ii) being applicable to large areas by using satellite data. The approach allowed retrieving the irrigation volumes and dates from optical/thermal-derived ET and RZSM as first-guess estimates. In practice, the approach relies on: i) partitioning the Landsat LST to derive the crop water stress coefficient Ks; ii) retrieving RZSM diagnostic estimates from thermal-derived Ks by using the FAO-2Kc formalism; iii) estimating irrigation amounts and dates along the season from differences of (first-guess) LST-derived RZSM; and iv) forcing the FAO-2Kc model by the retrieved irrigations to re-analyze the RZSM and ET on a daily basis. Consequently,

daily irrigation, daily RZSM and daily ET estimates are retrieved at crop field scale along the growing season by using daily ground-based optical/thermal measurements. Statistical results indicate that thermal-derived ET is more accurate than the ET simulated by the standard version of FAO-2Kc. The RMSE and slope of the linear regression between estimated and observed ET is decreased from 0.84 to 0.68 mm day^{-1} and closer to 1 from 1.21 to 1.07, respectively. First-guess RZSM is significantly improved when FAO-2Kc is implemented by using retrieved irrigation. The R^2 and slope of the linear regression between simulated and observed RZSM is increased from 0.42 to 0.67 and from 0.46 to 0.78, respectively, while the RMSE is decreased from 0.06 to 0.03 m^3m^{-3} and the bias (-0.04 m^3m^{-3}) is removed. Since this feasibility study was carried out with an availability of optical/thermal every day, a sensitivity analysis to the frequency revisit time of the data was adopted in order to assess the applicability to satellite optical/thermal data.

The second part of this thesis is devoted to implementing the proposed approach over extended areas by using readily available satellite optical/thermal data. Here, the main aim is facing two major issues in the implementation at large scales of crop water balance models like FAO-2Kc: the availability of (daily) irrigation spatially distributed and the need of calibration to obtain accurate estimations. For this purpose, the approach proposed in the first part is adapted to be implemented with temporally sparsely Landsat-7/-8 optical/thermal data over three agricultural areas of 12 by 12 km in the semi-arid region of Haouz Plain, in central Morocco. In these areas, the approach is evaluated over five experimental sites covered by winter wheat during four growing seasons with different irrigation techniques (drip, flood and no-irrigation). On the one side, the approach demonstrates its ability for retrieving irrigation at daily and field scale from high spatial resolution optical/thermal data. Total irrigation amounts are accurately estimated over all the fields and seasons with a RMSE equal to 44 mm and an R of 0.95. On the other side, an assessment of irrigation estimates is carried out at different time scales by accumulating the irrigation amounts from 1 to 90 days. This analysis depicts that acceptable errors are obtained for irrigations cumulated over 15 days (RMSE = 27 mm and R = 0.52) and the performance is gradually improved by increasing the accumulation period, reaching a very accurate estimation at seasonal scale. However, poor agreements at daily to weekly scales are found in terms of irrigation. Nevertheless, the irrigation estimates are still acceptable in order to accurately simulate the dynamics of ET and RZSM at daily and field crop scales throughout the season. Overall RMSE is equal to 0.04 m^3m^{-3} and 0.83 $mm.d^{-1}$ for RZSM and ET, respectively, which are very close to those estimated from FAO-2Kc forced by actual irrigations (RMSE equal to 0.04 m^3m^{-3} and 0.82 $mm.d^{-1}$). Moreover, the accuracy retrieved in ET estimates demonstrates that the formulation of generic coefficients Kcb and Ke allows FAO-2Kc to be implemented by using satellite data, hence avoiding calibration with in situ data, which are usually unavailable over extended areas. The 15-days period over which acceptable errors are obtained (for irrigations) is closely related to the revisit time of Landsat data, which can

be 16 days or even more in cloudy conditions. Therefore, the revisit time of current optical/thermal satellite data is a critical point in the proposed approach.

The third and last part of this thesis is devoted to implementing an operational disaggregation method for enhancing the spatial and temporal resolution of thermal data. Although Landsat data provide optical/thermal data at a spatial resolution suitable for monitoring crops, its temporal resolution is not optimal. The method is based on the combination of NDVI-LST and Landsat/MODIS relationship to provide LST at Landsat-pixel resolution every 8 days. This method is implemented over two different areas in terms of extension, crop cover and climate conditions: Copiapo Valley and Haouz Plain. The approach is applied in a slightly different way in each area in order to obtain different disaggregated LST data as main input for different approaches. In Copiapo Valley, the method is implemented to provide LST data representative of 8-day compositing periods, which are subsequently integrated into the SSEBop model for estimating cumulated ET over 8 days. In Haouz Plain, the method is implemented to provide LST data every 8 days, which is combined with Landsat-7/8 LST to be integrated into the FAO-based water balance model for applying the irrigation retrieval approach as it is proposed in the second part of this thesis. Combining both disaggregated LST and Landsat LST data sets, thanks to the increase in the temporal frequency of LST data, results in a better detection of irrigation events and amounts. The overall RMSE of cumulated irrigation at different time scales is decreased from 46 to 34 mm (meaning an improvement of 25%), while the R is increased from 0.50 to 0.64 (improvement of 29%). Consistently, the RZSM estimated using the disaggregated LST in addition to Landsat LST as input is improved by 26% and 14% in terms of RMSE and R, respectively. Despite the differences in both cases in terms of crops (tree versus winter wheat crops), extension areas (very narrow versus and extended agricultural area), climate (arid and semi-arid) and approach used (SSEBop and irrigation retrieval approach), the disaggregation procedure allowed to enhancing and ensuring the availability of LST data every 8 days, helping better estimate the water budget components.

In brief, this thesis demonstrates the utility of high spatial resolution optical/thermal data for estimating, for the first time, irrigation at field scale on a daily basis and for better closing the water budget over agricultural areas.

6.2. Identifying the main limitations of the methods

Despite the great value of the approaches developed in this thesis to better estimate and monitor the water use in agricultural areas, there are some limitations related to the assumptions, area of applicability and data used. It is therefore worth identifying the

limitations in order to provide insights on how to improve the methodology and to extend its applicability in future works. Given that the first part of this thesis is a feasibility study at in situ level and then it is adapted for the implementation over extended areas, as presented in the second part, only the limitations of this latter approach and the disaggregation methods are presented below.

6.2.1. Irrigation retrieval approach

The irrigation retrieval method is based on the RZSM simulated basically from a simple water balance model for which some assumptions are made. Some of the assumptions are common to the FAO-Kc model, while others are specific to the irrigation retrieval method. The assumptions deriving from the FAO-2Kc model and its related limitations are:

- The daily RZSM varies within a range defined by a minimum value set to the SM at wilting point (SM_{wp}) and by a maximum value set to the SM at field capacity (SM_{fc}). This assumption poses to a twofold challenge. On one side, an adequate knowledge of SM_{wp} and SM_{fc} is only possible in very controlled situations. These parameters are usually estimated using pedo-transfer functions from soil properties (texture) that are not exempt from errors. Moreover, knowledge of soil properties is required over the area (district irrigation), whose accuracy is limited by its great spatial variability. On the other side, setting the RZSM between SM_{wp} and $SM_{fc,}$ implies that once RZSM reaches SM_{fc}, any additional water supply is considered as water excess and is therefore drained from the soil bucket by deep percolation (occurring simultaneously to the water excess supply). Moreover, observations show that RZSM can be even less than SM_{wp} due to diffusion processes between surface and deeper soil layers and associated evaporation losses, among other factors (e.g. vegetation type).
- The RZSM is linearly related to Ks between SM_{wp} and the critical RZSM (SM_{crit}), which is estimated as a fraction of the total available water according to the water stress tolerance of crops (Allen et al., 1998). In the irrigation retrieval approach, this point is related to the saturation of Landsat-derived Ks (equal to 1) for SM values between SM_{crit} and SM_{fc}, where Landsat-derived Ks is not able to detect any RZSM change.

The assumptions specific to the irrigation retrieval approach together with its limitations are:

- The retrieved irrigation is the effective irrigation (irrigation minus drainage), meaning that the irrigation excess which triggers deep percolation is not taken into account. Despite optical/thermal data are used to derive a proxy for the RZSM

by means of vegetation temperatures, this kind of data is not able to get information on the deeper water flows.

- An irrigation event is detected on the day when the water balance-derived RZSM reaches SM_{fc}. This assumption limits the detection of irrigation event especially in drip-irrigated field where the water is supplied not necessarily to reach the SM_{fc}. Hence the number of irrigation events is reduced by missing events and the amount of water is thus overestimated for each detected event by compensation effect.
- The LST partitioning method assumes that LST is decomposed linearly into soil and vegetation components by means of fvg and the LST-fvg feature space. For simplicity, the soil and vegetation emissivities are not considered, even though they can be retrieved from ASTER GED data adjusted to Landsat thermal bands as detailed in the Section 2.4.1.2. Furthermore, the contextual nature of LST-fvg feature space implies a greater uncertainty in Ts when fvg is large, and conversely, a greater uncertainty in Tv when fvg is small. These uncertainties are transferable to the soil (Kr) and crop (Ks) water status and then to the initialization of the water balance to estimate RZSM dynamics.
- If two successive Landsat overpass dates both indicate unstressed conditions (Ks=1), it is assumed that the crop does not undergo water stress during that period. It is also assumed that Ks=1 between a Landsat date indicating unstressed conditions and an irrigation event detected before the next Landsat overpass date. When stressed conditions actually occur during this period, the irrigation retrieval method leads to the overestimation of irrigation amounts in order to maintain the unstressed conditions observed by sparsely Landsat data. The longer the revisit period of Landsat data by cloudy conditions, the more likely this problem is.
- In several agricultural areas of semi-arid to arid regions, the capillarity rise and runoff are neglected due to flat surfaces and water tables significantly deep. However, the runoff may be a source of error especially under flood irrigation techniques, where an important amount of water applied might be lost by runoff to nearby fields. Regarding the capillarity rise, deeper and wetter layers might provide water to the root zone layer by diffusion processes, which have not been taken into account in the approach.

6.2.2. LST disaggregation method

The approach is based on the combination of LST-NDVI and Landsat-MODIS LST relationships. Although the approach is within the state-of-the-art, only LST and NDVI variables have been considered for the purpose of an operational implementation by using readily available satellite data. The limitations deriving from the disaggregation approach are detailed below.

Since this approach is based on LST-NDVI relationships, all variations in LST coming from factors other than NDVI over agricultural areas cannot be explained. For instance, the use of only NDVI presents some shortcomings over areas with high spatial variability in SM, as warned by some authors (e.g. Agam et al., 2007b; Merlin et al., 2010). For this reason, some works have added other information that influence the LST in order to reflect changes in LST coming from SM or senescent vegetation (Amazirh et al., 2019; Merlin et al., 2012a, 2010).

The Landsat-MODIS LST relationship is based on the ratio between both sensors at different spatial resolutions by assuming that land cover types do not change along the study period. Consequently, the approach might be limited when changing the land cover with regard to the calibration period.

There is no doubt that the approach lacks the information on SM, but the use of only LST-NDVI information was prioritized in order to reach an operational implementation of the approach. An important result however is that despite the simplicity of the approach, an improvement in the water resources estimates was reached.

6.3. Perspectives

6.3.1. Towards the improvement in spatial and temporal resolution

One of the main constraints in the proposed approach is the availability of thermal data at both high spatial and temporal resolutions. The operational disaggregation method in the Chapter 5 demonstrated an improvement in the estimation of water budget components by enhancing the revisit time of LST data. However, this has not been enough to provide accurate irrigation estimates at time scale shorter than 2 weeks, which might be explained by the errors associated with the disaggregated LST data set. Such a result anticipates the expected improvements in the irrigation estimates by using LST data at an enhanced spatio-temporal resolution that will be directly achieved by future thermal missions like TRISHNA (Lagouarde and Bhattacharya, 2018). Regarding the uncertainty associated to the disaggregation method, the advent of the TRISHNA mission will lead to substantial improvements in the estimation of irrigation at daily to weekly scales due to three main improvements in the thermal infrared observation: i) a shorter revisit cycles (~3 days), ii) a higher spatial resolution (~50 m), iii) direct thermal observations much more accurate than disaggregated LST data. Here, in order to better foresee errors in irrigation estimates that might be achieved at time scales shorter than 2 weeks, a sensitivity analysis of errors associated to LST data should be carried out. That would allow differentiating the errors coming from both the revisit time and the uncertainty in thermal observation. It should be noted that such improvements are in accordance with

the two main objectives driving the TRISHNA mission: the monitoring of energy and water budgets of the continental biosphere and the monitoring of coastal and continental areas (Lagouarde and Bhattacharya, 2018).

Alternatively, disaggregation methods can be improved in order to enhance the spatial and temporal resolution of availability of data without losing accuracy in the LST estimates. For this purpose, future studies could make use of additional data to take into account soil moisture or fraction of senescent vegetation, as in Amazirh et al., (2019) or Merlin et al. (2012a, 2010). However, there is still significant work to do in order to reach an operational maturity. In this vein, the approach proposed in this thesis could be implemented by including albedo from optical data and radar data from the Sentinel-1 mission. Both optical and radar data as additional constraints on disaggregation method might consider additional factors that modulate the LST and, consequently, reducing the uncertainty in LST retrievals at fine scale.

6.3.2. Towards the use of radar data for a better representation of hydrological processes

The radar signal derived from active C-band Sentinel-1 data is highly sensitive to the SSM. Hence the use of radar data will not only serve as additional variable for the disaggregation LST method, but also to improve the representation of hydrological processes. The radar data can be introduced in the irrigation retrieval approach for, specifically, two objectives. First, it can be introduced to better constrain the surface soil water status that controls the soil evaporation and, second, to better constrain the timing (and hence the amount) of the retrieved irrigation.

Regarding the first objective, some improvements are foreseen to better represent the soil surface layer by means of Kr that modules the evaporation coefficient in the ET estimates. In practice, better constraining the topsoil layer could improve the estimation of Kr by integrating the SSM through a soil evaporative efficiency model as proposed by Merlin et al. (2018, 2016, 2011) and used in Amazirh et al. (2018). This latter study combined a radar-based SSM proxy with a thermal-based SM proxy (that corresponds to Kr used in this thesis) for retrieving SSM at high spatio-temporal resolution over bare soils. The implementation over bare soils (i.e. there is no influence of vegetation cover on thermal and radar observation) proved the synergy between optical/radar data for SSM estimates, raising the possibility of application over surface partially covered by vegetation canopy. Therefore, the synergy by means of optical/radar-based SSM proxies can be implemented for Kr estimates in order to improve the evaporation estimates. These improvements would represent an important step forward over semi-arid to arid regions since soil evaporation represents an important component in the water budget.

Regarding the second objective, the radar-derived SSM or alternatively a SSM proxy can be of great value to better estimate both amount and timing of irrigation. In the proposed approach of this thesis, the irrigation retrieval is based on RZSM dynamics, which is estimated from a water balance initialized by (first-guess) thermal-derived RZSM. Here, radar-derived SSM at high spatial and temporal resolution is a useful and complementary constraint for the crop water balance, allowing representing the temporal dynamics of the SSM.

Recent studies have attempted to estimate SSM at high (~100 m) spatial resolution from either Sentinel-1 radar data (Amazirh et al., 2018; Gao et al., 2017; Hajj et al., 2017) or by disaggregating passive microwave-derive SSM at coarse resolution (Eweys et al., 2017; Ojha et al., 2019). On one side for instance, the works of Amazirh et al. (2018) and Gao et al. (2017) proposed promising methods for operational implementation based on the contextual information observed in radar data. Amazirh et al. (2018) used the LST-backscattered signals feature space to estimate a SSM proxy, while Gao et al. (2017) used the difference between backscattered Sentinel-1 radar signals observed on two consecutive overpasses, expressed as a function of NDVI to retrieve SSM estimates. On the other side, Ojha et al. (2019) recently proposed a new disaggregation scheme for SMOS and SMAP derived SSM by using Landsat data through a sequential disaggregation approach based on the physical and theoretical scale change algorithm DisPATCH (Merlin et al., 2013, 2012b; Molero et al., 2016). DisPATCH was previously proposed to disaggregate the SSM to 1 km spatial resolution by using MODIS data. The advantage of this method is that parameters are calibrated using remote sensing data with no in situ data needed. The issue is that SSM at 100 m from DisPATCH data is available only under clear-sky days during Landsat overpasses, meaning that the revisit time is considerably reduced.

Notwithstanding, such SSM estimates or SSM proxy at high spatial resolution together with thermal-derived RZSM could be integrated into the crop water balance in order to better retrieve the temporal dynamics of RZSM, and consequently the irrigation estimates. In terms of timing of irrigation, the higher revisit time of Sentinel-1 (~5 days) with respect to current thermal mission like Landsat-7/8 (~8 days) is an additional asset in the crop water modelling in order to better determine the irrigation events. In terms of irrigation amounts, the inclusion of SSM into the water balance as a variable directly linked to water fluxes might allow to avoid the use of some soil parameters such as maximum and minimum SM values set to SM_{fc} and SM_{wp}, respectively. Instead, the temporal dynamics in SSM might allow determining the minimum values from drying periods as well as the SM values reached by water supplies. Consequently, such additional information is foreseen to improve the accuracy in irrigation amounts.

6.3.3. Partitioning soil/vegetation components

In the approaches proposed in this thesis, the partitioning of LST is the essential foundation for the partitioning of the soil and vegetation components, in terms of soil (Kr) and crop (Ks) water status, soil evaporation and plant transpiration, and hence key in the thermal-derived RZSM estimates. For simplicity in an operational implementation, the adopted LST partitioning method is based on contextual information observed only in the LST-fvg feature space. This method implies uncertainties in Ts and Tv for large and small fvg values, respectively, which may be transferable to the evaporation, transpiration and RZSM estimates. Therefore, a robust partitioning method, but at the same time that can be operationally implemented, is necessary in order to provide reliable Tv and Ts estimates. Such a method will require improving the algorithm of LST partitioning in addition to having appropriate in situ measurements to effectively assess the algorithm.

6.3.3.1. From remote sensing data

Improving the disaggregation algorithm could be addressed by means of a synergistic approach between optical-radar data by taking into account additional land surface variables that allows better differentiating the soil and vegetation components. For instance, surface albedo from visible/shortwave data allows differentiating soil types (clayey and sandy soils) and vegetation types (green and senescent vegetation) (Merlin et al., 2014). Surface emissivity from thermal data allows differentiating several soil types (Sobrino et al., 2009), whose low values are not confused with the larger values of green vegetation. Backscattered radar signals in VV polarization have demonstrated higher sensitivity to SSM than VH polarization (Amazirh et al., 2018), which allows distinguishing different soil water status (Amazirh et al., 2019). Most of these works have been validated over bare soil conditions. Given the higher sensitivity of VH polarization to vegetation effects, it might help differentiate surface types and extend the SAR-derived SSM to soils partially to fully covered by vegetation canopy (Amazirh et al., 2018). Therefore, the integration of these additional information from readily available data is a useful and practical tool to better represent the soil and vegetation components in order to partition the LST and its associated fluxes.

6.3.3.2. From EC-based measurements to validate remote sensing applications

This proposed approach based on FAO-2Kc allows retrieving the partitioning of ET into its soil evaporation and plant transpiration components. Partitioning ET is important for agricultural purposes such as assessing the impacts of management practices on the water use efficiency. However, these components are difficult to validate due to the

general unavailability of ground-based monitoring of evaporation and transpiration separately.

Commonly, the methods for monitoring evaporation and trasnpiration are based on infrequent or sparse measurements, such as sap flow, microlysimeters and chambers. The mismatch in footprints between the localized fluxes obtained by these instruments and the field scale from micrometeorological methods (EC) can lead to significant scaling issues. Therefore, a flux partitioning method only based on EC measurements is a useful tool for practical validation purposes. It is more meaningful in a context where CO2 and H2O fluxes are currently available through networks of EC stations across many ecosystems types around the world. In this vein, Scanlon and Sahu (2008) proposed a partitioning method based on the flux-variance similarity and correlation analyses of high-frequency eddy covariance data, which estimates transpiration/photosynthesis and evaporation/respiration using only high frequency EC measurements. The method has been applied over different ecosystems types, including different crops (Anderson et al., 2017; Perez-Priego et al., 2018; Rana et al., 2018; Scanlon and Kustas, 2012, 2010; Wang et al., 2016). This method has a great potential for calibration/validation purposes, such as the assessment of coefficients of FAO-2Kc as in Anderson et al. (2017). Furthermore, a validation against independent evaporation and transpiration measurements over the study area (Rafi et al., 2019) will be needed in order to use long series of EC measurements to validate the evaporation/transpiration derived from remote sensing data as those obtained in this thesis from the proposed irrigation retrieval approach.

Chapter 6. Conclusions et Perspectives (français)

Contents

6.1. Résumé des résultats 170

6.2. Principales limites des méthodes 173

6.2.1. Approche d'estimation d'irrigation 173

6.2.2. Méthode de désagrégation LST 175

6.3. Perspectives 176

6.3.1. Vers l'amélioration de la résolution spatiale et temporelle 176

6.3.2. Vers l'utilisation des données radar pour une meilleure représentation des processus hydrologiques 177

6.3.3. Partition entre les composants de sol et de végétation 178

Cette thèse de doctorat intitulée **"Suivi des ressources en eau des cultures irriguées par télédétection multi-spectrales optique/thermique"** est centrée sur le suivi des principales composantes du bilan hydrique (telles que l'ET, le RZSM et l'irrigation) des zones agricoles à l'échelle de la parcelle (résolution de 100 m) sur une base journalière et sur de surfaces larges (e.g. les districts d'irrigation à quelques kilomètres d'extension). A cette fin, de nouvelles approches sont proposées, basées sur le couplage entre des données optiques/thermiques de télédétection facilement disponibles et un modèle basé sur la FAO. Une partie importante de ce travail a été consacrée à l'élaboration d'une stratégie novatrice visant à tirer parti: i) de la disponibilité de données optiques/thermiques à une résolution spatiale appropriée pour le suivi des cultures, ii) de la simplicité des méthodes contextuelles à partir de données optiques/thermiques dans l'estimation de l'état hydrique de sol et de la végétation, iii) de l'utilité des données optiques/thermiques comme approximation de l'humidité de sol et de RZSM, et iv) améliorer la résolution temporelle des données thermiques à haute résolution spatiale pour mieux contraindre la dynamique des composantes du bilan hydrique.

6.1. Résumé des résultats

Bien que l'irrigation soit la principale source d'apport en eau dans les régions semi-arides à arides, on dispose rarement d'informations sur la distribution spatiale de l'irrigation. Ce manque d'information est donc l'un des principaux problèmes à surmonter par les modèles de bilan hydrique qui ont besoin d'apports d'eau comme forçage essentiel. La première partie de cette thèse est consacrée au développement et à l'évaluation d'une nouvelle approche d'estimation de l'irrigation et des variables associées (ET et RZSM) à partir de l'intégration des données optiques/thermiques dans le modèle FAO de bilan hydrique. L'estimation de l'irrigation est une étape clé dans le développement de l'approche puisqu'aucune méthode n'est encore disponible pour récupérer le timing et la quantité d'irrigation à la fois à l'échelle de la parcelle et à l'échelle journalière.

Une étude de faisabilité de l'approche proposée est réalisée à l'aide de mesures optiques/thermiques in situ sur une parcelle de blé d'hiver dans la zone R3 de la plaine du Haouz, au Maroc. L'approche adapte les modèles contextuels mis en œuvre avec les données de télédétection optique/thermique aux mesures in situ en simulant à partir d'un bilan énergétique de surface les conditions extrêmes en termes de couverture de sol/végétation et d'état hydriques. Cette procédure est adoptée avec un double objectif: i) tirer parti de la simplicité et de la robustesse des méthodes contextuelles et ii) être applicable à de larges zones en utilisant des données satellitaires. L'approche a permis d'estimer les volumes d'irrigation et les dates à partir d'ET et de RZSM dérivés du optique/thermique comme estimations de première approximation. En pratique, l'approche repose sur: i) la partition de la LST issue de Landsat pour dériver le coefficient

de stress hydrique Ks; ii) l'estimation de RZSM de première approximation à partir des Ks dérivés du thermique et du formalisme FAO-2Kc; iii) l'estimation des quantités et des dates de l'irrigation au cours de la saison à partir des différences du RZSM dérivé de la LST (première approximation); et iv) le forçage du modèle FAO-2Kc à partir des estimations d'irrigation pour ré-analyser les RZSM et ET journalières. Par conséquent, les estimations de l'irrigation journalière, la RZSM journalière et l'ET journalière sont obtenues à l'échelle de la parcelle tout au long de la saison agricole en utilisant des mesures in situ optiques/thermiques journalières. Les résultats statistiques indiquent que l'ET issue du thermique est plus précis que l'ET simulé par la version standard du modèle FAO-2Kc. La RMSE et la pente de la régression linéaire entre l'ET estimée et observée est diminuée de 0,84 à 0,68 mm jour^{-1} et plus près de 1 (de 1,21 à 1,07), respectivement. La RZSM de première approximation est considérablement améliorée lorsque FAO-2Kc est mis en œuvre en utilisant l'irrigation estimée. Le R^2 et la pente de la régression linéaire entre la RZSM simulée et la RZSM observée passent respectivement de 0,42 à 0,67 et de 0,46 à 0,78, tandis que le RMSE passe de 0,06 à 0,03 m^3m^{-3} et le biais (-0,04 m3m-3) est supprimé. Étant donné que cette étude de faisabilité a été réalisée avec une disponibilité journalière de données optiques/thermiques, une analyse de sensibilité au temps de revisite des données a été adoptée afin d'évaluer l'applicabilité aux données optiques/thermiques satellitaires.

La deuxième partie de cette thèse est consacrée à la mise en œuvre de l'approche proposée sur des zones larges en utilisant des données optiques/thermiques satellitaires facilement disponibles. Ici, l'objectif principal est de faire face à deux problèmes majeurs dans la mise en œuvre à grande échelle de modèles de bilan hydrique des cultures comme FAO-2Kc: la disponibilité de l'irrigation (journalière) distribuée spatialement et la nécessité d'une calibration pour obtenir des estimations précises. A cette fin, l'approche proposée dans la première partie est adaptée pour être mise en œuvre avec des données optiques/thermiques issue de Landsat-7/-8 à faible densité temporelle sur trois zones agricoles de 12 km par 12 km dans la région semi-aride de la plaine du Haouz, au centre du Maroc. Dans ces zones, l'approche est évaluée sur cinq sites expérimentaux couverts de blé d'hiver pendant quatre saisons de croissance avec différentes techniques d'irrigation (goutte à goutte, inondation et sans irrigation). D'une part, l'approche démontre sa capacité à obtenir l'irrigation à l'échelle journalière et sur la parcelle à partir de données optiques/thermiques à haute résolution spatiale. Les quantités totales d'irrigation sont estimées avec précision pour toutes les parcelles et toutes les saisons avec une RMSE égale à 44 mm et un R de 0,95. D'autre part, une évaluation des estimations d'irrigation est effectuée à différentes échelles de temps en accumulant les quantités d'irrigation de 1 à 90 jours. Cette analyse montre que des erreurs acceptables sont obtenues pour des irrigations cumulées sur 15 jours (RMSE = 27 mm et R = 0,52) et que la performance est progressivement améliorée en augmentant la période d'accumulation, atteignant une estimation très précise à l'échelle saisonnière. Cependant, on constate de mauvais accords à l'échelle journalière ou hebdomadaire en termes d'irrigation. Néanmoins, les estimations de l'irrigation sont toujours acceptables afin de

simuler avec précision la dynamique de l'ET et du RZSM à l'échelle journalière et à l'échelle de la parcelle agricole tout au long de la saison. La RMSE totale est égale à 0,04 m^3m^{-3} et 0,83 $mm.d^{-1}$ pour les RZSM et ET, respectivement, ce qui est très proche de ceux estimés par la FAO-2Kc forcée par des irrigations réelles (RMSE égale à 0,04 m^3m^{-3} et 0,82 $mm.d^{-1}$). De plus, la précision retrouvée dans les estimations d'ET démontre que la formulation des coefficients génériques Kcb et Ke permet de mettre en œuvre la modèle FAO-2Kc en utilisant des données satellitaires, évitant ainsi la calibration avec des données in situ, qui ne sont généralement pas disponibles sur des zones larges. La période de 15 jours pendant laquelle des erreurs acceptables sont obtenues (pour les irrigations) est étroitement liée au temps de revisite des données Landsat, qui peut être de 16 jours ou plus dans des conditions nuageuses. Par conséquent, le temps de revisite des données optiques/thermiques issue de satellites actuels est un point critique de l'approche proposée.

La troisième et dernière partie de cette thèse est consacrée à la mise en œuvre d'une méthode opérationnelle de désagrégation pour améliorer la résolution spatiale et temporelle des données thermiques. Bien que les données Landsat fournissent des données optiques/thermiques à une résolution spatiale appropriée pour le suivi des cultures, leur résolution temporelle n'est pas optimale. La méthode est basée sur la combinaison des relations NDVI/LST et Landsat/MODIS pour fournir un LST à résolution des pixels Landsat tous les 8 jours. Cette méthode est mise en œuvre dans deux zones différentes en termes d'extension, de couverture végétale et de conditions climatiques: Vallée de Copiapo et plaine du Haouz. L'approche est appliquée d'une manière légèrement différente dans chaque zone afin d'obtenir différentes données désagrégées de LST en tant qu'entrée principale pour différentes approches. Dans la vallée de Copiapo, la méthode est mise en œuvre pour fournir des données LST représentatives de périodes de 8 jours, qui sont ensuite intégrées dans le modèle SSEBop pour estimer l'ET cumulée sur 8 jours. Dans la plaine du Haouz, la méthode est mise en œuvre pour fournir des données LST tous les 8 jours, qui sont combinées avec de LST issue de Landsat-7/8 pour être intégrées dans le modèle de bilan hydrique basé sur la FAO-2Kc pour appliquer l'approche d'estimation d'irrigation comme il est proposé dans la deuxième partie de cette thèse. La combinaison des ensembles de données de LST désagrégées et LST de Landsat, grâce à l'augmentation de la fréquence temporelle des données LST, permet une meilleure détection des événements et des quantités d'irrigation. La RMSE globale de l'irrigation cumulée à différentes échelles de temps est diminuée de 46 à 34 mm (soit une amélioration de 25 %), tandis que la corrélation passe de 0,50 à 0,64 (soit une amélioration de 29 %). De façon cohérente, la RZSM estimée en utilisant la LST désagrégée en plus de la LST de Landsat comme entrée est amélioré de 26 % et 14 % en termes de RMSE et de R, respectivement. Malgré les différences dans les deux cas en termes de cultures (d'arbres et blé d'hiver), de zones d'extension (zones très étroites et zones agricoles larges), de climat (arides et semi-arides) et d'approche utilisée (SSEBop et approche d'estimation de l'irrigation), la procédure de désagrégation a permis de

renforcer et de garantir la disponibilité des données LST tous les 8 jours, permettant de mieux estimer les composants du bilan hydrique.

En résumé, cette thèse démontre l'utilité des données optiques/thermiques à haute résolution spatiale pour estimer, pour la première fois, l'irrigation à l'échelle de la parcelle sur une base journalière et pour mieux contraindre le bilan hydrique des zones agricoles.

6.2. Principales limites des méthodes

Malgré la grande valeur des approches développées dans cette thèse pour mieux estimer et surveiller l'utilisation de l'eau dans des zones agricoles, il y a certaines limites liées aux hypothèses, au domaine d'application et aux données utilisées. Il est donc utile d'identifier les limites afin de fournir des perspectives sur la manière d'améliorer la méthodologie et d'étendre son applicabilité dans les travaux futurs. Étant donné que la première partie de cette thèse est une étude de faisabilité au niveau in situ et qu'elle est ensuite adaptée pour la mise en œuvre sur des zones larges, comme présenté dans la deuxième partie, seules les limites de cette dernière approche et les méthodes de désagrégation sont présentées ci-dessous.

6.2.1. Approche d'estimation d'irrigation

La méthode de récupération de l'eau d'irrigation est basée sur le RZSM simulé à partir d'un modèle simple de bilan hydrique pour lequel certaines hypothèses sont faites. Certaines des hypothèses sont communes au modèle FAO-Kc, tandis que d'autres sont spécifiques à la méthode d'extraction par irrigation. Les hypothèses découlant du modèle FAO-2Kc et ses limites sont les suivantes:

- La RZSM journalière varie dans la limite d'une plage définie par une valeur minimale fixée à la SM au point de flétrissement (SM_{wp}) et par une valeur maximale fixée à la SM à la capacité du champ (SM_{fc}). Cette hypothèse pose un double défi. D'une part, une connaissance adéquate du SM_{wp} et du SM_{fc} n'est possible que dans des situations très contrôlées. Ces paramètres sont généralement estimés à l'aide de fonctions pédo-transfert à partir de propriétés du sol (texture) qui ne sont pas exemptes d'erreurs. De plus, la connaissance des propriétés du sol est nécessaire sur la zone (périmètre d'irrigation), dont la précision est limitée par sa grande variabilité spatiale. D'un autre côté, le réglage de la RZSM entre SM_{wp} et SM_{fc}, implique qu'une fois que la RZSM atteint SM_{fc}, tout apport d'eau supplémentaire est considéré comme un excès d'eau et est donc drainé du réservoir de stockage par percolation profonde (se produisant

simultanément à l'excédent d'eau). De plus, les observations montrent que la RZSM peut être encore plus faible que la SM_{wp} en raison des processus de diffusion entre les couches superficielles et profondes du sol et des pertes par évaporation associées, entre autres facteurs (e.g. le type de végétation).

- La RZSM est linéairement liée au Ks entre le SM_{wp} et le RZSM critique (SM_{crit}), qui est estimé comme une fraction de l'eau totale disponible selon la tolérance au stress hydrique des cultures (Allen et al., 1998). Dans l'approche d'estimation de l'irrigation, ce point est lié à la saturation des Ks dérivés de Landsat (égale à 1) pour les valeurs SM entre SM_{crit} et SM_{fc}, où les Ks dérivés de Landsat ne peuvent détecter aucun changement de RZSM.

Les hypothèses spécifiques à l'approche d'estimation d'irrigation ainsi que ses limites sont les suivantes:

- L'irrigation estimée est l'irrigation effective (irrigation moins drainage), ce qui signifie que l'excès d'irrigation qui déclenche une percolation profonde n'est pas pris en compte. Malgré l'utilisation de données optiques/thermiques pour dériver une approximation de la RZSM au moyen de la température de la végétation, ce type de données n'est pas capable d'obtenir des informations sur les fluxes d'eau profonde.
- Un événement d'irrigation est détecté le jour où la RZSM dérivée du bilan hydrique atteint la SM_{fc}. Cette hypothèse limite la détection de l'événement d'irrigation, en particulier dans les parcelles irriguées par goutte à goutte où l'eau n'est pas nécessairement fournie pour atteindre la SM_{fc}. Ainsi, le nombre d'événements d'irrigation est réduit par des événements manquants et la quantité d'eau est donc surestimée pour chaque événement détecté par effet de compensation.
- La méthode de partition de LST suppose que la LST est décomposée linéairement en composantes du sol et de la végétation au moyen de fvg et de l'espace caractéristique LST-fvg. Pour des raisons de simplicité, les émissivités du sol et de la végétation ne sont pas prises en compte, même si elles peuvent être extraites des données ASTER GED ajustées aux bandes thermiques de Landsat comme indiqué à la section 2.4.1.2. De plus, la nature contextuelle de l'espace LST-fvg implique une plus grande incertitude dans Ts lorsque fvg est grand, et inversement, une plus grande incertitude dans Tv lorsque fvg est petit. Ces incertitudes sont transférables à l'état hydrique du sol (Kr) et de la culture (Ks) puis à l'initialisation du bilan hydrique pour estimer la dynamique de la RZSM.
- Si deux dates successives de passages de Landsat indiquent des conditions non stressées (Ks=1), on suppose que la culture ne subit pas de stress hydrique pendant cette période. On suppose également que Ks=1 entre une date Landsat indiquant des conditions non stressées et un événement d'irrigation détecté avant la date du prochain passage de Landsat. Lorsque des conditions de stress surviennent durant cette période, la méthode d'estimation de l'irrigation conduit

à surestimer les quantités d'irrigation afin de maintenir les conditions non stressées observées par les données Landsat éparses. Plus la période de revisite des données Landsat par temps nuageux est longue, plus ce problème est probable.

- Dans plusieurs zones agricoles en régions semi-arides à arides, l'augmentation de la capillarité et le ruissellement sont négligés en raison de surfaces planes et de nappes phréatiques très profondes. Cependant, le ruissellement peut être une source d'erreur, en particulier dans les techniques d'irrigation par inondation, où une quantité importante d'eau appliquée peut être perdue par ruissellement dans les parcelles voisines. En ce qui concerne l'augmentation de la capillarité, des couches plus profondes et plus humides pourraient fournir de l'eau à la couche de la zone racinaire par des processus de diffusion, qui n'ont pas été pris en compte dans l'approche.

6.2.2. Méthode de désagrégation LST

L'approche est basée sur la combinaison des relations LST-NDVI et LST Landsat-MODIS. Bien que l'approche soit dans l'état de l'art, seules les variables LST et NDVI ont été prises en compte aux fins d'une mise en œuvre opérationnelle en utilisant des données satellitaires facilement accessibles. Les limites dérivées de l'approche de désagrégation sont détaillées ci-dessous.

Étant donné que cette approche est basée sur les relations LST-NDVI, toutes les variations de LST provenant de facteurs autres que NDVI sur les zones agricoles ne peuvent être expliquées. Par exemple, l'utilisation de l'NDVI seulement présente certaines lacunes dans les régions où la variabilité spatiale de la SM est élevée, comme l'ont signalé certains auteurs (e.g. Agam et al., 2007b; Merlin et al., 2010). Pour cette raison, certains travaux ont ajouté d'autres informations qui influencent la LST afin de refléter les changements de la LST provenant de la SM ou de la végétation sénescente (Amazirh et al, 2019; Merlin et al, 2012a, 2010).

La relation LST entre Landsat-MODIS est basée sur le rapport entre les deux capteurs à différentes résolutions spatiales en supposant que les types de couverture ne changent pas au cours de la période étudiée. Par conséquent, l'approche pourrait être limitée lors d'un changement de l'occupation du sol par rapport à la période de calibration.

Il ne fait aucun doute que l'approche manque d'informations sur la SM, mais l'utilisation des seules informations LST-NDVI a été priorisée afin de parvenir à une mise en œuvre opérationnelle de l'approche. Un résultat important est toutefois que, malgré la simplicité de l'approche, une amélioration des estimations des ressources en eau a été obtenue.

6.3. Perspectives

6.3.1. Vers l'amélioration de la résolution spatiale et temporelle

L'une des principales contraintes de l'approche proposée est la disponibilité de données thermiques à des résolutions spatiales et temporelles élevées. La méthode de désagrégation opérationnelle du Chapitre 5 a démontré une amélioration dans l'estimation des composantes du bilan hydrique en augmentant le temps de revisite des données de LST. Cependant, cela n'a pas été suffisant pour fournir des estimations précises de l'irrigation à une échelle de temps inférieure à deux semaines, ce qui pourrait s'expliquer par les erreurs associées à l'ensemble de données désagrégées de LST. Un tel résultat anticipe les améliorations attendues dans les estimations de l'irrigation en utilisant les données de LST à une résolution spatio-temporelle améliorée qui sera directement obtenue par de futures missions thermiques comme TRISHNA (Lagouarde et Bhattacharya, 2018). En ce qui concerne l'incertitude associée à la méthode de désagrégation, l'arrivée de la mission TRISHNA entraînera des améliorations substantielles dans l'estimation de l'irrigation à l'échelle journalière ou hebdomadaire grâce à trois améliorations principales dans l'observation infrarouge thermique: i) des cycles de revisite plus courts (~3 jours), ii) une résolution spatiale supérieure (~50 m), iii) des observations thermiques directes beaucoup plus précises que des données de LST désagrégées. Ici, afin de mieux prévoir les erreurs dans les estimations de l'irrigation qui pourraient être obtenues à des échelles de temps inférieures à 2 semaines, une analyse de sensibilité des erreurs associées aux données de LST devrait être effectuée. Cela permettrait de différencier les erreurs provenant à la fois du temps de revisite et de l'incertitude de l'observation thermique. Il est à noter que ces améliorations sont en accord avec les deux objectifs principaux de la mission TRISHNA: le suivi des bilans énergétiques et hydriques de la biosphère continentale et le suivi des zones côtières et continentales (Lagouarde et Bhattacharya, 2018).

Par ailleurs, les méthodes de désagrégation peuvent être améliorées afin d'améliorer la résolution spatiale et temporelle de la disponibilité des données sans perdre la précision des estimations de LST. À cette fin, des études futures pourraient utiliser des données supplémentaires pour tenir compte de l'humidité du sol ou de la fraction de végétation sénescente, comme dans Amazirh et al (2019) ou Merlin et al (2012a, 2010). Toutefois, il reste encore beaucoup à faire pour atteindre une maturité opérationnelle. Dans cet esprit, l'approche proposée dans cette thèse pourrait être mise en œuvre en incluant l'albédo des données optiques et radar de la mission Sentinel-1. Les données optiques et radar, en tant que contraintes supplémentaires à la méthode de désagrégation, pourraient tenir compte d'autres facteurs qui modulent le LST et, par conséquent, réduisent l'incertitude dans les estimations de la LST à une échelle fine.

6.3.2. Vers l'utilisation des données radar pour une meilleure représentation des processus hydrologiques

Le signal radar dérivé des données Sentinel-1 en bande C active est très sensible au SSM. Par conséquent, l'utilisation des données radar servira non seulement de variable supplémentaire pour la méthode de désagrégation de LST, mais aussi pour améliorer la représentation des processus hydrologiques. Les données radar peuvent être introduites dans l'approche d'estimation de l'irrigation pour, spécifiquement, deux objectifs. Premièrement, il peut être introduit pour mieux contraindre l'état hydrique de surface du sol qui contrôle l'évaporation du sol et, deuxièmement, pour mieux contraindre le timing (et donc la quantité) de l'irrigation estimée.

En ce qui concerne le premier objectif, certaines améliorations sont prévues pour mieux représenter la couche superficielle du sol au moyen du Kr qui module le coefficient d'évaporation dans les estimations de l'ET. En pratique, une meilleure contrainte de la couche superficielle pourrait améliorer l'estimation du Kr en intégrant la SSM à un modèle d'efficacité d'évaporation du sol proposé par Merlin et al. (2018, 2016, 2011) et utilisé dans Amazirh et al. (2018). Cette dernière étude a combiné un proxy SSM radar avec un proxy SM thermique (qui correspond au Kr utilisé dans cette thèse) pour récupérer la SSM à haute résolution spatio-temporelle sur des sols nus. La mise en œuvre sur des sols nus (i.e. qu'il n'y a pas d'influence du couvert végétal sur l'observation thermique et radar) a prouvé la synergie entre les données optiques/radar pour les estimations de SSM, soulevant la possibilité d'application sur une surface partiellement couverte par la canopée végétale. Par conséquent, la synergie au moyen d'approximations de SSM issue de l'optique/radar peut être mise en œuvre pour les estimations du Kr afin d'améliorer les estimations de l'évaporation. Ces améliorations représenteraient une avancée importante par rapport aux régions semi-arides à arides, car l'évaporation du sol représente un élément important du bilan hydrique.

En ce qui concerne le deuxième objectif, la SSM dérivée du radar ou une SSM proxy peut être très utile pour mieux estimer à la fois la quantité et le timing de l'irrigation. Dans l'approche proposée dans cette thèse, l'estimation de l'irrigation est basée sur la dynamique de la RZSM, qui est estimée à partir d'un bilan hydrique initialisé par de RZSM dérivée du thermique (premières approximations). Ici, la SSM dérivée par radar à haute résolution spatiale et temporelle est une contrainte utile et complémentaire pour le bilan hydrique des cultures, permettant de représenter la dynamique temporelle de la SSM.

Des études récentes ont tenté d'estimer la SSM à une haute résolution spatiale (~100 m) à partir de données radar Sentinel-1 (Amazirh et al., 2018; Gao et al., 2017; Hajj et al., 2017) ou en désagrégeant la SSM passive obtenue par micro-ondes à résolution grossière

(Eweys et al., 2017; Ojha et al., 2019). D'un côté par exemple, les travaux d'Amazirh et al (2018) et de Gao et al (2017) proposent des méthodes prometteuses de mise en œuvre opérationnelle basées sur les informations contextuelles observées dans les données radar. Amazirh et al. (2018) ont utilisé l'espace entre des signaux rétrodiffusés et LST pour estimer une approximation de SSM, tandis que Gao et al. (2017) ont utilisé la différence entre les signaux radar Sentinel-1 rétrodiffusés observés sur deux passages consécutifs, exprimée en fonction de NDVI pour obtenir des estimations de SSM. D'autre part, Ojha et al (2019) ont récemment proposé un nouveau schéma de désagrégation pour SSM dérivé de SMOS et de SMAP en utilisant les données Landsat par une approche séquentielle de désagrégation basée sur l'algorithme DisPATCH (Merlin et al., 2013, 2012b; Molero et al., 2016). DisPATCH a déjà été proposé pour désagréger la SSM à une résolution spatiale de 1 km en utilisant les données MODIS. L'avantage de cette méthode est que les paramètres sont calibrés à l'aide de données de télédétection sans qu'aucune donnée in situ ne soit nécessaire. Le problème est que les données de SSM à 100 m issue de DisPATCH ne sont disponibles que par conditions de ciel dégagé pendant les passages de Landsat, ce qui signifie que le temps d'observation est considérablement réduit.

Néanmoins, de telles estimations de SSM ou de telles approximations de SSM à haute résolution spatiale ainsi que les RZSM issue du thermique pourraient être intégrées dans le bilan hydrique des cultures afin de mieux estimer la dynamique temporelle des RZSM et, par conséquent, les estimations d'irrigation. En ce qui concerne le moment de l'irrigation, le temps de revisite plus élevé de Sentinel-1 (~5 jours) par rapport à de mission thermique actuelle comme Landsat-7/8 (~8 jours) est un atout supplémentaire dans la modélisation de l'eau des cultures afin de mieux déterminer les événements de l'irrigation. En termes de quantités d'irrigation, l'inclusion du SSM dans le bilan hydrique en tant que variable directement liée aux flux d'eau pourrait permettre d'éviter l'utilisation de certains paramètres du sol tels que les valeurs maximales et minimales de SSM fixées respectivement à SM_{fc} et SM_{wp}. Au lieu de cela, la dynamique temporelle dans la SSM pourrait permettre de déterminer les valeurs minimales à partir des périodes de séchage ainsi que les valeurs de SM atteintes par les apports en eau. Par conséquent, ces informations supplémentaires sont prévues pour améliorer l'exactitude des quantités d'eau d'irrigation.

6.3.3. Partition entre les composants de sol et de végétation

Dans les approches proposées dans cette thèse, la partition de la LST est le fondement indispensable de la partition des composantes du sol et de la végétation, en termes d'état

hydrique du sol (Kr) et des cultures (Ks), d'évaporation du sol et de transpiration des plantes, et donc la clé des estimations de RZSM dérivées du thermique. Pour plus de simplicité dans une implémentation opérationnelle, la méthode de partition de la LST adoptée est basée sur des informations contextuelles observées uniquement dans l'espace à deux dimensions LST-fvg. Cette méthode implique des incertitudes dans les estimations de Ts et de Tv pour les grandes et petites valeurs de fvg, respectivement, qui peuvent être transférables aux estimations de l'évaporation, de la transpiration et de la RZSM. Par conséquent, une méthode de partition robuste, mais en même temps qui peut être mise en œuvre sur le plan opérationnel, est nécessaire afin de fournir des estimations fiables de Tv et de la Ts à l'aide de la télédétection. Une telle méthode nécessitera l'amélioration de l'algorithme de partition de la LST en plus d'avoir des mesures in situ appropriées pour évaluer efficacement l'algorithme.

6.3.3.1. A l'aide de la télédétection

L'amélioration de l'algorithme de désagrégation pourrait être abordée au moyen d'une approche synergique entre les données optiques-radar en tenant compte de variables de surface supplémentaires qui permettent de mieux différencier les composantes de sol et de la végétation. Par exemple, l'albédo de surface à partir de données sur les ondes visibles et les courtes longueurs d'ondes permet de différencier les types de sols (sols argileux et sableux) et les types de végétation (végétation verte et sénescente) (Merlin et al., 2014). L'émissivité de surface des données thermiques permet de différencier plusieurs types de sols (Sobrino et al., 2009), dont les faibles valeurs ne sont pas confondues avec les grandes valeurs de la végétation verte. Les signaux radar rétrodiffusés en polarisation VV ont démontré une plus grande sensibilité à la SSM que la polarisation VH (Amazirh et al., 2018), ce qui permet de distinguer différents états hydriques des surfaces (Amazirh et al., 2019). La plupart de ces travaux ont été validés sur des sols nues. Étant donné la plus grande sensibilité de la polarisation VH aux effets de la végétation, elle pourrait aider à différencier les types de surface et à étendre la SSM dérivée des données de SAR aux sols partiellement ou entièrement couverts par le couvert végétal (Amazirh et al., 2018). Par conséquent, l'intégration de ces informations supplémentaires à partir de données facilement disponibles est un outil utile et pratique pour mieux représenter les composantes du sol et de la végétation afin d'estimer la partition de la LST et ses flux associés.

6.3.3.2. Des mesures basées sur l'Eddy Covariance à la validation des applications de télédétection

Cette approche proposée basée sur la modèle FAO-2Kc permet d'estimer la partition de l'ET dans ses composantes d'évaporation du sol et de transpiration des plantes. La partition de la ET est important à des fins agricoles, par exemple pour évaluer les impacts des pratiques de gestion sur l'efficacité de l'utilisation de l'eau. Cependant, ces composantes sont difficiles à valider en raison de l'indisponibilité générale du suivi in situ de l'évaporation et de la transpiration séparément.

Généralement, les méthodes de suivi de l'évaporation et de la trasnpiration sont basées sur des mesures peu fréquentes ou rares, telles que le flux de sève, les micro-lysimètres et les chambres. L'inadéquation des empreintes entre les flux localisés obtenus par ces instruments et l'échelle de la parcelle des méthodes micro-météorologiques (EC) peut entraîner d'importants problèmes d'échelle. Par conséquent, une méthode de partition des flux basée uniquement sur des mesures EC est un outil utile à des fins de validation pratique. Elle est plus significative dans un contexte où les flux de CO2 et d'H2O sont actuellement disponibles par de réseaux de stations EC dans de nombreux types d'écosystèmes à travers le monde. Dans cet ordre d'idées, Scanlon et Sahu (2008) ont proposé une méthode de partitionnement basée sur la similarité flux-variance et d'analyses de corrélation de données d'*eddy covariance* à haute fréquence, qui estime la transpiration/photosynthèse et l'évaporation/respiration en utilisant uniquement des mesures EC à haute fréquence. La méthode a été appliquée à différents types d'écosystèmes, y compris différentes cultures (Anderson et al., 2017; Perez-Priego et al., 2018; Rana et al., 2018; Scanlon et Kustas, 2012, 2010; Wang et al., 2016). Cette méthode a un grand potentiel de calibration/validation, comme l'évaluation des coefficients utilisés dans le modèle FAO-2Kc comme dans Anderson et al (2017). De plus, une validation par rapport à des mesures indépendantes d'évaporation et de transpiration sur la zone d'étude (Rafi et al., 2019) sera nécessaire afin d'utiliser de longues séries temporelles de mesures EC pour valider l'évaporation/transpiration dérivée des données de télédétection comme celles obtenues dans cette thèse avec l'approche proposée pour l'estimation de l'irrigation.

Bibliography

Adams, M.L., W.D. Philpot, and W.A. Norvell, 1999. Yellowness index: An application of spectral second derivatives to esti- mate chlorosis of leaves in stressed vegetation, International Journal of Remote Sensing, 20(18), 3663–3675.

Agam, N., Kustas, W.P., Anderson, M.C., Li, F., Neale, C.M.U., 2007a. A vegetation index based technique for spatial sharpening of thermal imagery. Remote Sens. Environ. 107, 545–558. https://doi.org/10.1016/j.rse.2006.10.006

Agam, N., Kustas, W.P., Anderson, M.C., Li, F., Neale, C.M.U., 2007b. A vegetation index based technique for spatial sharpening of thermal imagery. Remote Sens. Environ. 107, 545–558.

Ait Hssaine, B., Merlin, O., Ezzahar, J., Ojha, N., Er-raki, S., Khabba, S., 2019. An evapotranspiration model self-calibrated from remotely sensed surface soil moisture, land surface temperature and vegetation cover fraction: application to disaggregated SMOS and MODIS data. Hydrol. Earth Syst. Sci. Discuss. 1–35. https://doi.org/10.5194/hess-2019-105

Albergel, C., Rüdiger, C., Pellarin, T., Calvet, J.-C., Fritz, N., Froissard, F., Suquia, D., Petitpa, a., Piguet, B., Martin, E., 2008. From near-surface to root-zone soil moisture using an exponential filter: an assessment of the method based on in-situ observations and model simulations. Hydrol. Earth Syst. Sci. Discuss. 5, 1603–1640. https://doi.org/10.5194/hessd-5-1603-2008

Allen, R.G., Pereira, L.S., 2009. Estimating crop coefficients from fraction of ground cover and height. Irrig. Sci. 28, 17–34. https://doi.org/10.1007/s00271-009-0182-z

Allen, R.G., Pereira, L.S., Howell, T. a., Jensen, M.E., 2011. Evapotranspiration information reporting: I. Factors governing measurement accuracy. Agric. Water Manag. 98, 899–920. https://doi.org/10.1016/j.agwat.2010.12.015

Allen, R.G., Pereira, L.S., Raes, D., Smith., M., 1998. Crop evapotranspiration - Guidlines for computing crop water requirements. Irrig. Drainage. Pap. 56, Food Agriciculture. Organ. United Nations, Rome, Italy.

Allen, R.G., Tasumi, M., Morse, A., Trezza, R., 2005. A Landsat-based energy balance and evapotranspiration model in Western US water rights regulation and planning. Irrig. Drain. Syst. 19, 251–268. https://doi.org/10.1007/s10795-005-5187-z

Amazirh, A., 2019. Monitoring crops water needs at high spatio-temporal resolution by synergy of optical / thermal and radar observations. Thesis. Université Paul Sabatier - Toulouse III.

Amazirh, A., Er-Raki, S., Chehbouni, A., Rivalland, V., Diarra, A., Khabba, S., Ezzahar, J., Merlin, O., 2017. Modified Penman–Monteith equation for monitoring evapotranspiration of wheat crop: Relationship between the surface resistance and remotely sensed stress index. Biosyst. Eng. 164, 68–84.

https://doi.org/10.1016/j.biosystemseng.2017.09.015

Amazirh, A., Merlin, O., Er-Raki, S., 2019. Including Sentinel-1 radar data to improve the disaggregation of MODIS land surface temperature data. ISPRS J. Photogramm. Remote Sens. 150, 11–26. https://doi.org/10.1016/j.isprsjprs.2019.02.004

Amazirh, A., Merlin, O., Er-Raki, S., Gao, Q., Rivalland, V., Malbeteau, Y., Khabba, S., Escorihuela, M.J., 2018. Retrieving surface soil moisture at high spatio-temporal resolution from a synergy between Sentinel-1 radar and Landsat thermal data: a study case over bare soil. Remote Sens. Environ. 211, 321–337. https://doi.org/10.1016/j.rse.2018.04.013

Anderson, M.C., Allen, R.G., Morse, A., Kustas, W.P., 2012a. Use of Landsat thermal imagery in monitoring evapotranspiration and managing water resources. Remote Sens. Environ. 122, 50–65. https://doi.org/10.1016/j.rse.2011.08.025

Anderson, M.C., Hain, C., Wardlow, B., Pimstein, A., Mecikalski, J.R., Kustas, W.P., 2011. Evaluation of drought indices based on Thermal remote sensing of evapotranspiration over the continental United States. J. Clim. 24, 2025–2044. https://doi.org/10.1175/2010JCLI3812.1

Anderson, M.C., Kustas, W.P., Alfieri, J.G., Gao, F., Hain, C., Prueger, J.H., Evett, S., Colaizzi, P., Howell, T., Chávez, J.L., 2012b. Mapping daily evapotranspiration at Landsat spatial scales during the BEAREX'08 field campaign. Adv. Water Resour. 50, 162–177. https://doi.org/10.1016/j.advwatres.2012.06.005

Anderson, M.C., Norman, J.M., Diak, G.R., Kustas, W.P., Mecikalski, J.R., 1997. A two-source time-integrated model for estimating surface fluxes using thermal infrared remote sensing. Remote Sens. Environ. 60, 195–216. https://doi.org/10.1016/s0034-4257(96)00215-5

Anderson, M.C., Norman, J.M., Kustas, W.P., Houborg, R., Starks, P.J., Agam, N., 2008. A thermal-based remote sensing technique for routine mapping of land-surface carbon, water and energy fluxes from field to regional scales. Remote Sens. Environ. 112, 4227–4241. https://doi.org/10.1016/j.rse.2008.07.009

Anderson, M.C., Norman, J.M., Mecikalski, J.R., Otkin, J.A., Kustas, W.P., 2007. A climatological study of evapotranspiration and moisture stress across the continental United States based on thermal remote sensing: 1. Model formulation. J. Geophys. Res. 112. https://doi.org/10.1029/2006JD007506

Anderson, R.G., Alfieri, J.G., Tirado-Corbalá, R., Gartung, J., McKee, L.G., Prueger, J.H., Wang, D., Ayars, J.E., Kustas, W.P., 2017. Assessing FAO-56 dual crop coefficients using eddy covariance flux partitioning. Agric. Water Manag. 179, 92–102. https://doi.org/10.1016/j.agwat.2016.07.027

Baldridge, A.M., Hook, S.J., Grove, C.I., Rivera, G., 2009. The ASTER spectral library version 2.0. Remote Sens. Environ. 113, 711–715. https://doi.org/10.1016/j.rse.2008.11.007

Bannari, A., Morin, D., Bonn, F., Huete, A.R., 1995. A review of vegetation indices. Remote Sens. Rev. 13, 95–120. https://doi.org/10.1080/02757259509532298

Bastiaanssen, W.G.M., Allen, R.G., Droogers, P., D'Urso, G., Steduto, P., 2007. Twenty-five years modeling irrigated and drained soils: State of the art. Agric. Water Manag. 92, 111–125. https://doi.org/10.1016/j.agwat.2007.05.013

Battude, M., Al, A., Brut, A., Tallec, T., Huc, M., Cros, J., Weber, J., Lhuissier, L., Simonneaux, V., 2017. Modeling water needs and total irrigation depths of maize crop in the south west of France using high spatial and temporal resolution satellite imagery. Agric. Water Manag. 189, 123–136. https://doi.org/10.1016/j.agwat.2017.04.018

Battude, M., Al Bitar, A., Morin, D., Cros, J., Huc, M., Marais Sicre, C., Le Dantec, V., Demarez, V., 2016. Estimating maize biomass and yield over large areas using high spatial and temporal resolution Sentinel-2 like remote sensing data. Remote Sens. Environ. 184, 668–681. https://doi.org/10.1016/j.rse.2016.07.030

Bausch, W.C., 1993. Soil background effects on reflectance-based crop coefficients for corn. Remote Sens. Environ. 46 (2), 213–222.

Bausch, W.C., 1995. Remote sensing of crop coefficients for improving the irrigation scheduling of corn. Agric. Water Manag. 27, 55–68. https://doi.org/10.1016/0378-3774(95)01125-3

Bausch, W.C., Neale, C.M.U., 1987. Crop coefficient derived from reflected canopy radiation: a concept. Trans. ASAE 30 (3), 703–709.

Bechtel, B., 2012. Robustness of annual cycle parameters to characterize the urban thermal landscapes. IEEE Geosci. Remote Sens. Lett. 9, 876–880. https://doi.org/10.1109/LGRS.2012.2185034

Bhattarai, N., Mallick, K., Brunsell, N.A., Sun, G., Jain, M., 2018. Regional evapotranspiration from an image-based implementation of the Surface Temperature Initiated Closure (STIC1.2) model and its validation across an aridity gradient in the conterminous US. Hydrol. Earth Syst. Sci. 22, 2311–2341. https://doi.org/10.5194/hess-22-2311-2018

Bindhu, V.M., Narasimhan, B., Sudheer, K.P., 2013. Development and verification of a non-linear disaggregation method (NL-DisTrad) to downscale MODIS land surface temperature to the spatial scale of Landsat thermal data to estimate evapotranspiration. Remote Sens. Environ. 135, 118–129. https://doi.org/10.1016/j.rse.2013.03.023

Bonan, G.B., 2008. Forests and climate change: Forcings, feedbacks, and the climate benefits of forests. Science (80-.). 320, 1444–1449. https://doi.org/10.1126/science.1155121

Boulet, G., Chehbouni, A., Gentine, P., Duchemin, B., Ezzahar, J., Hadria, R., 2007. Monitoring water stress using time series of observed to unstressed surface temperature difference. Agric. For. Meteorol. 146, 159–172. https://doi.org/10.1016/j.agrformet.2007.05.012

Bowman, W.D., 1989. The relationship between leaf water status, gas exchange, and spectral reflectance in cotton leaves, Re- mote Sensing of Environment, 30:249–255

Brisson, N., C. Gary, E. Justes, R. Roche, B. Mary, D. Ripoche, D. Zimmer, J. Sierra, P. Bertuzzi, P. Burger, F. Bussière, Y.M. Cabidoche, P. Cellier, P. Debaeke, J.P. Gaudillère, C. Hénault, F. Maraux, B. Seguin, and H. Sinoquet. 2003. An Overview of the Crop Model STICS, European Journal of Agronomy, 18, p. 309.

Brisson, N. , B. Mary, D. Ripoche, M.H. Jeuffroy, F. Ruget, B. Nicoullaud, P. Gate, F. Devienne-Baret, R. Antonioletti, C. Durr, G. Richard, N. Beaudoin, S. Recous, X. Tayot, D. Plenet, P. Cellier, J.M. Machet, J.M. Meynard, and R. Delécolle. 1998. STICS: A Generic Model for the Simulation of Crops and Their Water and Nitrogen Balances. I. Theory and Parameterization Applied to Wheat and Corn, Agronomie, 18, p. 311.

Brisson, N., F. Ruget, F. Gate, J. Lorgeou, B. Nicoullard, X. Tayot, D. Plenet, M-H. Jeuffroy, A. Brouthier, D. Ripoche, B. Mary, and E. Justes. 2002. STICS: A Generic Model for the Simulation of Crops and Their Water and Nitrogen Balances. II. Model Validation for Wheat and Maize, Agronomie, 22, p. 69.

Brocca, L., Ciabatta, L., Massari, C., Camici, S., Tarpanelli, A., 2017. Soil moisture for hydrological applications: Open questions and new opportunities. Water (Switzerland) 9. https://doi.org/10.3390/w9020140

Brocca, L., Tarpanelli, A., Filippucci, P., Dorigo, W., Zaussinger, F., Gruber, A., Fernández-Prieto, D., 2018. How much water is used for irrigation? A new approach exploiting coarse resolution satellite soil moisture products. Int. J. Appl. Earth Obs. Geoinf. 73, 752–766. https://doi.org/10.1016/j.jag.2018.08.023

Calera, A., Campos, I., Osann, A., D'Urso, G., Menenti, M., 2017. Remote sensing for crop water management: From ET modelling to services for the end users. Sensors (Switzerland) 17, 1–25. https://doi.org/10.3390/s17051104

Calvet, J.-C., Noilhan, J., 2000. From Near-Surface to Root-Zone Soil Moisture Using Year-Round Data. J. Hydrometeorol. 1, 393–411. https://doi.org/10.1175/1525-7541(2000)001<0393:FNSTRZ>2.0.CO;2

Calvet, J.-C., Noilhan, J., Bessemoulin, P., 1998. Retrieving the Root-Zone Soil Moisture from Surface Soil Moisture or Temperature Estimates: A Feasibility Study Based on Field Measurements. J. Appl. Meteorol. 37, 371–386. https://doi.org/10.1175/1520-0450(1998)037<0371:RTRZSM>2.0.CO;2

Cao, B., Liu, Q., Du, Y., Roujean, J.-L., Gastellu-Etchegorry, J.-P., Trigo, I.F., Zhan, W., Yu, Y., Cheng, J., Jacob, F., Lagouarde, J.-P., Bian, Z., Li, H., Hu, T., Xiao, Q., 2019. A review of earth surface thermal radiation directionality observing and modeling: Historical development, current status and perspectives. Remote Sens. Environ. 232, 111304. https://doi.org/10.1016/j.rse.2019.111304

Carter, G.A., 1991. Primary and secondary effects of water content on the spectral reflectance of leaves. American Journal of Botany, 78(7), 916–24.

Cheema, M.J.M., Bastiaanssen, W.G.M., 2010. Land use and land cover classification in the irrigated Indus Basin using growth phenology information from satellite data to support water management analysis. Agric. Water Manag. 97, 1541–1552. https://doi.org/10.1016/j.agwat.2010.05.009

Chehbouni, A., Escadafal, R., Duchemin, B., Boulet, G., Simonneaux, V., Dedieu, G., Mougenot, B., Khabba, S., Kharrou, H., Maisongrande, P., Merlin, O., Chaponnière, A., Ezzahar, J., Er-Raki, S., Hoedjes, J., Hadria, R., Abourida, A., Cheggour, A., Raibi, F., Boudhar, A., Benhadj, I., Hanich, L., Benkaddour, A., Guemouria, N., Chehbouni, A.H., Lahrouni, A., Olioso, A., Jacob, F., Williams, D.G., Sobrino, J.A., 2008. An integrated modelling and remote sensing approach for hydrological study in arid and semi-arid regions: The SUDMED programme. Int. J. Remote Sens. 29, 5161–5181. https://doi.org/10.1080/01431160802036417

Chehbouni, Abdelghani, Hoedjes, J.C.B., Rodriquez, J.-C., Watts, C.J., Garatuza, J., Jacob, F., Kerr, Y.H., 2008. Using remotely sensed data to estimate area-averaged daily surface fluxes over a semi-arid mixed agricultural land. Agric. For. Meteorol. 148, 330–342. https://doi.org/10.1016/j.agrformet.2007.09.014

Chen, L., Yan, G., Ren, H., Li, A., 2010. A modified vegetation index based algorithm for thermal imagery sharpening. Int. Geosci. Remote Sens. Symp. 2444–2447. https://doi.org/10.1109/IGARSS.2010.5651428

Chen, M., Senay, G.B., Singh, R.K., Verdin, J.P., 2016. Uncertainty analysis of the Operational Simplified Surface Energy Balance (SSEBop) model at multiple flux tower sites. J. Hydrol. https://doi.org/10.1016/j.jhydrol.2016.02.026

Chen, Y., Lu, D., Luo, L., Pokhrel, Y., Deb, K., Huang, J., Ran, Y., 2018. Detecting irrigation extent, frequency, and timing in a heterogeneous arid agricultural region using MODIS time series, Landsat imagery, and ancillary data. Remote Sens. Environ. 204, 197–211. https://doi.org/10.1016/j.rse.2017.10.030

Choudhury, B.J., Ahmed, N.U., Idso, S.B., Reginato, R.J., Daughtry, C.S.T., 1994. Relations between evaporation coefficients and vegetation indices studied by model simulations. Remote Sens. Environ. 50, 1–17. https://doi.org/10.1016/0034-4257(94)90090-6

Corbari, C., Ceppi, A., Telesca, V., Mancini, M., 2019. Smart irrigation forecast using satellite LANDSAT data and meteo- hydrological modeling. Agric. Water Manag. 212, 283–294. https://doi.org/10.1016/j.agwat.2018.09.005

Daughtry, C.S.T., Kustas, W.P., Moran, M.S., Pinter, P.J., Jackson, R.D., Brown, P.W., Nichols, W.D., Gay, L.W., 1990. Spectral estimates of net radiation and soil heat flux. Remote Sens. Environ. 32, 111–124. https://doi.org/10.1016/0034-4257(90)90012-B

Dejonge, K.C., Taghvaeian, S., Trout, T.J., Comas, L.H., 2015. Comparison of canopy temperature-based water stress indices for maize. Agric. Water Manag. 156, 51–62. https://doi.org/10.1016/j.agwat.2015.03.023

Droogers, P., Immerzeel, W.W., Lorite, I.J., 2010. Estimating actual irrigation application by remotely sensed evapotranspiration observations. Agric. Water Manag. 97, 1351–

1359. https://doi.org/10.1016/j.agwat.2010.03.017

Duan, S., Li, Z., Wu, H., Leng, P., Gao, M., Wang, C., 2018. Radiance-based validation of land surface temperature products derived from Collection 6 MODIS thermal infrared data. Int J Appl Earth Obs Geoinf. 70, 84–92. https://doi.org/10.1016/j.jag.2018.04.006

Duchemin, B., Goubier, J., Courrier, G., 1999. Monitoring phenological key stages and cycle duration of temperate deciduous forest ecosystems with NOAA/AVHRR data. Remote Sens. Environ. 67, 68–82. https://doi.org/10.1016/S0034-4257(98)00067-4

Duchemin, B., Hadria, R., Erraki, S., Boulet, G., Maisongrande, P., Chehbouni, A., Escadafal, R., Ezzahar, J., Hoedjes, J.C.B., Kharrou, M.H., Khabba, S., Mougenot, B., Olioso, A., Rodriguez, J.-C., Simonneaux, V., 2006. Monitoring wheat phenology and irrigation in Central Morocco: On the use of relationships between evapotranspiration, crops coefficients, leaf area index and remotely-sensed vegetation indices. Agric. Water Manag. 79, 1–27. https://doi.org/10.1016/j.agwat.2005.02.013

Duchemin, B., Maisongrande, P., Boulet, G., Benhadj, I., 2008. A simple algorithm for yield estimates: Evaluation for semi-arid irrigated winter wheat monitored with green leaf area index. Environ. Model. Softw. 23, 876–892. https://doi.org/10.1016/j.envsoft.2007.10.003

Dumedah, G., Walker, J.P., Merlin, O., 2015. Root-zone soil moisture estimation from assimilation of downscaled Soil Moisture and Ocean Salinity data. Adv. Water Resour. 84, 14–22. https://doi.org/10.1016/j.advwatres.2015.07.021

Entekhabi, D., Nakamura, H., Njoku, E.G., 1994. Solving the inverse problem for soil moisture and temperature profiles by sequential assimilation of multifrequency remotely sensed observations. IEEE Trans. Geosci. Remote Sens. 32, 438–448. https://doi.org/10.1109/36.295058

Entekhabi, D., Njoku, E.G., O'Neill, P.E., Kellogg, K.H., Crow, W.T., Edelstein, W.N., Entin, J.K., Goodman, S.D., Jackson, T.J., Johnson, J., Kimball, J., Piepmeier, J.R., Koster, R.D., Martin, N., McDonald, K.C., Moghaddam, M., Moran, S., Reichle, R., Shi, J.C., Spencer, M.W., Thurman, S.W., Tsang, L., Van Zyl, J., 2010. The soil moisture active passive (SMAP) mission. Proc. IEEE 98, 704–716. https://doi.org/10.1109/JPROC.2010.2043918

Er-Raki, S., Chehbouni, A., Duchemin, B., 2010. Combining satellite remote sensing data with the FAO-56 dual approach for water use mapping in irrigated wheat fields of a semi-arid region. Remote Sens. 2, 375–387. https://doi.org/10.3390/rs2010375

Er-Raki, S., Chehbouni, A., Guemouria, N., Duchemin, B., Ezzahar, J., Hadria, R., 2007. Combining FAO-56 model and ground-based remote sensing to estimate water consumptions of wheat crops in a semi-arid region. Agric. Water Manag. 87, 41–54. https://doi.org/10.1016/j.agwat.2006.02.004

Er-Raki, S., Chehbouni, A., Hoedjes, J., Ezzahar, J., Duchemin, B., Jacob, F., 2008. Improvement of FAO-56 method for olive orchards through sequential assimilation of thermal infrared-based estimates of ET. Agric. Water Manag. 95, 309–321. https://doi.org/10.1016/j.agwat.2007.10.013

Escorihuela, M.J., Quintana-Seguí, P., 2016. Comparison of remote sensing and simulated soil moisture datasets in Mediterranean landscapes. Remote Sens. Environ. 180, 99–114. https://doi.org/10.1016/j.rse.2016.02.046

Eweys, O.A., Escorihuela, M.J., Villar, J.M., Er-Raki, S., Amazirh, A., Olivera, L., Jarlan, L., Khabba, S., Merlin, O., 2017. Disaggregation of SMOS Soil Moisture to 100 m Resolution Using MODIS Optical/Thermal and Sentinel-1 Radar Data: Evaluation over a Bare Soil Site in Morocco. Remote Sens. 9, 1155. https://doi.org/10.3390/rs9111155

Felfelani, F., Pokhrel, Y., Guan, K., Lawrence, D.M., 2018. Utilizing SMAP Soil Moisture Data to Constrain Irrigation in the Community Land Model. Geophys. Res. Lett. 45, 12,892-12,902. https://doi.org/10.1029/2018GL080870

Findell, K.L., Gentine, P., Lintner, B.R., Kerr, C., 2011. Probability of afternoon precipitation in eastern United States and Mexico enhanced by high evaporation. Nat. Geosci. 4, 434–439. https://doi.org/10.1038/ngeo1174

Foley, J.A., Ramankutty, N., Brauman, K.A., Cassidy, E.S., Gerber, J.S., Johnston, M., Mueller, N.D., O'Connell, C., Ray, D.K., West, P.C., Balzer, C., Bennett, E.M., Carpenter, S.R., Hill, J., Monfreda, C., Polasky, S., Rockström, J., Sheehan, J., Siebert, S., Tilman, D., Zaks, D.P.M., 2011. Solutions for a cultivated planet. Nature 478, 337–342. https://doi.org/10.1038/nature10452

Ford, T.W., Harris, E., Quiring, S.M., 2014. Estimating root zone soil moisture using near-surface observations from SMOS. Hydrol. Earth Syst. Sci. 18, 139–154. https://doi.org/10.5194/hess-18-139-2014

Gao, Q., Zribi, M., Escorihuela, M., Baghdadi, N., 2017. Synergetic Use of Sentinel-1 and Sentinel-2 Data for Soil Moisture Mapping at 100 m Resolution. Sensors 17, 1966. https://doi.org/10.3390/s17091966

Gao, Z.Q., Liu, C.S., Gao, W., Chang, N.-B., 2011. A coupled remote sensing and the Surface Energy Balance with Topography Algorithm (SEBTA) to estimate actual evapotranspiration over heterogeneous terrain. Hydrol. Earth Syst. Sci. 15, 119–139. https://doi.org/10.5194/hess-15-119-2011

Garreaud, R.D., Alvarez-Garreton, C., Barichivich, J., Pablo Boisier, J., Christie, D., Galleguillos, M., LeQuesne, C., McPhee, J., Zambrano-Bigiarini, M., 2017. The 2010-2015 megadrought in central Chile: Impacts on regional hydroclimate and vegetation. Hydrol. Earth Syst. Sci. 21, 6307–6327. https://doi.org/10.5194/hess-21-6307-2017

Garreaud, R.D., Boisier, J.P., Rondanelli, R., Montecinos, A., Sepúlveda, H.H., Veloso-Aguila, D., 2019. The Central Chile Mega Drought (2010–2018): A climate dynamics perspective. Int. J. Climatol. 1–19. https://doi.org/10.1002/joc.6219

Garrido, A., Llamas, M.R., Varela-Ortega, C., Novo, P., Rodríguez-Casado, R., Aldaya, M.M., 2010. Water Footprint and Virtual Water Trade in Spain. Policy Implications. Series: Natural Resource Management and Policy, 35. IX, 150. https:///doi.org/10.1007/978-1-4419-5741-2

Gausman, H.W., 1977. Reflectance of leaf components. Remote Sensing of Environment, 6(1), 1–9.

Giorgi, F., 2006. Climate change hot-spots. Geophys. Res. Lett. 33, 1–4. https://doi.org/10.1029/2006GL025734

González-Dugo, M.P., Mateos, L., 2008. Spectral vegetation indices for benchmarking water productivity of irrigated cotton and sugarbeet crops. Agric. Water Manag. 95, 48–58. https://doi.org/10.1016/j.agwat.2007.09.001

Gowda, P.H., Chavez, J.L., Colaizzi, P.D., Evett, S.R., Howell, T.A., Tolk, J.A., 2008. ET mapping for agricultural water management: present status and challenges. Irrig. Sci. 26, 223–237. https://doi.org/10.1007/s00271-007-0088-6

Guillevic, P.C., Biard, J.C., Hulley, G.C., Privette, J.L., Hook, S.J., Olioso, A., Göttsche, F.M., Radocinski, R., Román, M.O., Yu, Y., Csiszar, I., 2014. Validation of Land Surface Temperature products derived from the Visible Infrared Imaging Radiometer Suite (VIIRS) using ground-based and heritage satellite measurements. Remote Sens. Environ. 154, 19–37. https://doi.org/10.1016/j.rse.2014.08.013

Gutman, G., Ignatov, A., 1998. The derivation of the green vegetation fraction from NOAA / AVHRR. Int. J. Remote Sens. 19, 1533–1543.

Guzinski, R., Nieto, H., 2019. Evaluating the feasibility of using Sentinel-2 and Sentinel-3 satellites for high-resolution evapotranspiration estimations. Remote Sens. Environ. 221, 157–172. https://doi.org/10.1016/j.rse.2018.11.019

Hadria, R., Duchemin, B., Jarlan, L., Dedieu, G., Baup, F., Khabba, S., Olioso, A., Le Toan, T., 2010. Potentiality of optical and radar satellite data at high spatio-temporal resolutions for the monitoring of irrigated wheat crops in Morocco. Int. J. Appl. Earth Obs. Geoinf. 12, 32–37. https://doi.org/10.1016/j.jag.2009.09.003

Hadria, R., Duchemin, B., Lahrouni, A., Khabba, S., Er-Raki, S., Dedieu, G., Chehbouni, A.G., Olioso, A., 2006. Monitoring of irrigated wheat in a semi-arid climate using crop modelling and remote sensing data: Impact of satellite revisit time frequency. Int. J. Remote Sens. 27, 1093–1117. https://doi.org/10.1080/01431160500382980

Hadria, R., Khabba, S., Lahrouni, A., Duchemin, B., Chehbouni, A., Carriou, J., Ouzine, L., 2007. Calibration and Validation of the STICS Crop Model for Managing Wheat Irrigation in the Semi-Arid Marrakech/Al Haouz Plain. Arab. J. Sci. Eng. 32, 87–101.

Hain, C.R., Mecikalski, J.R., Anderson, M.C., 2009. Retrieval of an Available Water-Based Soil Moisture Proxy from Thermal Infrared Remote Sensing. Part I: Methodology and Validation. J. Hydrometeorol. 10, 665–683.

https://doi.org/10.1175/2008JHM1024.1

Hajj, M. El, Baghdadi, N., Zribi, M., Bazzi, H., 2017. Synergic use of Sentinel-1 and Sentinel-2 images for operational soil moisture mapping at high spatial resolution over agricultural areas. Remote Sens. 9, 1–28. https://doi.org/10.3390/rs9121292

Hansen, J., Ruedy, R., Sato, M., Lo, K., 2010. Global surface temperature change. Rev. Geophys. 48. https://doi.org/10.1111/j.0033-0124.1951.35_28.x

Hulley, G., Hook, S., Fisher, J., Lee, C., 2017. ECOSTRESS, A NASA Earth-Ventures Instrument for studying links between the water cycle and plant health over the diurnal cycle. Int. Geosci. Remote Sens. Symp. 2017-July, 5494–5496. https://doi.org/10.1109/IGARSS.2017.8128248

Hulley, G., Hook, S., Malakar, E., Islam, T., Abrams, M., 2015. The ASTER Global Emissivity Database (ASTER GED): Mapping Earth's emissivity at 100 meter spatial resolution. Geophys. Res. Lett. 42, 7966–7976. https://doi.org/10.1002/2015GL065564.Received

Hunsaker, D.J., Pinter, P.J., Kimball, B.A., 2005. Wheat basal crop coefficients determined by normalized difference vegetation index. Irrig. Sci. 24, 1–14. https://doi.org/10.1007/s00271-005-0001-0

Ihuoma, S.O., Madramootoo, C.A., 2017. Recent advances in crop water stress detection. Comput. Electron. Agric. 141, 267–275. https://doi.org/10.1016/j.compag.2017.07.026

IPCC, 2013. Climate Change 2013: The Physical Science Basis. Contribution of Working Group I to the Fifth Assessment Report of the Intergovernmental Panel on Climate Change. Ed. Stocker, T.F., et al.. Cambridge University Press, Cambridge, United Kingdom and New York, NY, USA, 1535.0

Jackson, R.D., 1982. Canopy temperature and crop water stress. Advances in Irrigation, Volume 1 (D.I. Hillel, editor). Acade- mic Press, New York, N.Y., pp. 43–85.

Jackson, R.D., Idso, S.B., Reginato, R.J., Pinter, P.J., 1981. Canopy Temperature as a Crop Water Stress Indicator. Water Resour. Res. 17, 1133–1138.

Jalilvand, E., Tajrishy, M., Ghazi Zadeh Hashemi, S.A., Brocca, L., 2019. Quantification of irrigation water using remote sensing of soil moisture in a semi-arid region. Remote Sens. Environ. 231, 111226. https://doi.org/10.1016/j.rse.2019.111226

Jarlan, L., Khabba, S., Er-Raki, S., Le Page, M., Hanich, L., Fakir, Y., Merlin, O., Mangiarotti, S., Gascoin, S., Ezzahar, J., Kharrou, M.H., Berjamy, B., Saaïdi, A., Boudhar, A., Benkaddour, A., Laftouhi, N., Abaoui, J., Tavernier, A., Boulet, G., Simonneaux, V., Driouech, F., El Adnani, M., El Fazziki, A., Amenzou, N., Raibi, F., El Mandour, A., Ibouh, H., Le Dantec, V., Habets, F., Tramblay, Y., Mougenot, B., Leblanc, M., El Faïz, M., Drapeau, L., Coudert, B., Hagolle, O., Filali, N., Belaqziz, S., Marchane, A., Szczypta, C., Toumi, J., Diarra, A., Aouade, G., Hajhouji, Y., Nassah, H., Bigeard, G., Chirouze, J., Boukhari, K., Abourida, A., Richard, B., Fanise, P., Kasbani, M., Chakir, A., Zribi, M., Marah, H., Naimi, A., Mokssit, A., Kerr, Y., Escadafal, R., 2015. Remote Sensing of

Water Resources in Semi-Arid Mediterranean Areas: the joint international laboratory TREMA. Int. J. Remote Sens. 36, 4879–4917. https://doi.org/10.1080/01431161.2015.1093198

Jiang, L., Islam, S., 2003. An intercomparison of regional latent heat flux estimation using remote sensing data. Int. J. Remote Sens. 24, 2221–2236. https://doi.org/10.1080/01431160210154821

Jiménez-Muñoz, J.C., Mattar, C., Barichivich, J., Santamaría-Artigas, A., Takahashi, K., Malhi, Y., Sobrino, J.A., Schrier, G. van der, 2016. Record-breaking warming and extreme drought in the Amazon rainforest during the course of El Niño 2015–2016. Sci. Rep. 6, 33130. https://doi.org/10.1038/srep33130

Jiménez-Muñoz, J.C., Sobrino, J. a., Gillespie, A., Sabol, D., Gustafson, W.T., 2006. Improved land surface emissivities over agricultural areas using ASTER NDVI. Remote Sens. Environ. 103, 474–487. https://doi.org/10.1016/j.rse.2006.04.012

Jiménez-muñoz, J.C., Sobrino, J.A., Skokovi, D., Mattar, C., Cristóbal, J., Bands, A.L.-T., 2014. Land Surface Temperature Retrieval Methods From Landsat-8 Thermal Infrared Sensor Data. IEEE Geosci. Remote Sens. Lett. 11, 1840–1843.

Jimenez-Munoz, J.C., Sobrino, J.A., Sòria, G., Cristobal, J., Pons, X., Ninyerola, M., 2009. Revision of the single-channel algorithm for land surface temperature retrieval from landsat thermal-infrared data. IEEE Trans. Geosci. Remote Sens. 47, 339–349. https://doi.org/10.1109/TGRS.2008.2007125

Kalma, J.D., McVicar, T.R., McCabe, M.F., 2008. Estimating land surface evaporation: A review of methods using remotely sensed surface temperature data. Surv. Geophys. 29, 421–469. https://doi.org/10.1007/s10712-008-9037-z

Kerr, Y.H., Waldteufel, P., Wigneron, J.-P., Delwart, S., Cabot, F., Boutin, J., Escorihuela, M.-J., Font, J., Reul, N., Gruhier, C., Juglea, S.E., Drinkwater, M.R., Hahne, A., Martín-Neira, M., Mecklenburg, S., 2010. The SMOS Mission: New Tool for Monitoring Key Elements of the Global Water Cycle. Proc. IEEE 98, 666–687. https://doi.org/10.1109/JPROC.2010.2043032

Kornelsen, K.C., Coulibaly, P., 2014. Root-zone soil moisture estimation using data-driven methods. Water Resour. Res. 50, 7513–7522. https://doi.org/10.1002/2016WR018954.Received

Kullberg, E.G., DeJonge, K.C., Chávez, J.L., 2016. Evaluation of thermal remote sensing indices to estimate crop evapotranspiration coefficients. Agric. Water Manag. 179, 64–73. https://doi.org/10.1016/j.agwat.2016.07.007

Kumar, S. V., Peters-Lidard, C.D., Santanello, J.A., Reichle, R.H., Draper, C.S., Koster, R.D., Nearing, G., Jasinski, M.F., 2015. Evaluating the utility of satellite soil moisture retrievals over irrigated areas and the ability of land data assimilation methods to correct for unmodeled processes. Hydrol. Earth Syst. Sci. 19, 4463–4478. https://doi.org/10.5194/hess-19-4463-2015

Kustas, W.P., Daughtry, C.S.T., 1990. Estimation of the soil heat flux/net radiation ratio from spectral data. Agric. For. Meteorol. 49, 205–223. https://doi.org/10.1016/0168-1923(90)90033-3

Kustas, W.P., Norman, J.M., Anderson, M.C., French, A.N., 2003. Estimating subpixel surface temperatures and energy fluxes from the vegetation index–radiometric temperature relationship. Remote Sens. Environ. 85, 429–440. https://doi.org/10.1016/S0034-4257(03)00036-1

Lagouarde, J., Bhattacharya, B.K., 2018. TRISHNA : a new high spatio-temporal resolution Indian-French mission in the thermal infrared, in: Remote Sensing and Hydrology Symposium (ICRS-IAHS).

Lawston, P.M., Santanello, J.A., Franz, T.E., Rodell, M., 2017a. Assessment of irrigation physics in a land surface modeling framework using non-traditional and human-practice datasets. Hydrol. Earth Syst. Sci. 21, 2953–2966. https://doi.org/10.5194/hess-21-2953-2017

Lawston, P.M., Santanello, J.A., Kumar, S. V., 2017b. Irrigation Signals Detected From SMAP Soil Moisture Retrievals. Geophys. Res. Lett. 44, 11,860-11,867. https://doi.org/10.1002/2017GL075733

Le Page, M., Toumi, J., Khabba, S., Hagolle, O., Tavernier, A., Hakim Kharrou, M., Er-Raki, S., Huc, M., Kasbani, M., Moutamanni, A. El, Yousfi, M., Jarlan, L., 2014. A life-size and near real-time test of irrigation scheduling with a sentinel-2 like time series (SPOT4-Take5) in Morocco. Remote Sens. 6, 11182–11203. https://doi.org/10.3390/rs61111182

Li, M., Qu, J.J., Hao, X., 2010. Investigating phenological changes using MODIS vegetation indices in deciduous broadleaf forest over continental U.S. during 2000-2008. Ecol. Inform. 5, 410–417. https://doi.org/10.1016/j.ecoinf.2010.04.002

Li, Z.-L., Tang, B.-H., Wu, H., Ren, H., Yan, G., Wan, Z., Trigo, I.F., Sobrino, J. a, 2013. Satellite-derived land surface temperature: Current status and perspectives. Remote Sens. Environ. 131, 14–37. https://doi.org/10.1016/j.rse.2012.12.008

Li, Z.-L., Tang, R., Wan, Z., Bi, Y., Zhou, C., Tang, B., Yan, G., Zhang, X., 2009. A review of current methodologies for regional evapotranspiration estimation from remotely sensed data. Sensors (Basel). 9, 3801–53. https://doi.org/10.3390/s90503801

Li, Z.L., Wu, H., Wang, N., Qiu, S., Sobrino, J.A., Wan, Z., Tang, B.H., Yan, G., 2013. Land surface emissivity retrieval from satellite data. Int. J. Remote Sens. 34, 3084–3127. https://doi.org/10.1080/01431161.2012.716540

Liang, S., 2001. Narrowband to broadband conversions of land surface albedo I Algorithms. Remote Sens. Environ. 76, 213– 238.

Liu, Y., Hill, M.J., Zhang, X., Wang, Z., Richardson, A.D., Hufkens, K., Filippa, G., Baldocchi, D.D., Ma, S., Verfaillie, J., Schaaf, C.B., 2017. Using data from Landsat, MODIS, VIIRS and PhenoCams to monitor the phenology of California oak/grass savanna and open grassland across spatial scales. Agric. For. Meteorol. 237–238, 311–325.

https://doi.org/10.1016/j.agrformet.2017.02.026

Long, D., Singh, V.P., 2012. A Two-source Trapezoid Model for Evapotranspiration (TTME) from satellite imagery. Remote Sens. Environ. 121, 370–388. https://doi.org/10.1016/j.rse.2012.02.015

Malakar, N.K., Hulley, G.C., Hook, S.J., Laraby, K., Cook, M., Schott, J.R., 2018. An Operational Land Surface Temperature Product for Landsat Thermal Data: Methodology and Validation. IEEE Trans. Geosci. Remote Sens. 5717–5735. https://doi.org/10.1109/TGRS.2018.2824828

Malbéteau, Y., 2016. Suivi des ressources en eau par une approche combinant la télédétection multi-capteur et la modélisation phénomménologique.

Malbéteau, Y., Merlin, O., Balsamo, G., Er-Raki, S., Khabba, S., Walker, J.P., Jarlan, L., 2018. Toward a Surface Soil Moisture Product at High Spatiotemporal Resolution: Temporally Interpolated, Spatially Disaggregated SMOS Data. J. Hydrometeorol. 19, 183–200. https://doi.org/10.1175/jhm-d-16-0280.1

Malbéteau, Y., Merlin, O., Gascoin, S., Gastellu, J.P., Mattar, C., Olivera-Guerra, L., Khabba, S., Jarlan, L., 2017. Normalizing land surface temperature data for elevation and illumination effects in mountainous areas: A case study using ASTER data over a steep-sided valley in Morocco. Remote Sens. Environ. 189, 25–39. https://doi.org/10.1016/j.rse.2016.11.010

Mattar, C., Durán-Alarcón, C., Jiménez-Muñoz, J.C., Santamaría-Artigas, A., Olivera-Guerra, L., Sobrino, J.A., 2015. Global Atmospheric Profiles from Reanalysis Information (GAPRI): a new database for earth surface temperature retrieval. Int. J. Remote Sens. 36, 5045–5060. https://doi.org/10.1080/01431161.2015.1054965

Mattar, C., Santamaría-artigas, A., Durán-alarcón, C., Olivera-guerra, L., Fuster, R., Borvarán, D., 2016. The LAB-Net Soil Moisture Network : Application to Thermal Remote Sensing and Surface Energy Balance. Data 1, 1–14. https://doi.org/10.3390/data1010006

McVicar, T.R., Jupp, D.L.B., 1998. The current and potential operational uses of remote sensing to aid decisions on drought exceptional circumstances in Australia: A review. Agric. Syst. 57, 399–468. https://doi.org/10.1016/S0308-521X(98)00026-2

Merlin, O., 2013. An original interpretation of the wet edge of the surface temperature-albedo space to estimate crop evapotranspiration (SEB-1S), and its validation over an irrigated area in northwestern Mexico. Hydrol. Earth Syst. Sci. 17, 3623–3637. https://doi.org/10.5194/hess-17-3623-2013

Merlin, O., Al Bitar, A., Rivalland, V., Béziat, P., Ceschia, E., Dedieu, G., 2011. An analytical model of evaporation efficiency for unsaturated soil surfaces with an arbitrary thickness. J. Appl. Meteorol. Climatol. 50, 457–471.

Merlin, O., Chehbouni, A., 2004. Different approaches in estimating heat flux using dual

angle observations of radiative surface temperature. Int. J. Remote Sens. 25, 275–289. https://doi.org/10.1080/0143116031000116408

Merlin, O., Chehbouni, A., Boulet, G., Kerr, Y., 2006. Assimilation of Disaggregated Microwave Soil Moisture into a Hydrologic Model Using Coarse-Scale Meteorological Data. J. Hydrometeorol. 7, 1308–1322. https://doi.org/10.1175/JHM552.1

Merlin, O., Chirouze, J., Olioso, A., Jarlan, L., Chehbouni, G., Boulet, G., 2014. An image-based four-source surface energy balance model to estimate crop evapotranspiration from solar reflectance/thermal emission data (SEB-4S). Agric. For. Meteorol. 184, 188–203. https://doi.org/10.1016/j.agrformet.2013.10.002

Merlin, O., Duchemin, B., Hagolle, O., Jacob, F., Coudert, B., Chehbouni, G., Dedieu, G., Garatuza, J., Kerr, Y., 2010. Disaggregation of MODIS surface temperature over an agricultural area using a time series of Formosat-2 images. Remote Sens. Environ. 114, 2500–2512. https://doi.org/10.1016/j.rse.2010.05.025

Merlin, O., Escorihuela, M.J., Mayoral, M.A., Hagolle, O., Al Bitar, A., Kerr, Y., 2013. Self-calibrated evaporation-based disaggregation of SMOS soil moisture: An evaluation study at 3km and 100m resolution in Catalunya, Spain. Remote Sens. Environ. 130, 25–38. https://doi.org/10.1016/j.rse.2012.11.008

Merlin, O., Jacob, F., Wigneron, J.P., Walker, J., Chehbouni, G., 2012a. Multidimensional disaggregation of land surface temperature using high-resolution red, near-infrared, shortwave-infrared, and microwave-L bands. IEEE Trans. Geosci. Remote Sens. 50, 1864–1880. https://doi.org/10.1109/TGRS.2011.2169802

Merlin, O., Olivera-guerra, L., Aït, B., Amazirh, A., Ra, Z., Ezzahar, J., Gentine, P., Khabba, S., Gascoin, S., Er-raki, S., 2018. A phenomenological model of soil evaporative efficiency using surface soil moisture and temperature data. Agric. For. Meteorol. 256–257, 501–515. https://doi.org/10.1016/j.agrformet.2018.04.010

Merlin, O., Rüdiger, C., Bitar, A. Al, Richaume, P., Walker, J.P., Kerr, Y.H., 2012b. Disaggregation of SMOS Soil Moisture in Southeastern Australia. IEEE Trans. Geosci. Remote Sens. 50, 1556–1571.

Merlin, O., Stefan, V.G., Amazirh, A., Chanzy, A., Ceschia, E., Tallec, T., Beringer, J., Gentine, P., Er-Raki, S., Bircher, S., Khabba, S., 2016. Modeling soil evaporation efficiency in a range of soil and atmospheric conditions: A downward approach based on multi-site data. Water Resour. Res. 52, 3663–3684. https://doi.org/10.1002/2015WR018233.

Molero, B., Merlin, O., Malbéteau, Y., Al Bitar, A., Cabot, F., Stefan, V., Kerr, Y., Bacon, S., Cosh, M.H., Bindlish, R., Jackson, T.J., 2016. SMOS disaggregated soil moisture product at 1 km resolution: Processor overview and first validation results. Remote Sens. Environ. 180, 361–376. https://doi.org/10.1016/j.rse.2016.02.045

Montanaro, M., Lunsford, A., Tesfaye, Z., Wenny, B., Reuter, D., 2014. Radiometric calibration methodology of the landsat 8 thermal infrared sensor. Remote Sens. 6, 8803–8821. https://doi.org/10.3390/rs6098803

Moran, M.S., Clarke, T.R., Inoue, Y., Vidal, A., 1994. Estimating crop water deficit using the

relation between surface-air temperature and spectral vegetation index. Remote Sens. Environ. 49, 246–263. https://doi.org/10.1016/0034-4257(94)90020-5

Moran, M.S., Scott, R.L., Keefer, T.O., Emmerich, W.E., Hernandez, M., Nearing, G.S., Paige, G.B., Cosh, M.H., O'Neill, P.E., 2009. Partitioning evapotranspiration in semiarid grassland and shrubland ecosystems using time series of soil surface temperature. Agric. For. Meteorol. 149, 59–72. https://doi.org/10.1016/j.agrformet.2008.07.004

Mukherjee, S., Joshi, P.K., Garg, R.D., 2014. A comparison of different regression models for downscaling Landsat and MODIS land surface temperature images over heterogeneous landscape. Adv. Sp. Res. 54, 655–669. https://doi.org/10.1016/j.asr.2014.04.013

Neale, C.M.U., Bausch, W.C., Heerman, D.F., 1989. Development of reflectance-based crop coefficients for corn. Trans. ASAE 32 (6), 1891–1899.

Njoku, E.G., Jackson, T.J., Lakshmi, V., Chan, T.K., Nghiem, S. V., 2003. Soil moisture retrieval from AMSR-E. IEEE Trans. Geosci. Remote Sens. 41, 215–228. https://doi.org/10.1109/TGRS.2002.808243

Noilhan, J., Planton, S., 1989. A Simple Parameterization of Land Surface Processes for Meteorological Models. Mon. Weather Rev. https://doi.org/10.1175/1520-0493(1989)117<0536:ASPOLS>2.0.CO;2

Norman, J.M., Kustas, W.P., Humes, K.S., 1995. A two-source approach for estimating soil and vegetation energy fluxes in observations of directional radiometric surface temperature. Agric. For. Meteorol. 77, 263–293. https://doi.org/10.1016/0168-1923(95)02265-Y

Ogawa, K., Schmugge, T., 2004. Mapping Surface Broadband Emissivity of the Sahara Desert Using ASTER and MODIS Data. Earth Interact. 8, 1–14. https://doi.org/10.1175/1087-3562(2004)008<0001:MSBEOT>2.0.CO;2

Ojha, N., Merlin, O., Molero, B., Suere, C., Olivera-guerra, L., Hssaine, B.A., Amazirh, A., Bitar, A. Al, Escorihuela, M.J., Er-raki, S., 2019. Stepwise Disaggregation of SMAP Soil Moisture at 100 m Resolution Using Landsat-7 / 8 Data and a Varying Intermediate Resolution. Remote Sens. 11, 1–23. https://doi.org/10.3390/rs11161863

Oki, T., Kanae, S., 2006. Global Hydrological Cycles and World Water Resources. Science (80-.). 313, 1068–1072. https://doi.org/10.1126/science.1128845

Olioso, A., Soria, G., Sobrino, J., Duchemin, B., 2007. Evidence of Low Land Surface Thermal Infrared Emissivity in the Presence of Dry Vegetation. IEEE Geosci. Remote Sens. Lett. 4, 112–116. https://doi.org/10.1109/LGRS.2006.885857

Oyarzún, J., Oyarún, R., 2011. Sustainable development threats, inter-sector conflicts and environmental policy requirements in the arid, mining rich, Northern Chile territory. Sustain. Dev. 19, 263–274. https://doi.org/10.1002/sd.441

Peng, J., Loew, A., Merlin, O., Verhoest, N.E.C., 2017. A review of spatial downscaling of satellite remotely sensed soil moisture. Rev. Geophys. 55, 341–366. https://doi.org/10.1002/2016RG000543

Pereira, L.S., Allen, R.G., Smith, M., Raes, D., 2015. Crop evapotranspiration estimation with FAO56: Past and future. Agric. Water Manag. 147, 4–20. https://doi.org/10.1016/j.agwat.2014.07.031

Perez-Priego, O., Katul, G., Reichstein, M., El-Madany, T.S., Ahrens, B., Carrara, A., Scanlon, T.M., Migliavacca, M., 2018. Partitioning eddy covariance water flux components using physiological and micrometeorological approaches. J. Geophys. Res. Biogeosciences. https://doi.org/10.1029/2018JG004637

Pinter, P.J., Hatfield, J.L., Schepers, J.S., Barnes, E.M., Moran, M.S., Daughtry, C.S.T., Upchurch, D.R.. 2003. Remote Sensing for Crop Management. Photogramm. Eng. Remote Sensing 69, 647–664.

Pinter, P.J., B.A. Kimball, J.R. Mauney, G.R. Hendrey, K.F. Lewin, and J. Nagy. 1994. Effects of free-air carbon dioxide enrichment on PAR absorption and conversion efficiency by cotton. Agricultural and Forest Meteorology, 70, 209–230.

PMV (Plan Maroc Vert), 2013. Plan Maroc Vert: Région de Marrakech Tensift Al Haouz. Rabat. http://www.agriculture.gov.ma/sites/default/files/sam_fr_10.pdf

Poblete-Echeverría, C.A., Ortega-Farias, S.O., 2013. Evaluation of single and dual crop coefficients over a drip-irrigated Merlot vineyard (Vitis viniferaL.) using combined measurements of sap flow sensors and an eddy covariance system. Aust. J. Grape Wine Res. 19, 249–260. https://doi.org/10.1111/ajgw.12019

Pokhrel, Y., Hanasaki, N., Koirala, S., Cho, J., Yeh, P.J.F., Kim, H., Kanae, S., Oki, T., 2012. Incorporating anthropogenic water regulation modules into a land surface model. J. Hydrometeorol. 13, 255–269. https://doi.org/10.1175/JHM-D-11-013.1

Pokhrel, Y.N., Hanasaki, N., Wada, Y., Kim, H., 2016. Recent progresses in incorporating human land-water management into global land surface models toward their integration into Earth system models. Wiley Interdiscip. Rev. Water 3, 548–574. https://doi.org/10.1002/wat2.1150

Qu, Y., Liang, S., Liu, Q., He, T., Liu, S., Li, X., 2015. Mapping surface broadband albedo from satellite observations: A review of literatures on algorithms and products. Remote Sens. 7, 990–1020. https://doi.org/10.3390/rs70100990

Rafi, Z., Merlin, O., Le Dantec, V., Khabba, S., Mordelet, P., Er-raki, S., Amazirh, A., Olivera-guerra, L., Ait Hssaine, B., 2019. Partitioning evapotranspiration of a drip-irrigated wheat crop : Inter- comparing eddy covariance-, sap flow-, lysimeter- and FAO-based methods. Agric. For. Meteorol. 265, 310–326. https://doi.org/10.1016/j.agrformet.2018.11.031

Rana, G., Palatella, L., Scanlon, T.M., Martinelli, N., Ferrara, R.M., 2018. CO2and H2O flux partitioning in a Mediterranean cropping system. Agric. For. Meteorol. 260–261, 118–130. https://doi.org/10.1016/j.agrformet.2018.06.007

Rango, A., 1995. Application of remote sensing methods to hydrology and water resources. Hydrol. Sci. J. 39, 309–320.

Roerink, G.J., Su, Z., Menenti, M., 2000. S-SEBI: A simple remote sensing algorithm to estimate the surface energy balance. Phys. Chem. Earth, Part B Hydrol. Ocean. Atmos. 25, 147–157. https://doi.org/10.1016/S1464-1909(99)00128-8

Sabater, J.M., Jarlan, L., Calvet, J.-C., Bouyssel, F., De Rosnay, P., 2007. From Near-Surface to Root-Zone Soil Moisture Using Different Assimilation Techniques. J. Hydrometeorol. 8, 194–206. https://doi.org/10.1175/JHM571.1

Sandholt, I., Rasmussen, K., Andersen, J., 2002. A simple interpretation of the surface temperature/vegetation index space for assessment of surface moisture status. Remote Sens. Environ. 79, 213–224. https://doi.org/10.1016/S0034-4257(01)00274-7

Scanlon, B.R., Faunt, C.C., Longuevergne, L., Reedy, R.C., Alley, W.M., McGuire, V.L., McMahon, P.B., 2012. Groundwater depletion and sustainability of irrigation in the US High Plains and Central Valley. Proc. Natl. Acad. Sci. U. S. A. 109, 9320–9325. https://doi.org/10.1073/pnas.1200311109

Scanlon, T.M., Kustas, W.P., 2012. Partitioning Evapotranspiration Using an Eddy Covariance-Based Technique: Improved Assessment of Soil Moisture and Land–Atmosphere Exchange Dynamics. Vadose Zo. J. 11, 0. https://doi.org/10.2136/vzj2012.0025

Scanlon, T.M., Kustas, W.P., 2010. Partitioning carbon dioxide and water vapor fluxes using correlation analysis. Agric. For. Meteorol. 150, 89–99. https://doi.org/10.1016/j.agrformet.2009.09.005

Scanlon, T.M., Sahu, P., 2008. On the correlation structure of water vapor and carbon dioxide in the atmospheric surface layer: A basis for flux partitioning. Water Resour. Res. 44, 1–15. https://doi.org/10.1029/2008WR006932

Schmugge, T., Kustas, W.P., Ritchie, J.C., Jackson, T.J., Rango, A., 2002. Remote sensing in hydrology. Adv. Water Resour. 25, 1367–1385. https://doi.org/10.1029/EO064i052p01012

Scott, N.A., Chedin, A., 1981. A Fast Line-by-Line Method for Atmospheric Absorption Computations: The Automatized Atmospheric Absorption Atlas. J. Appl. Meteorol. https://doi.org/10.1175/1520-0450(1981)020<0802:aflblm>2.0.co;2

Senay, G.B., Bohms, S., Singh, R.K., Gowda, P.H., Velpuri, N.M., Alemu, H., Verdin, J.P., 2013a. Operational Evapotranspiration Mapping Using Remote Sensing and Weather Datasets: A New Parameterization for the SSEB Approach. JAWRA J. Am. Water Resour. Assoc. 49, 577–591. https://doi.org/10.1111/jawr.12057

Senay, G.B., Bohms, S., Singh, R.K., Gowda, P.H., Velpuri, N.M., Alemu, H., Verdin, J.P., 2013b. Operational Evapotranspiration Mapping Using Remote Sensing and Weather

Datasets: A New Parameterization for the SSEB Approach. J. Am. Water Resour. Assoc. 49, 577–591. https://doi.org/10.1111/jawr.12057

Senay, G.B., Friedrichs, M., Singh, R.K., Velpuri, N.M., 2016. Evaluating Landsat 8 evapotranspiration for water use mapping in the Colorado River Basin. Remote Sens. Environ. 185, 171–185. https://doi.org/10.1016/j.rse.2015.12.043

Senay, G.B., Gowda, P.H., Bohms, S., Howell, T. a., Friedrichs, M., Marek, T.H., Verdin, J.P., 2014. Evaluating the SSEBop approach for evapotranspiration mapping with landsat data using lysimetric observations in the semi-arid Texas High Plains. Hydrol. Earth Syst. Sci. Discuss. 11, 723–756. https://doi.org/10.5194/hessd-11-723-2014

Seneviratne, S.I., Corti, T., Davin, E.L., Hirschi, M., Jaeger, E.B., Lehner, I., Orlowsky, B., Teuling, A.J., 2010. Investigating soil moisture – climate interactions in a changing climate : A review. Earth-Sciences Rev. 99, 125–161. https://doi.org/10.1016/j.earscirev.2010.02.004

Simonneaux, V., Duchemin, B., Helson, D., Er-Raki, S., Olioso, A., Chehbouni, A.G., 2008. The use of high-resolution image time series for crop classification and evapotranspiration estimate over an irrigated area in central Morocco. Int. J. Remote Sens. 29, 95–116. https://doi.org/10.1080/01431160701250390

Singh, R., Senay, G., Velpuri, N., Bohms, S., Scott, R., Verdin, J., 2014. Actual Evapotranspiration (Water Use) Assessment of the Colorado River Basin at the Landsat Resolution Using the Operational Simplified Surface Energy Balance Model. Remote Sens. 6, 233–256. https://doi.org/10.3390/rs6010233

Singh, R.K., Irmak, A., 2009. Estimation of crop coefficients using satellite remote sensing. J. Irrig. Drain. Eng. 135, 597–608. https://doi.org/10.1061/(ASCE)IR.1943-4774.0000052

Sobrino, J. a, Mattar, C., Pardo, P., Jiménez-Muñoz, J.C., Hook, S.J., Baldridge, A., Ibañez, R., 2009. Soil emissivity and reflectance spectra measurements. Appl. Opt. 48, 3664–70.

Sobrino, J.A., Caselles, V., Becker, F., 1990. Significance of the remotely sensed thermal infrared measurements obtained over a citrus orchard. ISPRS J. Photogramm. Remote Sens. 44, 343–354. https://doi.org/10.1016/0924-2716(90)90077-O

Sobrino, J.A., Del Frate, F., Drusch, M., Jiménez-Muñoz, J.C., Manunta, P., Regan, A., 2016. Review of thermal infrared applications and requirements for future high-resolution sensors. IEEE Trans. Geosci. Remote Sens. 54, 2963–2972. https://doi.org/10.1109/TGRS.2015.2509179

Sobrino, José A, Jiménez-muñoz, J.C., Sòria, G., Romaguera, M., Guanter, L., Moreno, J., Plaza, A., Martínez, P., 2008. Land Surface Emissivity Retrieval From Different VNIR and TIR Sensors. IEEE Trans. Geosci. Remote Sens. 46, 316–327.

Sobrino, J. A., Jiménez-Muñoz, J.C., Sòria, G., Gómez, M., Ortiz, a. B., Romaguera, M., Zaragoza, M., Julien, Y., Cuenca, J., Atitar, M., Hidalgo, V., Franch, B., Mattar, C., Ruescas, A., Morales, L., Gillespie, A., Balick, L., Su, Z., Nerry, F., Peres, L., Libonati, R., 2008. Thermal remote sensing in the framework of the SEN2FLEX project: field

measurements, airborne data and applications. Int. J. Remote Sens. 29, 4961–4991. https://doi.org/10.1080/01431160802036516

Sobrino, J.A., Li, Z.L., Stoll, M.P., Becker, F., 1996. Multi-channel and multi-angle algorithms for estimating sea and land surface temperature with ATSR data. Int. J. Remote Sens. 17, 2089–2114. https://doi.org/10.1080/01431169608948760

Stefan, V.G., Merlin, O., Er-Raki, S., Escorihuela, M.J., Khabba, S., 2015. Consistency between In Situ, model-derived and high-resolution-image-based soil temperature endmembers: Towards a robust data-based model for multi-resolution monitoring of crop evapotranspiration. Remote Sens. 7, 10444–10479. https://doi.org/10.3390/rs70810444

Su, Z., 2002. The Surface Energy Balance System (SEBS) for estimation of turbulent heat fluxes. Hydrol. Earth Syst. Sci. 6, 85–100. https://doi.org/10.5194/hess-6-85-2002

Suárez, F., Muñoz, J., Fernández, B., Dorsaz, J.-M., Hunter, C., Karavitis, C., Gironás, J., 2014. Integrated Water Resource Management and Energy Requirements for Water Supply in the Copiapó River Basin, Chile. Water 6, 2590–2613. https://doi.org/10.3390/w6092590

Twine, T.E., Kustas, W.P., Norman, J.M., Cook, D.R., Houser, P.R., Meyers, T.P., Prueger, J.H., Starks, P.J., Wesely, M.L., 2000. Correcting eddy-covariance flux underestimates over a grassland. Agric. For. Meteorol. 103, 279–300. https://doi.org/10.1016/S0168-1923(00)00123-4

Velpuri, N.M., Senay, G.B., Singh, R.K., Bohms, S., Verdin, J.P., 2013. A comprehensive evaluation of two MODIS evapotranspiration products over the conterminous United States: Using point and gridded FLUXNET and water balance ET. Remote Sens. Environ. 139, 35–49. https://doi.org/10.1016/j.rse.2013.07.013

Vermote, E., Justice, C., Claverie, M., Franch, B., 2016. Preliminary analysis of the performance of the Landsat 8/OLI land surface reflectance product. Remote Sens. Environ. 185, 46–56. https://doi.org/10.1016/j.rse.2016.04.008

Vermote, E., Tanré, D., Deuzé, J.L., Herman, M., Morcrette, J., 1997. Second Simulation of the Satellite Signal in the Solar Spectrum, 6S: An Overview. IEEE Trans. Geosci. Remote Sens. 35, 675–686.

Wagner, W., Lemoine, G., Rott, H., 1999. A method for estimating soil moisture from ERS Scatterometer and soil data. Remote Sens. Environ. 70, 191–207. https://doi.org/10.1016/S0034-4257(99)00036-X

Walker, J.P., Willgoose, G.R., Kalma, J.D., 2001. One-dimensional soil moisture profile retrieval by assimilation of near-surface observations: A comparison of retrieval algorithms. Adv. Water Resour. 24, 631–650. https://doi.org/10.1016/S0309-1708(00)00043-9

Wang, L., Qu, J.J., 2009. Satellite remote sensing applications for surface soil moisture

monitoring: A review. Front. Earth Sci. China 3, 237–247. https://doi.org/10.1007/s11707-009-0023-7

Wang, W., Smith, J.A., Ramamurthy, P., Baeck, M.L., Bou-Zeid, E., Scanlon, T.M., 2016. On the correlation of water vapor and CO2: Application to flux partitioning of evapotranspiration. Water Resour. Res. 52, 9452–9469. https://doi.org/10.1002/2015WR018161

Werner, B.; Collins, R. et. al., 2012. Towards efficient use of water resources in Europe. EEA Report | No 1/2012, European Environment Agency, Copenhagen. https://doi.org/10.2800/95096

Wetzel, P.J., Atlas, D., Eoodward, R.H., 1984. Determining soil moisture from geosynchronous satellite infrared data: A feasibility study. J. Clim. Appl. Meteorol. https://doi.org/10.1175/1520-0450(1984)023<0375:DSMFGS>2.0.CO;2

Yang, G., Pu, R., Zhao, C., Huang, W., Wang, J., 2011. Estimation of subpixel land surface temperature using an endmember index based technique: A case examination on ASTER and MODIS temperature products over a heterogeneous area. Remote Sens. Environ. 115, 1202–1219. https://doi.org/10.1016/j.rse.2011.01.004

Yang, H., Cong, Z., Liu, Z., Lei, Z., 2010. Estimating sub-pixel temperatures using the triangle algorithm. Int. J. Remote Sens. 31, 6047–6060. https://doi.org/10.1080/01431160903376373

Zhan, W., Chen, Y., Zhou, J., Wang, J., Liu, W., Voogt, J., Zhu, X., Quan, J., Li, J., 2013. Disaggregation of remotely sensed land surface temperature: Literature survey, taxonomy, issues, and caveats. Remote Sens. Environ. 131, 119–139. https://doi.org/10.1016/j.rse.2012.12.014

Zhang, X., Qiu, J., Leng, G., Yang, Y., Gao, Q., 2018. The Potential Utility of Satellite Soil Moisture Retrievals for Detecting Irrigation Patterns in China. Water 10, 1–19. https://doi.org/10.3390/w10111505

Zhao, P., Li, S., Li, F., Du, T., Tong, L., Kang, S., 2015. Comparison of dual crop coefficient method and Shuttleworth-Wallace model in evapotranspiration partitioning in a vineyard of northwest China. Agric. Water Manag. 160, 41–56. https://doi.org/10.1016/j.agwat.2015.06.026

Zribi, M., André, C., Decharme, B., 2008. A method for soil moisture estimation in Western Africa based on the ERS scatterometer. IEEE Trans. Geosci. Remote Sens. 46, 438–448. https://doi.org/10.1109/TGRS.2007.904582

Zribi, M., Chahbi, A., Shabou, M., Lili-Chabaane, Z., Duchemin, B., Baghdadi, N., Amri, R., Chehbouni, A., 2011. Soil surface moisture estimation over a semi-arid region using ENVISAT ASAR radar data for soil evaporation evaluation. Hydrol. Earth Syst. Sci. 15, 345–358. https://doi.org/10.5194/hess-15-345-2011

Zribi, M., Dechambre, M., 2003. A new empirical model to retrieve soil moisture and roughness from C-band radar data. Remote Sens. Environ. 84, 42–52. https://doi.org/10.1016/S0034-4257(02)00069-X

Appendices

Appendix 1. Reference evapotranspiration (ET_0)

Reference evapotranspiration (ET_0) is estimated according to ASCE standardized for a short crop based on Penman-Monteith method as follows:

$$ET_0 = \frac{0.408 * \Delta * (Rn - G) + \gamma * \frac{900}{Ta + 273} * u_2 * (e^0 - e_a)}{\Delta + \gamma * (1 + 0.34 * u_2)}$$ Eq. A.1 1

$$\Delta = \frac{4098 * 0.6108 * exp\left(\frac{17.27 * Ta}{Ta + 273}\right)}{(Ta + 273.3)^2}$$ Eq. A.1 2

$$\gamma = 0.665.10^{-3} * Pa$$ Eq. A.1 3

$$e_a = \frac{e^0(Ta_{min})\frac{RH_{max}}{100} + e^0(Ta_{max})\frac{RH_{min}}{100}}{2}$$ Eq. A.1 4

$$e^0(Ta) = 0.6108 * exp\left[\frac{17.27\,Ta}{Ta + 273.3}\right]$$ Eq. A.1 5

$$u_2 = u_z \frac{4.87}{ln(67.8 * z - 5.42)}$$ Eq. A.1 6

$$Pa = 101.3\left(\frac{293 - 0.0065 * z}{293}\right)^{5.26}$$ Eq. A.1 7

$$Ra = \frac{24 * 60}{\pi} * G_{sc} . d_r\,[\omega_s . sin(\delta) . sin(\varphi) + cos(\varphi) . cos(\delta) . sin(\omega_s)]$$ Eq. A.1 8

$$d_r = 1 + 0.033 * cos\left(\frac{2\pi}{365} J\right)$$ Eq. A.1 9

$$\delta = 0.409 * sin\left(\frac{2\pi}{365} * J - 1.39\right)$$ Eq. A.1 10

$$\omega_s = acos[-tan(\varphi)\ tan(\delta)]$$ Eq. A.1 11

$$Rns = (1 - \alpha) * Rg$$ Eq. A.1 12

$$Rnl = \sigma \left[\frac{T_{max,K}^4 + T_{min,K}^4}{2}\right] \left(0.34 - 0.14\sqrt{e_a}\right) \left(1.35\ \frac{Rg}{Rso} - 0.35\right)$$ Eq. A.1 13

$$Rso = (0.75 + 2 * 10^{-5} z) * Ra$$ Eq. A.1 14

$$Rn = Rns - Rnl$$ Eq. A.1 15

where ET_0 : reference evapotranspiration (mm day^{-1})

Rg : incident solar radiation at short wavelengths (MJ day^{-1})

Rn : net radiation (MJ day^{-1})

Rns : net shortwave radiation (MJ day^{-1})

Rnl : net longwave radiation (MJ day^{-1})

Rso : solar radiation in clear sky condition (MJ day^{-1})

G : soil heat flux (MJ m^{-2}day^{-1})

Ta : daily mean air temperature at 2 m height (°C)

RH : relative humidity (%)

Pa : atmospheric pressure at elevation z (kPa)

z : elevation (m)

u_2 : wind speed at 2 m height (m s^{-1})

e_a : actual vapour pressure (kPa)

e^0 : saturation vapour pressure function (kPa)

G_{sc} : solar constant (equal to 0.0820 MJ m^{-2} min^{-1})

d_r : inverse relative distance Earth-Sun (-)

J : day of the year (-)

α : albedo (-)

Δ : slope vapour pressure curve (kPa $°C^{-1}$)

γ : psychrometric constant (kPa $°C^{-1}$)

ω_s : sunset hour angle (rad)

φ : latitude (rad)

σ : Stefan-Boltzmann constant ($4.903*10^{-9}$ MJ $K^{-4}m^{-2}day^{-1}$)

Appendix 2. Energy balance model for bare soil

The soil surface energy balance can expressed as:

$$Rn_s - G_0 = H_s + LE_s \quad \text{Eq. A.2 1}$$

With Rn_s being the net radiation, G_0 the soil heat flux, H_s sensible heat flux and LE_s the latent heat flux for soil surface.

The Rn_s is estimated as follows:

$$Rn_s = (1 - a_1)Rg + \varepsilon_s(Ra - \sigma T_s^4) \quad \text{Eq. A.2 2}$$

where α_s (-) is the soil albedo, Rg (Wm^{-2}) the incident solar radiation at short wavelengths, ε_s (-) the soil emissivity, Ra ($W\ m^{-2}$) the incident radiation at long wavelengths, σ ($Wm^{-2}K^{-4}$) the Stefan–Boltzmann constant and Ts (K) the soil temperature. For the feasibility study in R3 area (Section 3.4), ε_s was obtained from measurements made by Olioso et al. (2007) over the area. Note that for the spatial application with remote sensing data over the area, ε_s was obtained according to the method presented in Section 2.4.1.2.

The G_0 was approximated as a fraction of the Rn_s according to Kustas and Daughtry (1990):

$$G_0 = 0.32Rn_s \quad \text{Eq. A.2 3}$$

The H_s is computed as:

$$H_s = \frac{\rho C_p (T_s - T_a)}{r_{ah}} \quad \text{Eq. A.2 4}$$

where ρ ($Kg\ m^{-3}$) is the air density, C_p ($J\ Kg^{-1}K^{-1}$) the specific heat of air at constant pressure and r_{ah} the aerodynamic resistance. The LE_s is estimated as:

$$LE_s = \frac{\rho C_p}{\gamma}\left(\frac{e(T_s) - e_a}{r_a + r_{ss}}\right) \quad \text{Eq. A.2 5}$$

with γ being the psychrometric constant (Pa), $e(T_s)$ the saturated vapor pressure at soil temperature (Pa), e_a the vapor pressure in the canopy air space (Pa), and r_{ss} the soil surface resistance ($s\ m^{-1}$). r_{ss} is considered as a function of surface soil moisture (Sellers et al., 1992):

$$r_{ss} = exp\left[A - B\frac{SM}{SM_{fc}}\right] \quad \text{Eq. A.2 6}$$

where the two best fit parameters A (unitless) and B (unitless) are considered as 8 and 5 re- spectively (Kustas et al., 1993; Crow et al., 2008). By prescribing a soil evaporation resistance rss equal to zero and infinity (in practice a very large number), the minimum and maximum soil temperatures (Ts_{max} and Ts_{min}) can be estimated for a given atmospheric forcing.

The r_{ah} is estimated as:

$$r_a = \frac{1}{ku_*}\left[ln\left(\frac{z_r - d}{z_{0m}}\right) - \psi_h\right] \quad \text{Eq. A.2 7}$$

with k being the von Karman constant (k = 0.4), u_* (ms^{-1}) the friction velocity, z_r (m) the height of reference data, d the zero plane displacement (0 for bare soil), z_{0m} (m) the soil surface roughness length for momentum transport, ψ_h the stability correction for heat transfer which is estimated as function of Monin-Obukhov length (L_{MO}). The r_{ah} is estimated by implementing an iterative computation to estimate the T_s at equilibrium by using the formalism based on the Monin-Obukhov similarity theory, taking into account the L_{MO}:

$$L_{MO} = -\frac{\rho C_p T_a u_*^3}{kg\left(H + 0.61 C_p T_a L E_s\right)} \quad \text{Eq. A.2 8}$$

with u∗ (ms−1) being the friction velocity and expressed as:

$$u_* = \frac{uk}{ln\left(\frac{z_r - d}{z_{0m}}\right) - \psi_m} \quad \text{Eq. A.2 9}$$

with ψ_m being the stability correction for momentum transfer and is estimated as:

$$\psi_m = \frac{\psi_h}{2} + 2ln\frac{1+x}{2} - 2\arctan(x) + 0.5\pi \quad \text{Eq. A.2 10}$$

*T*he ψ_h is given by:

$$\psi_h = 2ln\frac{1+x^2}{2}$$ Eq. A.2 11

with x being function of the L_{MO} and of the reference height for wind speed observations (z_r):

$$x = \left(1 - 16\frac{z_r}{L_{MO}}\right)^{0.25}$$ Eq. A.2 12

Appendix 3. List of publications

1. **L. Olivera-Guerra**, O. Merlin, S. Er-Raki. 2020. Irrigation retrieval from Landsat optical/thermal data integrated into a crop water balance model. *Remote Sensing of Environment , 239, 11627*, https://doi.org/10.1016/j.rse.2019.111627.
2. **L. Olivera Guerra**, O. Merlin, S. Er-raki, S. Khabba, M-J. Escorihuela. 2018. Estimating the water budget components of irrigated crops: Combining the FAO-56 dual crop coefficient with surface temperature and vegetation index data. *Agricultural Water Management*, 208, 120-131, https://doi.org/10.1016/j.agwat.2018.06.014
3. **L. Olivera-Guerra**, C. Mattar, O. Merlin, C. Durán-Alarcón, A. Santamaría-Artigas, R. Fuster. 2017. An operational method for the disaggregation of land surface temperature to estimate actual evapotranspiration in the arid region of Chile. *ISPRS Journal of Photogrammetry and Remote Sensing,* 128, 170–181, http://dx.doi.org/10.1016/j.isprsjprs.2017.03.014
4. N. Ojha, O. Merlin, **L. Olivera-Guerra**, G. Indrio, B. Aït Hssaine, A. Amazirh, C. Suere, A. Al-Bitar, B. Molero, M. J. Escorihuela, S. Er-Raki. 2019. Stepwise disaggregation of SMOS and SMAP soil moisture at 100 m resolution using a varying intermediate resolution *Remote Sensing*, 11, 1863, https://doi.org/10.3390/rs11161863.
5. Rafi Z., O. Merlin, V. Le Dantec, S. Khabba, P. Mordelet, S. Er-Raki, A. Amazirh, **L. Olivera-Guerra**, B. Ait Hssaine, V. Simonneaux, J. Ezzahar, & F. Ferrer. 2019. Partitioning evapotranspiration of a drip-irrigated wheat crop: inter-comparing eddy covariance-, sap flow-, lysimeter- and FAO-based methods. *Agricultural and Forest Meteorology*, 265, 310–326, https://doi.org/10.1016/j.agrformet.2018.11.031.
6. O. Merlin, **L. Olivera-Guerra**, B. Aït Hssaine, A. Amazirh, Y. Malbéteau, Z. Rafi, Y. Ezzahar, P. Gentine, S. Khabba, S. Gascoin, S. Er-Raki. 2018. A phenomenological model of soil evaporative efficiency using surface soil moisture and temperature data. *Agricultural and Forest Meteorology*, 256–257, 501–515, https://doi.org/10.1016/j.agrformet.2018.04.010.
7. O.A. Eweys, M.J. Escorihuela, J.M. Villar, S. Er-Raki, A. Amazirh, **L. Olivera-Guerra**, L. Jarlan, S. Khabba, O. Merlin. 2017. Disaggregation of SMOS Soil Moisture to 100 m Resolution Using MODIS Optical/Thermal and Sentinel-1 Radar Data: Evaluation over a Bare Soil Site in Morocco. *Remote Sensing*, 9(11), 1155, https://doi.org/10.3390/rs9111155

Appendix 4. List of presentations and posters in peer reviewed conferences

1. **L. Olivera-Guerra**, O. Merlin, S. Er-Raki, M. J. Escorihuela, F. Fontanet. Irrigation Mapping at the Crop Field Scale Using a Combined Optical/Thermal Data and FAO-Based Modeling. ESA Living Planet Symposium 2019 (LPS19), Milan, Italy, May 13 – 17, 2019.
2. Ojha N., O. Merlin, **L. Olivera-Guerra**, M. J. Escorihuela, S. Er-Raki. Disaggregation of SMOS Soil Moisture at 100 m resolution using Landsat data and a stepwise approach. Living Planet Symposium 2019 (LPS19), Milan, Italy, May 13 – 17, 2019.
3. **L. Olivera-Guerra**, O. Merlin, S. Er-Raki, M. J. Escorihuela, F. Ferrer. Mapping of crop stress coefficient from high-resolution thermal and vegetation index data for irrigation management. Remote Sensing & Hydrology Symposium (RSHS18), Cordoba, Spain, May 8 – 10, 2018.
4. **L. Olivera-Guerra**, O. Merlin, S. Er-Raki, S. Khabba, M. J. Escorihuela, F. Ferrer. Estimation of root-zone soil moisture by combining the FAO-56 dual crop coefficient model with land surface temperature and vegetation index data for irrigation management. In Proc. EGU, Vienna, Austria, April 8 – 13, 2018.
5. Rafi Z., O. Merlin, V. Le Dantec, S. Khabba, P. Mordelet, S. Er-Raki, A. Amazirh, **L. Olivera-Guerra**, B. Ait Hssaine, V. Simonneaux, J. Ezzahar, & F. Ferrer. Partitioning of evapotranspiration into soil evaporation and plant transpiration of a drip-irrigated crop: combining various approaches. In Proc. EGU, Vienna, Austria, April 8 – 13, 2018.
6. Ojha N., O. Merlin, B. Molero-Rodenas, C. Suere, **L. Olivera**, V. Rivalland, S. Er-Raki. Sequential downscaling of the SMOS soil moisture at 100 m resolution via a variable intermediate spatial resolution. In Proc. IGARSS, Valencia, Spain. 2018.
7. Merlin, O., **Olivera-Guerra, L.**, Aït Hssaine, B., Amazirh, Malbéteau, Y., Stefan, V., Molero, B., Rafi, Z., Escorihuela, M-J., Ezzahar, Khabba, S., Walker, J., Kerr, Y., Simonneaux, S., Er-Raki, S. Evaporation-based disaggregation of surface soil moisture data: the dispatch method, the catds product and on-going research. In Proc. IGARSS, Texas, USA, July 23 – 28, 2017.
8. S. Er-Raki, A. Amazirh, **L. Olivera-Guerra**, S. Khabba, O. Merlin, J. Ezzahar, V. Simonneaux, A. Chehbouni, L. Jarlan. Using the selective assimilation procedure of soil moisture data in FAO- 56 model for improving evapotranspiration estimates over wheat crop in a semi-arid region. In Proc. 5th International Symposium on Recent Advances in Quantitative Remote Sensing (RAQRS' V), Valencia, Spain, September 18 – 22, 2017.
9. M. J. Escorihuela, O. Merlin, S. Er-Raki, F. Ferrer, Q. Gao, O. A. Eweys, **L. Olivera-Guerra**, A. Amazirh, B. AitHssaine, M. Fontanet, S. Khabba, M. Zribi. Estimation of high temporal and spatial resolution soil moisture for crop irrigation management by multi-sensor remote sensing approach. In Proc. 5th International Symposium on Recent Advances in Quantitative Remote Sensing (RAQRS' V), Valencia, Spain, September 18 – 22, 2017.

AUTHOR: Luis Enrique OLIVERA GUERRA

TITLE: Monitoring the water budget of irrigated crops from multi-spectral optical/thermal remote sensing data

THESIS DIRECTOR: Olivier MERLIN
THESIS CO-DIRECTOR: Salah ER-RAKI

PLACE AND DATE OF DEFENSE: CESBIO - Centre d'Etudes Spatiales de la Biosphère
Le 11 décembre 2019

ABSTRACT

Irrigation represents an important pressure on water resources in arid and semi-arid regions. Monitoring irrigation is thus crucial for a sustainable management of water resources. We propose an innovative approach to quantify the crop water budget of agricultural areas by means of irrigation, evapotranspiration and root-zone soil moisture estimates at crop field scale (100 m) on a daily basis over extended areas. The methodology relies on the integration of readily available optical/thermal satellite data into a simplified crop water balance model. Since the frequency of current satellite data is a critical point, we propose an operational disaggregation method to enhance the spatial and temporal resolution of thermal data. This thesis demonstrates the utility of high spatial resolution optical/thermal data to estimate, for the first time, daily irrigations at field scale and hence to better close the water budget over agricultural areas.

KEYWORDS: remote sensing, optical/thermal, irrigation, root-zone soil moisture, evapotranspiration, water balance model.

ADMINISTRATIVE DISCIPLINE: Continental surfaces and interfaces, Hydrology

---

TITLE AND ADDRESS OF THE U.F.R. OR THE LABORATORY: CESBIO - Centre d'Etudes Spatiales de la Biosphère

AUTEUR : Luis Enrique OLIVERA GUERRA

TITRE : Suivi des ressources des cultures irriguées à par télédétection multi-spectrales optique/thermique

DIRECTEUR DE THESE : Olivier MERLIN
CO-DIRECTEUR DE THESE : Salah ER-RAKI

LIEU ET DATE DE SOUTENANCE : CESBIO - Centre d'Etudes Spatiales de la Biosphère
Le 11 décembre 2019

RESUME

L'irrigation est une pression importante sur les ressources en eau dans les régions arides et semi-arides. Le suivi de l'irrigation est donc crucial pour assurer une gestion durable de l'eau. Nous proposons une approche innovante pour quantifier le bilan d'eau à travers l'estimation journalière de l'irrigation, l'évapotranspiration et l'humidité en zone racinaire à l'échelle de la parcelle (ou 100 m de résolution). La méthodologie se base sur l'intégration de données satellitaires optiques/thermiques dans un modèle simplifié du bilan d'eau. La fréquence des données satellitaires actuelles étant un point critique, nous proposons une méthode opérationnelle de désagrégation pour améliorer la résolution spatio-temporelle des données thermiques. Cette thèse démontre l'utilité des données optiques/thermiques à haute résolution spatiale pour estimer, pour la première fois, les irrigations journalières à l'échelle de parcelle et ainsi pour mieux contraindre le bilan d'eau des zones agricoles.

MOTS-CLES : télédétection optique/thermique, irrigation, humidité en zone racinaire, évapotranspiration, modèle de bilan hydrique.

DISCIPLINE ADMINISTRATIVE : Surfaces et interfaces continentales, Hydrologie

---

INTITULE ET ADRESSE DE L'U.F.R. OU DU LABORATOIRE : CESBIO - Centre d'Etudes Spatiales de la Biosphère